2007

PFI-ZEKE SPECTROSCOPY AND THEORETICAL CALCULATIONS OF TRANSITION METAL-AROMATIC HYDROCARBON COMPLEXES

Bradford Raymond Sohnlein
University of Kentucky, brsohn0@uky.edu

ABSTRACT OF DISSERTATION

Bradford Raymond Sohnlein

The Graduate School

University of Kentucky

2007

PFI-ZEKE SPECTROSCOPY AND THEORETICAL CALCULATIONS OF TRANSITION METAL-AROMATIC HYDROCARBON COMPLEXES

ABSTRACT OF DISSERTATION

A dissertation submitted in partial fulfillment of the
requirements for the degree of Doctor of Philosophy in the
College of Arts and Sciences
at the University of Kentucky

By
Bradford Raymond Sohnlein

Lexington, Kentucky

Director: Dr. Dong-Sheng Yang, Professor of Chemistry

Lexington, Kentucky

2007

ABSTRACT OF DISSERTATION

PFI-ZEKE SPECTROSCOPY AND THEORETICAL CALCULATIONS OF TRANSITION METAL-AROMATIC HYDROCARBON COMPLEXES

Transition metal-aromatic hydrocarbon complexes were generated in a supersonic jet and studied by zero electron kinetic energy (ZEKE) photoelectron spectroscopy and theoretical calculations. The target metal complexes were identified using time-of-flight mass spectrometry, and their ionization thresholds were located via photoionization efficiency spectroscopy. ZEKE spectroscopy was used to measure the ionization energies and vibrational frequencies of the metal complexes. Their electronic states and corresponding molecular structures were determined by comparing the experimental spectra to quantum chemical calculations and Franck-Condon simulations.

In this dissertation, the metal complexes of four different aromatic hydrocarbon ligands were studied: benzene (bz), naphthalene (np), biphenyl (bp) and 1-phenyl naphthalene (phnp). In these complexes, the metal atom or ion was determined to bind to either one or two π-rings. Three different bonding schemes were observed in these complexes. A twofold bonding scheme was observed in M^+/M-np (M = Sc, Y, Ti, Zr, Hf), while a sixfold bonding scheme was observed in Sc^+/Sc-bz and M^+/M-bz_2 (M = Sc, Ti, V, Cr, Mo, W). In the metal-polyphenyl complexes (i.e. Sc-, La-, and Ti-bp and Sc-phnp), twelve-fold metal-ligand bonding occurred, sixfold to two π-rings of the ligand. This twelve-fold bonding mechanism requires rotation of the π-rings by ~ 42 ^{o} and bending of the π-rings by 40 to 57 ^{o} to clamp the metal atom or ion between the two π-surfaces.

Although the ground state spin multiplicities of the bare metal atoms and ions varied quite extensively, the multiplicities of the metal complexes were determined to be either singlet or doublet, except for Sc^+/Sc-bz, V^+-bz_2, Ti-np, and Zr-np, where the triplet or quartet spin multiplicities were favored. The low spin and relatively narrower range of electron-spin multiplicities in the complexes were the result of *d* orbital splitting, where the degeneracy of the *d* orbitals was broken. Thus, the valence electrons were paired in each metal *d*-based molecular orbital of the complex to form low-spin singlet or doublet spin states. Some complexes favored triplet and quartet multiplicities, because the energy difference between the two highest occupied molecular orbitals was smaller than the electron pairing energy.

KEYWORDS: Photoionization Efficiency Spectroscopy, ZEKE Spectroscopy, Transition Metal-Aromatic Hydrocarbon Complexes, Quantum Chemical Calculations, Franck-Condon Simulations

Brad Sohnlein

July 23, 2007

PFI-ZEKE SPECTROSCOPY AND THEORETICAL CALCULATIONS OF TRANSITION METAL-AROMATIC HYDROCARBON COMPLEXES

By

Bradford Raymond Sohnlein

Dr. Dong-Sheng Yang
Director of Dissertation

Dr. Robert Grossman
Director of Graduate Studies

July 23, 2007

RULES FOR THE USE OF DISSERTATIONS

Unpublished dissertations submitted for the Doctor's degree and deposited in the University of Kentucky Library are as a rule open for inspection, but are to be used only with due regard to the rights of the authors. Bibliographical references may be noted, but quotations or summaries of parts may be published only with the permission of the author, and with the usual scholarly acknowledgements.

Extensive copying or publication of the dissertation in whole or in part also requires the consent of the Dean of the Graduate School of the University of Kentucky.

A library that borrows this dissertation for use by its patrons is expected to secure the signature of each user.

Name	Date

DISSERTATION

Bradford Raymond Sohnlein

The Graduate School

University of Kentucky

2007

PFI-ZEKE SPECTROSCOPY AND THEORETICAL CALCULATIONS OF TRANSITION METAL-AROMATIC HYDROCARBON COMPLEXES

DISSERTATION

A dissertation submitted in partial fulfillment of the
requirements for the degree of Doctor of Philosophy in the
College of Arts and Sciences
at the University of Kentucky

By
Bradford Raymond Sohnlein

Lexington, Kentucky

Director: Dr. Dong-Sheng Yang, Professor of Chemistry

Lexington, Kentucky

2007

Dedicated to my family, mentor, and friends…

ACKNOWLEDGEMENTS

This work could not have been accomplished without the support that I received from my mentor, advisory committee members, lab mates, departmental staff workers, friends, and family. I am grateful for their assistance, whether it was monetary, intellectual, or emotional, and I appreciated the time, effort, and patience that they have devoted towards my scientific aspirations and life goals.

My advisor, Dr. Dong-Sheng Yang, provided numberless, and much needed, discussions about my research progress and agendas over the past seven years during my studies as an undergraduate and graduate research assistant. His research methods and ideas motivated me to learn science and apply this knowledge to the field of physical chemistry. His dedication and commitment to scientific research is very admirable and inspiring. His sincerity, friendliness, and compassion generated an enjoyable environment in which to live, learn, work, and study. The knowledge and character he instilled in me will certainly be valued as I continue to pursue my career objectives.

My committee members have supplied the appropriate guidance and attention towards my intellectual growth as well. Dr. Dennis J. Clouthier taught me many of the fundamental aspects of my research inside and outside the classroom. His vast knowledge in spectroscopy and theoretical chemistry is impressive and served as a valuable resource during my academic career at the University of Kentucky (UK). As a crystallographer, Dr. Carolyn P. Brock provided a different perspective in our data analysis and research planning. Her broad awareness in the various fields of chemistry was very insightful and meaningful. Dr. Keith B. MacAdam, Professor of Physics, jogged my memory about some basic principles of physics that were used to further

understand various experimental measurements and phenomena. His scientific opinions were greatly appreciated and helpful. Over the past five years, all committee members were eager to share their wisdom with me. I, too, hope to pass on this wisdom to the next generation of scientists.

Co-workers Dr. Shenggang Li, Dr. Yuxiu Lei, Dr. Sergiy Krasnokutskiy, Dr. Jason F. Fuller, Dr. Gretchen Rothschopf, Dr. Xu Wang, Mr. Jung S. Lee, Ms. Paragranjita Bhowmik, and Mr. Benjamin M. Wilson are acknowledged for their intellectual insight and friendship. I have enjoyed working with such a culturally diverse group of people who are kind, compassionate, and supportive. I am also very grateful for their help in executing various experimental tasks and solving computational dilemmas. I especially want to acknowledge Dr. Shenggang Li who has offered his expertise with no hesitation, even after graduating and leaving UK in 2004. The simulation program he wrote is amazingly fast and accurate. His exceptional technological skills and friendship will always be remembered and valued.

As an experimental scientist, I am especially appreciative to those who helped maintain the performance of our instrument: Mr. Art Sebesta (electronics), Mr. Herb Mefford (instrumental hardware), Mr. Jeff Babbitt (glassware), and Mr. Edward Duhr and the late Mr. Terry Todd (computer software and hardware). Without their keen assistance, instrument performance would not have been maximized, and unnecessary downtime would have been distressing to our research efforts.

I am indebted to the Department of Chemistry for teaching assistantships, the Chemistry Teaching Assistant of the Year Award, and the Fast Start Award; to the Graduate School for financial assistance in my travels to the International Symposia on

Molecular Spectroscopy at the Ohio State University and for the annually renewed Tuttle Fellowships; and to my mentor for research assistantships, which were funded through grants from the National Science Foundation, the Petroleum Research Fund administrated by the American Chemical Society, the Center for Computational Sciences at UK, and the Kentucky Science and Engineering Fund.

Last but not least, I am grateful for the guidance and support of my loving family. My parents, Barbara L. Sohnlein and E. Ray Sohnlein, instilled in me at an early age the importance of higher education. Without their financial support, my undergraduate career would have been extremely exhausting and unpleasant. Besides their monetary assistance, I also appreciate their confidence in my intellectual ability. Over the years, they have increased my self-confidence by recognizing my academic and personal achievements. I now feel that I can accomplish any goal set before me. Thank you, mom and dad; the most I ever wanted, was the least I got.

TABLE OF CONTENTS

LIST OF TABLES

LIST OF FIGURES

CHAPTER 1: INTRODUCTION

1.1 Metal-Aromatic Hydrocarbon Complexes

The term *aromatic* was initially used to classify a group of organic compounds based on their sweet-smelling scent, even before their molecular structures were determined. Of the aromatic hydrocarbon compounds, benzene (bz = C_6H_6) is one of the simplest and most extensively studied. Michael Faraday was the first to isolate this arene by collecting the liquid that condensed from the gas that was burned in street lamps of London, England in 1825.[1] However, the currently accepted molecular structure of benzene was not proposed until 1874 by Wilhelm Korner prior to the development of resonance theory, but after the bromo substitution experiments by Kekulé.[1] As advances in research continued in the following years, the definition of aromaticity evolved. To a modern-day scientist, an aromatic compound is a cyclic molecule that is especially stabilized through resonance. Due to the nature of the molecular orbitals (MOs), this resonance stabilization requires $4n + 2$ electrons in its conjugated π-system(s), where n = 0, 1, 2, …

The $4n + 2$ rule can be understood by comparing, for instance, the MO diagrams of aromatic benzene and antiaromatic cyclobutadiene (C_4H_4). The corresponding MO diagrams are drawn in Figure 1.1. In these MO diagrams, the nonbonding orbitals are arbitrarily labeled at zero energy units as designated by the blue dashed line. Accordingly, bonding and anti-bonding orbitals must lie below and above the blue line, respectively. From the relative molecular orbital energies, the six π electrons in benzene and the four π electrons in cyclobutadiene must fill the MOs as depicted by Figure 1.1. In the case of benzene, all electrons are paired and occupy the three sets of bonding orbitals. In cyclobutadiene, on the other hand, the degenerate pair of highest occupied molecular orbitals (HOMOs) contains two unpaired electrons. Furthermore, the HOMOs of cyclobutadiene are nonbonding, which provide no energy stabilization. Hence, the highly reactive cyclobutadiene can only be prepared at temperatures lower than 35 K.[1]

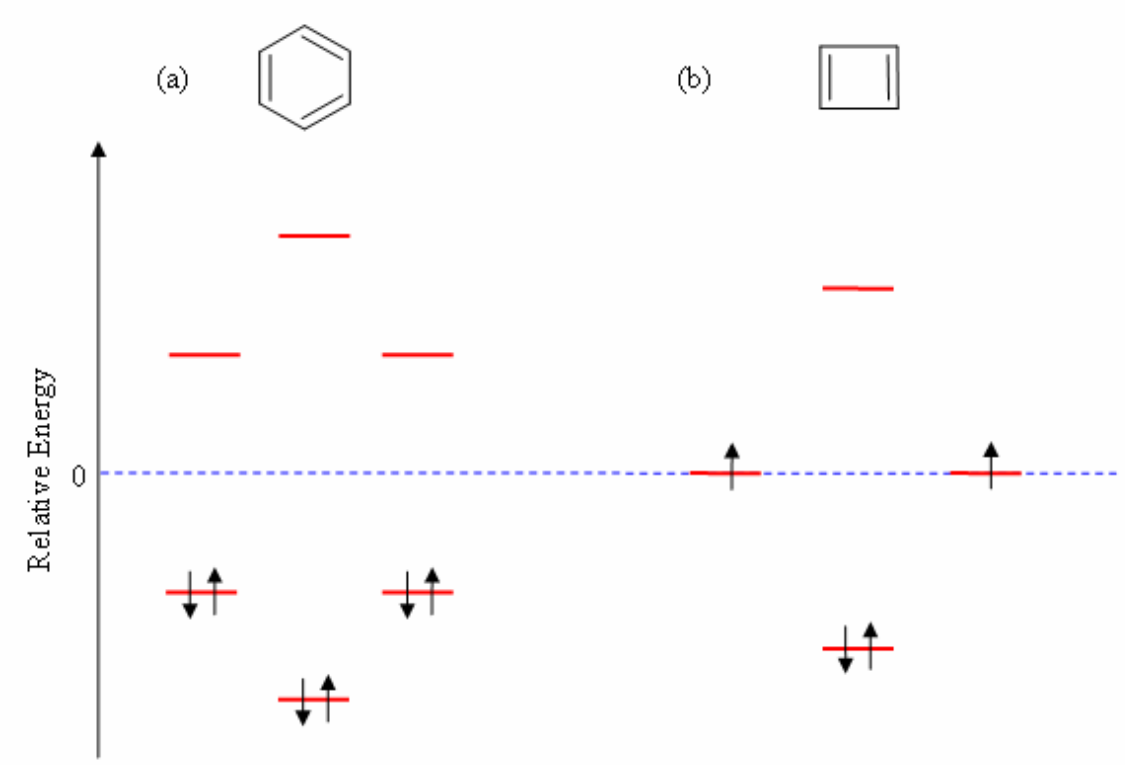

Figure 1.1. MO diagram of aromatic benzene (a) and antiaromatic cyclobutadiene (b).

Cyclobutadiene and other cyclic compounds that contain only $4n$ conjugated π electrons are termed antiaromatic.

The field of organometallic chemistry was established in 1827 when W.C. Zeise synthesized the first organometallic complex, $K[PtCl_3(C_2H_4)]\cdot H_2O$, commonly known as Zeise's salt.[2] In this complex, the $PtCl_3$ moiety was determined to bind to ethene (C_2H_4) in a side-on fashion. Despite their knowledge of the molecular structure, theoretical chemists could not explain the bonding in this relatively simple organometallic compound for over 125 years. Finally, in the early 1950's, the bonding in this and other similar organometallic complexes was understood via a synergistic bonding scheme. In this bonding model, today known as the Dewar-Chatt-Duncanson model, the organic ligand donates π electrons to empty *d* orbitals of the metal, while the metal atom or ion back-donates *d* electrons to the empty π* antibonding orbitals of the ligand. Both donation and back-donation increases the bond order of the metal-ligand bond, while reducing the bond order of the participating ligand bonds. The number of ligand atoms that participate in metal-ligand bonding is called the hapticity and is denoted by η^x, where the superscripted *x* is the number of metal-ligand bonds. For example, Zeise's salt is more appropriately written as $K[PtCl_3(\boldsymbol{\eta^2}\text{-}C_2H_4)]\cdot H_2O$, since platinum binds to both carbon atoms of the ethene molecule.

In 1952, organometallic chemistry was revolutionized by the discovery of the metal-aromatic hydrocarbon compound, ferrocene. Ferrocene consists of one Fe^{2+} cation sandwiched between two cyclopentadiene anions. Like many molecules composed of main block elements, the stability of inorganic transition metal complexes depends not on the octet rule, but the so-called 18-electron rule. The incorporation of transition metals into organic compounds introduces the *d* subshell. The *d* subshell has five different components; each of these components is typically abbreviated by a subscripted z^2, $x^2\text{-}y^2$, xy, xz, or yz as a label for each of the differently shaped orbitals. Because an additional 10 electrons are needed to fill the *d* subshell, the total number of electrons required to form a noble gas-like electron configuration is 18. Transition metal complexes that obey the 18-electron rule are said to have closed shells and are, consequently, very stable. Ferrocene satisfies the 18-electron rule, because the Fe^{2+} center and both cyclopentadiene anions each have six bonding electrons ($3 \times 6 = 18$). Hence, this compound can be easily

synthesized, bottled, and distributed. Which brings about an important question: why do chemists want to study metal-aromatic compounds?

1.2 Motivations

The industrialized world is constantly developing new technologies to improve the quality of life on modern earth. These technological advances have been the result of ongoing scientific research. In many cases, the initial motivations for such investigations are not clearly predefined, especially in the field of physical chemistry. For example, the work of Wilhelm Conrad Röntgen was not initiated to discover X-ray radiation. Rather, in the course of his studies on cathode rays, Röntgen speculated that an invisible form of radiation existed.[3] Due to the unknown nature of these rays, he called them X-rays. Today, X-rays are widely used in medical, industrial, and research facilities for a variety of purposes. These applications were certainly not the incentive for Röntgen's work, but provide an example of how fundamental research can lead to the development of new technologies. Like the motivation behind Röntgen's work, the primary motivation for studying the energetics of and bonding in metal-aromatic systems is fundamental curiosity. However, such research could ultimately lead to a number of useful applications, as did the discovery X-ray radiation.

The theme of this dissertation revolves around the interaction between transition metals and aromatic hydrocarbon molecules such as benzene, naphthalene (np), biphenyl (bp), and 1-phenylnaphthalene (phnp). The structures and corresponding molecular formulas of these aromatic ligands are presented in Figure 1.2. The molecular structures of these ligands have many similarities but vast differences as well. All four molecules are composed of only carbon and hydrogen atoms and have at least one benzene ring. In the benzene molecule, each carbon atom is chemically identical via resonance. Accordingly, the molecular symmetry of benzene can be represented by the D_{6h} point group. In naphthalene, biphenyl, and 1-phenylnaphthalene, on the other hand, many of the carbon atoms have different chemical environments. As a result, these ligands will have different C-C bond lengths, bond strengths, and, of course, reactivity. In addition,

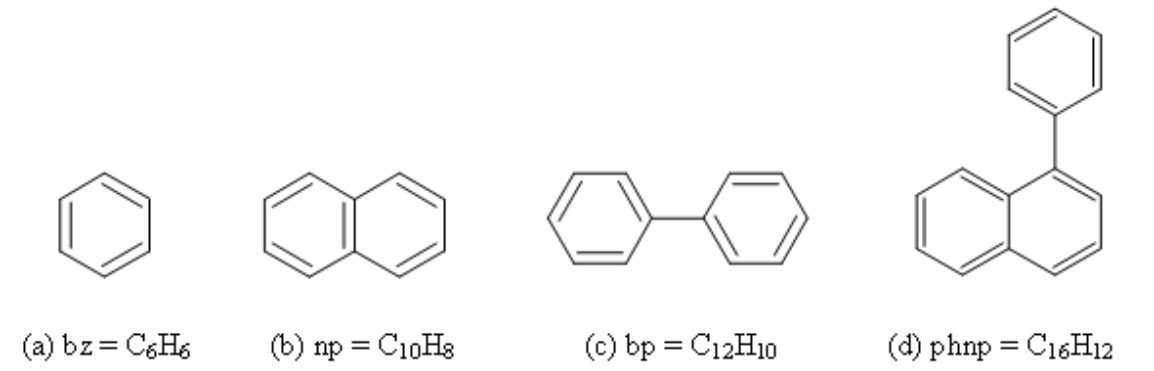

Figure 1.2. Structures and molecular formulas of (a) benzene, (b) naphthalene, (c) biphenyl, and (d) 1-phenylnaphthalene. The associated abbreviations are also provided below each structure.

these three ligands have different structural aspects. In naphthalene, the two chemically equivalent benzene rings are joined together by a fused C-C bond. Thus, naphthalene is a flat, rigid structure represented by the D_{2h} point group. On the other hand, the two equivalent benzene rings in biphenyl are connected by a junction C-C σ bond, where the two rings are able to rotate at room temperature. Consequently, a biphenyl molecule is generally non-planar and has D_2 symmetry. The dihedral angle between the two phenyl rings ($\sim 40^{o}$) is maintained by a balance between steric repulsions of the ortho hydrogen atoms and π conjugation. The former interaction favors a twisted configuration, whereas the latter favors a planar configuration. In phenylnaphthalene, the three inequivalent rings are connected by both a fused C-C bond and a junction C-C σ bond. Due to the junction bond, 1-phenylnaphthalene is not flat either and has no symmetry (C_1).

From a fundamental point of view, it would be very interesting to determine how various transition metal atoms and ions bind to these similar, yet structurally different aromatic hydrocarbon molecules. Such gas phase studies could expand the scientific community's knowledge about intrinsic metal-ligand bonding, where interferences from surrounding solvent and counterion molecules are removed. Further background and motivations for studying each specific complex is presented in the introduction section of each chapter.

1.3 Structural Determination via Spectroscopy

The primary objective of this work is to determine the molecular structures of various metal-aromatic hydrocarbon complexes. Assuming these molecular species can be generated, how can their structures be determined? In this day and age, the structures of such subnanoscopic particles are deduced primarily by spectroscopic measurements.

Spectroscopy was developed in the 1800's after the discovery of the Fraunhofer absorption lines in the sun's spectrum and Herschel's observation of various flame colors when burning different metal salts.[4] Continuous interest and motivation to understand these peculiar phenomena ultimately led to the establishment of modern-day spectroscopy. These days, applications in spectroscopy are quite broad: from the

nondestructive dating of ancient artifacts,[5, 6] to the detection of various biochemical hazards in the environment,[7, 8] to petroleum fractionation and hydrocarbon analysis in oil production.[9] Scientists also use a range of spectroscopic methods for structural determination of various inorganic, organic, and biological molecular systems to continue to expand our knowledge of chemistry, physics, and biology. Certainly, spectroscopy has been beneficial to the progress of mankind; but, how does it work?

1.3.1 Conventional Photoelectron Spectroscopy

Spectroscopy requires a light source, a sample, and a detector. The sample is irradiated by the light source, and the resulting event is recorded by the detector. The detected event can have different forms like photons, electrons, or ions. The spectroscopic method used in our research laboratory is based on the photoelectric effect in which electrons are detected. First, the target molecule absorbs a photon of light with known energy, $\Delta E = h\nu$, where h is Planck's constant and ν is the frequency of the light source. If the energy of the initial photon is greater than or equal to the ionization energy, then an electron will be ejected. Because this electron is removed by light energy, the resultant free electron is called a photoelectron. When the various energy levels of a molecule are probed by detecting these emitted photoelectrons, the spectroscopic technique is called photoelectron spectroscopy (PES).

In conventional PES, light with a fixed wavelength is used to remove electrons from a particular sample. Figure 1.3(a), for example, shows a diagram of a generic molecule, A, that absorbs a photon (indicated by a vertical blue/red arrow) with fixed energy significantly larger than the ionization energy of A. Some of the light energy will be consumed as internal energy by shifting population from the ground electronic state of the neutral molecule to that of the ionic molecule [left arrow in Figure 1.3(a)]. The excess light energy not used in this ionization process is converted to kinetic energy (KE) of the ejected electron. Thus, the ionization energy (IE) can be calculated by measuring the KE of the photoelectron: $IE = h\nu - KE$. However, more light energy could also be consumed by populating higher energy levels of the corresponding ionic molecule. In

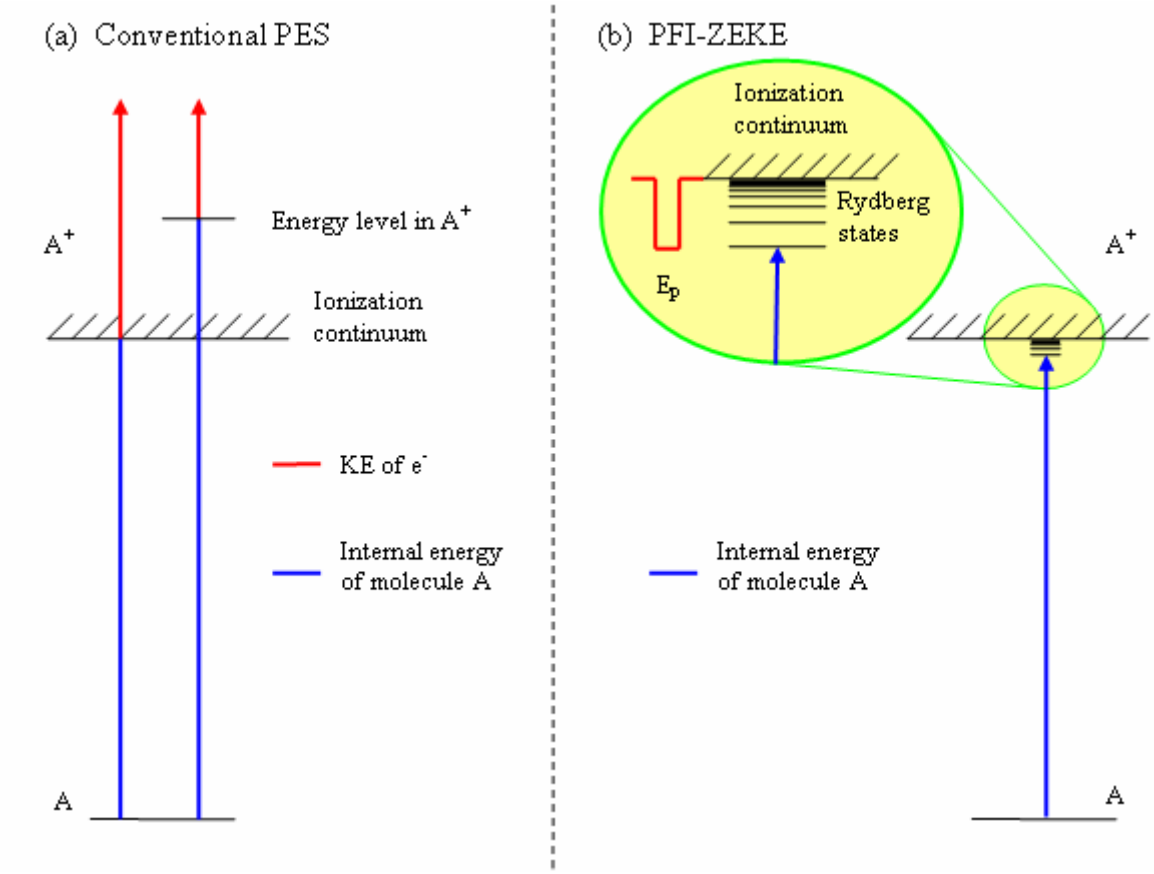

Figure 1.3. In conventional PES (a), the wavelength is fixed and the kinetic energies (KE) of the ejected electrons are measured. In PFI-ZEKE PES (b), the wavelength is scanned while only those electrons with zero kinetic energy are detected. In this method, the molecule is first photoexcited to high-lying Rydberg states followed by delayed pulsed electric field (E_p) ionization.

this case, the ejected electrons will have comparatively less KE as indicated by the right photon in Figure 1.3(a). Using this conventional PES method, the IEs of the neutral molecule are determined by recording the KE distribution of the photoelectrons. From these IE values, the molecular orbital energies may be derived according to Koopman's theorem: IE = $-e_i$, where e_i is the molecular orbital energy. Thus, PES provides direct insight into the bonding and molecular structures. The conventional PES method is advantageous, because a tunable light source is not required. In addition, the conventional PES method has no fundamental limitation on its resolution. However, the practical resolution of PES is unfortunately limited by difficulties in separating electrons with very small KE differences. An alternative method is to collect electrons with fixed KE while scanning the laser frequency. When the electron KE is fixed at zero, this spectroscopic method is called zero electron kinetic energy (ZEKE) spectroscopy.

1.3.2 Pulsed Field Ionization-ZEKE Spectroscopy

In 1984, Müller-Dethlefs, Sander, and Schlag developed the ZEKE spectroscopic method to overcome the practical resolution of the conventional PES technique (~ 10 meV), where separating electrons with very small KE differences is currently limited.[10] In the ZEKE method, on the other hand, the resolution depends primarily on the linewidth of the light source. In pulsed field ionization (PFI) ZEKE spectroscopy, the laser frequency is scanned through ionization thresholds. At particular resonant frequencies during the scan, the neutral molecule is photoexcited to high-lying Rydberg states (principal quantum number $n > 150$) as indicated in Figure 1.3(b). These high-lying Rydberg states of the neutral molecule converge to various eigenstates of the corresponding ionic species. In these Rydberg states, the electron is considered to orbit an ionic core that closely resembles the ionized molecule. Due to the high principal and angular momentum quantum numbers (n and l), the electron has a spherically shaped orbit in these states, and the electron-core interaction can essentially be described by a simple Coulomb force. In other words, the electron-core distance is so large that the ionic core resembles a point charge with respect to the orbiting electron. Strong l- and

m_l-mixing (m_l = the magnetic component of l), as a result of stray fields and nearby ions, is known to significantly enhance these Rydberg state lifetimes to the microsecond scale.[11]

These high-lying Rydberg states can be ionized by supplying a small pulsed electric field as shown in Figure 1.3(b). Hence, this technique is commonly referred to as the pulsed field ionization method (PFI-ZEKE). Prior to triggering the pulsed electric field, the high-lying Rydberg states are located in a pseudocontinuum with a high density of states, just a few cm^{-1} below the real ionization continuum. When the pulsed electric field is fired, the pseudocontinuum is converted to a real ionization continuum, and the Rydberg electrons are removed. Besides inducing ionization, the pulsed electric field also accelerates the generated ZEKE electrons towards the detector. Because these Rydberg electrons are originally located in pseudocontinua just below the ionization threshold, ionization energies measured via PFI-ZEKE spectroscopy are red shifted. This field-induced IE shift ($\delta = d \cdot \sqrt{E_P}$, where δ is the IE shift in cm^{-1}, E_P is the magnitude of the pulsed electric field in V cm^{-1}, and d is a fitting constant) can be determined by recording IE measurements as a function of field strength (E_P) and extrapolating to zero field. Such measurements have shown that the typical field-induced shift is much smaller than the linewidths measured in the ZEKE spectra of metal organic complexes.[12] As a result, this field-induced shift is usually neglected in our data analysis, but appears as a part of our measurement uncertainty.

The main advantage of PFI-ZEKE spectroscopy is that electrons with kinetic energy can be efficiently separated from ZEKE electrons. To speed up the removal of prompt electrons produced directly by photoionization, a small DC field is applied to the extraction cans (details of the experimental apparatus and procedures are discussed in Chapter 2). This small field efficiently removes all kinetic energy electrons within ~ 1 μs of firing the photoexcitation laser. After this short time period, the long-lived, high-lying Rydberg states will have still survived. Furthermore, ionization of these Rydberg states via the pulsed electric field generates ZEKE electrons that provide the same information as those produced directly from photoionization, because ionization cross-sections are continuous through the threshold. Additionally, resolutions on the order of a few cm^{-1} for a variety of metal-ligand complexes have routinely been achieved via ZEKE spectro-

scopy.[12-28] Consequently, many research groups have turned to PFI-ZEKE spectroscopy as a means by which to improve their spectral resolution. Moreover, this PES technique is fairly easy to implement as long as a tunable laser light source is available.

ZEKE spectroscopy provides direct evidence for the structures of metal complexes, because low-frequency metal-ligand vibrational modes are measured. Metal-ligand vibrational modes typically have frequencies below 500 cm^{-1} due to the relatively weak bonding between the metal atom or ion and the organic ligand. Using a simple harmonic oscillator approximation, the vibrational frequency is directly proportional to the square root of the force constant and inversely proportional to the square root of the reduced mass. In molecules, the stretching force constant between two atoms is related to the bond dissociation energy (*BDE*) along that coordinate. In other words, harmonic stretch force constants measure the binding strength at the bottom of the potential energy well. Nevertheless, compared to carbon-carbon covalent bonds, metal-carbon bonds are much weaker. For example, the *BDE*s of CH_3-CH_3 and Sc-CH_3 are 90.2 ± 0.2 and 28 ± 2 kcal mol^{-1}, respectively.[29] Hence, the frequencies of metal-ligand vibrational modes ($\lesssim$ 500 cm^{-1}) are lower than those of the corresponding ligand-based modes ($\gtrsim$ 500 cm^{-1}). Furthermore, nearly all metal elements are heavier than the corresponding component elements of most organic ligands, i.e. hydrogen, carbon, nitrogen, and oxygen. Therefore, the reduced mass along the metal-ligand coordinate is larger than those along ligand-based coordinates. Thus, metal-ligand vibrational modes have inherently lower frequencies than ligand-based vibrational modes.

One advantage of ZEKE spectroscopy is that low-frequency modes of the ionic complex can be measured, because the photoexcitation laser is scanned through the ionization thresholds. Although the same information can be obtained through IR spectroscopic measurements, generating laser frequencies below 500 cm^{-1} is generally more difficult than scanning through UV regions of the electromagnetic spectrum. Also, vibrational (IR) transitions are generally weaker than electronic (UV) transitions. Moreover, various IR windows are required to permit different IR wavelengths to penetrate the detection chamber. Fortunately, ZEKE spectroscopy provides a simpler means by which to measure vibrational frequencies below 500 cm^{-1}.

In addition to measuring metal-ligand vibrational frequencies, the ionization

energies of metal complexes can be determined very accurately via ZEKE spectroscopy. These measured ionization energies can be used in a thermodynamic cycle to derive the bond dissociation energy of the neutral metal complex. Figure 1.4 illustrates the relationship between ionization energies and bond dissociation energies of metal-ligand (M-L) complexes. In this figure, two potential energy curves for the neutral and ionic metal-ligand complexes are represented by the red and blue curved lines, respectively. Neutral molecules have lower energies than the corresponding ionized molecule, because ionization processes require energy (i.e. light) to remove an electron. The molecular structure at the bottom of the potential energy well corresponds to the equilibrium geometry of the M^+/M-L complex. Careful inspection of these two potential energy wells reveals some subtle differences between the two. First of all, the shapes of these curves are not identical, because the potential energy surface is a function of the geometrical structure. Depending on the chemical system and ionization process, the difference between potential energy surfaces of the neutral and ionized molecules may vary substantially. The relationship between the potential energy surfaces of neutral and ionized molecules will be discussed in more detail in the "Theoretical Calculations" section of this chapter. In addition to these well shape differences, both potential wells may have different zero point energies, as indicated by the black horizontal line at the bottom of each well. Zero point energies are related to the vibrational energy associated with molecules when the vibrational quantum number (v) is zero. The quantum mechanic harmonic oscillator energy levels (E_v) are related to the vibrational quantum number by

$$E_v = \hbar\omega_i(v + ½) \qquad v = 0, 1, 2, \ldots \qquad \textbf{(1-1)},$$

where $\hbar = h/2\pi$ and ω_i is the vibrational frequency of mode i. Thus, even at v = 0, the vibrational energy takes on a positive value ($½\hbar\omega_i$). The total zero point energy is the sum of the $E_{v=0}$ terms over all 3N-6 (nonlinear molecules) or 3N-5 (linear molecules) vibrational modes of the molecule. Hence, if zero point energies are incorporated with the electronic energy (E_{ele}), the term is abbreviated by E_0.

Metal-ligand bond strengths in the ion complex are typically stronger than those in the corresponding neutral complex, because the addition of an ion-multipole inter-

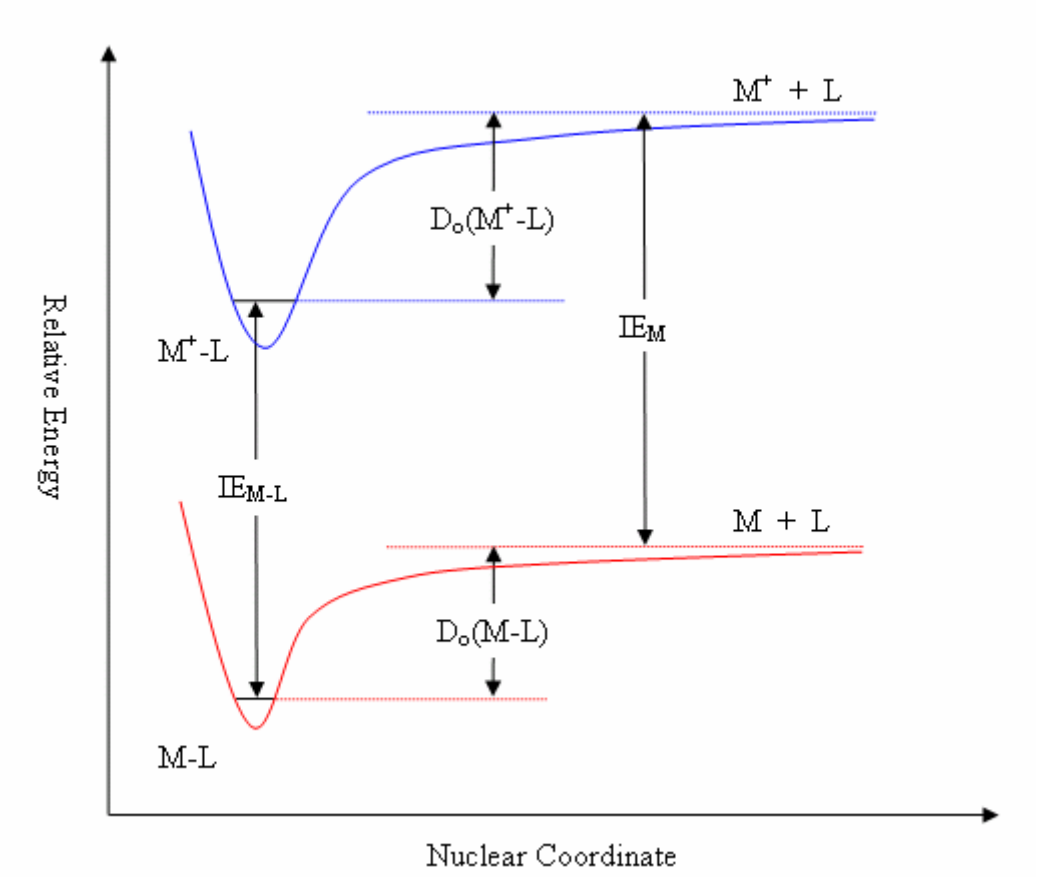

Figure 1.4. Thermodynamic relationship between BDEs and IEs of metal complexes as a function of the potential energy surfaces. IE_{M-L} = ionization energy of M-L complex; IE_M = ionization energy of bare metal atom; D_o(M-L) = bond dissociation energy neutral M-L complex; $D_o(M^+-L)$ = bond dissociation energy of ionic M^+-L complex. Further details are explained in the text.

action that is not present in neutral molecules. Hence, vibrational frequencies in the corresponding ionic complex are often larger than those in the neutral complex, because frequencies are directly proportional to the square root of the force constant. Thus, the zero point energy of ionic molecules is generally larger than the corresponding neutral complex, as drawn in the potential energy surface diagram. This zero point energy is a result of the Heisenberg uncertainty principle,[30] which states that the exact location and momentum of a particle cannot be simultaneously measured to infinite precision. Mathematically, the Heisenberg uncertainty principle is often expressed as

$$\Delta x \Delta p_x > \hbar \quad \textbf{(1-2)}$$

where Δx is the uncertainty in position, and Δp_x is the uncertainty in momentum. This uncertainty principle requires nonzero momenta for all particles; otherwise, the uncertainty in momentum would be zero (infinite precision). In addition, the position of such a stationary particle would be precisely known, because the particle is not moving. Thus, all particles must have momentum, and, therefore, kinetic energy. However, the uncertainty principle only has a practical impact at the molecular scale due to the magnitude of $\hbar$. A molecule consists of two or more atoms, and the momenta of these atoms must be nonzero according to equation 1-2. Thus, these atoms will have kinetic energy. However, chemical bonds within a molecule prevent the atoms from drifting far away from one another. As a result, the molecule must vibrate even at v = 0. Physically, this means atoms of a molecule are constantly moving, and the molecular structure at one point in time may vary slightly from the molecular structure at a different point in time.

Due to the uncertainty principle, experimental measurements will always include vibrational zero point energies. In other words, when recording the ionization energies of M-L complexes (IE_{M-L}), only the difference between the two potential energy surfaces at the zero point energy of each well can be measured. Of course, the IE of bare metal atoms (IE_M) does not include a vibrational zero point energy correction, because free atoms cannot vibrate; only molecules vibrate. Similarly, measured bond dissociation energies will include vibrational zero point energies. These bond dissociation energies are determined by measuring the energy difference as the metal atom or ion is pulled

infinitely far away from the ligand. When vibrational zero point energies are considered, the dissociation energies are typically abbreviated by D_o. As indicated by Figure 1.4, the dissociation energy of the ionic complex, $D_o(M^+\text{-}L)$, is generally larger than the dissociation energy of the corresponding neutral complex, $D_o(M\text{-}L)$. Stronger binding in the ion is attributed to the addition of an ion-multipole interaction not present in neutral molecules.

Figure 1.4 also illustrates that these energies are related to one another in a thermodynamic cycle by

$$D_o(M\text{-}L) + IE_{M\text{-}L} = IE_M + D_o(M^+\text{-}L) \quad \textbf{(1-3)}.$$

The ionization energies of bare transition metal atoms have already been determined very accurately by various experimental methods.[29] Thus, if the dissociation energy of the ionic complex is known, then the dissociation energy of the neutral complex can be derived by measuring the ionization energy of the metal complex. In our experiments, we do not measure the bond dissociation energies of the ionic complex. However, a number of research groups have measured bond dissociation energies of ionic complexes by methods such as collision-induced dissociation or photodissociation. By combining the results from these studies with the accurately measured ionization energies from ZEKE spectroscopy, the bond dissociation energy of the neutral complex is derived.

From ZEKE spectroscopy, vibrational frequencies and ionization energies are measured very accurately. These experimental results can be compared to results from *ab initio* theoretical calculations. Because metal-aromatic chemical systems are more complicated than ordinary organic molecules, our data also provide theoreticians with a benchmark for improving theoretical models. In addition, current theoretical methods that can reproduce the experimental results may be used to extrapolate additional information, such as the molecular structures and electronic states of the neutral and ionic complexes. Further reliability in the theoretical results is provided by comparing the experimental ZEKE spectra to multidimensional Franck-Condon (FC) simulations. The details of these calculations and simulations are discussed in the following two sections.

1.4 *Ab Initio* Theoretical Calculations

Ab initio calculations are considered to be from first principles, because the physical and chemical properties of molecules are derived only from fundamental postulates, such as those from quantum mechanical theory. In quantum mechanics, the essence of a molecule is described by its unique wavefunction, ψ. If the exact wavefunction is known, then the corresponding energy, *E*, of the molecule in an eigenstate can be solved for by the time-independent Schrödinger equation

$$\hat{H}\psi = E\psi \quad \textbf{(1-4)},$$

where $\hat{H}$ is a mathematical operator called the Hamiltonian and *E* is an eigenvalue (a constant) of the eigenfunction, ψ. Although the wavefunction of a system evolves with time, the probability density of a molecule in a given eigenstate is time-independent.[30] According to classical physics, the total energy of the molecular system is the sum of the kinetic energy and potential energy. The kinetic energy of any particle is related to its momentum, *p*, and mass, *m*, by

$$KE = \frac{p^2}{2m} \quad \textbf{(1-5)},$$

and the corresponding quantum mechanical operator for kinetic energy, $\hat{KE}$, is

$$\hat{KE} = -\frac{\hbar^2}{2m}\nabla^2 \quad \textbf{(1-6)},$$

where

$$\nabla^2 = \left(\frac{\partial^2}{\partial x^2} + \frac{\partial^2}{\partial y^2} + \frac{\partial^2}{\partial z^2}\right) \quad \textbf{(1-7)}.$$

These partial derivatives are taken over all space, that is the *x*, *y*, and *z* coordinates. Because molecules are composed of charged particles (protons and electrons), the potential energy term of the Hamiltonian must express the Coulomb interactions among these charged particles. For example, the Hamiltonian of a helium atom with fixed nucleus is

$$\hat{H}_{He} = -\frac{\hbar^2}{2m}\nabla_1^2 - \frac{\hbar^2}{2m}\nabla_2^2 - \frac{Ze^2}{4\pi\varepsilon_0 r_1} - \frac{Ze^2}{4\pi\varepsilon_0 r_2} + \frac{e^2}{4\pi\varepsilon_0 r_{12}} \quad \textbf{(1-8)},$$

where the subscripted 1 and 2 are electron labels, *m* is the mass of the electron, *Z* is the atomic number, *e* is the charge of an electron, r_1 and r_2 are the respective electron-nucleus distances for electron 1 and 2, r_{12} is the electron-electron distance, and ε_0 is the permittivity of free space. Because electrons generally move at a much higher speed than the nuclei, the nuclear kinetic energy term is often removed from the Hamiltonian as depicted in Equation 1-8. This reasonable approximation, proposed by Born and Oppenheimer in 1927, greatly simplifies quantum mechanical calculations.[31] Further Hamiltonian simplifications are often made using atomic units, where all the physical constants are set to unity. Thus, the electronic Hamiltonian operator for a helium atom in atomic units reduces to

$$\hat{H}_{He} = -\frac{1}{2}\nabla_1^2 - \frac{1}{2}\nabla_2^2 - \frac{Z}{r_1} - \frac{Z}{r_2} + \frac{1}{r_{12}} \quad \textbf{(1-9)},$$

and the units are called Hartrees, which are abbreviated by a.u. As complicated as the helium atom Hamiltonian seems, the energies could be solved for exactly, if the electron-electron repulsion term could be neglected. However, in molecular and atomic systems, the orbital paths of electrons are in fact correlated to one another due to like-like repulsions. This electron repulsion potential energy term of the Hamiltonian is consequently called the electron correlation energy. Because this equation cannot be solved directly, a variety of methods has been developed to approximate solutions to the Schrödinger equation for non-hydrogen-like systems (i.e. multi-electron systems). A

brief overview of the three methods employed in this dissertation, Hartree-Fock, Møller-Plesset perturbation, and density functional theories, will be described in more detail in the following three subsections.

1.4.1 Hartree-Fock Theory

The metal-aromatic systems studied in this work were calculated by either density functional theory (DFT) or so-called post-HF methods such as perturbation and coupled cluster theories. These calculations typically begin with an HF calculation. Although considered by many modern theoreticians to be a low-level calculation, HF mathematics is quite complicated. Some of these details are discussed in the following text.

In a generic molecular system of M nuclei and N electrons, the electronic Hamiltonian operator can be expressed in atomic units by

$$\hat{H} = \sum_{i}^{N}\left(-\frac{1}{2}\nabla_i^2 - \sum_{A}^{M}\frac{Z_A}{r_{iA}} + \sum_{j>i}^{N}\frac{1}{r_{ij}} \right) \quad \textbf{(1-10)},$$

where i and j are electron labels and A are nuclei labels. Again, the nuclear kinetic energy term is dropped according to the Born-Oppenheimer approximation.[31] In the HF Hamiltonian, the two-electron repulsion operator is replaced by a one-electron repulsion operator, where the ith electron is described as traveling in a mean field generated by the remaining $N-1$ electrons. This HF Hamiltonian operates on the HF molecular wavefunction, which was first expressed as a product of one-electron orbital functions, ϕ, as

$$\psi(r_1, r_2 \ldots r_n) = \phi_1(r_1)\phi_1(r_2)\ldots\phi_1(r_n) \quad \textbf{(1-11)}.$$

Later, Fock illustrated that the HF wavefunction as written in equation 1-11 violates the Pauli Exclusion Principle, because this wavefunction is not anti-symmetric with respect to the interchange of any two electrons. However, the wavefunction in Slater's

determinant notation

$$\psi = \frac{1}{\sqrt{N!}} \begin{vmatrix} \phi_1(r_1)\alpha(1) & \phi_1(r_1)\beta(1) & \phi_2(r_1)\alpha(1) & \cdots & \phi_{\frac{N}{2}}(r_1)\beta(1) \\ \phi_1(r_2)\alpha(2) & \phi_1(r_2)\beta(2) & \phi_2(r_2)\alpha(2) & \cdots & \phi_{\frac{N}{2}}(r_1)\beta(2) \\ \phi_1(r_3)\alpha(3) & \phi_1(r_3)\beta(3) & \phi_2(r_3)\alpha(3) & \cdots & \phi_{\frac{N}{2}}(r_1)\beta(3) \\ \vdots & \vdots & \vdots & \ddots & \vdots \\ \phi_1(r_N)\alpha(N) & \phi_1(r_N)\beta(N) & \phi_2(r_N)\alpha(N) & \cdots & \phi_{\frac{N}{2}}(r_1)\beta(N) \end{vmatrix} \quad \textbf{(1-12)},$$

where α and β represent the two spin orbitals in ϕ_N (i.e. spin up and spin down) for an N electron system is anti-symmetrized. The one-electron orbital functions in these anti-symmetrized HF wavefunctions are approximated as linear combinations of atomic orbitals (LCAOs); the atomic orbitals in these LCAOs are usually expressed as linear combinations of Gaussian-type basis functions. Using this anti-symmetrized wavefunction and the electronic Hamiltonian, the wavefunction and corresponding energies are solved by an iterative mathematical process known as the self-consistent field (SCF) procedure. In the first SCF cycle, the orbital coefficients of the wavefunction are guessed, and the electronic energy is calculated. In subsequent cycles, the predicted electronic energy is compared to the energy calculated in the previous cycle. Following the variational principle, the best solution to this SCF procedure is the set of coefficients of a given basis set that generates the lowest electronic energy. However, solutions to the Schrödinger equation using the HF method will never converge to the true energy, because HF calculations do not treat electron correlation. Thus, even for an infinitely large basis set, the Hartree-Fock limit will lie above the true energy. As a result, other methods have been developed to approximate the correlation energies due to instantaneous electron-electron interactions.

1.4.2 Møller-Plesset Perturbation Theory

Perturbation theories treat electron correlation as a small perturbation to the electronic HF Hamiltonian to address instantaneous electron-electron interactions. In perturbation theory, the total Hamiltonian operator, $\hat{H}$, is expressed as

$$\hat{H} = \hat{H}_0 + \lambda \hat{H}_1 \quad \textbf{(1-13)},$$

where $\hat{H}_0$ is the HF Hamiltonian operator, $\hat{H}_1$ is the difference between the exact electronic Hamiltonian and HF Hamiltonian operators, and λ is a perturbation parameter. As indicated by equation 1-13, these perturbation methods are often called post-HF theoretical methods, because the exactly solvable portion of the Schrödinger equation corresponds to the HF Hamiltonian operator. In perturbation theory, the wavefunction and energy of the system are expressed by the power series

$$\psi = \psi_0 + \psi_1 + \psi_2 + \cdots, \quad \textbf{(1-14)}$$

and

$$E = \lambda^0 E_0 + \lambda^1 E_1 + \lambda^2 E_2 + \cdots, \quad \textbf{(1-15)}$$

where ψ_n and E_n are the nth order corrections to the wavefunction and energy, respectively. Møller-Plesset perturbation calculations that include nth order corrections to the energy and wavefunction are denoted as MPn. In this dissertation, only second order corrections to the total energy were calculated (i.e. MP2). These MP2 calculations typically account for ~ 80 to 90 % of the electron correlation energy. Hence, MP2 is a widely used *ab initio* method for treating electron correlation, and it scales as the fifth power of the size of the system, relatively small compared to coupled cluster and configuration interaction *ab initio* methods. Because MPn calculations are nonvariational and frequently diverge from the true energy with increasing order, MP($n > 2$) calculations are rarely implemented. Additionally, calculations that involve several correction terms are often more difficult to converge using standard SCF algorithms. Nevertheless, MP2

calculations have predicted reliable structures and frequencies for a variety of metal-ligand complexes according to the good agreement between our experimental and simulated ZEKE spectra.[16, 18, 32-34]

1.4.3 Density Functional Theory

DFT, unlike MP2 and HF, is not a wavefunction-based method. Instead, the energy of the molecular system is expressed by a functional of electron density, $E[\rho(r)]$, by

$$E[\rho(r)] = T[\rho] + E_{ne}[\rho] + E_{ee}[\rho] \quad \textbf{(1-16)},$$

where the first, second, and third terms are kinetic energy, nuclear-electron attraction energy, and electron-electron repulsion energy, respectively, and $\rho(r)$ is the electron density, a function of three spatial coordinates. In a simple HF calculation, the single-electron repulsion operator works on an *average* electric field generated by the remaining N-1 electrons. In DFT, this average field is replaced by a probability term (i.e. the electron density). Because electrons are indistinguishable and their motions are correlated, the electron kinetic energy cannot be solved for exactly. In the Kohn-Sham approach to density functional theory, most of the electron kinetic energy is calculated, while the remaining unknown components are approximated. These unknown components of the electron energy are combined into a single term called the exchange-correlation energy, which is a functional of the electron density. Unfortunately, DFT lacks a systematic scheme for improving this approximate functional. Nevertheless, several approaches to describe the exchange-correlation functional have been proposed. For example, the DFT methods used in this dissertation are based on a generalized gradient approximation (GGA). Further mathematical details and more information about DFT, in general, can be found in a book by Koch and Holthausen.[35]

Due to the nature of the mathematics involved, DFT calculations are computationally cheap compared to wavefunction-based methods. In addition, many of

the metal-aromatic complexes in this dissertation could be described sufficiently by DFT methods alone.[12, 36-40] In some cases, DFT calculations predicted more reliable structures than those from MP2 theory according to the agreement between our experimental and simulated ZEKE spectra.[36, 41] Either way, these inexpensive calculations can quickly locate several ionic and neutral electronic states. Then the appropriate electronic states can be calculated using more expensive post-HF computational methods, if necessary.

1.5 Franck-Condon Spectral Simulations

1.5.1 The Franck-Condon Principle

The spectroscopist measures the transition energies and intensities among the states of a given chemical system. However, only specific transitions are allowed, and their intensities are normally governed by the Franck-Condon (FC) principle.[42-44] In ZEKE spectroscopy, both electronic and vibrational transitions are measured, and their intensities are proportional to the square of the transition moment integral, M_{ev},

$$M_{ev} = \int \psi^{*}_{e'v'} \hat{\mu} \psi_{e''v''} d\tau \quad \textbf{(1-17)},$$

where $\psi_{e'v'}$ and $\psi_{e''v''}$ are vibronic wavefunctions of the final and initial states, respectively, $\hat{\mu}$ is the transition dipole moment operator, and the asterisk denotes a complex conjugate. The transition dipole moment operator can be expressed as a linear combination of the electronic $\hat{\mu}_e$ and nuclear $\hat{\mu}_N$ dipole operators

$$\hat{\mu} = \mu_e + \mu_N \quad \textbf{(1-18)}.$$

According to the Born-Oppenheimer approximation,[31] the electrons move much faster than the nuclei in a vibronic transition. Thus, the electronic and nuclear components of the wavefunction and dipole operator can be treated separately. In this case, the transition moment integral becomes

$$M_{ev} = \left(\int \psi^*_{e'} \hat{\mu}_e \psi_{e''} d\tau_e\right)\left(\int \psi^*_{v'} \psi_{v''} d\tau_N\right) \quad \textbf{(1-19)},$$

where the first integral corresponds to the electronic transition moment integral and the second integral is the vibrational overlap integral, called the FC overlap integral. Thus, for a given electronic transition, where the electronic transition moment integral is nonzero, the intensities of vibrational transitions within that electronic band system are proportional to the Franck-Condon Factor (FCF), which is the square of the FC overlap integral,

$$I_{e'v' \leftarrow e''v''} \propto \left|\int \psi^*_{v'} \psi_{v''} d\tau_N\right|^2 \quad \textbf{(1-20)}.$$

According to group theory, the FCF will be nonzero when the direct product of the vibrational wavefunctions gives the totally symmetric representation. In an efficient supersonic expansion, the population is largely restricted to the v = 0 state of the neutral molecule. Consequently, only totally symmetric modes of the ion complex are ordinarily observed. However, the frequencies of asymmetric modes can also be measured through overtone transitions (e.g. $v' = 2 \leftarrow v'' = 0$), because the direct product of any two identical representations will at least contain the totally symmetric representation (e.g. $b_1 \otimes b_1 = a_1$). Likewise, combination transitions involving asymmetric vibrational modes may also be observed, if their direct product contains the totally symmetric representation.

The relative intensities of the vibronic transitions give direct information about the structural differences between the two electronic states. Consider, for example, the two vibronic transitions depicted in Figure 1.5. The three potential energy curves represent three different electronic states, labeled *A*, *B*, and *C*. In each of these electronic states, the wavefunction of various vibrational quanta of a single vibrational mode is drawn. According to this figure, the molecular structures in states *A* and *B* are similar, because the location of the equilibrium geometries is very similar. The molecular structure in state *C*, on the other hand, is quite different from those in states *A* and *B*. Because electronic transitions occur extremely fast, the heavy nuclei are considered to be frozen and the transitions are vertical. Thus, the FC overlap of the 0-0 transition in the

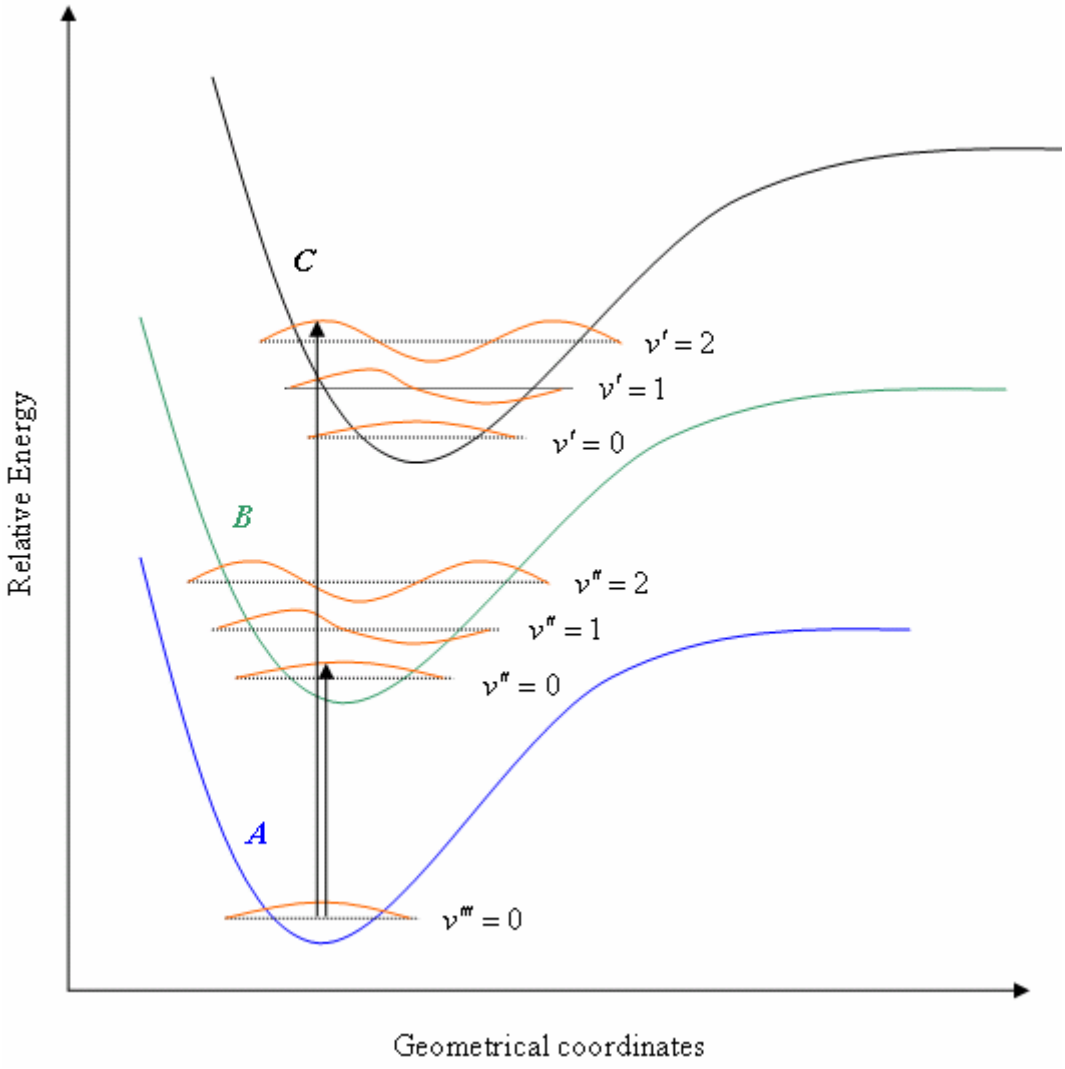

Figure 1.5. Vibrational overlap in two generic electronic transitions: B ← A and C ← A. The vibrational wavefunctions are designated by the orange curvy lines in each electronic state. The two vertical transitions are indicated by the black arrows.

B ← A transition is larger than that in the C ← A transition. On the other hand, the FC overlap of the 2-0 transition in the C ← A transition is larger than that in the B ← A transition. Therefore, spectra that contain strong 0-0 transitions and short vibrational progressions should probe initial and final states with similar molecular structures according to the FC principle. Spectra dominated by long vibrational progressions and weak 0-0 transitions, on the other hand, should probe initial and final electronic states with large structural differences. These spectral patterns can be modeled by calculating FCFs from the theoretical equilibrium geometries, harmonic frequencies, and normal coordinates of the neutral and ionic states obtained from *ab initio* calculations. Some of the details for this mathematical procedure are discussed in the next subsection.

1.5.2 Multidimensional Franck-Condon Factors

Although the calculation of multidimensional FCFs is typically simplified through the harmonic approximation, the mathematics is still quite complex. Further complications arise from the slightly displaced and rotated normal modes of the initial and final states. This slight deviation between the two normal coordinates of each state induces a mode-mixing effect that was first discovered and treated by Duschinsky in 1937.[45] Despite these complications, several theoreticians have developed an exact expression to calculate multidimensional FC overlap integrals.[46-63] These integrals are typically evaluated by transforming various matrices containing the calculated force-fields and equilibrium geometries. In effect, the FCFs are proportional to a displacement parameter, which is a function of the **L** transformation matrix, the masses, and the difference in equilibrium Cartesian coordinates of the initial and final states. The **L** matrix defines the transformation between the normal mode coordinates and displacements of the mass-weighted Cartesian coordinates from the equilibrium geometry. This matrix contains the set of eigenvectors of the mass-weighted Cartesian force constant matrix, **F**. Thus, this **L** matrix is typically generated by diagonalization of the force constant matrix.

The Duschinsky transformation assumes a linear and orthogonal transformation

between the normal coordinates of the two electronic states. Frequently, this transformation is neither linear nor orthogonal according to the axis-switching effect that is active during an electronic transition.[64-66] Thus, the simulations in this dissertation were calculated by the FCF program first developed in the mid-1990's[67, 68] and later improved by Li and Clouthier.[69, 70] The improved FCF program accounts for axis-switching effects by implementing a zero-th order Eckart matrix to ensure that the off-diagonal elements are diminished with each rotation. Further mathematical and computer programming details of this FCF simulation program can be found in Shenggang Li's Ph.D. dissertation[69] and elsewhere.[70]

1.5.3 FCF Simulation Program

The FCF simulation program used in this dissertation was written by Dr. Shenggang Li, who currently works at the University of Alabama in Tuscaloosa. This program calculates multidimensional FCFs using the recursion relations formulated by Doktorov et al.[47] Because the intensities of vibronic transitions are proportional to the square of the FCFs, spectral simulations are generated as a function of energy position, E, by

$$I(E) \propto \sum_{v} \sum_{v'} \left(\langle v|v'\rangle^2\right)\left(e^{\frac{-Ev}{kT}}\right)\left\{\frac{\gamma}{2\pi}\left[\left(E_o + E_{v'} - E_v - E\right)^2 + \left(\frac{\gamma}{2}\right)^2\right]^{-1}\right\} \quad \textbf{(1-21)},$$

where $I(E)$ is the relative intensity at an energy position, E; the first, second, and third terms in the product of the summations are the FCFs, the Boltzmann factor, and the line shape function, respectively; E_v and $E_{v'}$ are the vibrational energies of the initial and final states, respectively; and E_0 is the adiabatic ionization energy. This summation runs over all initial and final vibrational states, v and v', respectively. The Lorentzian line shape is adjusted according to the experimental linewidth that is measured as the full width at half maximum (FHWM), γ.

1.6 Overview of Thesis

The molecular structures of several transition metal-aromatic hydrocarbon complexes were determined via PFI-ZEKE spectroscopy. Structural determination was facilitated by combining spectroscopic measurements with *ab initio* theoretical calculations and spectral simulations. These experimental and computational methodologies are discussed in the next chapter. Chapters 3, 4, and 5 present the results and discussions for the transition metal-benzene complexes; Chapters 6 and 7 present the results and discussions for the transition metal-naphthalene complexes; and Chapters 8 and 9 present the results and discussions for the transition metal-polyphenyl complexes. Each of these chapters also introduces specific motivations for studying those particular molecular systems. Chapter 10 summarizes the ionization energies, electronic states, and metal-ligand stretch frequencies of all the transition metal complexes in this dissertation. The bibliography and my curriculum vita are attached to the end.

CHAPTER 2: METHODOLOGY

2.1 General Experimental Procedures

Metal-ligand complexes were prepared in a supersonic jet and studied by ZEKE spectroscopy. A general scheme of our experimental setup is illustrated by the block diagram in Figure 2.1. Metal-ligand complexes are prepared by the interaction of metal atoms with the appropriate organic ligand. The metal atoms are generated by laser vaporization of the appropriate metal rod and carried by an inert gas such as helium, argon, or a mixture thereof. The ligand is introduced downstream from the ablation source in a small collision chamber prior to expansion into the vacuum chamber. The supersonic molecular beam travels to the spectroscopy chamber, where the molecular species are photoionized or photoexcited by the second harmonic output of a dye laser (Lumonics, HD-500) pumped by the second or third harmonic of a Nd:YAG laser (Continuum, Surelite II). Molecular species are ionized, and the intensity of electrons or cations is recorded by a dual microchannel plate detector (MCP: Burle, 25/12/12 D EDR 40:1 MS). This analog signal is amplified by a preamplifier (Stanford Research Systems SR445), averaged by a boxcar integrator (Stanford Research Systems SR250), and digitally converted by an analog-to-digital converter. The resulting digital output is stored in a personal computer. To record a photoionization efficiency (PIE) or ZEKE spectrum, the photoionization or photoexcitation laser is scanned while recording the intensity of the cation or electron signal, respectively. These laser scans are controlled by the personal computer unit, which is directly interfaced with the dye laser.

Such an experimental scheme requires a specific sequence of events. The timings of each event are controlled by a pulsed delay generator (Stanford Research Systems DG535). The triggering sequence is labeled in the block diagram by 1^{st}, 2^{nd}, 3^{rd}, and V (variable). First, the pulsed valve driver is triggered (T_0) to open the pulsed valve. The time width and voltage magnitude of this pulse is adjusted manually on a homemade pulsed valve driver. As the gas pulse travels across the metal rod, the ablation laser is fired to entrain the metal atoms in the carrier gas. The timing of the ablation laser (T_{abl})

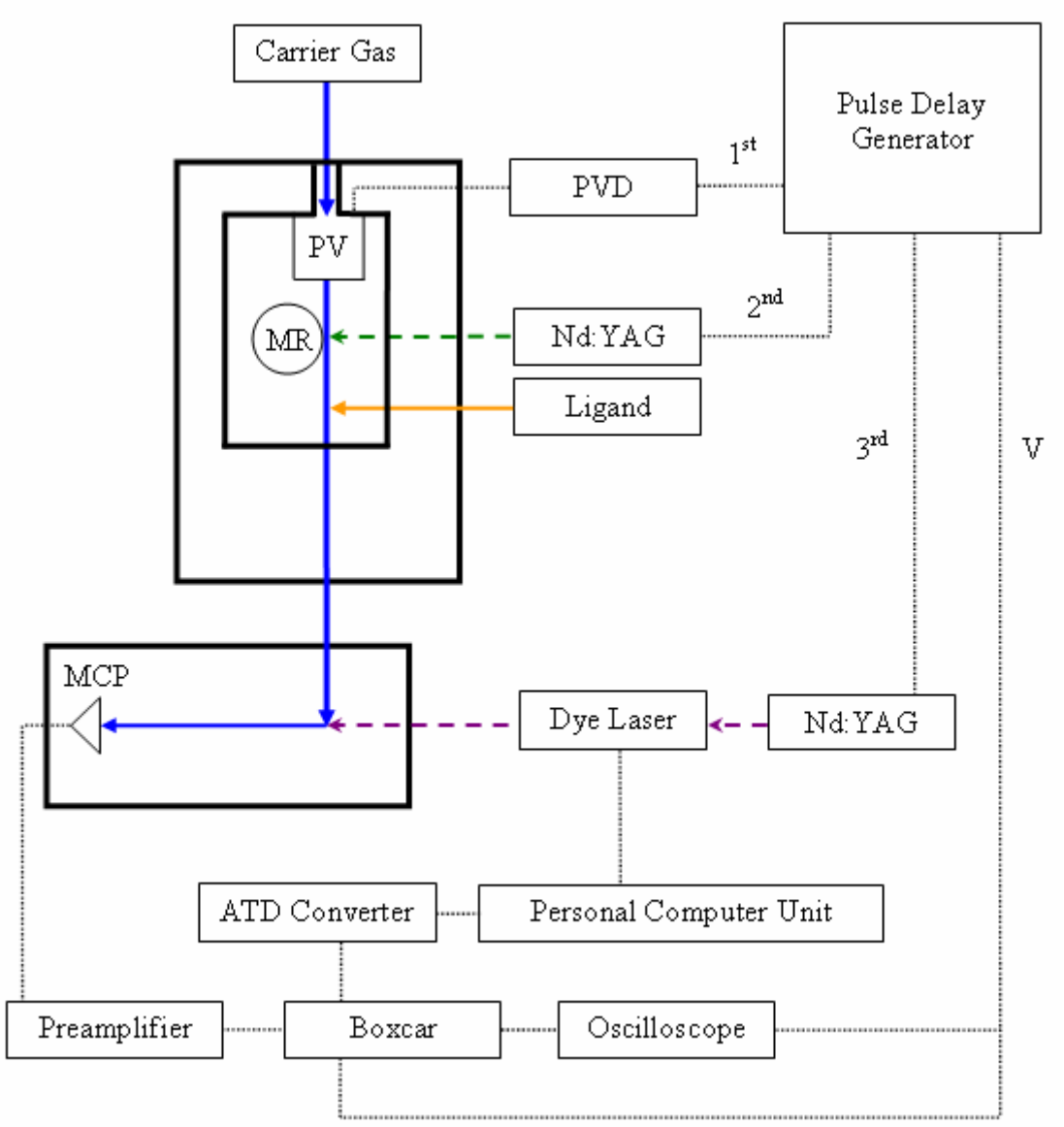

Figure 2.1. Block diagram of the experimental setup. PV = piezoelectric pulsed valve; MR = metal rod; MCP = microchannel plate detector; Boxcar = boxcar gated integrator; ATD Converter = analog-to-digital converter; PVD = pulsed valve driver; Nd:YAG = neodymium: yttrium aluminum garnet laser. The PVD, both Nd:YAG lasers, and the oscilloscope are triggered by the pulse delay generator 1st, 2nd, 3rd, and variable (V) in time, respectively. Solid colored arrows indicate the paths of molecules, atoms, ions, or electrons; dashed colored arrows represent the laser beam directions; dotted black lines represent wired connections between hardware.

is controlled relative to T_0 by $T_{abl} = T_0 + x$, where x is the time variable that is adjusted. Shortly after the ablation laser is fired, the seeded metal atoms enter a small collision chamber (~ 1.5 mL) containing vapors of the organic ligand. In this small cell, atom-molecule collisions occur, and various products are formed. After supersonic expansion, the cold molecular species are photoionized or photoexcited by a second laser. The timing of this event is adjusted by $T_{UV} = T_0 + y$, where T_{UV} is the relative timing of the ionization or excitation laser from T_0 at some variable time, y. As indicated by the subscripted UV, the laser used for ionization or excitation of the metal-ligand complexes usually falls within the ultra-violet region of the electromagnetic spectrum. A fourth trigger must be applied to the oscilloscope (Tektronix Digital Phosphor Oscilloscope TDS3000) to monitor the various outputs of each event. This trigger is also referenced against T_0 and covers a user-specified time range on the oscilloscope. This time range can be adjusted on the oscilloscope by changing, for example, the horizontal scale, which corresponds to the time axis.

2.2 Specific Experimental Details

A more detailed schematic of the ZEKE spectrometer is shown in Figure 2.2. This spectrometer is very similar to the one used by Li et al.[69] This apparatus consists of two vacuum chambers separated by a gate valve (GV). The cubic source chamber (14″ × 14″ × 14″) houses a laser ablation rod source for producing metal atoms. This chamber is evacuated to ~ 10^{-7} Torr by a 2200 L/s oil diffusion pump (Edwards Diffstak 250/2000M) backed by a two-stage rotary pump (Edwards E2M40). The pressure in this chamber is measured with an ion gauge (Edwards AIM-S-NW26) and monitored by an Active Gauge Controller (Edwards D386-51-800). A homemade piezoelectric pulsed valve[71] is used to deliver intense gas pulses of helium, argon, or helium-argon mixtures (UHP, Scott-Gross). The backing pressure of the carrier gas is generally in the range of 40 to 80 psi. About 1 cm after the pulsed valve, the second harmonic output from an Nd:YAG laser (Lumonics YM-800, 532 nm, 0.5 – 1.0 mJ) is focused onto a metal rod using a double convex lens. A motor-driven device (Micro Motor Electronics,

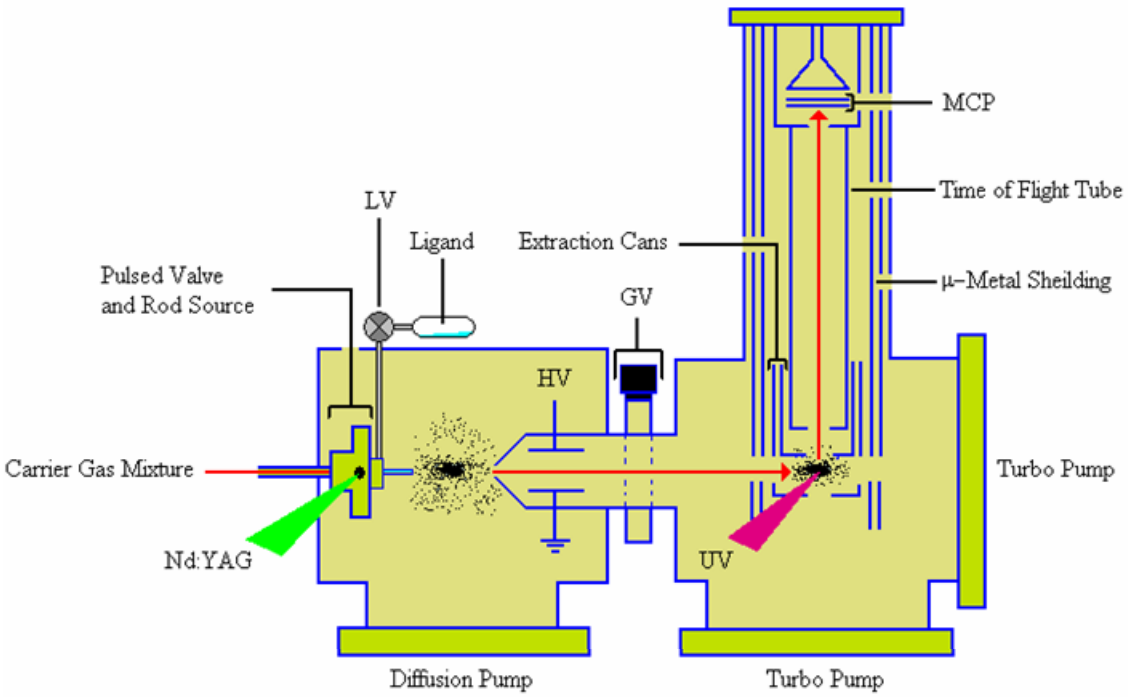

Figure 2.2. Schematic of the ZEKE spectrometer. Nd:YAG = ablation laser; LV = leak valve; HV = high voltage; GV = gate valve; UV = photoexcitation or photoionization laser; MCP = microchannel plate detector.

1516E012S) translates and rotates this metal rod to ensure that each laser pulse ablates a clean, fresh surface. Prior to recording spectra, any oxide coating on the surface of the metal rod is removed by higher-power laser ablation (~ 1.5 to 2.0 mJ) for approximately one hour. Seeded metal atoms are carried to the collision chamber containing the vapor of the aromatic ligand. The amount of ligand vapor is controlled by adjusting a leak valve (LV) that separates the ligand from the collision cell. Upon supersonic expansion, the internal energies of molecular species are converted to translational energy along the expansion axis. Depending on the relative ratio of argon and helium carrier gas, the vibrational temperatures of the metal complexes have been estimated to be in the 20 to 300 K range. Typically, molecules are cooled to the lowest vibrational level of the ground electronic state with v = 0, where v is the vibrational quantum number. On the other hand, low frequency modes ($\lesssim 400$ cm^{-1}) of the neutral complex may be populated in the v = 1 or 2 vibrational levels.

The cold molecular beam is directed towards the spectroscopy chamber by a 2 cm long and 2 mm inner diameter (i.d.) clustering tube. This molecular beam is collimated by a skimmer (4 mm i.d.) to select a portion of molecules and atoms that are traveling in nearly the same direction. Immediately after the skimmer is a pair of deflection plates (HV = +500 V) that removes residual ionic species from the molecular beam that were produced in the laser ablation process. This voltage is provided by a high voltage power supply (Stanford Research Systems PS300). Finally, the skimmed molecular beam enters the spectroscopy chamber where the seeded molecules are ionized, and the resulting charged particles are detected.

The spectroscopy chamber is evacuated to ~ 10^{-9} Torr by two 450 L/s turbomolecular pumps (Seiko Seiki STP451), each backed by a two stage rotary pump (Edwards RV12). This chamber houses a two-field, space-focused, Wiley-McLaren time-of-flight (TOF) mass spectrometer used to detect ions and electrons.[72] The TOF tube, 13″ long and 1.5″ in diameter, is surrounded by a double layer of μ-metal shield to isolate the spectrometer from external magnetic fields. At the bottom end of the TOF tube is a pair of aluminum extraction cans used to accelerate ions or electrons towards the detector consisting of two MCPs. This dual MCP detector is located on the opposite end of the TOF tube and counts the number of electrons or ions produced by ionization. The

inner and outer extraction cans were drilled with 1″-diameter holes to allow the molecular beam and light to travel through the spectroscopy chamber. The light source used for photoionization or photoexcitation is directed perpendicular to the direction of the molecular beam. This light penetrates the spectroscopy chamber through a pair of 1″-diameter UV windows. The ions or electrons are deflected perpendicular to both the direction of the UV light and the molecular beam towards the MCP detector. To reduce inhomogeneity of the electric field, a gold mesh (95 % transmittance) was used to cover the extraction can holes between the molecular beam and the MCP detector. This spectrometer is used to record TOF mass spectra, PIE spectra, and PFI-ZEKE spectra. The details of each procedure are described in the next three subsections.

2.2.1 Time-of-Flight Mass Spectrometry

Molecular and atomic masses within the molecular beam are determined by TOF mass spectrometry. Cations are produced by direct photoionization and accelerated to the MCP detector through a field-free TOF tube by applying voltages to the extraction cans. The ions are detected by a dual MCP detector in a chevron configuration (Figure 2.3). Each MCP is composed of an array of electron multiplier channels. Thus, when an ion enters a channel with sufficient kinetic energy, an electron is ejected from the channel wall. Additional electron-wall collisions generate secondary (tertiary, quaternary, etc.) electrons, which ultimately amplifies the signal output. Large electric fields are required to accelerate the electrons to a high enough velocity to ensure electron-channel wall collisions were effective in producing secondary electrons. The magnitude of the electric field within a given channel is calculated to be ~ 21 kV/cm.

The electric fields in the detector are generated by a high voltage power supply connected to a homemade voltage divider. The schematic (Figure 2.3) shows the electronic circuit and the resultant voltages on each plate of the detector used in the cation mode. A potential of -1950 V (DC) is supplied to the input of the voltage divider, a simple resistor circuit. The recorded voltages on each plate and the anode are indicated in the figure, and the relative distances and thickness of these plates are drawn in red.

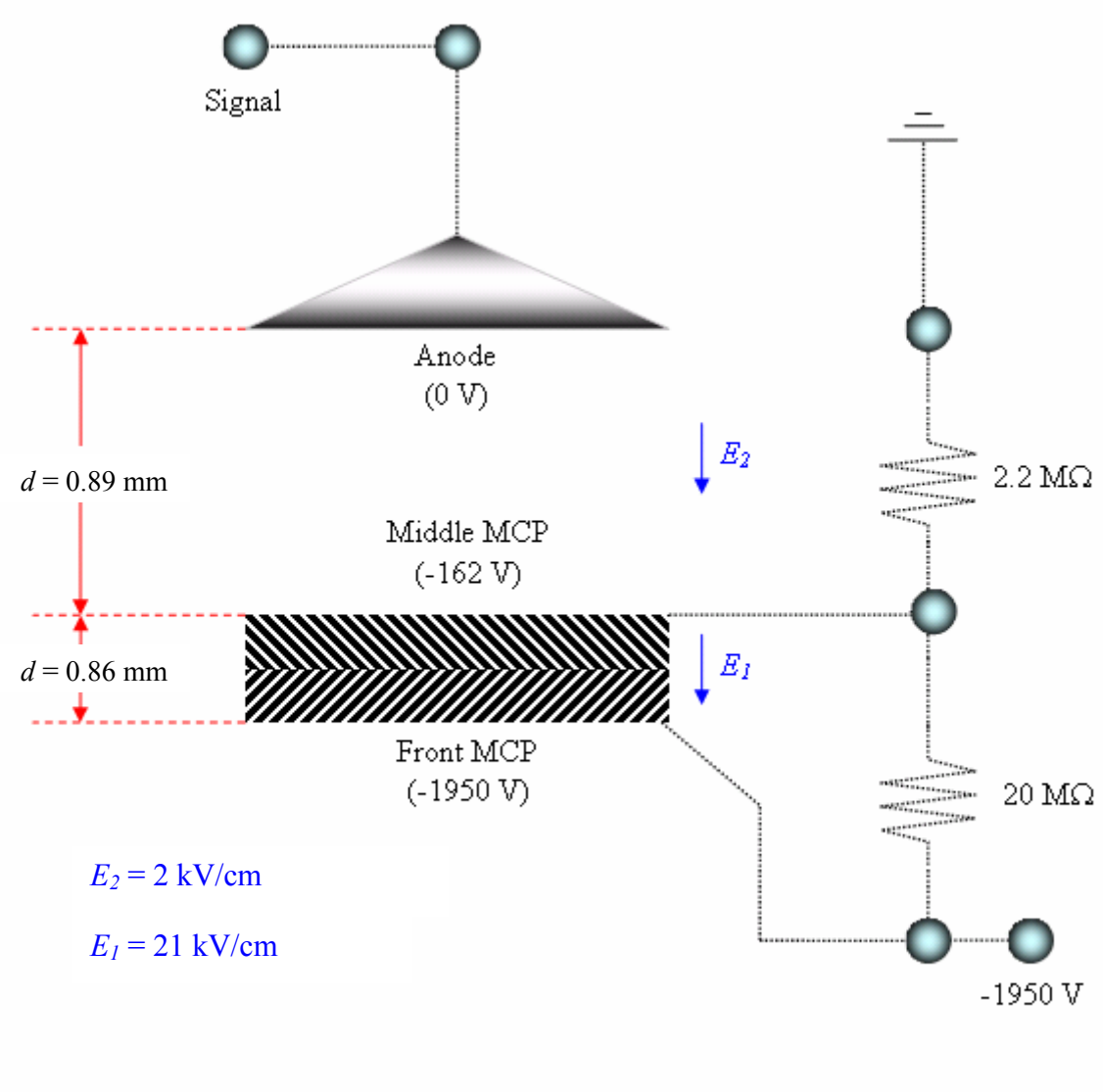

Figure 2.3. Electronic diagram of the voltage divider used for cation detection. MCP = microchannel plate; *d* = distance; *E* = electric field. -1950 V is supplied to the input of the voltage divider, and the resultant recorded voltages on each plate are drawn in the figure. The calculated electric fields are indicated in blue.

From these voltage and distance values, the electric fields were calculated (blue). By definition, electric field lines point away from positive charges and towards negative charges.[73] Thus, the electric fields generated in our detector must point down (blue arrow), opposite to the direction of electron flow. From this MCP detector setup, signals are amplified by about 10^6 to 10^7. The electric field between the middle MCP and anode is much smaller, because the main purpose of this field is to direct the resultant amplified electron signal to the anode. This anode receives the electrons, and the resulting electric current is monitored on the oscilloscope as voltages. These voltages are directly proportional to the ion signal intensities.

The various mass-to-charge ratios are easily determined by their relative flight times. The potential energy used to accelerate these monocations is kept constant. Thus, the total kinetic energy of all ions during their travel from the ionization region to the front MCP must be the same. Therefore, two ions with masses m_1 and m_2 will have equal total kinetic energies (*KE*) of

$$KE = \frac{1}{2} m_1 v_1^{\,2} = \frac{1}{2} m_2 v_2^{\,2} \quad \textbf{(2-1)},$$

where v_1 and v_2 are the velocities of each ion. The average velocities of these ions can be determined, because the traveling distance is fixed ($d \sim 34$ cm) and the relative timings (t_1 and t_2) are recorded. Using $v = d / t$, equation 2-1 can be rewritten as

$$\frac{1}{2} m_1 \left(\frac{34}{t_1} \right)^2 = \frac{1}{2} m_2 \left(\frac{34}{t_2} \right)^2 \quad \textbf{(2-2)},$$

which simplifies to

$$m_1 = m_2 \left(\frac{t_1}{t_2} \right)^2 \quad \textbf{(2-3)}.$$

Thus, if the flight time of one mass is known, then the mass of any other species can be

determined using the relative flight time and equation 2-3. The flight time of a reference ion can be inferred by specific experimental conditions. For example, a small ion peak is always observed in the mass spectrum at 1.42 μs when helium carrier gas is used. However, this ion peak disappears when using, for instance, argon carrier gas. Hence, this ion peak is assigned to the helium cation, which takes 1.42 μs to reach the detector.

Using this scheme, a mass spectrum can be recorded using the oscilloscope and stored in the laboratory computer. Mass spectra are recorded to determine the molecular masses of the species that are ionized in the molecular beam. The molecular formula of each mass can typically be inferred, because only two components (neglecting the inert carrier gas) are generally introduced into the molecular beam: a metal and a ligand. In addition, the ligand usually remains intact during the weak reaction and photoionization processes. Metallic character of the molecular species is confirmed by blocking / unblocking the ablation laser. Once the target metal complex is identified, its production (ion intensity) is maximized by adjusting the backing pressure of the carrier gas, the timings and powers of the ablation and ionization lasers, the concentration of the ligand, and the rotation speed of the metal rod. Prior to ZEKE measurements, the ionization thresholds are located by PIE spectroscopy.

2.2.2 PIE Spectroscopy

A molecule is photoionized when the light energy is greater than the ionization energy of the molecule. Thus, ionization thresholds of the target metal complex can be located by recording the ion intensity as a function of laser frequency. These scans are called PIE spectra, because the ionization efficiency of a particular molecule is measured at various wavelengths. These spectra are acquired by using a mass-selected gated integrator to record the intensity of a particular ion as the wavelength is scanned across ionization thresholds. An ion intensity onset in the PIE curve indicates that an ionization continuum has been reached. Because ionic state populations are not separated in PIE spectroscopy, the spectra are integrated among all populated ionic states. Consequently, vibrational structure is rarely observed in the PIE spectra of metal-ligand complexes. In

addition, autoionization processes also decrease the chance of observing such structure. If any vibrational structure is resolved, then the spectrum has a staircase-shaped profile due to the integral nature of this spectroscopic method.

Although PIE spectroscopy is a low-resolution method, the ionization energy can be estimated by locating a point at which a line drawn through the baseline intersects with a line drawn through the signal onset. This ionization energy estimation needs to be corrected by the energy shift induced by the extraction field. This field-induced shift, δ, is determined by $\delta = d \cdot \sqrt{E_P}$, where E_P is the magnitude of the extraction field and d is a fitting constant. The fitting constant can be extrapolated by a series of PIE measurements at various extraction field strengths. Generally, d is taken to be ~ 6.1 $V^{-½}$ $cm^{-½}$, which gives an energy correction of about +110 cm^{-1}. This relatively large field-induced IE shift is due to the requirement of a much larger extraction field necessary to accelerate the heavy cations towards the detector. The search for a ZEKE signal is greatly simplified by locating the ionization thresholds of the metal complexes via PIE spectroscopy.

2.2.3 ZEKE Spectroscopy

ZEKE measurements are rather similar to PIE measurements, except electrons are detected instead of cations. The principle of this technique has already been described in Chapter 1, but specific details of the procedure have not been discussed. First of all, the polarity on the extraction cans must be reversed in order to repel the oppositely charged electrons towards the detector. Likewise, the voltages on the MCP detector must also be inverted to attract the incoming electrons.

Figure 2.4 shows the specific time scheme and mechanism used to generate, isolate, and detect the ZEKE electrons. First, the photoexcitation laser (UV) is fired such that the laser beam intersects the lower mass-distribution portion of the molecular beam, because our target metal complex (typically the 1-1 or 1-2 metal-ligand complex) is generally much lighter than the other products in the molecular beam (e.g. the 1-3, 2-2, or 2-3 complexes). This mass selection is beneficial, because the chance of observing un-

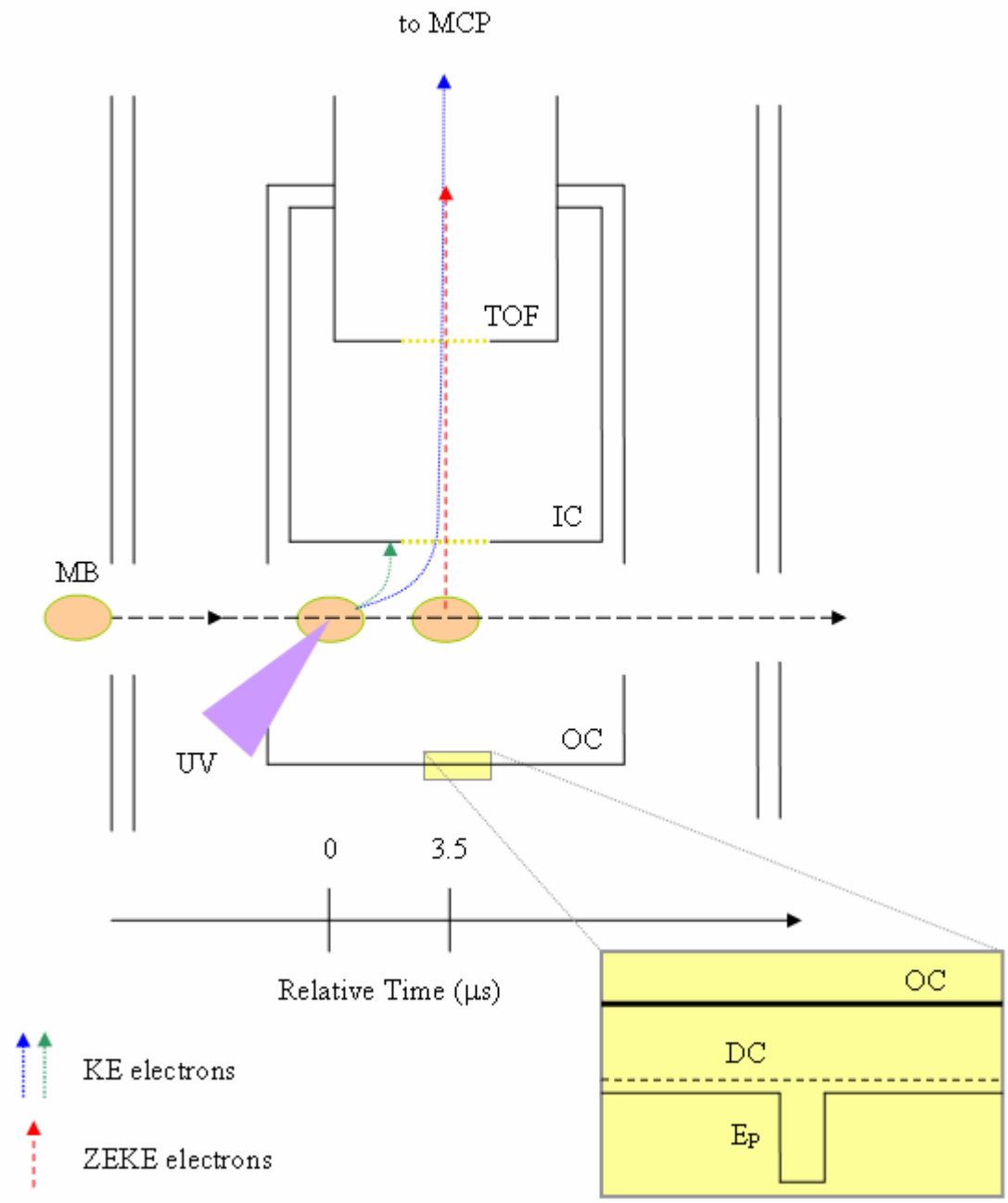

Figure 2.4. In ZEKE measurements, neutral species within the molecular beam (MB) are photoionized and/or photoexcited by a laser (UV). Prompt kinetic energy electrons (KE electrons = blue and green dotted arrows) produced directly by photoionization are accelerated by a small DC field (-0.08 V/cm) towards the MCP detector. About 3.5 microseconds after firing the UV laser, a small pulsed electric field (E_P = -1.2 V/cm) is applied to the outer extraction can (OC) to ionize the long-lived Rydberg states that were formed during photoexcitation. This electric field also acts as an accelerator to direct the resultant electrons (ZEKE electrons = red dashed arrow) towards the MCP detector. TOF = time-of-flight tube; IC = inner extraction can.

wanted ZEKE background signals from heavier complexes is reduced significantly. Meanwhile, some molecules or atoms will be directly photoionized by this laser. A small continuous DC field (-0.08 V/cm) repels these KE electrons (blue dotted arrow) towards the MCP detector, while others are blocked by the aperture (green dotted arrow). Any prompt KE electrons that reach the detector are generally collected within ~ 50 ns of firing the photoexcitation laser. However, if the photoexcitation laser is tuned just below the ionization threshold of the target metal complex, then the complex will be converted to some high-lying Rydberg state. These Rydberg states lie about 3 to 5 cm^{-1} below the ionization threshold, but are still states of the neutral molecule. Hence, molecules in these Rydberg states will not be repelled by the small DC field. After a 3.5 μs delay, a pulsed electric field (-1.2 V/cm) is applied to the outer extraction can (OC) to remove the ZEKE electron from these Rydberg states (red dashed arrow). The 3.5 μs delay is a sufficient amount of time to completely separate all the KE electrons from the ZEKE electrons. Consequently, the resolution of the PFI-ZEKE technique depends primarily on the linewidth of the photoexcitation source and the magnitude of the pulsed electric field. The resultant electrons are directed towards the MCP detector by focusing the electrons into the TOF tube by applying a small DC voltage (+5 V) to this tube.

In contrast to cation detection, the electrons are accelerated to high speeds by applying a *positive* potential on the front MCP. Thus, a different voltage divider is required to supply the appropriate potentials on each plate of the detector for ZEKE measurements. This resistor-capacitor circuit (Figure 2.5) is more complicated than the circuit used for ion detection. Because the polarity on each plate is reversed with respect to ion detection, a large positive potential must be applied to the anode to attract the amplified electron signal. In order to prevent high voltage damage to other electronic devices such as the preamplifier, boxcar integrator, and oscilloscope, this electron signal is capacitively decoupled from the anode. Hence, this circuit contains capacitors to facilitate this process. The measured voltages on each plate and the calculated electric fields (blue) generated by this voltage divider are drawn in Figure 2.5. Although the potentials applied on each plate in ZEKE measurements are rather different from those during ion measurements, the directions and magnitudes of the resultant electric fields are quite similar. This similarity is desired, because both detection schemes ultimately

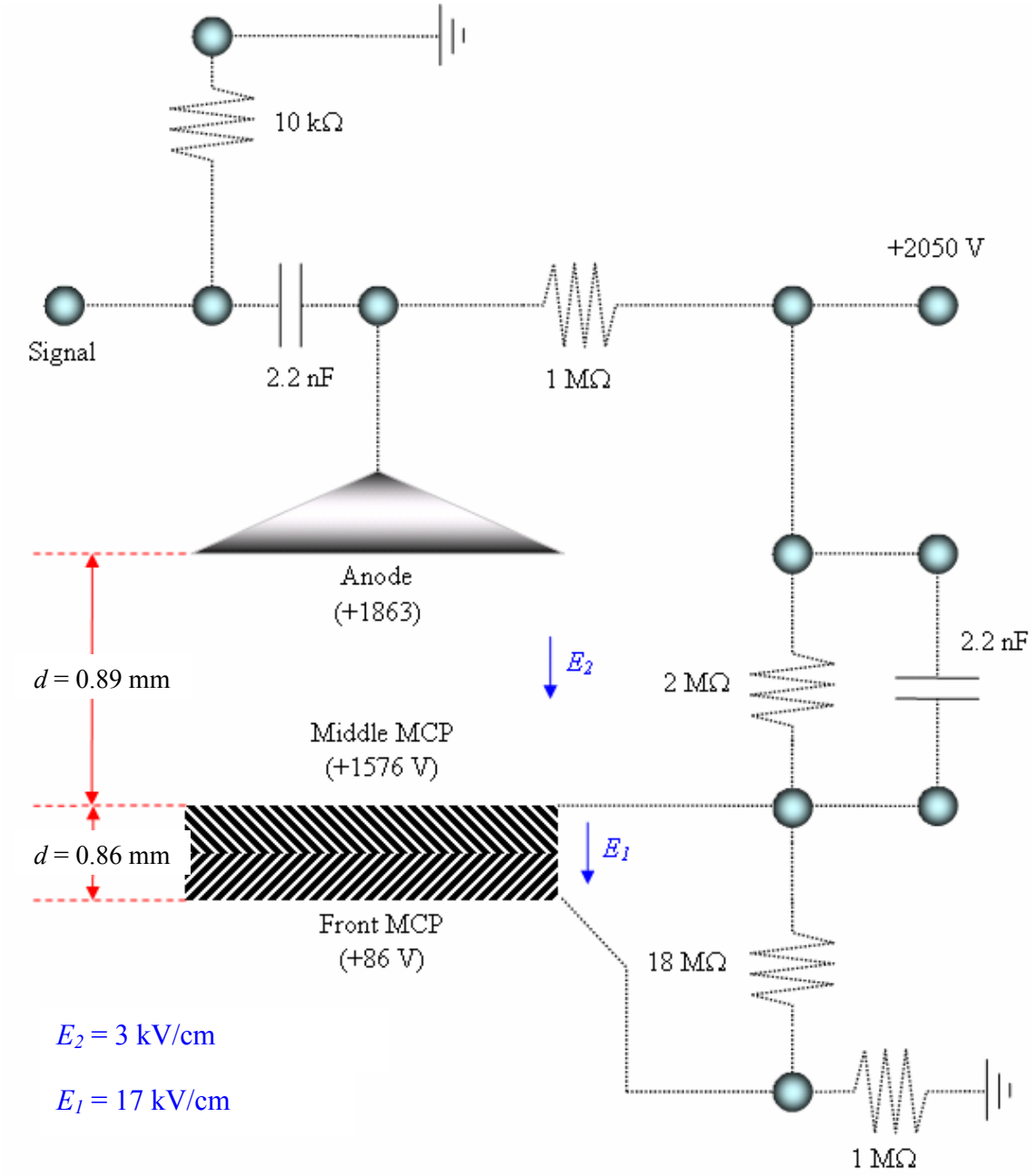

Figure 2.5. Electronic diagram of the voltage divider used for electron detection. MCP = microchannel plate; *d* = distance; *E* = electric field. +2050 V is supplied to the input of the voltage divider, and the resultant recorded voltages on each plate are drawn in the figure. The calculated electric fields are indicated in blue.

involve the collection of an amplified electron signal. Nonetheless, a ZEKE spectrum can be recorded by monitoring the intensity of the ZEKE electron signal while scanning the wavelength of the photoexcitation laser.

2.3 Computational Procedures

In addition to experimental measurements, these molecular systems are also studied by *ab initio* theoretical calculations. In this work, geometry optimizations and frequency calculations were done with the *GAUSSIAN98* and/or *03* program package[74] via the University of Kentucky Hewlett-Packard Superdome Cluster. These molecular systems were first modeled using DFT methods such as B3LYP, B3P86, and BPW91. In most cases, the all electron 6-311+G(d,p) basis set was used to treat each atom. In this basis set, diffuse and polarization functions are included on the heavy elements (i.e. carbon and metal atoms), whereas only polarization functions are added to the hydrogen atoms. For heavier elements that are not in the 6-311+G(d,p) basis set range, a pseudo effective core potential (ECP) basis set such as LANL2DZ is used instead. In these ECP basis functions, the valence electrons are treated independently, while the core electrons and nucleus are approximated as a single, uniform potential. Depending on how well DFT can handle the molecular system, further calculations using wavefunction-based methods (i.e. MP2) were implemented as well.

In our theoretical methodology, various structures of the free ligand are located first. These geometry optimizations are used to determine the molecular structure of the free ligand and the possible metal binding sites. In addition, geometrical perturbations induced by metal coordination can be deduced by comparing the optimized geometry of the free ligand to that in the neutral metal complex. For those extensively studied organic ligands, the reliability of the theoretical method can also be assessed by comparing the calculated molecular structures to those determined by experiment.

Frequency analyses are used to determine whether each molecular structure is a local minimum energy structure on the potential energy surface of the molecule. Those molecular configurations that contain at least one imaginary frequency (i.e. a negative

frequency) are transition state species or saddle points on the potential energy surface. Local minimum energy structures have only real frequencies (i.e. positive frequencies), and the global minimum energy structure is the configuration with the lowest electronic energy.

After locating the appropriate structures of the free ligand, the neutral and monopositive ionic metal complexes are studied using the same theoretical method and basis set. However, calculations on these transition metal complexes are inherently much more complicated due to the addition of many more electrons and the variety of different electron-spin multiplicities that are possible. In this dissertation, group 3, 4, 5, and 6 transition metal complexes with 3, 4, 5, and 6 valence electrons, respectively, were calculated. If none of these valence electrons are paired, then the highest electron-spin multiplicity (2S + 1) for group 3, 4, 5, and 6 transition metal complexes is 4, 5, 6, and 7, respectively. Thus, for each configuration of the transition metal complexes, several electron-spin states need to be considered as well. However, the broadness of these theoretical surveys is reduced by referring to previous theoretical or experimental investigations of related molecular systems. For example, the bis(benzene) chromium complex is well known to conform to the so-called 18-electron rule, where all electrons are paired to form a low-spin singlet electronic state. Thus, only singlet and doublet electronic states were calculated for this chromium complex. Such knowledge helped to simplify our theoretical work greatly since triplet, quartet, quintet, sextet, and septet electronic states were neglected in our theoretical survey of the neutral and ionic bis(benzene) chromium complexes.

To simulate ZEKE spectra, multidimensional FCFs are calculated via the FCF simulation program written by Li. These FCFs are calculated from the equilibrium geometries, harmonic vibrational frequencies, and normal coordinates of the neutral and ionic complexes obtained from the *ab initio* calculations. The mathematical procedure for evaluating these FC integrals is quite similar to that used previously.[67] The Duschinsky effect[45] is considered to account for normal mode differences between the neutral and ionic states in these FCF calculations. Spectral broadening is simulated by giving each line a Lorentzian line shape with experimental linewidth. Transitions from excited vibrational levels of the neutral complexes are simulated by assuming thermal

excitations at specific temperatures using a Boltzmann distribution. The appropriate vibrational temperatures are selected by simulating spectra from 0 to 300 K in 10 K increments and choosing the best match with experiment. In this dissertation, all simulations have vibrational temperatures of 10 K, unless otherwise noted in the text. To simplify comparisons of the calculated and measured FC profiles, the calculated transition energies are shifted to the experimental ionization energy of the metal complexes. In addition, the experimental and calculated intensities are normalized by scaling the strongest peak in the spectra to unity.

CHAPTER 3: ELECTRON-SPIN MULTIPLICITIES AND MOLECULAR STRUCTURES OF NEUTRAL AND IONIC SCANDIUM-BENZENE COMPLEXES

3.1 Introduction

Transition metal-benzene complexes are truly classic among organometallic compounds and crucial intermediates in homogeneous catalysis in organic synthesis.[75-77] The bonding between metal centers and aromatic ligands has been extensively studied in organometallic and surface chemistry.[75-83] In organometallic compounds, benzene usually binds to metal centers in an η^6 six-electron π-donating mode, although η^4 four-electron and η^2 two-electron modes are also known to exist.[77] On metal surfaces, benzene is found to lie parallel to the surface and bound to one or more surface atoms, with six-, three-, or twofold local symmetries.[82, 83] In the gas phase, metal-benzene complexes have been extensively studied as well. Some of these studies include photodissociation,[84-97] photoionization,[98-105] photoelectron,[106-112] threshold photoelectron-photoion coincidence,[113, 114] collision-induced dissociation,[115-118] ion mobility,[119] magnetic[120] and electric dipole moments,[121-124] reaction kinetics,[125-140] and computations.[141-167] Recently, matrix isolation infrared spectroscopy has also been reported for early transition metal-benzene complexes in solid argon.[168] Similar to the condensed phase, η^6, η^4, and η^2 bonding modes are possible in gaseous metal-benzene complexes. For example, resonance-enhanced multiphoton infrared photodissociation measurements of the benzene vibrations in Al^+-bz suggested that Al^+ binds to the benzene molecule in a symmetric η^6 configuration.[86] On the other hand, measurements of electric dipole moments indicated that two Al-bz isomers were present in a supersonic cluster beam, one an asymmetric η^2 complex and the other a nearly C_{6v} η^6 symmetric structure.[121] The asymmetric structure was more stable than the symmetric one. For complexes containing multiple benzenes/metal atoms, multi-decker sandwich and rice-ball structures were proposed.[101-108, 119, 161]

In spite of extensive studies, little electronic spectroscopy with resolved metal-

ligand vibrational structures has been reported for any coordinately unsaturated metal-benzene complex, and electron spin multiplicities and binding modes of transition metal complexes remain to be addressed in detail. Recently, studies of infrared dissociation vibrational spectroscopy, in combination with density functional theory (DFT) calculations, have begun to tackle these issues, and clear differences were found between vibrational spectra of electronic states with different spin multiplicities[87-89] or different binding modes.[85] However, in some ionic systems where comparison was possible [e.g. Ti^+-bz_2, V^+-bz_2], measured spectra did not agree with the spectral patterns predicted for the ionic ground electronic states. The discrepancy arose either because the ions were produced in excited states or the DFT calculations failed for these open shell transition metal ion complexes.

In this chapter, the pulsed field ionization zero electron kinetic energy (ZEKE) spectra of Sc-bz and Sc-bz_2 are reported. The spectra are interpreted in combination with DFT and FCF calculations. The good agreement between the experimental measurements and theoretical calculations has enabled the determination of the preferred molecular structures and electron spin multiplicities in the neutral and ionic electronic states of these two complexes.

3.2 Experimental and Computational Methods

The details of our ZEKE spectrometer have been discussed in Chapter 2. Sc-benzene complexes were prepared by reactions of Sc atoms with the vapor of benzene in molecular beams. The scandium atoms were produced by pulsed laser (Nd:YAG, Lumonics YM-800, 532 nm, 0.7 mJ) vaporization of a Sc rod (99.9%, Alfa Aesar) in the presence of a carrier gas or gas mixtures (He or Ar, UHP, Scott-Gross) at ~ 40 psi delivered by a piezoelectric pulsed valve.[71] The metal rod was translated and rotated by a motor-driven mechanism to ensure each laser pulse ablated a fresh surface. Benzene vapor was introduced at room temperature through a stainless steel capillary to a small collision chamber (~1.5 mL) down stream from ablation, where the ligand interacted with metal atoms entrained in the carrier gas. Benzene was purchased from Aldrich (≥ 99%)

and used without further purification.

Molecular masses were measured by photoionization time-of-flight mass spectrometry. Ionization thresholds of Sc-$bz_{1,2}$ were located by recording the mass-selected ion signal as a function of laser wavelength. Prior to ZEKE experiments, the production of the 1:1 and 1:2 complexes was maximized by adjusting the timing and power of the vaporization laser, backing pressure of the carrier gas, and amount of benzene vapor. ZEKE electrons were produced by photoexcitation of the neutral complexes to high-lying Rydberg states, followed by delayed, pulsed electric field ionization (1.2 V/cm, 100 ns) of these Rydberg states. A small DC field of 0.08 V/cm was applied to speed up the separation of the ZEKE electrons from the kinetic electrons produced by direct photoionization. The photoionization and photoexcitation light was provided by a frequency-doubled dye laser (Lumonics HD-500), pumped by a XeCl excimer laser (Lumonics PM-884). The pulsed electric field was generated by a delay pulse generator (Stanford Research Systems DG535). Ion and electron signals were detected by a dual microchannel plate detector (Galileo), amplified by a preamplifier (Stanford Research Systems SR445), averaged by a gated integrator (Stanford Research Systems SR250), and stored in a laboratory computer. Laser wavelengths were calibrated against vanadium atomic transitions.[169] The field dependence of the ZEKE signal was not measured; however, the anticipated energy shift from the small electric field (~ 1 V cm^{-1}) is much smaller than the observed spectral linewidth.

Geometry and frequency calculations were carried out with the B3LYP (Becke's three parameter hybrid functional with the correlation functional of Lee, Yang, and Parr) hybrid functional and the 6-311+G(d,p) basis, implemented in the Gaussian 03 program package.[74] Multidimensional FC factors were calculated from the equilibrium geometries, harmonic vibrational frequencies, and normal coordinates of the neutral and ionic complexes.[67, 68] The Duschinsky effect[45] was considered to account for normal mode differences between the neutral and ion. A Lorentzian line shape with the linewidth of the experimental spectrum was used to simulate spectral broadening.

3.3 Results and Discussion

3.3.1 Sc-bz

Figure 3.1(a) shows the ZEKE spectrum of Sc-bz. The spectrum originates at 41600 (8) cm^{-1}, or 5.158(1) eV, with a linewidth of ~ 8 cm^{-1}. It consists of a major progression with an energy interval of 375 cm^{-1}. Superimposed on each member of the 375 cm^{-1} progression are satellite peaks, separated by ~ 50 cm^{-1}. In addition, a peak at 324 cm^{-1} and two sharp lines marked by asterisks appear below the 0-0 transition. All peak positions are listed in Table 3.1.

The 375 cm^{-1} interval seems to be comparable to the wavenumber of a free benzene vibrational mode (ν_{20}, 398 cm^{-1}).[170] However, ν_{20} is an e_{2g} degenerate mode in D_{6h} benzene, transformed to e_2 representation in a C_{6v} metal-benzene complex, and unlikely active in fundamental excitation. The vibrational wavenumbers of all other modes in the ground electronic state of the free ligand are greater than 600 cm^{-1}. Thus, the 375 cm^{-1} progression must arise from a Sc^+-benzene vibration. The observation of a metal-ligand vibration is not surprising as ionization removes a metal-based electron and affects mostly the bond distance or angles between the Sc atom and ligand. The nature of the 375 cm^{-1} vibration can also be confirmed by measuring the spectra of the benzene complexes with other metals in the Sc group (e.g., Y, La). If the vibration is localized on the ligand, varying metal atoms should have little effect on the vibrational wavenumbers; otherwise, a significant difference is expected. We have thus measured the spectra of Y- and La-bz, and observed a 328 cm^{-1} progression for the yttrium-benzene complex and a 292 cm^{-1} progression for the lanthanum analogue.[171] The decrease of the vibrational wavenumbers from Sc to Y to La is consistent with the increase of the atomic masses down the triad and supports the assignment of the 375 cm^{-1} interval to a Sc^+-benzene vibration.

The 324 cm^{-1} transition below the 0-0 peak originates from a vibrationally excited level of the neutral complex, as its intensity depended on the condition of the molecular beam. Assuming the 324 and 375 cm^{-1} interval are associated with the same vibrational mode in Sc- and Sc^+-bz, the ionic mode is then ~ 50 cm^{-1} larger than the neutral mode.

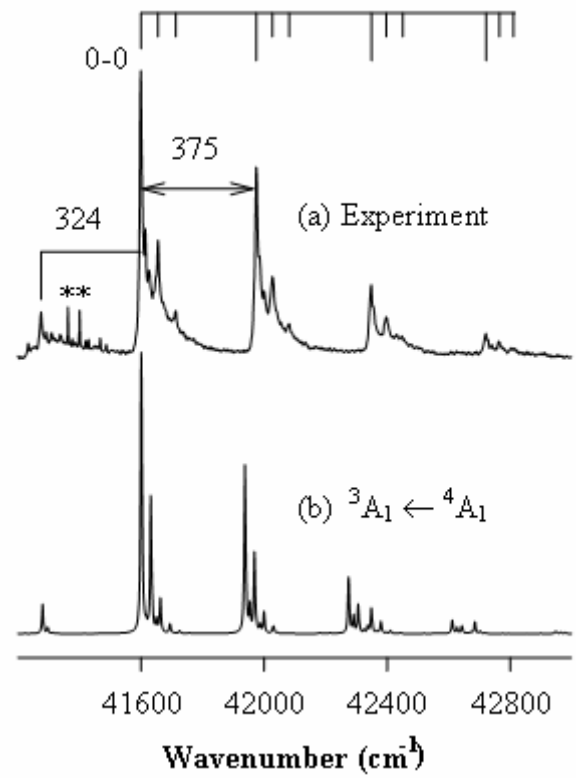

Figure 3.1. Experimental ZEKE spectrum recorded with He carrier (a) and simulation [300 K] of the $^3A_1 \leftarrow {}^4A_1$ (b) transition of Sc-bz.

Table 3.1. Peak positions (cm^{-1}) and assignments of the Sc-$bz_{1,2}$ ZEKE spectra. The absolute uncertainties are ~ 8 cm^{-1} for the Sc-bz $^3A_1 \leftarrow {}^4A_1$ and Sc-bz_2 $^3A_{1g} \leftarrow {}^2B_{3g}$ transitions and ~ 20 cm^{-1} for the Sc-bz_2 $^1A_{1g} \leftarrow {}^2B_{3g}$ transition. ν^+ and ν stand for the Sc^+-$bz_{1,2}$ and Sc-$bz_{1,2}$ stretch modes and δ^+ and δ for the out-of-plane benzene ring twist in the ion and neutral complexes, respectively. The transitions of Sc-bz_2 are assigned according to the eclipsed conformer.

Sc-bz		Sc-bz_2					
$^3A_1 \leftarrow {}^4A_1$		$^1A_{1g} \leftarrow {}^2B_{3g}$			$^3A_{1g} \leftarrow {}^2B_{3g}$		
Position	ν^+-ν	Position	ν^+-ν	δ^+-δ	Position	ν^+-ν	δ^+-δ
41276	0-1	40883	Origin[b]		42112	Origin	
41364	a	41089	1-0		42313	1-0	
41401	a	41185		1-0	42512	2-0	
41600	Origin	41295	2-0		42534		1-0
41656	1-1	41394	1-0	1-0	42712	3-0	
41713	2-2	41501	3-0		42735	1-0	1-0
41975	1-0	41599	2-0	1-0	42911	4-0	
42028	2-1	41706	4-0		42936	2-0	1-0
42082	3-2	41800	3-0	1-0	43004	c	
42349	2-0	41909	5-0		43109	5-0	
42399	3-1	41993	4-0	1-0	43135	3-0	1-0
42450	4-2				43307	6-0	
42720	3-0				43335	4-0	1-0
42767	4-1				43357	2-0	2-0
42810	5-2						

[a] Atomic transitions of tantalum, an impurity of the scandium rod. [b] Upper limit of the ionization energy. [c] Possibly a C-H out-of-plane bend.

With this assumption, the satellite peaks can be assigned to sequence transitions from excited levels of the 324 cm^{-1} neutral mode to levels of the 375 cm^{-1} ion mode. As to the two asterisked peaks, they are much narrower than others, and their intensities more strongly depended on the excitation laser power. These sharp peaks are atomic transitions of tantalum, an impurity of the scandium rod.

For further spectral analysis, theoretical calculations must be involved. Recently, a number of computational studies have been reported on the ground-state electron spin multiplicities of Sc- and Sc^+-bz. For the neutral complex, Pandey et al.[140] obtained a quartet ground state in the C_{6v} point group by using the BPW91 (Becke's one parameter hybrid functional with Perdew and Wang's 1991 gradient-corrected correlation functional) method; Kambalapalli and Ortiz predicted a doublet ground state ($^2A_1$,C_{2v}) and a quartet excited state ($^4A_2$, C_{6v}) at 0.22 eV higher in energy with the MP2 method;[143] Hong et al. predicted a quartet ground state ($^4A_1$, C_{6v}) with the multireference-based CASSCF+MRCI (complete active space self-consistent field and a multireference configuration interaction) method;[154, 155] and Rabilloud et al. found a quartet minimum ($^4E_2$ or $^4A_2$, C_{6v}) with a short metal-benzene distance (2.12 Å) and a doublet ($^2E_2$, C_{6v}) with a much longer distance (4.96 Å) using the CASSCF+MRCI approach.[123, 144] The long-range doublet state is 1.05 eV more stable but has a much smaller binding energy (0.02eV) than the short-range quartet (0.8 eV). The doublet has no pronounced minimum at short distances. Rabilloud et al. also performed an electric deflection experiment on this complex and compared the experimental measurement with their theoretical prediction. However, it was not straightforward from the comparison whether the long-range doublet or the short-range quartet state was probed in that experiment.[123, 124] For the charged complex, Pandey et al.[140] and Bauschlicher et al.[145] predicted a triplet state by using the BPW91 and MCPF (modified coupled-pair functional) methods, respectively. However, no vibrational analysis was reported in any of these studies.

We calculated the electronic energies and vibrational frequencies for low-lying spin states of the neutral and ionic complexes by using the B3LYP method. Since the Sc atom has three outer valence electrons, the electron spin multiplicity of the ground state of Sc-bz should be either 2 or 4, and that of Sc^+-bz should be 1 or 3. Thus, our calculations were restricted to these four spin states. Since previous calculations

indicated that the complex could be in either C_{2v} or C_{6v} point group, initial structures for all spin states were carried out under C_{2v} point group. The neutral quartet and ionic triplet were converged to C_{6v}, while the neutral doublet and ionic singlet remained C_{2v}. To determine the electronic species of the quartet and triplet states, further calculations were performed under C_{6v} point group.

Figure 3.2(a) presents the two views for the calculated Sc^+/Sc-bz structures, and Table 3.2 lists the predicted bond lengths, dihedral angles and relative energies. For the neutral molecule, the ground state is predicted to be a quartet ($^4A_1$, C_{6v}), and an excited doublet ($^2A_2$, C_{2v}) is calculated at 1211 cm^{-1}. However, the $^2A_2$ state has an imaginary frequency of 1004*i* cm^{-1}, indicating that it is not a local minimum. We have attempted to locate a doublet minimum but were not successful. For the ion, the lowest energy state is a singlet ($^1A_1$, C_{2v}), and an excited triplet ($^3A_2$, C_{2v}) is located at 847 cm^{-1}. The relative energy orderings of the spin states are reversed from that in the atomic Sc and Sc^+.[169] The energies of the $^3A_1 \leftarrow {}^4A_1$, $^3A_1 \leftarrow {}^2A_2$, and $^1A_1 \leftarrow {}^2A_2$ transitions are predicted to be 41345, 40498, and 39287 cm^{-1}, respectively. Compared to the measured ionization energy of 41600 cm^{-1}, the calculated value for $^3A_1 \leftarrow {}^4A_1$ is in much better agreement than the other two transitions.

Figure 3.1(b) displays the spectral simulation of the $^3A_1 \leftarrow {}^4A_1$ transition. In this simulation, the 0-0 transition energy is shifted to the experimental value for clarity. The excellent agreement between the calculation and experiment makes the spectral assignment straightforward. The major progression is assigned to transitions from the ground vibrational level of the $^4A_1$ state to the excited levels of the Sc^+-bz stretch in the $^3A_1$ state. The 324 cm^{-1} peak is due to the transition from the first Sc-bz stretch level of the neutral $^4A_1$ state to the vibronic ground state of the $^3A_1$ ion. The satellite peaks within the major progression are due to sequence transitions from the first or second Sc-bz excited stretch level. The assignment for each ZEKE peak is summarized in Table 3.1. The FC structures of the $^1A_1 \leftarrow {}^2A_2$ and $^3A_1 \leftarrow {}^2A_2$ transitions are expected to be much different from the observed spectrum because of a large change in the equilibrium Sc-benzene distance or variation in molecular symmetry (Table 3.2). Also, the metal complex is unlikely produced at the doublet transition state. Therefore, the $^1A_1 \leftarrow {}^2A_2$ and $^3A_1 \leftarrow {}^2A_2$ transitions can be excluded from the ZEKE spectrum.

Table 3.2. Bond lengths (R, Å), dihedral angles (δ, °), and relative electronic energies (ΔE_e, cm^{-1}) of Sc-$bz_{1,2}$ from B3LYP/6-311+G(d,p) calculations.

State	Point group	R_{Sc-C}	R_{C-C}	R_{C-H}	$\angle_{C-C-C-C}$	ΔE_e
Sc-bz						
$^4A_1$	C_{6v}	2.44	1.42	1.08	0.0	0
$^2A_2$[a]	C_{2v}	2.43 / 2.42	1.42 / 1.41	1.08	1.6	1211
$^1A_1$	C_{2v}	2.39 / 2.20	1.46 / 1.38	1.08	22.3	40498
$^3A_1$	C_{6v}	2.38	1.42	1.08	0.0	41345
Sc-bz_2, eclipsed						
$^2B_{3g}$	D_{2h}	2.44 / 2.39	1.43 / 1.41	1.08	5.9	0
$^4A_{1g}$	D_{6h}	2.55	1.41	1.08	0.0	6990
$^1A_{1g}$	D_{2h}	2.50 / 2.40	1.43 / 1.39	1.08	11.6	39490
$^3A_{1g}$	D_{6h}	2.49	1.41	1.08	0.0	39696
Sc-bz_2, Staggered						
$^2B_1$	D_{2d}	2.44 / 2.40	1.43 / 1.41	1.08	5.1	143
$^4B_2$	D_{6d}	2.55	1.41	1.08	0.0	7045
$^1A_1$	D_{2d}	2.50 / 2.41	1.43 / 1.39	1.08	10.6	39653
$^3A_1$	D_{6d}	2.49	1.41	1.08	0.0	39727

[a] An imaginary frequency (1004*i* cm^{-1}) was calculated for the $^2A_2$ state.

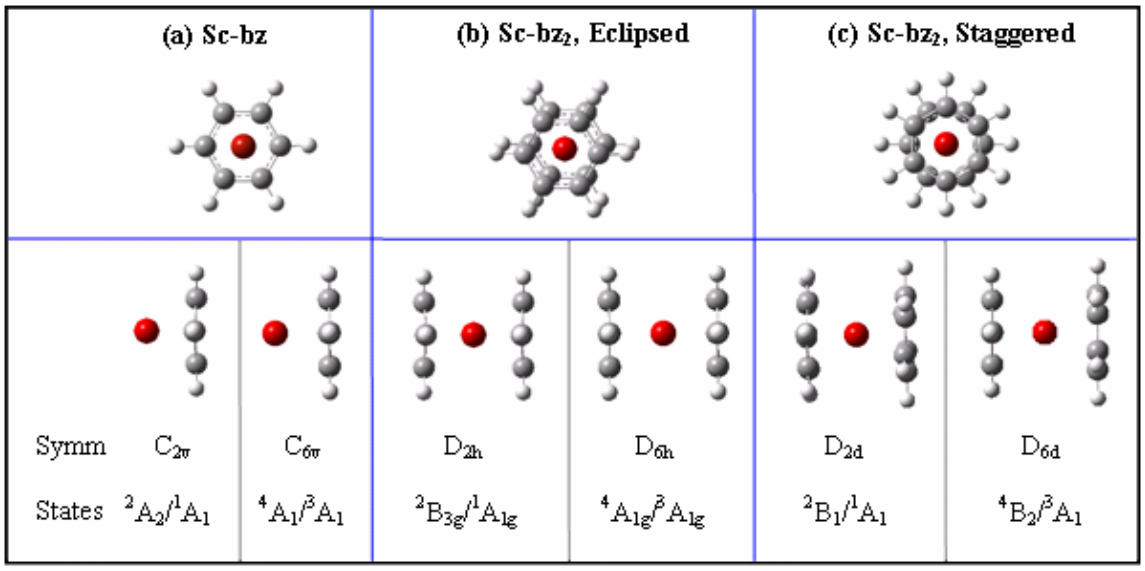

Figure 3.2. Top and side views of Sc-bz (a), eclipsed Sc-bz$_2$ (b), and staggered Sc-bz$_2$ (c) structures, along with molecular symmetries and electronic states.

3.3.2 Sc-bz_2

The ZEKE spectrum of Sc-bz_2 is strikingly different from that of Sc-bz, as shown in Figure 3.3(a). The spectrum at the lower energy region displays rather broad peaks with a linewidth up to ~ 40 cm^{-1}, whereas the spectrum at the higher energy region shows sharp transitions with a linewidth of ~ 8 cm^{-1}. The very different line profiles indicate that the spectrum probably consists of two electronic band systems. In the lower energy region, the first broad peak begins at 40883(20) cm^{-1} and is followed by a number of peaks separated by ~ 200 cm^{-1}. This progression is labeled as *a*. An additional progression, *b*, is formed by combining the 200 cm^{-1} interval with a weak transition at 300 cm^{-1} above the first peak. In the higher energy region, the first narrow peak is observed at 42112 (8) cm^{-1}. This and six additional peaks with a separation of ~ 200 cm^{-1} form progression *a′*. Like in the lower energy region, a second progression, *b′*, is observed to be the combination of the ~200 cm^{-1} interval with a 420 cm^{-1} transition. In addition, a strong asterisked peak appears at ~ 890 cm^{-1} from the first sharp peak.

The eclipsed and staggered conformers of the dibenzene complex are presented in Figure 3.2(b) and (c), and the geometries and relative energies are listed in Table 3.2. Like the monobenzene complex, the singlet and doublet states have a lower symmetry than the triplet and quartet states. The loss of the sixfold symmetry in the singlet and doublet states results from the distortion of the benzene plane, i.e., the benzene rings are slightly bent from the sandwiched Sc atom. In contrast to the mono-ligand species, however, the dibenzene complex has a neutral doublet ground state, with an excited quartet at about 7000 cm^{-1}. For the corresponding ion, the singlet is slightly more stable than the triplet. The eclipsed and staggered conformers have nearly identical bond distances, bond angles, and the electronic energies. These should not be surprising because the two benzene rings are far apart and thus, their interaction is expected to be very weak. The energies of the $^1A_g \leftarrow {}^2B_{3g}$, $^3A_{1g} \leftarrow {}^2B_{3g}$, and $^3A_{1g} \leftarrow {}^4A_{1g}$ transitions of the eclipsed conformer are predicted to be 39490, 39696, and 32706 cm^{-1}, respectively. Since the energy of the $^3A_{1g} \leftarrow {}^4A_{1g}$ transition is much lower than the experimental value of 40883 or 42112 cm^{-1}, and the $^4A_{1g}$ state is nearly 1 eV above the ground state, the $^3A_{1g}$

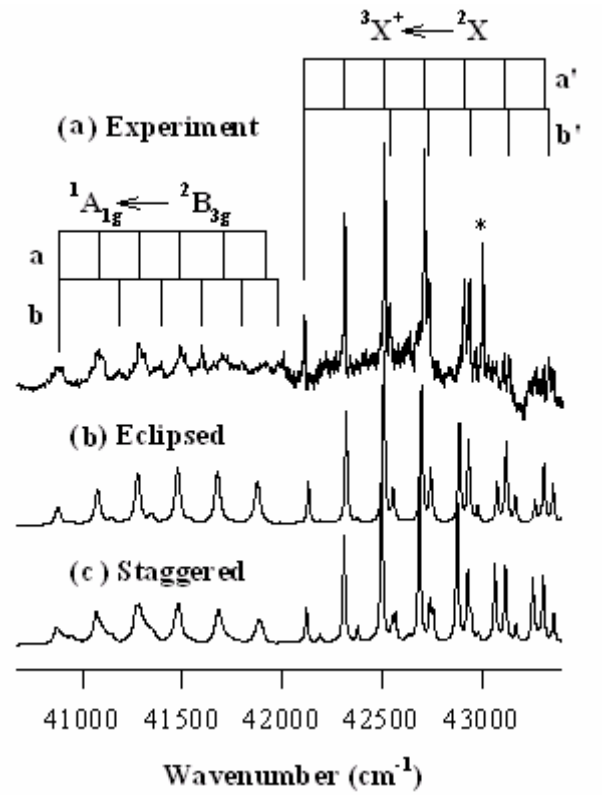

Figure 3.3. Experimental ZEKE spectrum of Sc-bz_2 recorded in a He/Ar mixture carrier (a) and simulations [100 K] from eclipsed (b) and staggered (c) conformations. The electronic species are labeled based on the D_{6h} point group of the eclipsed form.

$\leftarrow {}^4A_{1g}$ transition is unlikely a part of the observed spectrum.

Figure 3.3(b) displays the spectral simulations of the $^1A_g \leftarrow {}^2B_{3g}$ and $^3A_{1g} \leftarrow {}^2B_{3g}$ of the eclipsed conformer. These simulations well reproduce the major progressions *a* and *a′*, and are in reasonably good agreement with progressions *b* and *b′* as well. Based on the comparisons between the experimental and calculated spectra, *a* and *a′* are assigned to the symmetric bz-Sc^+-bz stretch in $^1A_{1g}$ and $^3A_{1g}$, respectively. In these stretching motions, two benzene rings move back and forth, while Sc^+ remains almost stationary. Progressions *b* and *b′* are attributed to an out-of-plane ring twist in the ion states. The 890 cm^{-1} peak (*) is not clearly shown in the $^3A_{1g} \leftarrow {}^2B_{3g}$ simulation, but it is close to the calculated wavenumber of a C-H out-of-plane bend, 860 cm^{-1}. This peak is tentatively assigned to the bending mode. Simulations from the $^1A_1 \leftarrow {}^2B_1$ and $^3A_1 \leftarrow {}^2B_1$ transitions of the staggered conformers [Figure 3.3(c)] are rather similar to the eclipsed form. Thus, differentiation of these two conformers is not straightforward from the current study. However, since the eclipsed and staggered forms are predicted to be close in energy, both may exist in the molecular beams.

The ZEKE peaks in the $^1A_{1g} \leftarrow {}^2B_{3g}$ band system are about three times broader than those in the $^3A_{1g} \leftarrow {}^2B_{3g}$. This may indicate a severe predissociation of the $^1A_{1g}$ state. However, scans of the potential energies as a function of the distance between Sc^+-bz and bz do not show much difference between the $^1A_{1g}$ and $^3A_{3g}$ states. Other factors appear to cause the spectral broadening of the $^1A_{1g} \leftarrow {}^2B_{3g}$ transition.

3.3.3 Electron spin multiplicities and bond energies

This study determines that the short-range ground states of Sc-bz and -bz_2 are quartet and doublet, respectively. The determination of the quartet ground state of Sc-bz confirms the BPW91,[140] CASSCF,[144, 154-158] and MCPF predictions.[145] The long-range doublet predicted by CASSCF may exist in our molecular beam, but transitions between the long-range doublet and the short-range singlet or triplet would have very unfavorable FC intensities due to large structural differences. For the dibenzene complex, a doublet ground state has also been predicted by BPW91[140] and CASSCF[154-158] calculations.

Why does Sc-bz prefer a high electron spin state, whereas Sc-bz_2 favors a low spin state? This can be rationalized by considering frontier orbital interactions between Sc and benzene. For Sc-bz in the C_{6v} point group, the Sc 4s atomic orbital belongs to the a_1 representation, and the fivefold degenerate 3d orbitals split into e_1 ($d_{xz,yz}$), a_1(d_{z^2}), and e_2 ($d_{x^2-y^2,xy}$) irreducible representations by assuming that the z-axis is collinear with the sixfold rotational axis. The highest occupied and lowest unoccupied orbitals of benzene are both doubly degenerate with e_1 ($\pi_{2,3}$) and e_2 ($\pi_{4,5}$) representations, respectively. Since the Sc 3d/4s orbitals are located higher in energy than the benzene filled e_1 orbital and lower in energy than the benzene empty e_2 orbital, the metal-ligand interaction should stabilize the Sc $3d_{x^2-y^2}$ and $3d_{xy}$ orbitals by π electron back donation to the benzene empty e_2 orbital and destabilize the Sc $3d_{xz}$ and $3d_{yz}$ orbitals by anti-phase mixing with the benzene filled e_1 orbital. The Sc 4s and $3d_{z^2}$ orbitals may also be destabilized by the anti-phase interaction with the benzene filled a_1 (π_1) orbital. However, this destabilization should be less extensive than the metal $3d_{xz}$ and $3d_{yz}$ orbitals, because the a_1 orbital is located at much lower energy. As a result, the Sc atomic orbitals are expected to be in an energy order of $e_2 < a_1 < e_1$. If the energy separation between e_2 and a_1 is relatively large, the three outermost valence electrons of Sc atom are expected to occupy the lowest energy e_2 orbital only and, in this case, the electron spin multiplicity should be two. On the other hand, one of the three valence electrons is expected to occupy the higher energy a_1 orbital if the $e_2 - a_1$ energy separation is smaller than the energy required for electron pairing. In such a case, the electron spin multiplicity should be four by following Hund's rule. Assuming that the interaction of two benzene molecules and a metal atom is with approximately the same strength, the *d* orbital splitting should be doubled in scandium-dibenzene. Therefore, the electron pairing is likely to form a lower spin state in Sc-bz_2 than in Sc-bz.

The dissociation energies of the neutral complexes can be derived from a thermochemical cycle, $D_o(M\text{-}L_n) = D_o^+(M^+\text{-}L_n) - IE(M\text{-}L_{n-1}) + IE(ML_n)$, where D_o and D_o^+ are the dissociation energies of M-L_n and M^+-L_n, and IE are the ionization energies of M-L_{n-1} and M-L_n. Table 3.3 summarizes the dissociation and ionization energies. The relatively large uncertainty of D_o(Sc-bz) is due to the error of $D_o^+(Sc^+\text{-bz})$ from ion-molecule reaction measurements.[145] The value of 0.7(2) eV for the quartet state of Sc-bz

Table 3.3. Electronic transition energies (T_{00}, eV), adiabatic bond dissociation energies (D_o or D_o^+, eV), and vibrational frequencies (cm^{-1}) of the scandium-benzene complexes.

		ZEKE	B3LYP[a]	PIE[b]
Sc-bz				
$^3A_1 \leftarrow {}^4A_1$	T_{00}	5.158(1)	5.16	5.07(4)
	D_0[c]	0.7 (2)		
	D_0^+	2.1 (2)[d]		
	Sc^+-C_6H_6 stretch	375	336	
	Sc-C_6H_6 stretch	324	320	
$Sc\text{-}bz_2$				
$^1A_{1g} \leftarrow {}^2B_{3g}$	T_{00}	5.069(3)[e]	5.02	5.05 (5)
	C_6H_6-Sc^+-C_6H_6 stretch	206	196	
	Ring out-of-plane twist	302	260	
$^3A_{1g} \leftarrow {}^2B_{3g}$	T_{00}	5.221(1)	5.05	
	C_6H_6-Sc^+-Bz stretch	201	192	
	Ring out-of-plane twist	422	426	

[a] Includes vibrational zero point energy corrections. [b] Photoionization efficiency measurements from references 101-105. [c] For Sc-bz ($^4A_1$) → bz ($^1A_1$) + Sc ($^2D_{1\frac{1}{2}}$). [d] From reference 145. [e] Upper limit.

is in good agreement with the prediction by the CASSCF+MRCI method (0.80 eV),[144] but is much smaller than the BPW91 value (1.78 eV).[140] For Sc-bz_2, the dissociation energy of the doublet state is not obtained as the ion dissociation energy is not available either from experimental measurements or high level *ab initio* calculations.

CHAPTER 4: ELECTRONIC STATES OF NEUTRAL AND CATIONIC BIS(BENZENE) TITANIUM AND VANADIUM SANDWICH COMPLEXES: HIGH-RESOLUTION PHOTOELECTRON SPECTROSCOPY AND THEORETICAL CALCULATIONS

4.1 Introduction

Recently, Duncan and coworkers measured the IR photodissociation spectra of the ionic Ti^+- and V^+-bz sandwich complexes by using rare gas tagging techniques.[172-174] By comparison of their experimental measurements to DFT calculations, the IR spectrum of Ti^+-bz_2 was assigned to the $^4A_1$ state, and that of V^+-bz_2 was attributed to the $^5B_{2g}$ state. However, the $^4A_1$ and $^5B_{2g}$ states of Ti^+-bz_2 and V^+-bz_2 were calculated to be less strongly bound than the predicted low-spin $^2B_{3g}$ and $^3B_{3g}$ states, respectively. The discrepancy between their experimental and computational results was rationalized by two possibilities: the ions were produced in excited states or the relative energies or vibrational patterns of the different electron spin states were predicted incorrectly by the DFT method.[174] As pointed out by these authors, both concerns warrant further investigations, and the latter is probably more serious since DFT calculations are being widely used in studying transition metal-containing molecules and ions.

In addition to the issue of the ground electronic states of these ions, previous measurements have shown discrepancies about the IE of the corresponding neutral complexes. For example, the IE value of Ti-bz_2 was measured to be 5.68(4) and 5.71(2) eV by PIE spectroscopy[101, 103] and 5.5 to 6.0 eV via He I and He II PES.[175] The IE of V-bz_2 was measured to be 5.75(3) and 5.59(4) eV by PIE spectroscopy,[133, 176] 5.95 eV by He I and He II PES,[175, 177] and 6.16(2) eV by Rydberg series UV absorption spectroscopy.[178-181]

Thus, our motivation was to resolve any ambiguity regarding the ground electronic states and improve the IE values of these two complexes. In this work, Ti-bz_2 and V-bz_2 are prepared with the laser-ablation molecular beam technique and seeded in helium supersonic expansions. Their IE values are measured with pulsed field

ionization-zero electron kinetic energy (ZEKE) photoelectron spectroscopy, and the electronic states of the neutral and ionic species are determined by comparison of the experimental spectra and theoretical calculations.

4.2 Experimental and Theoretical Methods

Details of our ZEKE spectrometer have been discussed in Chapter 2. M-bz_2 (M = Ti or V) sandwich complexes were formed by reactions of gaseous metal atoms with benzene (99.0%, EM Sciences) in molecular beams. The metal atoms were produced by pulsed laser vaporization of a metal rod (Ti or V, 99.7 %, Aldrich) with the second harmonic output of a Nd:YAG laser (Lumonics, YM-800, 532 nm, ~1 mJ). The metal atoms were seeded in helium gas (UHP, Scott-Gross), which were delivered by a piezoelectric pulsed valve[71] with a stagnation pressure of ~ 40 psi. A motor-driven device continuously rotated and translated the metal rod to ensure each laser pulse ablated a fresh surface. At room temperature, benzene vapor was introduced through a stainless steel capillary to a small collision chamber (~1.5 mL), located a few centimeters downstream from the ablation region, where the ligand interacted with the metal atoms entrained in the carrier gas.

Molecular masses were measured by photoionization time-of-flight mass spectrometry. Ionization thresholds of the M-bz_2 complexes were located using PIE spectroscopy by recording the mass-selected ion signal as a function of ionization laser wavelength. Prior to ZEKE experiments, the production of the M-bz_2 complexes was maximized by adjusting the timing and power of the vaporization and ionization lasers, backing pressure of the carrier gas, and benzene concentration. ZEKE electrons were generated by photoexcitation of neutral molecules to high-lying Rydberg states, followed by delayed pulsed electric field ionization (1.2 V/cm, 100 ns) of these Rydberg states. A small DC field (~ 0.08 V/cm) was applied to help discriminate ZEKE electrons from kinetic electrons produced directly by photoionization. The photoionization and photoexcitation light was generated by the doubled-frequency output of a dye laser (Lumonics, HD-500) pumped by the third harmonic of a Nd:YAG laser (Continuum,

Surelite-II, 355 nm). A delay generator (Stanford Research Systems DG535) provided the pulsed electric field used for ionization. The ion and electron signals were detected by a dual microchannel plate detector (Burle), amplified by a preamplifier (Stanford Research Systems SR445), averaged by a gated integrator (Stanford Research Systems SR250), and stored in a laboratory computer. Laser wavelengths were calibrated against vanadium or titanium atomic transitions.[169] A field-dependent study was not performed, because the field-induced IE shift is likely much smaller than the spectral linewidth.[182]

Theoretical calculations were carried out with the hybrid B3LYP DFT method implemented in the *GAUSSIAN03* program package.[183] In these calculations, the all electron 6-311+G(d,p) basis was used for all atoms. Although transition metal-benzene sandwich complexes can have staggered and eclipsed configurations, we have previously determined M-bz_2 (M=Sc, Cr, Mo, W) to be in the eclipsed structure,[182, 184] and Kandalam et al. have predicted that eclipsed V-bz_2 is more stable than the staggered one as well.[185] Therefore, we only considered eclipsed configuration for these M-bz_2 (M = Ti, V) complexes. Since Ti/Ti^+ and V/V^+ have 4/3 and 5/4 valence electrons, we considered electron spin multiplicities of 1, 3, and 5 for Ti-bz_2, 2 and 4 for Ti^+-bz_2, 2, 4, and 6 for V-bz_2, and 1,3, and 5 for V^+-bz_2. The eclipsed sandwich M^+/M-bz_2 complexes were optimized with (D_{6h}, D_{2h}, or C_{2h}) and without (C_1) symmetry constraints. Using the optimized geometries from the B3LYP/6-311+G(d,p) calculations, single point energy calculations with CCSD(T)/6-311+G(d,p) were performed on some of the electronic states to check the relative electronic energy ordering of these states.

To simulate spectra, multi-dimensional Franck-Condon (FC) factors were calculated from the theoretical equilibrium geometries, harmonic vibrational frequencies, and normal coordinates of the neutral and ionic complexes.[47] The Duschinsky effect[45] was considered to account for normal mode differences between the neutral and ionic states in the FC calculations. Spectral broadening was simulated by giving each line a Lorentzian line shape with the experimental linewidth. To account for non-Boltzmann temperatures in the molecular beam, the vibrational temperatures for low frequency modes ($\lesssim 600$ cm^{-1}) were specified separately. The calculated IEs are shifted to the experimental value to allow simple comparison of the measured and calculated FC profiles.

4.3 Results and Discussion

4.3.1 Ti-bz_2

4.3.1.1 Low-Lying Electronic States of Ti-Bz_2

Table 4.1 lists the results of eclipsed Ti^+/Ti-bz_2 sandwich complexes from the B3LYP geometry optimization and frequency analyses. All electron spin states have η^6-binding between each benzene ring and the metal atom or ion. For the neutral Ti-bz_2 complex, all geometry optimizations, including the symmetry-relaxed calculations, converged to either D_{6h} or D_{2h} symmetry. The D_{6h} structures have completely flat benzene rings ($\angle_{C\text{-}C\text{-}C\text{-}C} = 0\ ^o$), while the D_{2h} structures have slightly puckered benzene rings ($\angle_{C\text{-}C\text{-}C\text{-}C} = 3 \sim 6\ ^o$), with four out of the six carbon atoms slightly further away from the metal center.

The bonding in bis(benzene) transition metal complexes is generally described by the Dewar-Chatt-Duncanson model. For a D_{6h} geometry with the z-axis being the proper rotation axis, this bonding scheme involves electron donation from filled benzene π orbitals (a_{1g}, a_{2u}, e_{1u}, e_{1g}) to unfilled metal *d* orbitals and back-donation from filled metal *d* orbitals to empty benzene π^* (e_{2g}) antibonding orbitals. The relative energies of the metal *d*-based orbitals are expected to be e_{2g} ($d_{x^2-y^2,\ xy}$) < a_{1g} (d_{z^2}) < e_{1g} ($d_{xy,\ xz}$). For group 4 bis(benzene) metal complexes, the back-donation interaction is believed to be the predominant component of this bonding scheme.[146] Ti-bz_2 is a 16 valence electron complex, 12 of which are benzene π electrons, and 4 are Ti valence electrons. The ligand π electrons have lower energies than the metal electrons, and the electron configuration of the complex is determined by the way of the metal-based electrons filling into outermost molecular orbitals. If metal-ligand interactions are sufficiently strong such that the energy separations between the metal-based orbitals are larger than the energy required for electron pairing, the resultant electronic states should have fewer unpaired electrons and thus lower electron spin multiplicities; vice versa, the resultant electronic states would have higher multiplicities. From the DFT calculations, the lowest-energy Ti-bz_2 structure is in the $^1A_{1g}$ state (D_{6h}) and is characterized by short Ti-C

Table 4.1. Electronic states, point groups (PG), bond lengths (R, Å), dihedral angles (∠, degrees), symmetric bz-M-bz stretch frequencies (ν_s^+ / ν_s, cm^{-1}), and relative electronic energies (E_{ele}, cm^{-1}) of eclipsed Ti- and V-bz_2 sandwich complexes from B3LYP/6-311+G(d,p) calculations. The predicted free benzene structure is also given at this level of theory.

State[a]	PG	R_{M-C}	R_{C-C}	$\angle_{C-C-C-C}$	ν_s^+/ν_s	E_{ele}
Ti-bz_2						
$^1A_{1g}$	D_{6h}	2.27	1.42	0	245	0
$^3B_{1g}$	D_{2h}	2.36, 2.31	1.40, 1.43	6	214	2193
^5A_u	D_{2h}	2.44, 2.41	1.43, 1.39	3	190	12744
Ti^+-bz_2					228[c]	
$^4A_{1g}$	D_{6h}	2.43	1.41	0	183	42323
$^2B_{1g}$	D_{2h}	2.35, 2.29	1.40, 1.42	6	223	43807
V-bz_2						
$^2A_{1g}$	D_{6h}	2.22	1.42	0	250	0
^4A	C_1	2.31, 2.22, 2.32, 2.82, 2.34, 2.26	1.39, 1.44, 1.43, 1.40, 1.37, 1.45	11, 1, 10, 23	228	12532
^6A[b]	C_1	2.31, 3.00, 3.56, 2.38, 2.41, 2.46	1.43, 1.42, 1.39, 1.41	1	219	17843
V^+-bz_2					231[c]	
$^3B_{1g}$	D_{2h}	2.25, 2.31	1.40, 1.42	6	219	43675
$^1A_{1g}$	D_{6h}	2.21	1.42	0	253	50851
bz						
$^1A_{1g}$	D_{6h}		1.39	0		

[a] Electronic symmetry species of all states are labeled with the same Cartesian coordinate system used in the D_{6h} point group. In DFT calculations with Gaussian software, the B_{1g} symmetry species was incorrectly labeled B_{3g}. [b] Slipped sandwich structure. [c] From ZEKE spectra.

distances (2.27 Å). The highest occupied molecular orbital (HOMO) of the $^1A_{1g}$ state is a doubly degenerate $e_{2g}{}^4$ orbital formed by the Ti $3d_{x2-y2,\,xy}$ bonding interaction with an empty benzene e_{2g} orbital. An excited triplet state in D_{2h} symmetry was calculated to be 2193 cm^{-1} higher in electronic energy with slightly longer Ti-C distances (2.36 and 2.31 Å). The single-point energy calculations at the CCSD(T) level of theory yield the same energy ordering of these two states, with their energy separation being increased to 4682 cm^{-1}. The formation of this triplet state can be viewed by promoting an electron from the e_{2g} HOMO to the lowest unoccupied molecular orbital (LUMO) a_{1g} (d_{z2}) of the $^1A_{1g}$ ground state. From D_{6h} to D_{2h} symmetry, the e_{2g} orbital degeneracy breaks into $a_g + b_{1g}$, and the a_{1g} representation becomes a_g. If a b_{1g} electron is excited, the resultant electronic symmetry should be the direct product of $b_{1g} \otimes a_g$. Therefore, the excited triplet state should be $^3B_{1g}$ with the outermost electron configuration of $a_g{}^2(d_{x2-y2,\,xy})b_{1g}{}^1(d_{xy})a_g{}^1(d_{z2})$. In the outputs of the DFT calculations with Gaussian 03,[183] this triplet state was incorrectly labeled $^3B_{3g}$ state because of switching the Cartesian axes when the molecular symmetry lowers from D_{6h} to D_{2h}.

In addition to the singlet and triplet, a quintet neutral state is expected to be even higher energy than the $^3B_{1g}$ state. This state should be much higher in energy, because the formation of such a quintet state requires excitation of two electrons from the e_{2g} HOMO of the $^1A_{1g}$ ground state: one to the a_{1g} LUMO, and the other to the e_{1g} second LUMO. Our DFT calculations predict a ^5A_u (D_{2h}) state at 12744 cm^{-1} above the $^1A_{1g}$ state, with even longer Ti-C distances (2.44 Å). Since this quintet state has much higher energy than both the singlet and triplet states, we do not expect that more expensive calculations will change the energy ordering of these states predicted by the DFT calculations. Therefore, the CCSD(T) single-point calculations were not performed on the ^5A_u state. The prediction of the singlet ground state for the neutral Ti-bz_2 complex is consistent with previous DFT or *ab initio* calculations.[154, 156, 161, 186-189]

For the ionized complex, we have located a $^4A_{1g}$ state in D_{6h} symmetry and a $^2B_{1g}$ state in a slightly puckered D_{2h} symmetry. The $^2B_{1g}$ state is 1484 cm^{-1}above the $^4A_{1g}$ state. The $^4A_{1g}$ state showed a small imaginary frequency (29i) associated with a benzene torsion when the geometry optimization was carried out under the D_{6h} symmetry constraint. However, this imaginary frequency disappeared when the optimization was

performed without symmetry constraint, although both optimization procedures yielded the same molecular geometries. With the CCSD(T) single-point energy calculations, the energy difference between the $^2B_{1g}$ and $^4A_{1g}$ states is reduced to 500 cm^{-1}. The very small energy difference between these two spin states indicates the challenge faced by theory in identifying the ground electronic state of the Ti^+-bz_2 ion. In fact, Rao and co-workers predicted a doublet ground state using the BPW91 density functional and double numerical basis sets with polarization functions.[187] In their calculations, the geometry optimization was constrained in D_{6h} symmetry, allowing only the metal-benzene distances to vary. The energy separation between the doublet and quartet states was not reported in their study. Additionally, accompanying their IR spectroscopic measurements, Jaeger et al. calculated metal-benzene bond dissociation energies of Ti^+-bz_2 using the B3LYP/6-311++G(d,p) method.[174] They reported that the dissociation energy of the $^2B_{1g}$ state (53.5 kcal mol^{-1}) is larger than that of the $^4A_1$ state (47.4 kcal mol^{-1}) for the dissociation process Ti^+-$bz_2 \rightarrow Ti^+$-bz + bz. However, it is not clear if the calculated bond energies reflect the relative stabilities of these two states due to possible spin changes in the dissociation process. For example, our calculations yield the dissociation energies of 104.3 kcal mol^{-1} for Ti^+-bz_2 ($^4A_{1g}$) $\rightarrow$ 2bz ($^1A_{1g}$) + Ti^+ (a ^4F), and 101.3 and 120.7 kcal mol^{-1} for Ti^+-bz_2 ($^2B_{1g}$) $\rightarrow$ 2bz ($^1A_{1g}$) + Ti^+ (a ^4F) and Ti^+-bz_2 ($^2B_{1g}$) $\rightarrow$ 2bz ($^1A_{1g}$) + Ti^+ (a ^2F), respectively. The (a^2F) state of Ti^+ is 13.2 kcal mol^{-1} above the (a ^4F) ground state. Thus, although the $^4A_{1g}$ state has a lower energy than the $^2B_{1g}$ state, the adiabatic dissociation energy of the quartet state (104.3 kcal mol^{-1}) is smaller than the diabatic dissociation energy of the doublet state (120.7 kcal mol^{-1}).

4.3.1.2 PIE and ZEKE Spectra of Ti-bz_2

Figure 4.1(a) presents the PIE spectrum of Ti-bz_2 seeded in a helium jet. The first ionization threshold of this complex (~ 46400 ± 200 cm^{-1}) is obtained by locating a point at which a line drawn through the first onset intersects with a line drawn through the base line and corrected by + 110 cm^{-1}, the energy shift induced by the DC extraction field (320 V / cm). This threshold energy is used to correlate with the ZEKE experiment.

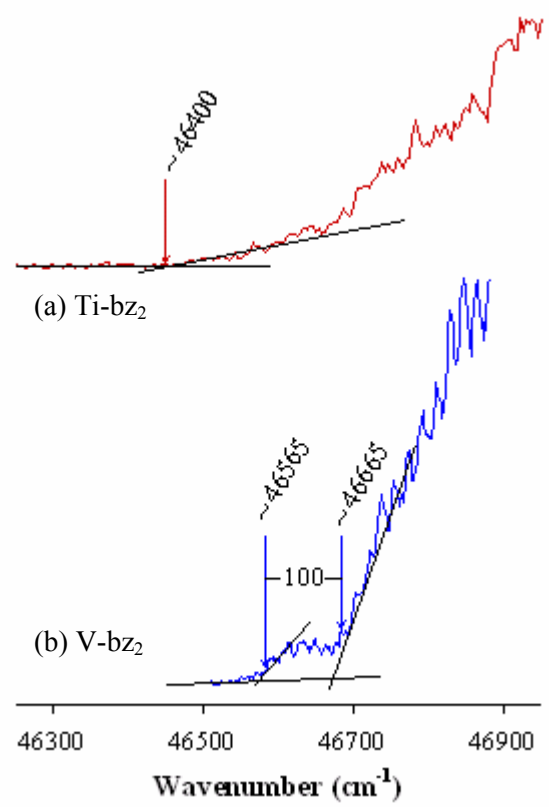

Figure 4.1. PIE spectra of Ti-bz_2 (a) and V-bz_2 (b) complexes seeded in helium carrier. The ionization thresholds are indicated by the vertical arrows.

Figure 4.2(a) presents the experimental ZEKE spectrum of Ti-bz_2 seeded in helium carrier. The ZEKE spectrum begins with a small peak at 46228(8) cm^{-1}. This peak corresponds to the onset of the ion signal observed in the PIE spectrum. To the higher energy side of this small peak is a major vibrational progression with 228 cm^{-1} intervals. Superimposed on each peak of the main progression are small satellite peaks on the higher energy side with a separation of about 12 cm^{-1} from the main peaks. In addition, the spectrum shows a transition at 741 cm^{-1} above the first peak and its combination with the 228 cm^{-1} intervals. The width of each major peak, measured as the full width at half-maximum (FWHM), is approximately 40 cm^{-1} wide. This spectral linewidth is much broader than those previously observed for other transition metal-benzene complexes (FWHM ~ 8 cm^{-1})[182, 184] and is likely due to the unresolved rotational transitions and overlaps of vibrational sequence transitions. Experiments with heavier carrier gases would reduce the spectral broadening, but were not successful due to the limited size of the ZEKE signal.

Previously, we reported the ZEKE spectra of other M-bz_2 (M = Sc, Cr, Mo, W) complexes;[182, 184] Ketkov et al.[190, 191] and Choi et al.[192] reported the mass analyzed threshold ionization spectra of Cr-bz_2. These spectra were dominated by the symmetric M^+-bz_2 stretch vibrations (ν_s^+). For the 14-electron Sc^+-bz_2 complex, the symmetric stretch frequency was measured to be 206 and 201 cm^{-1} in the $^1A_{1g}$ and $^3A_{1g}$ states, respectively. For the 17-electron Cr^+-bz_2 complex, the stretch frequency was measured to be 264 cm^{-1} in the $^2A_{1g}$ state. By comparing with these first-row transition metal complexes, the 228 cm^{-1} vibrational progression in the Ti-bz_2 ZEKE spectrum can be rationally assigned to the symmetric Ti^+-bz_2 stretch. In addition to the metal-ligand stretch progression, satellite peaks in the group 6 M-bz_2 spectra were attributed to overtones of the benzene torsion (ν_t^+) with frequencies of 11, 21, and 45 cm^{-1} as the group was descended. Thus, the small satellite peaks observed in the Ti-bz_2 ZEKE spectrum are assigned to overtones of the benzene torsion mode as well. This assignment gives the fundamental benzene torsion frequency of 6 cm^{-1} for Ti-bz_2, which is about half the magnitude observed for Cr-bz_2. The large variation of the benzene torsion frequency in different metal sandwich complexes should not be surprising, because such torsion motions strongly depend on the metal-ligand binding strength.[182] From the IR photo-

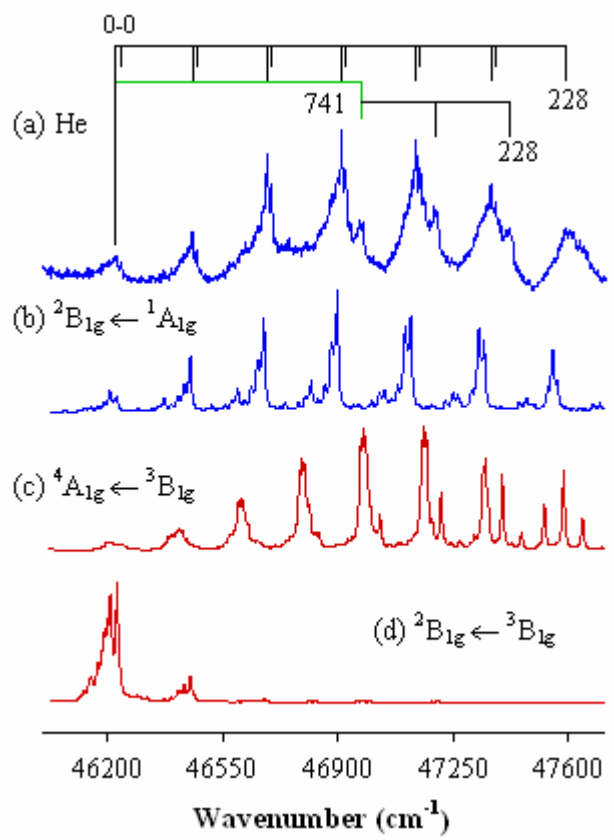

Figure 4.2. Experimental ZEKE spectrum in helium carrier (a) and B3LYP simulations [150 K] of spin-allowed transitions of eclipsed Ti-bz_2 (b) – (d).

dissociation spectrum of Ti^+-bz_2, Jaeger et al. measured a frequency of 739 cm^{-1} for a C-H out-of-plane bending mode.[174] Thus, the 741 cm^{-1} transition in the ZEKE spectrum is assigned to the same C-H bending excitation. From this vibrational assignment, the first peak at 46228 cm^{-1} can easily be attributed to the vibrationless (0-0) transition from the ground electronic state of the neutral complex to an electronic state of the ionic complex.

All the peak positions and corresponding assignments of the Ti-bz_2 ZEKE spectrum are listed in Table 4.2, and IE and vibrational frequencies are summarized in Table 4.3. From the assignment of the origin band, the IE of this complex is determined to be 5.732 ± 0.001 eV, which is at least 20-fold improvement over previous measurements.[101, 103, 175] The measured IE and vibrational frequencies have the best match with the predicted values for the $^2B_{1g} \leftarrow {}^1A_{1g}$ transition. Further details about the assignment of the electronic transition are discussed by comparison of the experimental and simulated spectra.

4.3.1.3 Observed Electronic Transition of Ti-Bz_2

The spectroscopy of transition metal complexes is complicated by the existence of multiple electron spin states in a relative small energy window. Figure 4.3 displays possible spin-allowed transitions from the predicted $^1A_{1g}$ and $^3B_{1g}$ states. The transition from the ^5A_u state is not included in this figure, because this state is predicted at very high energy (12744 cm^{-1}) and, thus, is unlikely responsible for the observed spectrum. In photoelectron spectroscopy, the difference in the electron spin multiplicities must be ±1 between the initial and final states. Therefore, from the $^1A_{1g}$ ground electronic state, only the $^2B_{1g}$ state is accessible; from the $^3B_{1g}$ state, however, both the doublet and quartet states are accessible. The energy of the $^2B_{1g} \leftarrow {}^1A_{1g}$ transition (43807 cm^{-1}) is closer to the measured IE value than that of the other two transitions. The spectral simulations of these spin-allowed transitions are compared to the experimental spectrum in Figure 4.2. The $^2B_{1g}$ (D_{2h}) $\leftarrow {}^3B_{1g}$ (D_{2h}) transition is characterized by the removal of a non-bonding, unpaired electron from the a_g^1 (d_{z2}) HOMO of the triplet neutral state. In this transition, the geometric change is small (Table 4.1), and thus the FC intensity largely congregates

Table 4.2. Peak positions (cm^{-1}) and assignments for the ZEKE spectra of the Ti- and V-bz_2 complexes. *s* stands for the symmetric metal-benzene stretching mode, *t* stands for the benzene torsion mode, and *b* stands for the C-H out-of-plane bending mode.

Ti-bz_2 $^2B_{1g} \leftarrow {}^1A_{1g}$				V-bz_2 $^3B_{1g} \leftarrow {}^2A_{1g}$	
Position[a]	Assignment	Position[a]	Assignment	Position[a]	Assignment
46228	Origin	47137	s_0^4	46655	Origin
46240	t_0^2	47149	$s_0^4\ t_0^2$	46885	s_0^1
46456	s_0^1	47197	$b_0^1\ s_0^1$	47115	s_0^2
46470	$s_0^1\ t_0^2$	47363	s_0^5	47347	s_0^3
46684	s_0^2	47377	$s_0^5\ t_0^2$	47576	s_0^4
46697	$s_0^2\ t_0^2$	47421	$b_0^1\ s_0^2$		
46910	s_0^3	47590	s_0^6		
46921	$s_0^3\ t_0^2$	47601	$s_0^6\ t_0^2$		
46971	b_0^1				

[a] **The uncertainties in peak positions are ~ 8 cm^{-1} for the Ti-bz_2 $^2B_{1g} \leftarrow {}^1A_{1g}$ transition and ~ 15 cm^{-1} for the V-bz_2 $^3B_{1g} \leftarrow {}^2A_{1g}$ transition.**

Table 4.3. Electronic transition energies (T_{00}, eV) and vibrational frequencies (cm^{-1}) of the Ti- and V-bz_2 sandwich complexes from ZEKE spectra and B3LYP/6-311+G(d,p) calculations.

		ZEKE	B3LYP
Ti-bz_2			
T_{00}	$^2B_{1g} \leftarrow {}^1A_{1g}$	5.732(1)	5.484[a]
ν_s^+	C_6H_6-Ti^+-C_6H_6 stretch	228	223
ν_b^+	C-H out-of-plane bend	741	766
ν_t^+	Benzene torsion	6	5*i*
V-bz_2			
T_{00}	$^3B_{1g} \leftarrow {}^2A_{1g}$	5.784(2)	5.458[a]
ν_s^+	C_6H_6-V^+-C_6H_6 stretch	230	219

[a] **With zero-point vibrational energy corrections.**

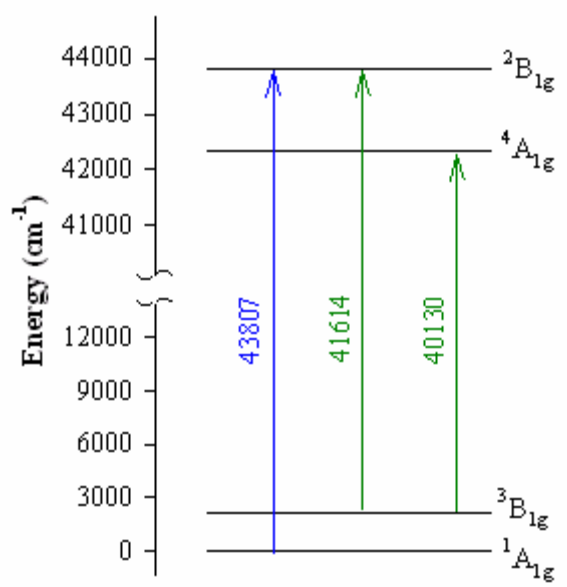

Figure 4.3. Relative energies of the electronic states of Ti^+/Ti-bz_2 predicted at the B3LYP/6-311+G(d,p) level of theory. The spin-allowed transitions [$\Delta(2S+1) = \pm 1$] are indicated by the vertical arrows.

around the 0-0 transition. On the other hand, the $^2B_{1g}$ (D_{2h}) ← $^1A_{1g}$ (D_{6h}) and $^4A_{1g}$ (D_{6h}) ← $^3B_{1g}$ (D_{2h}) transitions are characterized by the removal of a bound electron from the e_{2g}^4 ($d_{x^2-y^2}$ and d_{xy}) HOMO of the $^1A_{1g}$ (D_{6h}) state or the a_{1g} ($d_{x^2-y^2}$) orbital of the $^3B_{1g}$ (D_{2h}) state. Thus, these two ionization processes yield a relatively large structural change (Table 4.1) and a relatively long FC profile.

The simulation of the $^2B_{1g}$ ← $^3B_{1g}$ transition does not match the experimental spectrum at all, and this transition can, thus, be excluded from further considerations. At first glance, both the $^2B_{1g}$ ← $^1A_{1g}$ and $^4A_{1g}$ ← $^3B_{1g}$ simulations correlate with the experimental spectrum. A closer comparison, however, shows significant differences between these two simulations, and the $^2B_{1g}$ ← $^1A_{1g}$ simulation has a much better match to the experimental spectrum than the $^4A_{1g}$ ← $^3B_{1g}$ simulation. First, the predicted Ti^+-bz_2 stretch frequency of 223 cm^{-1} for the $^2B_{1g}$ state matches well to the measured value of 228 cm^{-1}, while the predicted stretch frequency of 183 cm^{-1} for the $^4A_{1g}$ state is severely underestimated. This frequency underestimation in the $^4A_{1g}$ state is clearly observed from the misaligned peak positions (Figure 4.2) between the experimental spectrum and the $^4A_{1g}$ ← $^3B_{1g}$ simulation. Second, the length of the major vibrational progression in the $^2B_{1g}$ ← $^1A_{1g}$ matches better to the experiment than does the $^4A_{1g}$ ← $^3B_{1g}$ transition. The progression length can be assessed by locating the most intense peak in these spectra. In both the experimental and $^2B_{1g}$ ← $^1A_{1g}$ spectra, the most intense peak corresponds to the third-quantum excitation of the stretch mode. In the $^4A_{1g}$ ← $^3B_{1g}$ simulation, however, the most intense peak relates to either the fourth- or fifth-quantum excitation of the stretch mode. Furthermore, the $^2B_{1g}$ ← $^1A_{1g}$ transition energy (43807 cm^{-1}) matches the measured IE (46228 cm^{-1}) significantly better than the $^4A_{1g}$ ← $^3B_{1g}$ transition energy (40130 cm^{-1}). From the above comparisons, the observed spectrum is assigned to the $^2B_{1g}$ ← $^1A_{1g}$ transition.

Our measurement confirms that the ground electronic state of the neutral Ti-bz_2 complex is indeed the $^1A_{1g}$ state, and ionization of Ti-bz_2 in the $^1A_{1g}$ state produces an ion in the $^2B_{1g}$ state. The determination of the singlet ground state for the neutral Ti-bz_2 complex is consistent with previous electric dipole,[189] electron spin resonance,[175] and He I photoelectron measurements[175] in the gas phase and an infrared spectroscopic study in

an argon matrix.[188] However, the $^2B_{1g}$ state is not necessarily the ground electronic state of the ion since the $^4A_{1g}$ state is predicted to have a slightly lower energy than $^2B_{1g}$ in our calculations (Table 4.1). Also, the quartet state is inaccessible via ionization of the $^1A_{1g}$ state in our measurements. Further studies are required to determine the ground electronic state of the ionic Ti^+-bz_2 complex.

4.3.2 V-bz_2

4.3.2.1 Low-lying Electronic States of V-bz_2

The B3LYP results from our theoretical analysis of V-bz_2 are summarized in Table 4.1. The ground electronic state of V-bz_2 is predicted to be the $^2A_{1g}$ state in D_{6h} symmetry, consistent with previous studies.[120, 156, 161, 168, 177, 193-197] Above the doublet state, higher spin ^4A and ^6A states are calculated at 12532 and 17843 cm^{-1}, respectively, and have C_1 symmetry. The $^2A_{1g}$ ground state of V-bz_2 has very similar M-C (2.22 Å) and C-C (1.42 Å) distances to the $^1A_{1g}$ ground state of Ti-bz_2, and both complexes in their ground states have D_{6h} symmetry. The excited states of the two complexes are, however, in rather different structures: the ^4A and ^6A states of V-bz_2 have C_1 symmetry, whereas the $^3B_{1g}$ and ^5A_u states of Ti-bz_2 have D_{2h} symmetry. The ^6A state of V-bz_2 has a slipped structure in which the two benzene rings are still parallel, but not stacked directly atop one another. This slipped-type structure has not been predicted previously for V-bz_2, although similar structures were reported for Cu^+-bz_2 and Ni^+-bz_2.[174] Ionization of the $^2A_{1g}$ ground electronic state of V-bz_2 (D_{6h}) leads to the $^3B_{1g}$ ground state of V^+-bz_2. The V^+-bz_2 ion in the $^3B_{1g}$ state has a slightly distorted structure (D_{2h}), where the benzene rings pucker a few degrees. Above the triplet ion state, a local minimum in the $^1A_{1g}$ (D_{6h}) state is predicted at 7176 cm^{-1}, and a saddle point in the ^5A (C_1) state is locate at 8998 cm^{-1}. The $^1A_{1g}$ state has slightly shorter V^+-C distances (2.21 Å) than the $^3B_{3g}$ state (2.25 and 2.31 Å), while the structure at the saddle point has much longer V^+-C distances (2.51 to 2.55 Å).

4.3.2.2 PIE and ZEKE Spectra of V-bz_2

Figure 4.4(a) shows the ZEKE spectrum of V-bz_2, and Table 4.2 lists the peak positions and assignments. Like Ti-bz_2, the spectrum of V-bz_2 is predominantly composed of one vibrational progression and has a much broader peak width (FWHM ~ 60 cm^{-1}) than other metal sandwich complexes.[182, 184] This vibrational progression begins from a small peak at 46655 (15) cm^{-1}, followed by four peaks separated by 230 cm^{-1}. By analogy to the spectrum of Ti-bz_2, this progression is easily assigned to excitations of the V^+-bz_2 symmetric stretch. No other vibrations are completely resolved in this spectrum, although some shoulder structures appear to be superimposed on the major progression.

The determination of the 0-0 transition from the ZEKE spectrum is not as straight forward as in the case of Ti-bz_2. However, the 0-0 transition can be identified by combining the ZEKE and PIE spectra. The PIE spectrum of V-bz_2 [Figure 4.1(b)] shows two steps beginning at 46565 (50) and 46665 (50) cm^{-1}, respectively. The ion signal between the two onsets is small and rises sharply above the second one. The energy separation between the two steps, ~ 100 cm^{-1}, is much smaller than the 230 cm^{-1} interval observed in the ZEKE spectrum. The energy position of the second onset is within the position of the first ZEKE peak at 46655 (15) cm^{-1}. All these observations suggest that the ion signal below the second onset must arise from a thermally excited vibrational level of the neutral molecule, and the second onset corresponds to the 0-0 transition between the electronic-vibrational ground levels of the neutral and ionic species. Thus the ZEKE peak at 46655 cm^{-1} is assigned to the 0-0 transition as well, which gives an IE value of 5.784(2) eV for the V-bz_2 complex.

4.3.2.3 Observed Electronic Transitions of V-bz_2

The assignment of the electronic transition probed in the ZEKE spectrum is straightforward by comparing with the theoretical predictions. First, the $^2A_{1g}$ state of V-bz_2 is predicted to be 12532 cm^{-1} below the ^4A state and 17843 cm^{-1} below the ^6A state (Table 4.1). With such larger energy differences among these states, the observed

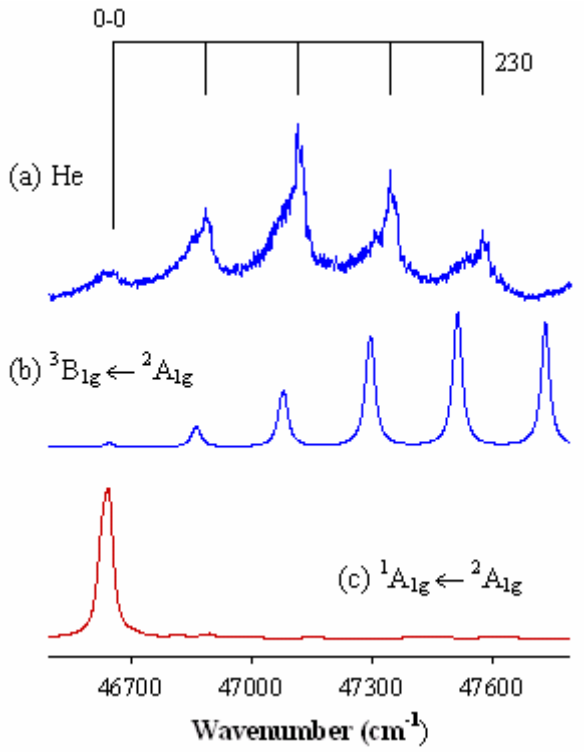

Figure 4.4. Experimental ZEKE spectrum in helium carrier (a) and B3LYP simulations [150 K] of spin-allowed transitions of eclipsed V-bz_2 (b) and (c).

transition must originate from the $^2A_{1g}$ ground state of the neutral molecule, because transitions from the higher-spin states are unlikely under these experimental conditions. Second, although both the $^3B_{1g}$ and $^1A_{1g}$ ion states are accessible from the initial $^2A_{1g}$ state in the ZEKE experiment, only the $^3B_{1g} \leftarrow {}^2A_{1g}$ transition is likely to be observed according to the predicted IE and metal-ligand stretch frequency. The calculated V^+-bz_2 stretch frequency of the $^3B_{1g}$ ion state (219 cm^{-1}) is close to the experimental value (230 cm^{-1}), while the stretch frequency of the $^1A_{1g}$ state (253 cm^{-1}) is too high. The predicted energy of the $^3B_{1g} \leftarrow {}^2A_{1g}$ transition (43675 cm^{-1}) is closer to the measured IE (46655 cm^{-1}) than the calculated $^1A_{1g} \leftarrow {}^2A_{1g}$ transition energy (50851 cm^{-1}). Moreover, the calculated FC intensity of the $^3B_{1g} \leftarrow {}^2A_{1g}$ transition matches the experiment better than that of the $^1A_{1g} \leftarrow {}^2A_{1g}$ as shown in Figure 4.4, although the intensity of the former transition is overestimated.

The determination of the $^2A_{1g}$ ground electronic state for the neutral V-bz_2 complex is consistent with previous electron spin resonance and photoelectron,[175] electric dipole,[189] and magnetic moment measurements[120] in the gas phase and resonance Raman[194] and infrared[168] spectroscopic measurements in nitrogen or argon matrices. Although both the $^3B_{1g}$ and $^1A_{1g}$ ion states are accessible via the $^2A_{1g}$ state, only the $^3B_{1g}$ state is observed in our experiment. The ^5A ion state is inaccessible via the doublet state, but this state is a saddle point with a much higher energy. It is interesting to note that the photodissociation IR spectra of V^+-bz_2 seemed to be more consistent with a quintet state, even though a triplet state was predicted to be more stable.[173, 174] Based on our ZEKE measurements, the ground-state spin multiplicity of V^+-bz_2 is a triplet, not a quintet.

CHAPTER 5: PULSED-FIELD IONIZATION ELECTRON SPECTROSCOPY OF GROUP 6 METAL (Cr, Mo, and W) BIS(BENZENE) SANDWICH COMPLEXES

5.1 Introduction

Since the first synthesis of bis(benzene) metal compounds by Fischer and Hafner in 1955,[198] extensive studies in the condensed phase have been reported on their bonding, structure, and reactivity.[199-205] For transition metal bis(benzene) complexes, the bonding is generally described by the Dewar-Chatt-Duncanson model, which involves electron direct-donation from benzene to metal and back-donation from the metal to the ligand.[204, 205] Most of the sandwich complexes have a sixfold metal binding mode, although four- and twofold fashions also exist.[204, 205]

Group 6 metal bis(benzene) are formally 18-electron, coordinately saturated compounds in their neutral states and can, therefore, be used as stable precursors for gas-phase studies. The studies of these complexes in the gas phase began in the late 1960's,[206-208] and most of the early measurements concerned their ionization energies (IEs).[102, 209-214] However, the reported IE values were inconsistent with each other and had large uncertainties. For example, the IE of Cr-bz_2 was measured to be in the range of 43500 – 47600 cm^{-1}, depending on the experimental methods used.[102, 206-213] The IEs of Mo-bz_2 and W-bz_2 were measured to be 44520 (400)[214] and 43550[175] cm^{-1} by He I photoelectron spectroscopy, respectively. More recently, the best fits of photoabsorption Rydberg transitions yielded the IE values of 44150,[215] 44090.3 (5),[216] and 44030 (30)[217] cm^{-1} for Cr-bz_2 and 43610 (80) cm^{-1} for W-bz_2.[112] Although the Rydberg spectroscopic experiments have narrowed down the range of the IE of Cr-bz_2, significant discrepancies still exist among these studies. The latest IE value of Cr-bz_2 was reported as 44087 (5) cm^{-1} by mass-analyzed threshold ionization (MATI) measurements.[100, 218] However, the IE values of Mo- and W-bz_2 remain to be improved.

In addition to the IE measurements, bond dissociation energies of the cationic and neutral bis(benzene)chromium complexes have been determined by collision-induced dissociation,[219] radiative association kinetics,[220] and threshold photoelectron-photoion

coincidence spectroscopy;[114] their vibronic spectra have been measured by MATI[100] and resonance enhanced two-photon ionization (R2PI) measurements.[98, 99] In the one-photon MATI spectrum, only the Cr^+-bz_2 stretching vibration (264 cm^{-1}) was identified for the ionic ground state, and other peaks were assigned to autoionizing rotational transitions.[100] On the other hand, the Cr-bz_2 stretch (264 cm^{-1}), a C-H bend (788 cm^{-1}), and the benzene torsion (40 cm^{-1}) modes were observed in the lowest Rydberg *p* state of the R2PI spectrum.[99] This brings about an interesting question why the C-H bend and benzene torsion modes were observed in the Rydberg state, but not in the ionic ground state.

This chapter reports the pulsed-field ionization zero electron kinetic energy (ZEKE) spectra of the group 6 M-bz_2 (M = Cr, Mo, W) complexes. The spectra yield adiabatic IEs and vibrational frequencies and determine the electronic states and geometries for the three complexes. This work represents the first vibronic spectroscopy of Mo- and W-bz_2 and greatly improves the IE values for the two complexes. Furthermore, compared to the previous MATI study, additional vibrations are identified for the chromium complex.

5.2 Experimental and Computational Methods

Details of our ZEKE spectrometer have been discussed in Chapter 2. M-bz_2 sandwich complexes were formed by reactions of gaseous metal atoms with benzene vapor (bz: 99.0%, EM Sciences; C_6D_6: 99.5%, Cambridge Isotope Laboratories, Inc.) in molecular beams. The metal atoms were produced by pulsed laser vaporization of a metal rod (Cr, 99.7%, Goodfellow; Mo, 99.95%, Aldrich; W, 99.95%, Goodfellow) with the second harmonic output of a Nd:YAG laser (Lumonics, YM-800, 532 nm, ~1 mJ). The metal atoms were seeded in He, Ar or a He/Ar mixture (UHP, Scott-Gross), which were delivered by a home-made piezoelectric pulsed valve with stagnation pressures of 40 – 60 psi.[221] A motor-driven device continuously rotated and translated the metal rod to ensure each laser pulse ablated a fresh surface. To synthesize Mo- and W-bz_2, benzene vapor was introduced at room temperature, through a stainless steel capillary to a small collision chamber (~1.5 mL). This chamber was located a few centimeters downstream

from the ablation region, where the ligand interacted with the metal atoms entrained in the carrier gas. To synthesize the Cr-bz_2 complex, the benzene vapor was mixed with the carrier gas prior to expansion through the pulse valve nozzle at a very small concentration (~ 0.05 %).

Molecular masses were measured by photoionization time-of-flight mass spectrometry. Ionization thresholds of the M-bz_2 complexes were located using PIE spectroscopy by recording the mass-selected ion signal as a function of ionization laser wavelength. Prior to ZEKE experiments, the production of the M-bz_2 complexes was maximized by adjusting the timing and power of the vaporization and ionization lasers, backing pressure of the carrier gas, and benzene concentration. ZEKE electrons were generated by photoexcitation of neutral molecules to high-lying Rydberg states, followed by delayed (~ 3.5 μs) pulsed electric field ionization (1.2 V/cm, 100 ns) of these Rydberg states. A small DC field (~ 0.08 V/cm) was applied to help discriminate ZEKE electrons from kinetic electrons produced directly by photoionization. The photoionization and photoexcitation light was provided by the doubled-frequency output of a dye laser (Lumonics, HD-500) pumped by the third harmonic of a Nd:YAG laser (Continuum, Surelite-II, 355 nm). A delay generator (Stanford Research Systems DG535) generated the pulsed electric field used for ionization. The ion and electron signals were detected by a dual microchannel plate detector (Burle), amplified by a preamplifier (Stanford Research Systems SR445), averaged by a gated integrator (Stanford Research Systems SR250), and stored in a laboratory computer. Laser wavelengths were calibrated against vanadium or titanium atomic transitions.[169] A field-dependent study from 1 to 12 V/cm for the Cr-bz_2 complex resulted in a field shift of $\Delta E = (1.2 \pm 0.7)\sqrt{F}$, where F is the electric field strength (V cm^{-1}) used for ionization, and ΔE is the shift in measured IE (cm^{-1}). This field effect resulted in an IE shift of -1.1 (7) cm^{-1} with a field strength of 1.2 V cm^{-1} used for recording ZEKE spectra. Since the energy shift is much smaller than the spectral linewidth (~ 7 cm^{-1}), the transition energies reported in this work were not corrected for the field effect. The relatively large uncertainty in the energy shift induced by the ionization field was due to the irregular peak shape, which made accurate location of the signal onsets or maxima difficult.

Geometry optimization and frequency calculations were carried out with the

hybrid density functional B3LYP method and implemented in the GAUSSIAN98 program package.[222] In these calculations, the all electron 6-311+G(d,p) basis was used for the hydrogen and carbon atoms, and the pseudo core potential LanL2DZ basis set was used for the metal atoms. Although the all electron 6-311+G(d,p) basis set could have been used to treat the Cr atom, the pseudo core potential basis was used instead for comparison to the heavier Mo and W atoms, for which the triple-split valence basis is not available.

To simulate spectra, multi-dimensional Franck-Condon (FC) factors were calculated from the equilibrium geometries, harmonic vibrational frequencies, and normal coordinates of the neutral and ionic complexes.[68, 223] The Duschinsky effect[45] was considered to account for normal mode differences between the neutral and ionic states in the FC calculations. Spectral broadening was simulated by giving each line a Lorentzian line shape with experimental linewidth. Transitions from excited vibrational levels of the neutral complexes were simulated by assuming thermal excitations at specific temperatures. The Cr-bz_2 ZEKE spectra were simulated at a vibrational temperature of 100 K. The Mo-bz_2 ZEKE spectra were simulated using a vibrational temperature of 10 K, except for the 8, 113, and 120 cm^{-1} modes of the neutral complex which were specified to have temperatures of 1, 200, and 300 K, respectively.

5.3 Results and Discussion

5.3.1 Theoretical Electronic States and Geometries

Figure 5.1 shows the eclipsed and staggered conformers of the M-bz_2 sandwich complexes, and Table 5.1 lists the bond lengths and dihedral angles for the neutral $^1A_{1g}$ and ionic $^2A_{1g}$ states of the eclipsed form. The M-C and C-C distances of the staggered conformers are nearly the same as that of the eclipsed forms and, thus, not included in Table 5.1. The staggered conformers of the neutral Cr-, Mo- and W-bz_2 complexes are predicted to be 300, 99, and 121 cm^{-1} higher in electronic energy than the corresponding eclipsed forms. The higher-energy staggered forms are not local minimum energy structures, because these calculations resulted in one or more imaginary frequencies. The

Table 5.1. Bond lengths (R, Å) and dihedral angles (∠, °) of eclipsed (D_{6h}) equilibrium geometries of M-bz_2 (M = Cr, Mo, W) from B3LYP calculations.

	R(M-bz)	R(C-C)	R(C-H)	∠(CCCH)
bz		1.394	1.084	0.00
Cr-bz_2[a]				
$^1A_{1g}$	1.655	1.416	1.083	2.42
$^2A_{1g}$	1.676	1.415	1.081	2.76
Mo-bz_2				
$^1A_{1g}$	1.835	1.420	1.083	0.16
$^2A_{1g}$	1.849	1.419	1.082	1.07
W-bz_2				
$^1A_{1g}$	1.819	1.422	1.083	0.58
$^2A_{1g}$	1.818	1.423	1.082	1.04

[a] **Experimental geometry of Cr-bz_2: R(Cr-bz) = 1.616 Å, R(C-C) = 1.416 Å, R(C-H) = 0.95 Å, and ∠(CCCH) = 0.46 °, from reference 224.**

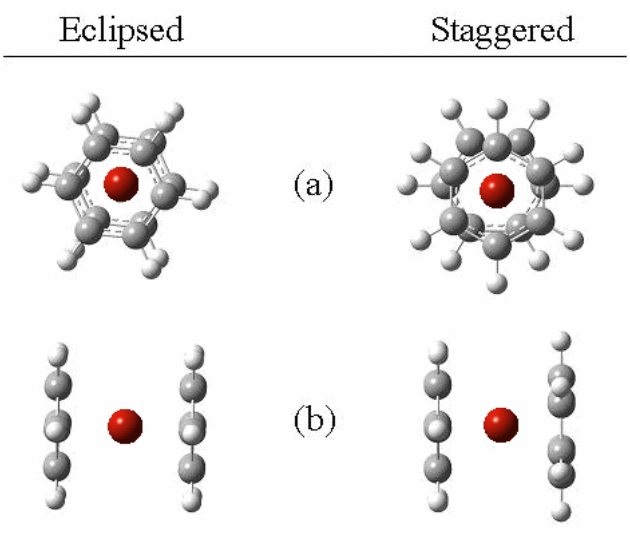

Figure 5.1. Eclipsed and staggered conformers of M-bz$_2$ (M = Cr, Mo, W) sandwich complexes projected along the C_6-axis (a) and perpendicular to the C_6-axis (b).

prediction of a stable eclipsed configuration is consistent with x-ray crystallography,[224, 225] electron diffraction measurements,[226] and previous theoretical calculations.[167, 227-234]

The M-bz distances, R(M-bz), are defined as the distance between the metal and the center of the benzene ring. Each complex is converged to an eclipsed D_{6h} structure in which the C-H bonds are slightly bent towards the metal center by less than 3 °. The metal-bz distances increase in the order Cr < W < Mo for both the neutral and ionic complexes. The shorter W-bz distances are the result of the well-known relativistic effect on the heavier W element, which shrinks the metal atomic *s* orbitals and thus enhances the metal-ligand interactions. The calculated C-C bond distances in all three complexes are longer than those in the benzene free ligand (1.394 Å) due to electron back-donation from the filled metal *d* orbitals to the empty benzene orbitals. The extent of C-C bond lengthening increases slightly with increasing atomic number.

The ground electronic state of the neutral complex is $^1A_{1g}$, and ionization of the neutral ground states leads to a $^2A_{1g}$ ionic state. As expected, the eclipsed doublet state is calculated to be the ground state for the Cr^+, Mo^+, and W^+ complexes and is 200, 64, and 99 cm^{-1} lower in energy than the corresponding staggered states, according to our B3LYP calculations. The geometry differences between the neutral and ionic states are calculated to be small for all three complexes [ΔR(M-bz) < 0.022 Å, ΔR(C-C) < 0.002 Å, and $\Delta\angle$(CCCH) < 1°]. The $^1A_{1g}$ state has 18 valence electrons, six from the metal center (Cr, $3d^5 4s^1$; Mo, $4d^5 5s^1$; W $5d^4 6s^2$) and 12 from the two bz rings. These electrons are configured as $e_{2u}^4 e_{1u}^4 e_{1g}^4 e_{2g}^4 a_{1g}^2$ for Cr-bz_2 and $e_{2u}^4 e_{1g}^4 e_{1u}^4 e_{2g}^4 a_{1g}^2$ for Mo- and W-bz_2, with the a_{1g}^2 electrons essentially non-bonding. Thus the small structural differences between the neutral and ionic states are expected, as ionization from a nonbonding orbital has little effect on the change in geometry.

5.3.2 Spectroscopy

5.3.2.1 PIE Spectra

Figure 5.2 presents the PIE spectra of the M-bz_2 complexes seeded in He carrier. The ionization thresholds determined from the sharp onsets are 44070 ± 50, 44570 ± 50,

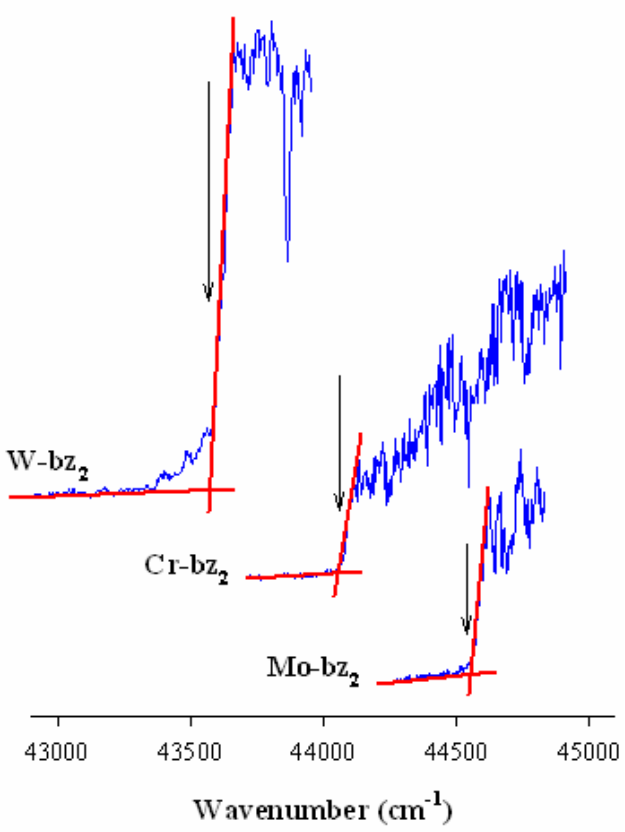

Figure 5.2. PIE spectra of Cr-, Mo-, and W-bz_2 complexes seeded in He carrier. The ionization thresholds are indicated by the arrows.

and 43590 ± 50 cm^{-1} for the Cr, Mo, and W complexes, respectively. These values are obtained by locating a point at which a line drawn through the sharp rise signal intersects with a line drawn through the baseline, and corrected by + 110 cm^{-1}, the energy shift induced by the DC extraction field (320 V/cm). The ionization thresholds from these PIE measurements are used to correlate with ZEKE signals.

5.3.2.2 Cr-bz_2 ZEKE Spectrum

Figure 5.3(a) shows the ZEKE spectrum of Cr-bz_2 seeded in He carrier gas. The spectrum displays a very short FC profile, in agreement with the predicted small difference between the geometries of the neutral and ionic complexes. The full widths at half maximum (FWHM) of the major peaks are about 7 cm^{-1}, which is somewhat broader than the linewidth of the MATI spectrum.[100] Generally, a ZEKE spectrum is expected to have better spectral resolution than that of a MATI spectrum because of the smaller electric field involved in ZEKE collection. The broader linewidth in the ZEKE spectrum is likely due to higher internal temperatures of the Cr-bz_2 complex. In the previous MATI experiment, Cr-bz_2 was purchased from a commercial vendor, vaporized at 100 ^oC, and seeded in Ar or Ne carrier gas. In the present work, the complex was synthesized by the reaction of the laser-vaporized Cr atoms with benzene vapor mixed with He gas. The temperature in the laser vaporization region can be as high as a few thousands of degrees, and He carrier provides less efficient cooling than Ar in the supersonic expansion.[100] Unfortunately, experiments with benzene seeded in Ar were not successful in this work. Nevertheless, the laser-vaporization molecular beam technique is a universal method for synthesizing metal-containing molecules, especially for coordinately unsaturated, short-lived species.

The peak positions and assignments are listed in Table 5.2. The first intense peak at 44081 cm^{-1} correlates to the sharp onset of the PIE spectrum in Figure 5.2 and is assigned to the vibrationless transition (0-0) between the ground electronic states of the neutral and ionic complexes. To the higher wavenumber side of this band origin is a vibrational progression (264 cm^{-1}) and a vibrational interval (787 cm^{-1}). In addition,

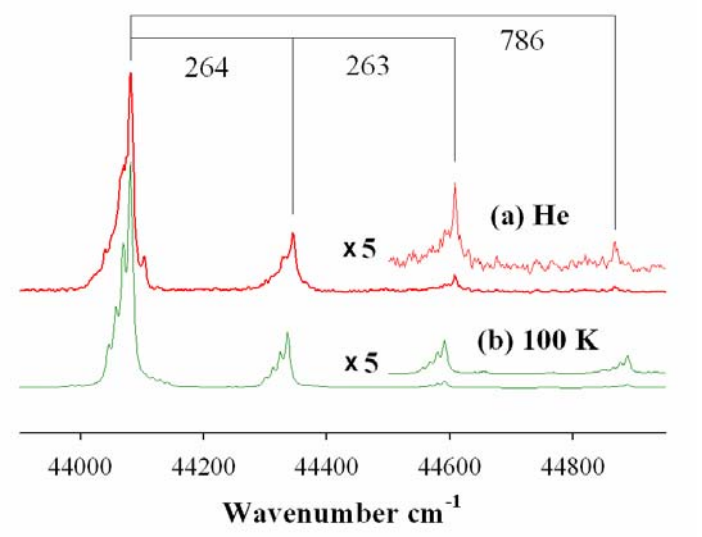

Figure 5.3. ZEKE spectrum of Cr-bz$_2$ seeded in He (a) and B3LYP simulation of the $^2A_{1g} \leftarrow {}^1A_{1g}$ transition from an eclipsed D_{6h} structure (b).

Table 5.2. Peak positions (cm^{-1}) and assignments for the ZEKE spectra of M-bz_2 (M = Cr, Mo, W). *t*, benzene torsion; *s*, bz-M-bz symmetric stretch; *b*, C-H out-of-plane bend, *b'*: C-C in-plane bend.

Cr-bz_2		Mo-bz_2		W-bz_2	
Position	Assignment	Position	Assignment	Position	Assignment
44064	t_3^3	44539	t_3^3	43634	*origin*
44071	t_2^2	44552	t_2^2	43725	t_0^2
44076	t_1^1	44566	t_1^1	43815	t_0^4
44081	*origin*	44581	*origin*	44004	s_0^1
44103	t_0^2	44609	t_1^3	44092	$t_0^2 s_0^1$
44334	$t_1^1 s_0^1$	44623	t_0^2	44248	b'^1_0
44345	s_0^1	44665	t_0^4	44371	s_0^2
44366	$t_0^2 s_0^1$	44681	t_1^5		
44596	$t_1^1 s_0^2$	44843	$t_1^1 s_0^1$		
44608	s_0^2	44858	s_0^1		
44629	$t_0^2 s_0^2$	44887	$t_1^3 s_0^1$		
44868	b_0^1	44899	$t_0^2 s_0^1$		

some unresolved structures appear at the lower energy side of each of these transitions, and a small peak exists just above the band origin. To better resolve the structures around the band origin, measurements were carried out with a slower scan rate, and a representative spectrum is presented in Figure 5.4(a). A few lower energy peaks, spaced ~ 6 cm^{-1} apart, and a higher energy peak, 21 cm^{-1} to the blue, can clearly be observed around the band origin.

Figure 5.3(b) presents the simulation of the $^2A_{1g} - {}^1A_{1g}$ transition of the Cr-bz_2 complex. In this simulation, the vibrational frequencies are not scaled although the calculated IE is shifted to the experimental value for comparison purposes. Furthermore, the conversion between the eclipsed and staggered configurations is assumed to be minimal under the supersonic expansion condition, and the observed spectrum is entirely attributed to the eclipsed form. Although the energy barrier associated with this conversion is expected to be low, this assumption appears to be justified by the good match between the measured and calculated spectra. Based on the theoretical and experimental comparison, the 264 cm^{-1} progression is assigned to the symmetric metal-benzene stretching mode of the ion (ν_s^+), which agrees with the MATI study.[100] The stretching frequency in the ionic $^2A_{1g}$ state is the same as that in the $4p_{x,y}$ Rydberg state (264 cm^{-1}) measured by REMPI spectroscopy,[99] and very similar to that in the neutral $^1A_{1g}$ ground state (277 cm^{-1}) measured by Raman spectroscopy.[235] The similar Cr-bz stretching frequencies in the ionic and neutral ground states confirm again that the HOMO of the neutral complex is essentially a non-bonding orbital.

The simulation shows that the 787 cm^{-1} interval is the fundamental of a C-H out-of-plane bending mode in the ion (ν_b^+). This C-H bend was also observed in the $4p_{x,y}$ Rydberg state, with virtually the same frequency of 788 cm^{-1}.[99] On the other hand, a 788 cm^{-1} transition in the MATI spectrum was attributed to the third quantum of the Cr^+-bz stretching mode, as the transition energy is almost three times the stretching fundamental (264 cm^{-1}).[100] However, this assignment is inconsistent with our theoretical predictions, which show that the FC factor of the third quantum stretch transition is only ~ 10 % of that for the fundamental C-H bend transition. In an attempt to provide additional evidence for the assignment of the 787 cm^{-1} peak, the ZEKE spectrum for the deuterated derivative, Cr-$(C_6D_6)_2$, was recorded. Unfortunately, the ZEKE signal of Cr-$(C_6D_6)_2$ was

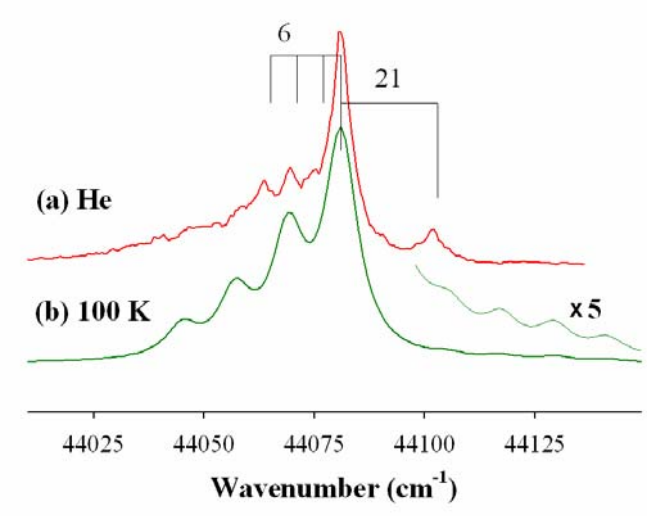

Figure 5.4. Expansion of the band origin for Cr-bz$_2$ seeded in He (a) and the spectral simulation of the $^2A_{1g} \leftarrow {}^1A_{1g}$ band origin from an eclipsed D_{6h} structure (b).

so weak that only the band origin (43996 cm^{-1}) and the fundamental transition of the Cr^+-C_6D_6 stretch (247 cm^{-1}) were identified from the spectrum.

The simulation around the band origin is expanded and presented in Figure 5.4(b), in comparison with the experimental expansion. The partially resolved peaks at the lower energy side of the origin band are attributed to sequence transitions originating from the asymmetric benzene torsion mode (ν_t) in the neutral complex, whereas the small peak at the higher energy side is assigned to the overtone of this torsion mode in the ion (ν_t^+). This assignment yields a torsion frequency of 17 cm^{-1} in the neutral $^1A_{1g}$ state and 11 cm^{-1} in the ionic $^2A_{1g}$ state. The previously reported MATI spectrum also displayed the lower energy peaks, but these peaks were ascribed to autoionizing rotational levels.[100] If the lower energy peaks were due to the transitions of molecular rotational levels, these transitions would not be resolved because the rotational constant of Cr-bz_2 is only ~ 0.04 cm^{-1} and the splitting of rotational levels would be much less than the observed spacing of ~ 6 cm^{-1}. If the low energy peaks were due to the internal rotation of the benzene rings, the energy barrier for the conversion of the eclipsed and staggered conformers should be smaller than the frequency of the benzene torsion mode. However, from our B3LYP calculations this barrier is on the order of hundreds of reciprocal centimeters, much larger than the torsion frequency. Thus, the lower energy peaks are unlikely due to rotational transitions. Torsion transitions were also identified in the $4p_{x,y}$ Rydberg state, but with a higher frequency (40 cm^{-1}).[99]

5.3.2.3 Mo-bz_2 ZEKE Spectrum

Figure 5.5(a) presents the Mo-bz_2 ZEKE spectrum, with the peak positions and assignments in Table 5.2. The Mo-bz_2 spectrum is analyzed by comparison to the Cr-bz_2 spectrum discussed above and to the spectral simulation in Figure 5.5(b). In this simulation, vibrational temperatures were set differently for different modes to account for non-Boltzmann behavior of the molecular beam. Similar to the Cr-bz_2 spectrum, the first strong peak at 44581 cm^{-1} (FWHM ~ 10 cm^{-1}) corresponds to the band origin, with a few weak peaks on each side. The 277 cm^{-1} interval is assigned to the Mo^+-bz symmetric

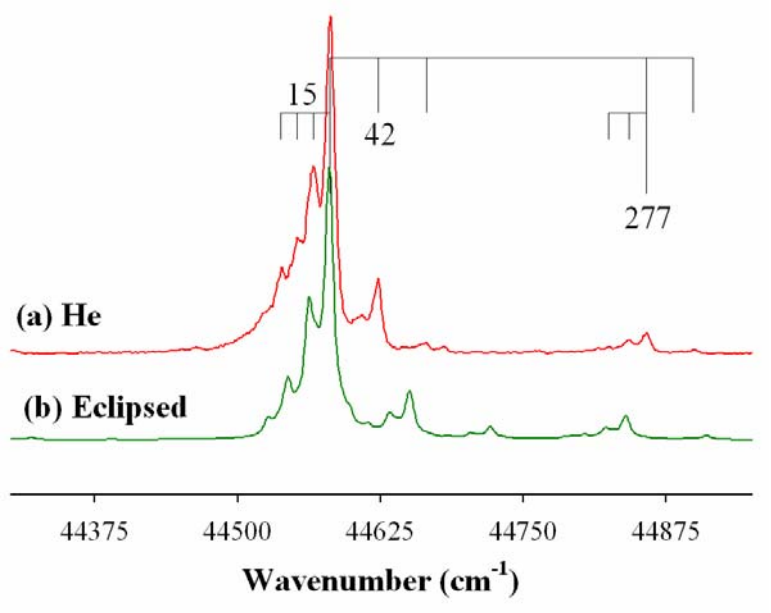

Figure 5.5. ZEKE spectrum of Mo-bz$_2$ seeded in He (a) and spectral simulation of the D_{6h} eclipsed structure (b).

stretch and the 42 cm^{-1} intervals above the band origin to the first and third overtones of the benzene torsion mode in the ionic complex. This assignment leads to a torsion frequency of 21 cm^{-1} in the ion $^2A_{1g}$ state, almost twice that in the corresponding Cr^+-bz_2 state (11 cm^{-1}). The 15 cm^{-1} spacing is due to the sequence transitions of the torsion mode. By combining the sequence and cold transitions, the torsion frequency in the neutral $^1A_{1g}$ state is derived to be 36 cm^{-1}.

5.3.2.4 W-bz_2 ZEKE Spectrum

Figure 5.6 shows the ZEKE spectra of W-bz_2 seeded in He and in Ar. The linewidth of the spectrum in He carrier is about 24 cm^{-1} and is reduced to about 7 cm^{-1} in Ar carrier. These spectra are similar to those of Cr- and Mo-bz_2 and can be conveniently assigned by comparison with these two complexes. Thus, the strongest peak at 43634 (7) cm^{-1} is assigned to the band origin. Above the origin, the 370 cm^{-1} intervals are attributed to the W^+-bz stretch, the 90 cm^{-1} intervals to the overtone transitions of the asymmetric benzene torsion, and the 614 cm^{-1} interval to a C-C in-plane bend. These assignments are summarized in Table 5.2. The active ligand-based bending mode observed in W^+-bz_2 is different from that in Cr^+-bz_2, as shown by their frequencies. In the case of Cr^+-bz_2, the C-H bend has a frequency of 787 cm^{-1} and is characterized by the out-of-plane motion of hydrogen atoms. On the other hand, the C-C-C bend in W^+-bz_2 (614 cm^{-1}) is featured by a distortion of the benzene rings through in-plane C-C-C bending. In addition, unlike the Cr and Mo complexes, the sequence transitions at energies below the band origin were not resolved with He carrier because of the broader linewidth (~ 24 cm^{-1}) of the spectrum. With Ar carrier, hot transitions were quenched, and the spectral linewidth was reduced to ~ 7 cm^{-1} due to more efficient cooling.[236] Unfortunately, experiments with Ar or Ar/He mixtures were not successful for the Cr and Mo complexes due to the inherently small-sized electron signal.

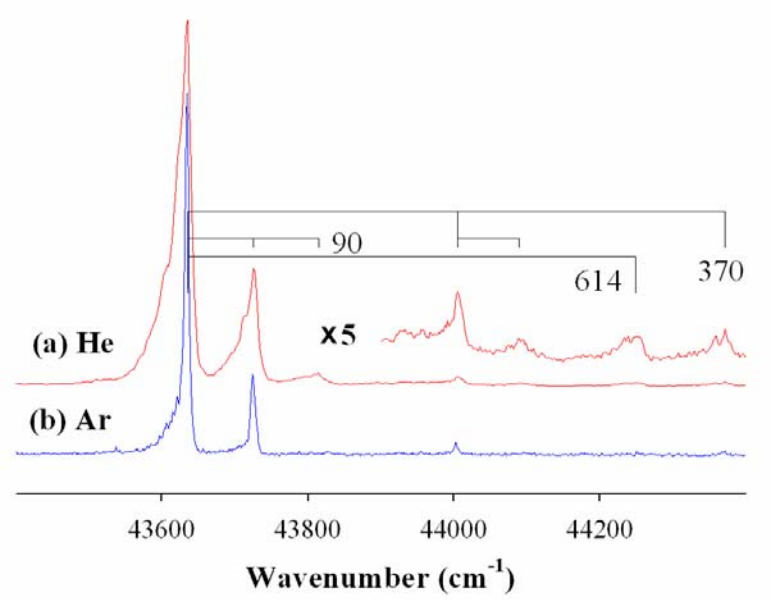

Figure 5.6. ZEKE spectra of W-bz$_2$ seeded in He (a) and Ar (b) carriers.

5.3.3 Comparison to Theoretical Calculations

Table 5.3 compares the experimental and theoretical IEs and vibrational frequencies for the three sandwich complexes. The agreement between the calculated and measured IE values is surprisingly good, which probably arises from the cancellation of the computational errors in both the neutral and ionic states. The theoretical and experimental Cr^+- and Mo^+-bz stretching frequencies are in reasonable agreement, whereas the calculated value for the W^+-bz stretch is much smaller than the measured value. The poor agreement for W-bz_2 indicates that the LanL2DZ effective core potential (ECP) basis is not good enough to correct the relativistic effect. As an attempt to improve the theoretical results of W-bz_2, we also performed calculations with other ECP basis sets for the W atom, and the results are listed in Table 5.4. Among these basis sets,[237-246] the CRENBS basis with averaged effective potentials and spin-orbital operators[237] appears to yield the best W^+-bz stretching frequency. For other vibrational modes, the theory did poorly for the low frequency torsion modes of all three complexes. This discrepancy should not be surprising as the potential energy surfaces along the torsion coordinates are expected to be very shallow.

5.3.4 Comparison to Previous IE Measurements

Previously, IEs of these compounds have been determined by a number of spectroscopic measurements.[100, 102, 112, 175, 206-217] For Cr-bz_2, a value of 44087 cm^{-1} was determined by MATI measurements,[100, 218] and values of 44150, 44090, and 44020 cm^{-1} were reported by three Rydberg series studies.[215-217] Why the IE values from the three Rydberg spectroscopic studies were inconsistent is not clear, but the agreement (within experimental uncertainties) between the ZEKE and MATI experiments indicates the value of 44150 cm^{-1} is too high, while the value of 44020 cm^{-1} is too low. For W-bz_2, the latest IE value of 43610 (80) cm^{-1} was reported from a Rydberg spectroscopic study;[112] our measurement of 43634 (7) cm^{-1} has considerably reduced the uncertainty. The only IE value of 44520 (400) cm^{-1} for Mo-bz_2 was from a He I photoelectron measurement,[214]

Table 5.3. Adiabatic ionization energies (AIE, cm^{-1}), bond dissociation energies (D_o / D_o^+, kcal mol^{-1}), and vibrational frequencies (cm^{-1}) of M-bz_2 (M = Cr, Mo, W). ν_s^+: M^+-bz stretch; ν_t^+ / ν_t: benzene torsion in ionic / neutral complexes; ν_b^+: C-H out-of-plane bend in the ion complex; and $\nu_{b'}^+$: C-C in-plane bend in the ion complex. The calculated values are for the eclipsed D_{6h} structures.

	Cr-bz_2		Mo-bz_2		W-bz_2	
	ZEKE	B3LYP	ZEKE	B3LYP	ZEKE	B3LYP
AIE	44081 ± 7 (43996± 30)[d]	44440	44581 ± 10	44630	43634 ± 7	43480
ΔAIE[a]	10494	-	12623	-	19793	-
ν_s^+	264 (247)[d]	255	277	259	370	282
ν_t^+	11	30	21	35	45	21
ν_t	17	42	36	8	-	23
ν_b^+	787	808	-	-	-	-
$\nu_{b'}^+$	-	-	-	-	614	610
D_0[b]	66(4)		118		145	
D_0^+[c]	96(4), 96(4),[e] 90(9)[f]		154		202	

[a] ΔAIE = IE(M) – IE(M-bz_2), where IE(M) is the ionization energy of the free atom from reference 247, and IE(M-bz_2) is the ionization energy of the M-bz_2 complex (this work). [b] D_0 (M-bz_2 → M + 2bz): D_0 (Cr-bz_2) from threshold photoelectron-photoion coincidence spectroscopy, reference 114; D_0 (Mo-bz_2) and D_0 (W-bz_2) from reference 248, where uncertainties were not reported. [c] D_0^+ (M^+-bz_2 → M^+ + 2bz) = D_0 + ΔAIE. [d] For Cr-C_6D_6. [e] From collision-induced dissociation, reference 219. [f] From radiative association kinetics, reference 220.

Table 5.4. Vibrational frequencies of the W^+-bz_2 complex from B3LYP calculations with various effective core potential (ECP) basis sets for W atom and 6-311+G(d,p) for C and H atoms. ν_s^+: bz-M^+-bz stretch; ν_t^+: benzene torsion; ν_b^+: C-H out-of-plane bend; and $\nu_{b'}^+$: C-C in-plane bend. The calculated values are for the eclipsed D_{6h} structures.

ECP basis	ν_s^+	ν_t^+	ν_b^+	$\nu_{b'}^+$
Experiment (ZEKE)	370	45		614
CRENBS[a]	321	49	823	657
CRENBL[a]	284	15	813	615
Hay-Wadt MB (n + 1)[b]	282	19	808	611
Hay-Wadt VDZ (n + 1)[b]	282	19	808	611
LanL2DZ[b]	282	21	809	610
SBKJC VDZ[c]	281	15	810	612
Stuttgart RSC 1997[d]	281	17	808	613

[a] From reference 237. [b] From references 238, 239, 249. [c] From references 242, 243, 250. [d] From references 244-246.

which is vastly improved to 44581 (10) cm^{-1} by this work.

5.3.5 Trends in Ionization and Bond Energies in Group 6 M-bz_2 Sandwich Complexes

Table 5.3 summarizes the ionization and bond dissociation energies of the group 6 sandwich complexes. Although the IE of the metal atoms increases as the atomic number increases (Cr, 54575 cm^{-1}; Mo, 57204 cm^{-1}; W, 63427 cm^{-1}),[247] the IE trend in the complexes follows the order W < Cr < Mo. The IE shifts (ΔIEs) from the metal atoms to the complexes are 10494, 12623, and 19793 cm^{-1} descending the metal group. This trend of ΔIEs is parallel to that of the bond dissociation energies of the neutral complexes (D_o).[248] By combining the ΔIE and D_o values,[114, 248] the bond dissociation energies of the ionic complexes (D_o^+) are calculated as 95.5, 154.1, and 201.8 kcal mol^{-1} down the group by using the thermochemical cycle: IE (M) – IE (M-bz_2) = D_o^+ (M^+-bz_2) – D_o (M-bz_2). Thus, the ΔIE, D_o, and D_o^+ values all increase as the metal group is descended.

Classically, the bonding in bis(benzene) transition metal complexes is described by the Dewar-Chatt-Duncanson model. For a D_{6h} geometry with the z-axis being the proper rotation axis, this model involves the π electron donation from the filled benzene π orbitals (a_{1g}, a_{2u}, e_{1u}, e_{1g}) to the unfilled metal *s* (a_{1g}), p_z (a_{2u}), $p_{x,y}$ (e_{1u}), d_{z^2} (a_{1g}), and $d_{xz,yz}$ (e_{1g}) orbitals and δ back-donation from the filled metal $d_{x^2-y^2,\,xy}$ orbitals (e_{2g}) to the unoccupied benzene π* (e_{2g}) antibonding orbitals. For the group 6 sandwich neutral complexes, the bonding has been described as highly covalent and dominated by strong metal to ligand δ back-donation which increases as the group is descended.[232, 233] The increasing back-donation has been correlated with the increasing bond energies of the neutral complexes. Ionization removes a non-bonding d_{z^2} electron (a_{1g}) from the neutral complex and creates additional electrostatic interactions. By assuming that the overall strength of the π electron donation and δ back-donation remains unchanged, the strength of the additional electrostatic interaction can be estimated from the difference between the ionic and neutral bond energies or the IE shifts from the metal atom to the complex. Thus, the energy of the electrostatic interaction accounts for 31% (Cr), 23 % (Mo), and

28% (W) of the ion bond energies. The relative strengths of the electrostatic interaction follows the same trend as the calculated metal-benzene distances: R(Cr-bz) < R(W-bz) < R(Mo-bz). This correlation should not be surprising as the charge-multipole interaction falls rapidly as the distance increases.

5.3.6 Trends in M-bz_2 (M = Sc, Ti, V, Cr)

Table 5.5 summarizes the electronic states and transitions of a number of transition metal sandwiches determined from ZEKE spectroscopy and quantum chemical calculations. A number of significant conclusions can be drawn from this table.

All these metal dibenzene neutral complexes prefer the low electron spin states. The determination of the low-spin electronic states of these sandwich complexes also confirms the previously theoretical predictions that the metal-ligand back donation is the major binding mechanism in these early transition metal complexes.[146, 154] Ideally, these molecules have a sixfold principal rotational axis and are in D_{6h} symmetry. Under this symmetry, metal atomic 3d orbitals span three irreducible representations, which are energetically ordered as $3de_{2g}$ (δ,$d_{x2-y2,\ xy}$) < $3da_{1g}$ (σ,d_{z2}) < $3de_{1g}$ (π,$d_{xz,\ yz}$).[251, 252] Electron occupation of the $3de_{2g}$ (δ) orbitals maximizes the electron back donation into the lowest unoccupied π^* orbitals on the benzene rings and increases the metal-ligand interaction. The $3de_{1g}$ (π) orbitals overlap with the benzene highest occupied π orbitals and are strongly antibonding because of favorable spatial overlap and small energy differences between the interacting orbitals. The overlap of the $3da_{1g}$ (σ) orbital with benzene should be small since it is compact and points into the center of the benzene ring, and it has a much higher energy than the benzene a_{1g} π orbitals. Ground electronic states of these metal bis(benzene) complexes will depend on how many valence electrons a metal atom has and how the metal electrons are filled in these orbitals. The number of valence electrons is 3, 4, 5, and 6 for Sc, Ti, V, and Cr, respectively. To maximize the metal-to-ligand electron back donation and thus metal-ligand interaction, all three electrons of Sc or four electrons of Ti are filled into the e_{2g} orbital to form a $^2E_{2g}$ ($3de_{2g}^3$) state for Sc-bz_2 or a $^1A_{1g}$ ($3de_{2g}^4$) state for Ti-bz_2. However, the degenerate $^2E_{2g}$ state of Sc-bz_2

Table 5.5. Electronic transitions, point groups, ionization energies (IE, eV), M^+/M-C distances (Å), symmetric bz-M^+-bz stretch frequencies (ν_s^+, cm^{-1}), and dissociation energies (D_o and D_o^+, eV) for M^+/M-bz_2 (M = Sc – Cr) complexes. IE and ν_s^+ are from ZEKE spectra, M^+/M-C distances from B3LYP calculations, D_o^+ from mass spectrometry-based measurements, and D_o from thermochemical cycles.

	Sc-bz_2[b]		Ti-bz_2	V-bz_2	Cr-bz_2[c]
Transition[a]	$^1A_{1g} \leftarrow {}^2B_{1g}$	$^3A_{1g} \leftarrow {}^2B_{1g}$	$^2B_{1g} \leftarrow {}^1A_{1g}$	$^3B_{1g} \leftarrow {}^2A_{1g}$	$^2A_{1g} \leftarrow {}^1A_{1g}$
Point group	$D_{2h} \leftarrow D_{2h}$	$D_{6h} \leftarrow D_{2h}$	$D_{2h} \leftarrow D_{6h}$	$D_{2h} \leftarrow D_{6h}$	$D_{6h} \leftarrow D_{6h}$
AIE	5.069 (3)	5.221(1)	5.732 (1)	5.784 (2)	5.465(1)
M-C	2.44, 2.39	2.44, 2.39	2.27	2.22	2.18
M^+-C	2.50, 2.40	2.49	2.35, 2.29	2.25, 2.31	2.19
ν_s^+	206	201	228	230	264
D_o^+[d]	4.2 (2)		5.3 (2)	5.0 (2)	4.2 (2)
D_o[e]	2.7 (2)		4.2 (2)	4.0 (2)	2.9 (2)

[a] Electronic symmetry species of all states are labeled with the same Cartesian coordinate system used in the D_{6h} point group. In DFT calculations with Gaussian software, the B_{1g} symmetry species was incorrectly labeled B_{3g}. [b] From reference 184. [c] From reference 182. [d] D_o^+ for M^+-$bz_2 \rightarrow M^+ +$ 2bz. D_0^+ (Sc^+-bz_2) is from reference 253 by assuming that the dissociation energy of Sc-bz_2 is twice as that of Sc-bz. D_0^+ of the other complexes are from reference 116. [e] $D_o = D_o^+ + IE(M\text{-}bz_2) - IE(M)$ for M-$bz_2 \rightarrow$ M + 2bz.

undergoes a Jahn-Teller distortion to form a structure of lower symmetry, which is determined to be D_{2h} with the ground state of $^2B_{1g}$. For V- and Cr-bz_2, the additional metal electrons are filled into the next higher energy $3da_{1g}$ orbital to form the $^2A_{1g}$ ($3de_{2g}^4 3da_{1g}^1$) ground state of V-bz_2 and the $^1A_{1g}$ ($3de_{2g}^4 3da_{1g}^2$) ground state of Cr-bz_2. Ionization of the singlet state of Ti-bz_2 or Cr-bz_2 leads to a doublet ion state, as expected from the selection rule of photoelectron spectroscopy (see Chapter 4). However, the ZEKE spectra of Ti- and Cr-bz_2 are rather different: the spectrum of Ti-bz_2 displays a weak 0-0 transition with a relatively long Ti^+-bz stretch progression, whereas the spectrum of Cr-bz_2 exhibits a strong 0-0 transition with a very short Cr^+-bz stretch progression.[182] This spectral difference is because ionization of Ti-bz_2 removes a bonding electron from the e_{2g}^4 orbital, while ionization of Cr-bz_2 removes a largely non-bonding electron from the a_{1g}^1 orbital. The lower molecular symmetry of the ionic Ti^+-bz_2 complex than that of the neutral Ti-bz_2 complex may also be due to Jahn-Teller distortion as in the case of Sc-bz_2. Ionization of the doublet ground state of Sc- or V-bz_2 may yield a singlet or a triplet ion or both. Indeed, both the singlet (^1A_g) and triplet ($^3A_{1g}$) states are observed in the ZEKE spectrum of Sc-bz_2, with the singlet being 1229 cm^{-1} more stable than the triplet. This observation suggests that the energy required for pairing electrons in Sc^+-bz_2 must be smaller than 1230 cm^{-1}. On the other hand, only a $^3B_{1g}$ state of V^+-bz_2 is probed from ionization of the V-bz_2 $^2A_{1g}$ state. The $^1A_{1g}$ state is predicted ~ 7000 cm^{-1} above $^3B_{1g}$ by the DFT calculations, but has not been observed in our experiment. The $^1A_{1g} \leftarrow {}^2A_{1g}$ transition could not be probed because the predicted transition energy is beyond the wavelength region of our frequency-doubled dye laser.

Metal-carbon distances in these metal bis(benzene) complexes decrease, and metal-benzene stretch frequencies increase from Sc to Cr. The reduction of the M-C distances is consistent with the size decrease from Sc to Cr. The larger reduction from the Sc-C to Ti-C distances may be associated with the increased metal-to-ligand electron back donation, which enhances the metal-ligand bonding. The Ti-, V-, and Cr-bz_2 all have four back-donating e_{2g}^4 electrons, while Sc-bz_2 has only three such electrons. Ionization increases the M-C distances except for Cr-bz_2 where the Cr-C distances are essentially the same in both the neutral and ionized species. This metal-ligand distance trend results, because ionization removes a bonding e_{2g} electron in Sc-, Ti-, and V-bz_2

and a non bonding a_{1g} electron in Cr-bz_2.

The trends in both the metal-carbon distances and metal-benzene stretch frequencies suggest that the bond energies in these complexes should increase from Sc to Cr. The bond energies of Ti^+-, V^+-, and Cr^+-bz_2 were measured by Armentrout and coworkers.[116] Although the bond energies of Sc^+-bz_2 are not available, that of Sc^+-bz was determined experimentally.[253] By assuming that Sc^+ has similar bonding strength with two benzene molecules, as in Ti^+- and V^+-$bz_{1,2}$, the bond dissociation energy of Sc^+-bz_2 can be estimated as twice as that of Sc^+-bz. Using the bond energies of the ion complexes and the ionization energies of the neutral complexes and metal atoms,[247] the bond energies of the neutral complexes have been calculated and are presented in Table 5.5. Although both the neutral and ion bond energies show an expected increase from the Sc to Ti complexes, this trend does not continue and is even reversed from the V to Cr complexes. This trend seems to be contradictory to the trends observed in the metal-ligand distances and stretch frequencies. Especially, one would expect that the 18-electron Cr-bz_2 should have the largest bond energy among these complexes. This discrepancy arises from different spin states between the metal complex and atom. The values in Table 5.5 correspond to adiabatic dissociations to form the ground state metal atoms. If diabatic dissociations are considered, the bond energy values would increase by the amount of the energy difference between metal atomic ground and excited states of the same electron configuration. For the neutral atoms, these energy differences are 1.428, 0.900, 1.711, and 3.966 eV for Sc, Ti, V, and Cr, respectively.[169] Adding these values to the adiabatic dissociation energies, the diabatic dissociation energies of the neutral complexes are calculated to be 4.1 (2), 5.1 (2), 5.7 (2), and 6.8 (2) eV for Sc-, Ti-, V-, and Cr-bz_2, respectively. Clearly, this trend is in accordance with those observed for the metal-ligand bond distances and stretch frequencies. For the ionized complexes, a similar trend has also been obtained for the diabatic dissociation energies.[116]

CHAPTER 6: ZEKE SPECTROSCOPY AND THEORETICAL CALCULATIONS OF NEUTRAL AND CATIONIC GROUP 3 METAL-η^2-NAPHTHALENE COMPLEXES

6.1 Introduction

Metal-arene complexes are of fundamental importance in chemical catalysis,[204, 205] and relevant to astrophysics[254, 255] and biology.[256] In the gas phase, metal-benzene systems have been studied extensively.[257] Studies on metal-polycyclic aromatic hydrocarbon (M-PAH) complexes, on the other hand, are much scarcer in the literature although these complexes could serve as excellent models for the interaction of metal atoms and ions with larger graphitic surfaces.

Naphthalene (np) is one of the smallest PAH molecules consisting of two fused π-rings, and its metal complexes are the most widely studied PAH complexes. In the solid phase, a number of complexes that contain M-np moieties have been studied by X-ray crystallography. For instance, Pomije et al. determined the molecular structure of V-np_2 via crystallographic measurements.[258] In this diligand complex, the two np molecules were established to be eclipsed with respect to one another, while the vanadium atom was sandwiched between two six-membered π-rings, one from each np ligand. In addition, both np molecules were found to be virtually flat in this complex where the V-C distances were nearly identical [2.21(4) Å among those significantly involved in bonding]. Hence, the vanadium atom was considered to be coordinated to two η^6-np ligands, where η denotes the hapticity of the ligand. Although metal coordination to η^6-np ligands has been more commonly observed,[258-260] η^4- and η^5-binding np complexes have been identified as well.[261, 262] For example, Ellis et al. structurally characterized a bis-np sandwich complex of titanium.[261] Like in the structure of V-np_2, the two np ligands were eclipsed in the titanium complex with the metal atom sandwiched between the two six-membered rings. In this complex, however, the two np ligands were strongly puckered into a boat configuration with a dihedral angle of ~ 35.4 ^{o}. Consequently, this metal complex is described as being coordinated to two η^4-np ligands. The titanium atom resides more closely to the four outer carbon atoms of each np ligand with Ti-C distances

of 2.30 to 2.34(1) Å. The other Ti-C distances were much longer, 2.92 to 3.00(1) Å. Thompson et al. has also isolated a M(η^4-np) complex with a puckered np ligand as well.[262] In this manganese complex, the np ligand has a dihedral angle of ~ 37.1 °. Four of the Mn-C distances were much shorter (2.09 to 2.20 Å) than the other two (2.98 and 2.99 Å). In addition, the protonated Mn-np$(CO)_3$ complex was proposed to have an η^5-np ligand, but no crystal structure was provided.[262]

In the condensed phase, a number of studies on alkali metal naphthalene ion pairs have been published. For example, Graceffa and Tuttle used electron paramagnetic resonance (EPR) spectroscopy[263] to measure the dissociation constants of alkali M-np ion pairs in tetrahydrofuran (THF), while Hush and Rowlands measured their electronic spectra via UV-visible absorption spectroscopy.[264] In the latter study, the energies of the absorption bands of anionic np ligands were slightly shifted in the presence of Li^+, K^+, or Na^+ which indicated that the ion-pairs were not completely dissociated in solutions with a concentration of ~ 10^{-3} M at 300 K. In other EPR and nuclear magnetic resonance (NMR) spectroscopic studies by Goldberg and Bolton, these alkali M-np ion pairs were proposed to contain one alkali metal ion binding atop a single anionic np π ring.[265, 266] In a later study by Konishi et al., the metal-np stretch frequencies of alkali metal-naphthalene ion pairs in THF were measured to be 420, 190, 142, and 130 cm^{-1} for the Li^+, Na^+, K^+, and Rb^+ metal ions, respectively, using IR spectroscopy.[267] From these measured frequencies, the effective force constants were calculated to be 0.690, 0.415, 0.355, and 0.510 mdyne/Å for Li^+, Na^+, K^+, and Rb^+ metal ions, respectively. From these force constants, Rb^+-np binding is determined to be stronger than that in Na^+- and K^+-np, but no explanations were given for this bond energy difference.

The matrix-isolation UV-visible spectra of M-np_2 (M = Cr, V, Ti) complexes have been reported by Morand and Francis.[268] These spectra are assigned based on a C_{2h} configuration, in which the naphthalene moieties are slipped with respect to each other. Three transitions of the Ti-np_2 complex at 540, 440, and 392 nm have been assigned to $A_u/B_u \leftarrow B_g$, $A_u \leftarrow A_g$, and $B_u \leftarrow A_g$, respectively. The spin multiplicities of these M-np_2 complexes, however, were not reported.

In the gas phase, Amunugama and Rodgers investigated the interaction of alkali metal ions with benzene, naphthalene, and indole.[269] They used a guided ion beam mass

spectrometer to follow dissociation pathways and measure bond dissociation energies through collision-induced dissociation (CID). Compared to metal-benzene complexes, the binding energy in metal-naphthalene compounds were determined to be stronger. The magnitude of the ion-quadrupole interaction in metal-benzene and -naphthalene systems were considered to be similar, because the quadrupole moments of these two ligands are nearly identical to one another.[269] The observed stronger metal-ligand binding in the naphthalene complexes was, therefore, attributed to the larger polarizability of the naphthalene ligand compared to benzene.[269] Boissel et al.[255, 270] and Dunbar et al.[271] have studied M^+-np ($M^+ = Fe^+, Si^+, Cr^+, Mn^+$) complexes in the gas phase using an ion trap. Boissel et al.[255, 270] studied the reactivities of Fe^+ ions towards naphthalene using Fourier transform mass spectrometry, while Dunbar et al. studied reaction rates and CID of these M^+-np complexes. In the CID experiments, Si^+ was proposed to σ bond to naphthalene, while the other metal ions were believed to form π-binding complexes. Although CID experiments provide information about the binding energies and reaction pathways, they do not provide direct evidence about the molecular structures of these complexes.

In the gas phase, M-np complexes have not been studied by any spectroscopic technique. However, molecular complexes, i.e. NO-np and O_2-np, were studied via anion photoelectron spectroscopy by Barbu et al.[272] From these measurements, the NO^- and O_2^- anions were determined to bind more strongly to naphthalene than benzene, and the stronger binding in the naphthalene complexes was attributed to the larger polarizability of naphthalene. The O_2^- binding strength to np was found to be about 50 % larger than that of N_2^-. While the bonding strengths of both molecular complexes depended on electrostatic interactions, a covalent bonding component was suggested to produce the observed binding energy difference.

Although the molecular structure of M-np complexes in the gas phase has not been directly investigated by experiment, their structures have been predicted using *ab initio* theory. Zhao et al. calculated the structures of M^+-np ($M^+ = Al^+, Li^+, Ca^+$) complexes using MP2 and DFT methods.[273] The structure of these M^+-np complexes was proposed to be in C_{2v} symmetry with the metal binding to the fused C-C bond of naphthalene. In their study, no frequency analyses were done to confirm whether or not those

structures were local minima on the potential energy surface of the molecule. On the other hand, Mecozzi et al. and Hashimoto and Ikuta predicted that the C_{2v} configuration of the Na^+-np complex is a transition state between the two global minimum C_s structures where the metal binds to a single π-ring.[274, 275] In a study by Dunbar et al., a binding energy map was calculated for the binding of Na^+, Mg^+, and Al^+ to most of the π-facial region of naphthalene.[276] These energies were obtained by HF theory, although a portion of the π surface was corrected using a single point energy calculation from MP2 theory. Consistent with other geometry optimizations of M-np complexes,[274, 275] the strongest metal ion binding region was located above one of the six-membered rings. Similarly, the silver cation was also determined to bind above one π-ring of np according to the MP2 calculations by Ma.[277] However, the electronic states or hapticities of these M^+-np complexes ($M^+ = Li^+$, Na^+, Mg^+, Al^+, Ag^+) were not reported in any of these studies.[273-277]

This chapter reports the first measured vibronic spectrum of Sc- and Y-np in the gas phase. These gas phase studies will help elucidate information about the intrinsic bonding in M-np complexes by removing interferences from surrounding solvent and counterion molecules. In addition, coordinately unsaturated compounds can exist in the gas phase, and the molecular configuration of these complexes could be different from the coordinately saturated analogs that have already been discovered. To determine the molecular structures, binding hapticities, and electronic states of the neutral and cationic group 3 M-np complexes, experimental ZEKE spectra are compared to simulations from DFT and MP2 calculations. Furthermore, the ability of DFT to adequately model these M-np systems is tested.

6.2 Experimental and Computational Methods

Details of our ZEKE spectrometer have already been discussed in Chapter 2. M-np (M = Sc, Y, La) complexes were produced by reactions of gaseous metal atoms with naphthalene (99 % $C_{10}H_8$, Aldrich) in a supersonic jet. The metal atoms were produced by pulsed laser vaporization of a metal rod [99.9 % Sc, Alfa Aesar; 99.9 % Y, Goodfellow; 99.9 % La, Alfa Aesar] with the second harmonic output of a Nd:YAG laser

(Lumonics, YM-800, 532 nm, ~ 1 mJ). The metal atoms were carried by a noble gas (He or Ar, UHP, Scott-Gross), which were delivered by a piezoelectric pulsed valve at a stagnation pressure of ~ 50 psi. At room temperature, naphthalene vapor was introduced through a stainless steel tube to a small reaction chamber (~ 1.5 mL), a few centimeters downstream from the ablation region, where the ligand interacted with the metal atoms entrained in the carrier gas.

Molecular masses were measured by photoionization time-of-flight mass spectrometry. Ionization thresholds of the target metal complex were located using PIE spectroscopy. Prior to ZEKE experiments, the production of the target metal complex was maximized by adjusting the timing and power of the vaporization and ionization lasers, backing pressure of the carrier gas, and amount of ligand vapor allowed to enter the source chamber. ZEKE electrons were generated by photoexcitation of neutral molecules to high-lying Rydberg states, followed by delayed (~ 3.5 μs) pulsed electric field ionization (1.2 V/cm, 100 ns) of these Rydberg states. The photoionization and photoexcitation light was provided by the doubled-frequency output of a dye laser (Lumonics, HD-500) pumped by the third harmonic of a Nd:YAG laser (Continuum, Surelite-II, 355 nm). The pulsed electric field was provided by a delay pulse generator (Stanford Research Systems DG535). The ion and electron signals were detected by a dual microchannel plate detector (Burle), amplified by a preamplifier (Stanford Research Systems SR445), averaged by a gated integrator (Stanford Research Systems SR250), and stored in a laboratory computer. Laser wavelengths were calibrated against titanium or vanadium atomic transitions.[169] A field-dependent study was not performed, because the anticipated field induced IE shift (1 ~ 2 cm^{-1}) is smaller than the measured linewidth of the peaks in our experiment.[278]

Geometry optimization and vibrational analysis were carried out with the GAUSSIAN98 and/or GAUSSIAN03 program packages.[74] In these calculations, density functional theory (DFT) and second order Møller-Plesset perturbation (MP2) theory were employed. Geometry optimizations were performed at four levels of basis sets: (B1) 6-311+G(d,p) for all C, H, and Sc atoms; (B2) 6-311+G(d,p) for C and H atoms, LanL2DZ for Sc and Y atoms; (B3) 6-31+G(d,p) for C and H atoms, 6-311+G(d) for Sc atom; and (B4) 6-31G(d) for C and H atoms, 6-311+G(d) for Sc atom. Only the results from struct-

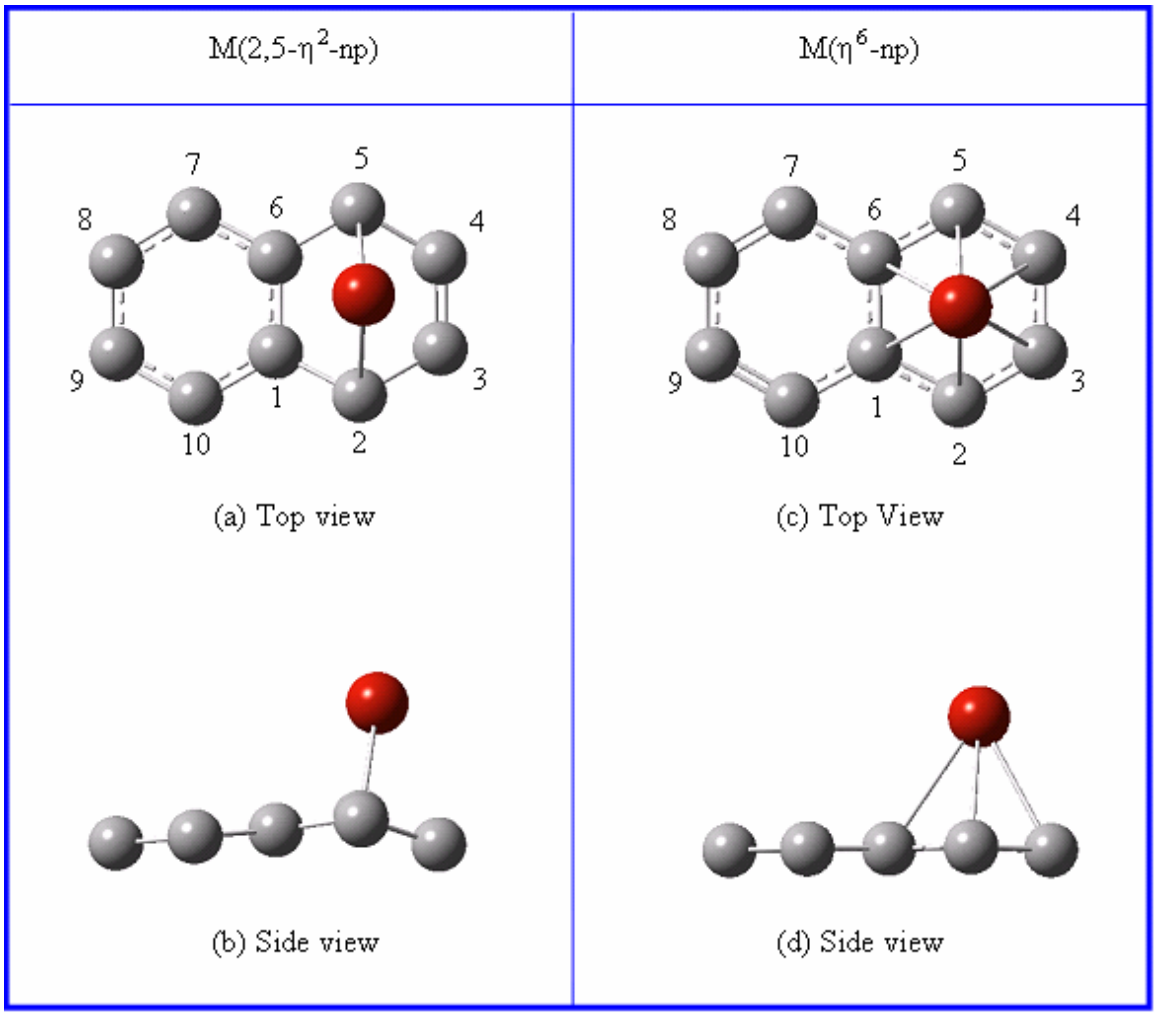

Figure 6.1. Molecular structures [C_s] of M(2,5-η^2-np) complexes from top (a) and side (b) views and M(η^6-np) complexes from top (c) and side (d) views. Metal atoms are red, carbon atoms are grey, and hydrogen atoms are omitted for clarity.

ures with the metal binding atop one of the naphthalene π-rings is presented (Figure 6.1), because the electronic states of Sc- and Y-np with the metal atom above the fused C-C bond were predicted to be transition states or saddle points on the potential energy surface of the metal complex according to our frequency analyses. Initial geometry optimizations were carried out under relaxed symmetry but converged to C_s symmetry. To determine the resultant electronic symmetry, a second set of geometry optimizations was carried out under the C_s symmetry constraint.

To simulate the ZEKE spectra, multidimensional FC factors were calculated from the theoretical equilibrium geometries, harmonic vibrational frequencies, and normal coordinates of the neutral and ionic complexes.[68] The Duschinsky effect[45] was considered to account for normal mode differences between the neutral and ion in the FC calculations. Spectral broadening was simulated by giving each line a Lorentzian line shape with the experimental linewidth. To account for non-Boltzmann temperatures in the molecular beam, the vibrational temperatures for low frequency modes ($\lesssim 600$ cm^{-1}) were specified separately. The theoretical ionization energies were shifted to the experimental values to allow easier comparison of the measured and calculated FC profiles.

6.3 Results and Discussion

6.3.1 Theoretical structures

6.3.1.1 Sc-np

The neutral and monocation np complexes of Sc and Y were investigated using *ab initio* calculations. First, geometry optimizations were performed on the neutral Sc-np complexes in doublet and quartet spin multiplicities, while the corresponding ion complex was optimized with singlet and triplet spin multiplicities at the B3LYP/B1 level of theory. In previous theoretical investigations of the Sc(η^6-bz) complex,[140, 142, 145, 279] the ground electronic states of the neutral and ion complexes were determined to have spin multiplicities of quartet and triplet, respectively. From our B3LYP/B1 calculations

on Sc-np, however, the lowest energy equilibrium structures for the neutral and ion complexes correspond to the $^2A'$ and $^1A'$ electronic states, respectively. Two excited states of the neutral complex, $^4A''$ and $^2A''$, are predicted to be 3330 and 3734 cm^{-1} above the $^2A'$ state. For ionic Sc^+-np, the ground electronic state is predicted to be $^1A'$ with the $^3A''$ state 2023 cm^{-1} higher in energy. The energy separation between the ground electronic states of the neutral and ion complexes is calculated to be 40780 cm^{-1}. Frequency analyses of these neutral and ionic structures indicate that all states are local minima on the potential energy surface.

The calculated structures and energies of each state are summarized in Table 6.1. The metal-ligand distances are reported as individual M-C_x distances, where *x* corresponds to the carbon numbering scheme shown in Figure 6.1. Metal-ligand distances are also reported as perpendicular distances to specific C-C bonds (e.g. Sc-$C_{1,6}$; Sc-$C_{2,5}$; and Sc-$C_{3,4}$). In these M-np complexes, the $\delta(C_3\text{-}C_2\text{-}C_5\text{-}C_6)$ dihedral angle [denoted hereafter as δ(B-ring)] is used as a point of reference to assess the degree of puckering on the bonding π ring, i.e. how puckered the np ligand becomes after coordination. The puckering on the nonbonding π ring is denoted by $\delta(\text{N-ring}) \equiv \delta(C_1\text{-}C_{10}\text{-}C_7\text{-}C_8)$. Throughout the rest of this dissertation, the π-rings that are coordinated to metal centers will be described in the text as either flat or *puckered by X°*, where $X = 180 - \delta(\text{B-ring})$ [i.e. the angle difference from the flat ring].

The bonding in the ground electronic state of Sc-np is quite different from that of Sc-bz. Instead of preserving a flat π-system as in the benzene complex, the scandium atom distorts the local C-C naphthalene framework, and the ligand puckers away from the metal center to form a boat conformation in the $^2A'$ state (Table 6.1). This ligand deformation was also observed in other np complexes, where the metal was proposed to bind to an η^4-np ligand.[261, 262] In those M(η^4-np) complexes, the metal atom or ion resided near the outer edge of the np ligand such that the M-C_i distances (i = 2, 3, 4, 5) were much shorter than the other M-C_j distances (j = 1, 6). Thus, no significant bonding between the metal and C_j atoms was expected to occur due to the rather large M-C_j distances in those M(η^4-np) complexes.[261, 262] Moreover, the much larger M-C_j distances in the M(η^4-np) complexes were also the result of a strongly deformed np ligand, where

Table 6.1. Predicted electronic states, point groups, relative electronic energies (ΔE, cm^{-1}), bond lengths (R, Å), and dihedral angles (δ, degrees)[a] for Sc^+/Sc-np complexes and free naphthalene ligand from B3LYP/B1[b] calculations. See Figure 6.1 for numeric labels.

	B3LYP/B1 (this work)						Expt.[c] (other)
	Sc-np (C_s)			Sc^+-np (C_s)		np (D_{2h})	np (D_{2h})
ΔE^d	0	3330	3734	40780	42803		
State	$^2A'$	$^4A''$	$^2A''$	$^1A'$	$^3A''$	^1A_g	
R(C_1-C_2)	1.473	1.437	1.457	1.475	1.439	1.420	1.422
R(C_2-C_3)	1.448	1.411	1.438	1.443	1.400	1.374	1.381
R(C_3-C_4)	1.377	1.416	1.398	1.387	1.407	1.415	1.417
R(C_1-C_6)	1.428	1.446	1.440	1.432	1.437	1.431	1.412
R(C_1-C_{10})	1.408	1.421	1.412	1.413	1.418	1.420	1.422
R(C_9-C_{10})	1.387	1.377	1.386	1.383	1.378	1.374	1.381
R(C_8-C_9)	1.400	1.414	1.405	1.405	1.411	1.415	1.417
R(Sc-C_1)	2.572	2.555	2.622	2.410	2.544		
R(Sc-C_2)	2.254	2.452	2.324	2.195	2.470		
R(Sc-C_3)	2.446	2.431	2.370	2.379	2.531		
R(Sc-$C_{1,6}$)[e]	2.471	2.450	2.521	2.301	2.441		
R(Sc-$C_{2,5}$)[f]	1.760	2.003	1.845	1.674	2.027		
R(Sc-$C_{3,4}$)[g]	2.347	2.326	2.265	2.275	2.432		
δ(B-ring)	152.4	176.5	161.9	157.9	173.1	180.0	180.0
δ(N-ring)	179.9	179.0	179.8	178.7	178.2	180.0	180.0

[a] Ring puckering is determined by the δ(C_3-C_2-C_5-C_6) ≡ δ(B-ring) and δ(C_1-C_{10}-C_7-C_8) ≡ δ(N-ring) dihedral angles. [b] B1 = 6-311+G(d,p) for all atoms. [c] Experimental values from X-ray diffraction measurements, reference 280. [d] The ΔE values are relative to the $^2A'$ state. [e] Perpendicular distance from Sc to C_1-C_6 bond. [f] Perpendicular distance from Sc to C_2-C_5 bond. [g] Perpendicular distance from Sc to C_3-C_4 bond.

the np framework was puckered by more than 30 °. Likewise, in the neutral $^2A'$ ground state of Sc-np, we find the π-ring that is involved in Sc bonding to be puckered by 27.6 °, while the nonbonding π-ring remains nearly flat, 0.1 ° of puckering. This ligand deformation seems to be the result of a change in hybridization on the C_2 and C_5 atoms from sp^2 towards sp^3. In addition, metal coordination disrupts the aromaticity of the ring binding to the Sc center, and π electron localization causes the C_3-C_4 bond to shorten significantly. The C_1-C_6 bond remains essentially the same length during this Sc coordination, because its π-electrons do not participate in metal bonding. Instead, these π-electrons remain in the conjugated π system of the nonbonding π-ring. Based on these structural considerations, the scandium atom is proposed to bind to an η^2-np molecule. This hapticity assignment is reasonable, because the scandium atom sits much closer to the C_2 and C_5 (2.254 Å) atoms than the C1, C3, C4, and C6 atoms (2.446 to 2.572 Å).

The ligand puckering observed in M-np systems is the result of partial covalent bonding where the carbon sp^2 hybridized orbitals are converted to a new hybrid orbital, i.e. between sp^2 and sp^3 hybridization. Thus, the magnitude of puckering is used as an indicator for the amount of covalent bonding between the metal and naphthalene ligand. From this point of view, the $^2A'$ state is expected to have the most covalent bonding out of all the neutral states considered in this work according to the largest degree of puckering. Hence, the ground electronic state of Sc-np is the $^2A'$ state, because more covalent bonding results in stronger metal-ligand binding, which ultimately contributes to a lower energy structure. In the $^4A''$ excited state, a Sc(η^6-np) complex is formed where both π-rings are essentially flat. Consequently, this state has less covalent bonding and is calculated to be higher in energy as summarized in Table 6.1. In this Sc(η^6-np) complex, six M-C distances are predicted to be nearly the same, and the magnitude of the C-C bond lengths are more evenly distributed, 1.411 to 1.446 Å in the η^6 complex versus 1.377 to 1.473 Å in the η^2 complex.

Whether the metal binds to two or six carbon atoms, coordination will also weaken specific C-C bonds. In general, metal-arene bonding is described by ligand π-donation to unfilled metal orbitals and back-donation from the metal to empty π* orbitals of the ligand. Both donation and back-donation weaken the C-C bonds, and,

consequently, their distances are lengthened with respect to the free ligand upon metal coordination. Specifically, the C_1-C_2 and C_2-C_3 bond lengths in the $^2A'$ state are elongated by 3.7 and 5.4 %, respectively, with respect to the free ligand. The other carbon 2pπ orbitals not significantly involved in metal-ligand bonding remain conjugated and have essentially the same bond lengths as those in the free ligand; for instance, the C_1-C_{10} and C_9-C_{10} bond lengths change by only 0.8 and 1.1 %, respectively. In contrast, the C_3-C_4 bond shortens by 2.7 %. These variations in C-C distances are consistent with our hapticity assignment to a M(2,5-η^2-np) complex in the ground electronic state. In the quartet excited state, on the other hand, all six C-C bonds on the coordinating π ring were elongated with respect to the free ligand, but to a lesser extent than those in the ground electronic state of the neutral complex. The sp^2 hybridization on these carbon atoms remained unchanged upon coordination as indicated by the flatness of the rings in this state. The excited doublet state, however, is predicted to be puckered by ~ 18.1 ^{o}. In this state, the scandium atom is coordinated to an η^4-np ligand, because four Sc-C distances are much shorter (2.324 and 2.370 Å) than the other two (2.622 Å). In addition, the C_3-C_4 bond length is significantly longer than that in the η^2 complex, which indicates that these two carbon atoms participate in metal-ligand bonding.

Ionization of the $^2A'$ state generates the lowest energy $^1A'$ state. Like in the ground electronic state of the neutral complex, the scandium ion is bound to an (η^2-np) molecule as well. Thus, similar structural differences between the free and coordinated np ligand of the singlet state are predicted. The np ligand is significantly puckered, and the C_3-C_4 bond is shortened. In addition, the Sc-C_2 and -C_5 distances (2.195 Å) are much shorter than others (2.379 to 2.410 Å). To produce this singlet state, an electron is removed from a metal-based *d* orbital. This singlet ionic state has shorter Sc-C distances compared to the $^2A'$ state as a result of the ion-quadrupole interaction, which is not present in neutral molecules. Upon ionization, the metal ion not only pulls closer to the np ligand, but also migrates towards the center of the π-ring as seen by comparing the relative ratios of the Sc-$C_{1,6}$ to Sc-$C_{3,4}$ distances. This migration is likely a result of the addition of the ion-quadrupole force. These electrostatic interactions are renowned for providing extra binding strength in ionic complexes. Thus, the total binding energy (BE), the sum of covalent and electrostatic interactions, should be larger for the ionic

complexes. An ionization energy (IE) measurement can confirm this prediction via a thermodynamic cycle: $\Delta IE = \Delta BE$, where ΔIE is the IE of the metal complex subtracted from the IE of the bare metal atom, and ΔBE is the BE of the neutral complex subtracted from the BE of the ionic complex. According to this relationship, the IE of the metal-ligand complex should be significantly smaller than the IE of the bare metal atom.

While the ground electronic state of the ion has a puckered ring, the first excited $^3A''$ state of the ion has virtually flat π rings to form an η^6-np complex. This triplet state has longer Sc-C distances, more evenly distributed C-C bond lengths, and less degree of puckering compared to the singlet state. All of these trends indicate that the triplet state is more loosely bound than the singlet state, which is analogous to the quartet state of the neutral complex. Hence, the molecular structures of Sc-np seem to be consistent with the predicted relative electronic energies at the B3LYP/B1 level of theory.

6.3.1.2 Y-np

Only singlet and doublet spin multiplicities are considered in our calculations of the Y-np complex, because theoretical investigations on the Sc-np complex have indicated that the ground electronic states have multiplicities of doublet and singlet for the neutral and ion, respectively. In addition, calculations on the yttrium complex is restricted to the B2 basis set, because the all-electron 6-311+G(d,p) basis set was not available for yttrium. At the B3LYP/B2 level of theory, the ground electronic state of the neutral Y-np complex is predicted to be the $^2A'$ state. An excited $^2A''$ state was calculated to be 5240 cm^{-1} above the ground electronic state. The energy separation between the ground electronic states of the neutral and ion ($^1A'$) was 41028 cm^{-1}, about the same difference predicted for that of the Sc-np complex. The energies and ground electronic state structures of the neutral and ionic Y-np complexes are summarized in Table 6.2.

The structures of the Y^+/Y-np complex in the ground electronic state were not all that different from that of Sc^+/Sc-np. In the ground electronic states of the neutral and ionic yttrium complex, the naphthalene ligand is puckered by 28.1 and 23.0 ^{o}, respect-

Table 6.2. Relative electronic energies (ΔE_{rel}, cm^{-1}), transition energies (T_{00}, cm^{-1}), vibrational frequencies of ion (ν^+, cm^{-1}), bond lengths (R, Å), and dihedral angles (δ, degrees)[a] of Y-np predicted by MP2 and DFT calculations with the B2 basis set.[b]

	ZEKE	B3LYP/B2	G96LYP/B2	BPW91/B2	MP2/B2
ΔE_{rel}					
$^2A'$		0	0	0	0
$^2A''$		5240	4654	4176	
$^1A'$		41028	39487	40172	39740
T_{00}[c]					
$^1A' \leftarrow {}^2A'$	40798	41263	39719	40397	39885
$^1A' \leftarrow {}^2A''$		36262	35339	36543	
Frequencies[d]					
ν_{26}^+ (a′)	93	93	89	91	89
ν_{50}^+ (a″)	173	479	460	457	160
ν_{25}^+ (a′)	279	266	257	264	262
ν_{24}^+ (a′)	314	300	290	299	298
ν_{23}^+ (a′)	378	385	373	376	383
ν_{22}^+ (a′)	516	489	474	507	497
ν_{20}^+ (a′)	597	607	589	585	597
Geometry[e]					
$R(C_1\text{-}C_2)$		1.478/1.475	1.486/1.482	1.483/1.477	1.485/1.480
$R(C_2\text{-}C_3)$		1.448/1.452	1.458/1.459	1.455/1.456	1.458/1.461
$R(C_3\text{-}C_4)$		1.385/1.377	1.394/1.386	1.393/1.386	1.389/1.384
$R(C_1\text{-}C_6)$		1.432/1.429	1.445/1.440	1.443/1.438	1.435/1.433
$R(C_1\text{-}C_{10})$		1.411/1.406	1.419/1.414	1.416/1.412	1.413/1.412
$R(C_9\text{-}C_{10})$		1.385/1.390	1.395/1.400	1.393/1.397	1.393/1.394
$R(C_8\text{-}C_9)$		1.403/1.398	1.409/1.405	1.407/1.403	1.407/1.405
$R(Y\text{-}C_1)$		2.589/2.773	2.599/2.792	2.566/2.740	2.546/2.668
$R(Y\text{-}C_2)$		2.355/2.429	2.361/2.443	2.341/2.418	2.301/2.363
$R(Y\text{-}C_3)$		2.555/2.626	2.564/2.637	2.538/2.610	2.547/2.609
$R(Y\text{-}C_{1,6})$[f]		2.488/2.679	2.497/2.698	2.463/2.644	2.443/2.570
$R(Y\text{-}C_{2,5})$[g]		1.879/1.980	1.881/1.992	1.853/1.960	1.797/1.880
$R(Y\text{-}C_{3,4})$[h]		2.460/2.576	2.467/2.544	2.441/2.517	2.450/2.516
δ(B-ring)		157.0/151.9	156.8/152.1	157.1/153.0	151.6/148.7
δ(N-ring)		178.9/179.9	178.9/179.9	178.9/180.0	179.4/179.7

[a] Ring puckering is determined by the $\delta(C_3\text{-}C_2\text{-}C_5\text{-}C_6) \equiv \delta$(B-ring) and $\delta(C_1\text{-}C_{10}\text{-}C_7\text{-}C_8) \equiv \delta$(N-ring) dihedral angles. [b] B2 = 6-311+G(d,p) for C and H atoms, LanL2DZ for Y atom. [c] Includes zero point energy corrections. [d] All active modes are totally symmetric (a′), except for ν_{50}^+ (a″), and originate in the $^1A'$ ionic state: ν_{26}^+ is ring bending about $C_1\text{-}C_6$ axis, ν_{25}^+ is ring puckering about $C_7\text{-}C_{10}$ axis with Y^+ rock, ν_{24}^+ is Y^+-np stretch with ring puckering about $C_7\text{-}C_{10}$ and $C_2\text{-}C_5$ axes, ν_{23}^+ is the Y^+-np stretch with ring puckering about $C_7\text{-}C_{10}$ axis, ν_{22}^+ is ring puckering about $C_7\text{-}C_{10}$ and $C_2\text{-}C_5$ axes, and ν_{20}^+ is an in-plane ring distortion, and ν_{50}^+ is an asymmetric (a″) out-of-plane ring distortion. [e] Optimized geometrical parameters for the $^1A'/{}^2A'$ states. See Figure 6.1 for numeric labeling scheme. [f] Perpendicular distance from Y to $C_1\text{-}C_6$ bond. [g] Perpendicular distance from Y to $C_2\text{-}C_5$ bond. [h] Perpendicular distance from Y to $C_3\text{-}C_4$ bond.

ively, to form Y(η^2-np) complexes. Also, the C-C distances in the neutral and ionic Y-np complexes are predicted to be nearly the same as those in the Sc-np complexes. In contrast to Sc^+/ Sc-np, the Y^+/Y-C distances were significantly longer. The longer Y^+/Y-C distances were attributed to the larger metal radius of Y^+/Y due to the higher principal quantum number in the valence shell compared to Sc^+/Sc. As a result, the metal-ligand binding in the Y^+-np complex is expected to be weaker compared to the Sc^+-np complex, because electrostatic forces are known to decrease rapidly as a function of distance. On the other hand, the bond dissociation energy of the neutral Y-np complex is expected to be larger than that of the Sc complex, because the Y atom is more polarizable. The calculated binding energies at the B3LYP and MP2 level of theory for the Sc and Y complexes are presented in Table 6.3. Indeed, the binding energy of the neutral Y-np complexes is predicted to be larger than that of the Sc-np complex by both the B3LYP and MP2 calculations. In contrast, the binding energy of the ionic complexes is surprisingly predicted to be stronger in the Y^+ complex. The stronger binding in the Y^+ complex must be due to a larger covalent bonding component, since the Y^+-C distances were predicted by theory to be longer than the Sc^+-C distances. The stronger covalent bonding in the ionic Y^+-np complex is consistent with the stronger Y covalent bonding of these two neutral complexes as predicted by theory. However, these theoretical energy comparisons may not be entirely practical, because the yttrium element could not be treated with the same basis set as scandium. To determine the credibility of these theoretical results, experimental measurements on these complexes are necessary as discussed in the following sections.

6.3.2 Spectroscopy

6.3.2.1 PIE spectra of Sc-, Y-, and La-np

Figure 6.2 presents the PIE spectra of the group 3 M-np complexes seeded in helium carrier gas. The ionization thresholds determined from the sharp onsets were 41190 ± 60, 40670 ± 300, and 36360 ± 300 cm^{-1} for the Sc, Y, and La complexes, respectively. These values were obtained by locating a point at which a line drawn through

Table 6.3. Ionization energies (IE, cm^{-1}), vibrational frequencies[a] (ν, cm^{-1}), and adiabatic bond dissociation energies (D_o^+/D_o, kcal•mol^{-1}) of M-np complexes (M = Sc, Y, La) determined by experimental measurements and/or theoretical calculations. The uncertainties of the IEs are ± 3 cm^{-1} for Sc- and Y-np; the uncertainty in the IE of La-np is about ± 300 cm^{-1}.

	Sc-np			Y-np			La-np	np
	ZEKE	MP2[b]	B3LYP[b]	ZEKE	MP2[c]	B3LYP[c]	PIE	TPES[d]
IE	41193	39071	41027	40798	39885	41263	36360	65687
ΔIE[e]	11729	9221	11854	9348	8317	12085	8620	
D_o^+ / D_o		49 / 23	57 / 23		81 / 57	66 / 31		
ν_{26}^+/ν_{26}	112/100	113/108	116/98	93/--	89/--	93/--		
ν_{25}^+/ν_{25}	298/256	295/268	295/240	279/--	262/--	266/--		
ν_{24}^+/ν_{24}	347/315	342/326	350/311	314/--	298/--	300/--		
ν_{23}^+/ν_{23}	389/370	412/438	401/385	378/--	383/--	385/--		436
ν_{21}^+, ν_{22}^+	516	524	528	516	497	489/--		501
ν_{20}^+		608	616	597	597	607/--		
ν_{50}^+		385	471	173	160	729/--		

[a] All active modes are totally symmetric (a′), except for ν_{50}^+ (a″), and correspond to the $^1A'$ / $^2A'$ states: ν_{26}^+/ν_{26} are ring bends about C_1-C_6 axis, ν_{25}^+/ν_{25} is ring puckering about C_7-C_{10} axis with M^+/M rocks, ν_{24}^+/ν_{24} and ν_{23}^+/ν_{23} are M^+-np stretches with ring puckering about C_7-C_{10} and C_2-C_5 axes, ν_{22}^+ (Y-np) or ν_{21}^+ (Sc-np) is ring puckering about C_7-C_{10} and C_2-C_5 axes, and ν_{20}^+ is an in-plane ring distortion, and ν_{50}^+ is an asymmetric out-of-plane ring distortion. [b] 6-311+G(d,p) for all atoms. [c] 6-311+G(d,p) for C and H atoms, LANL2DZ for Y atom. [d] From references 281, 282. Only frequencies < 600 cm^{-1} are listed. [e] ΔIE = IE(M) – IE(M-np), where IE(M) is the ionization energy of the bare metal atom from reference 247, and IE(M-np) is the ionization energy of the M-np complex (this work).

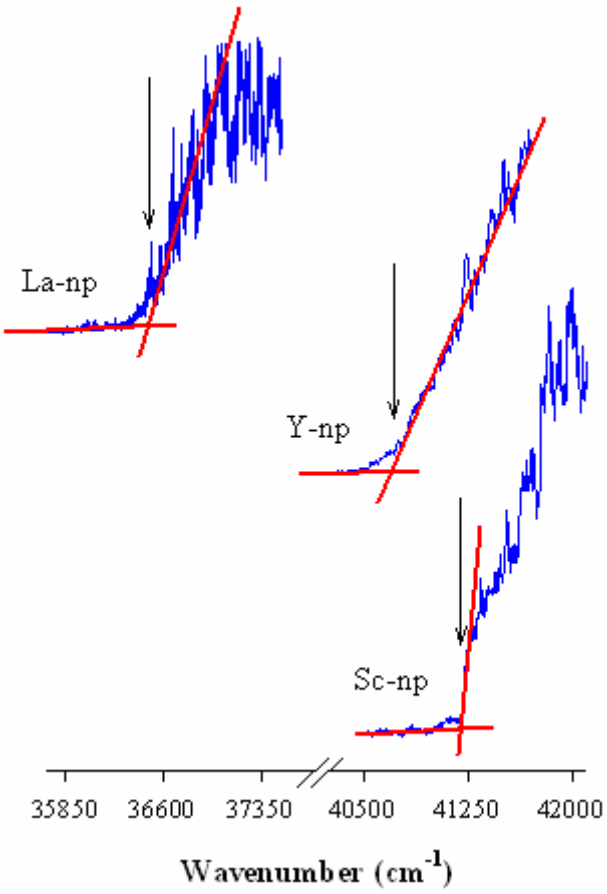

Figure 6.2. PIE spectra of the Sc-, Y-, and La-np complexes. The ionization thresholds are indicated by the arrows.

the sharp rise signal intersected with a line drawn through the baseline, and corrected by + 110 cm^{-1}, the energy shift induced by the DC extraction field (320 V/cm). The ionization thresholds from these PIE measurements were used to correlate with ZEKE signals.

Compared to the bare metal atoms, the IEs of the M-np complexes were red shifted by 11732, 9476, and 8620 cm^{-1}, respectively. These IE shifts indicated that the binding energy of each ionic complex was larger than the corresponding neutral complex. In addition, the monotonic decrease in the ΔIE values is consistent with our theoretical prediction that the bond dissociation energy of the neutral complexes increases as the group is descended. However, this trend could also indicate that the bond dissociation energy of the ionic complexes decreases as the group is descended.

6.3.2.2 ZEKE spectroscopy of Sc-np

Figure 6.3(a) shows the ZEKE spectrum of Sc-np seeded in a 1-1 mixture of helium and argon carrier gases; the relevant portion of the spectrum is also shown for the metal complex seeded in pure helium carrier gas. The full widths at half maximum of the major peaks are about 6 cm^{-1}. The peak positions and assignments are listed in Table 6.4. The first intense peak at 41193 cm^{-1} correlates to the sharp onset of the PIE spectrum in Figure 6.2 and is assigned to the vibrationless transition (0-0) between the ground electronic states of the neutral and ionic complexes. To the higher frequency side of the band origin are four vibrational progressions with frequencies of 112 (26_0^k), 298 (25_0^m), 347 (24_0^n), and 389 (23_0^p) cm^{-1} and one vibrational interval with a frequency of 516 (21_0^1) cm^{-1}. In addition, four vibrational intervals are identified on the lower energy side of the band origin at frequencies 100 (26_1^0), 254 (25_1^0), 315 (24_1^0), and 370 (23_1^0) cm^{-1}. All the other peaks in the spectrum, except those labeled by "#" and "*", are assigned to combinations of these vibrational intervals. The peak labeled by "#" is much narrower than others, and its intensity more strongly depended on the excitation laser power. This narrow peak was also identified in the ZEKE spectrum of Sc-bz and is attributed to an

Table 6.4. Peak positions (cm-1) and assignments (Assign.) for the Sc- and Y-np ZEKE spectra corresponding to the 1A' ¬ 2A' electronic transition.

Sc-np				Y-np			
Position	Assign.	Position	Assign.	Position	Assign.	Position	Assign.
40823	23_1^0	41709	21_0^1	40798	0_0^0	41479	$24_0^1 25_0^1 26_0^1$
40878	24_1^0	41763	$24_0^1 26_0^2$	40891	26_0^1	41488	$23_0^1 24_0^1$
40939	25_1^0	41788	25_0^2	40983	26_0^2	41515	$24_0^2 26_0^1$
40990	$24_1^0 26_0^1$	41805	$23_0^1 26_0^2$	40995	[b]	41546	$23_0^1 25_0^1 26_0^1$
41049	$25_1^0 26_0^1$	41825	$21_0^1 26_0^1$	41077	25_0^1	41570	$24_0^1 25_0^1 26_0^2$
41093	26_1^0	41838	$24_0^1 25_0^1$	41112	24_0^1	41580	$23_0^1 24_0^1 26_0^1$
41103	$24_1^0 26_0^2$	41879	$23_0^1 25_0^1$	41144	50_0^2	41606	$24_0^2 26_0^2$
41193	0_0^0	41887	24_0^2	41168	$25_0^1 26_0^1$	41629	25_0^3
41205	26_1^1	41928	$23_0^1 24_0^1$	41176	23_0^1	41671	$24_0^1 25_0^2$
41238	25_1^1	41949	$24_0^1 25_0^1 26_0^1$	41203	$24_0^1 26_0^1$	41699	$24_0^2 25_0^1$
41305	26_0^1	41971	23_0^2	41234	$50_0^2 26_0^1$	41708	$20_0^1 24_0^1$
41316	26_1^2	41991	$23_0^1 25_0^1 26_0^1$	41258	$25_0^1 26_0^2$	41734	24_0^3
41401	# [a]	41998	$24_0^2 26_0^1$	41268	$23_0^1 26_0^1$	41765	$23_0^1 24_0^1 25_0^1$
41415	26_0^2	42040	$23_0^1 24_0^1 26_0^1$	41295	$24_0^1 26_0^2$	41791	$24_0^2 25_0^1 26_0^1$
41435	$23_0^1 25_1^0 26_0^1$	42060	$24_0^1 25_0^1 26_0^2$	41314	22_0^1	41800	$23_0^1 24_0^2$
41491	25_0^1	42082	$23_0^2 26_0^1$	41355	25_0^2	41825	$24_0^3 26_0^1$
41540	24_0^1	42101	$23_0^1 25_0^1 26_0^2$	41360	$23_0^1 26_0^2$	41891	$23_0^1 24_0^2 26_0^1$
41582	23_0^1	42109	$24_0^2 26_0^2$	41389	$24_0^1 25_0^1$	41917	$24_0^3 26_0^2$
41603	$25_0^1 26_0^1$	42149	$23_0^1 24_0^1 26_0^2$	41395	20_0^1	41983	$20_0^1 24_0^1 25_0^1$
41614	[b]	42224	$23_0^1 24_0^1 25_0^1$	41423	24_0^2	42008	$24_0^3 25_0^1$
41651	$24_0^1 26_0^1$	42264	$23_0^2 25_0^1$	41454	$23_0^1 25_0^1$	42043	24_0^4
41693	$23_0^1 26_0^1$	42275	$23_0^1 24_0^2$				

[a] Corresponds to an atomic transition of tantalum, an impurity of the scandium rod. [b] These features, marked by * in the spectrum, are very small and cannot be assigned to combinations of fundamental frequencies. These small features are tentatively assigned to either a Fermi resonance or Coriolis interaction.

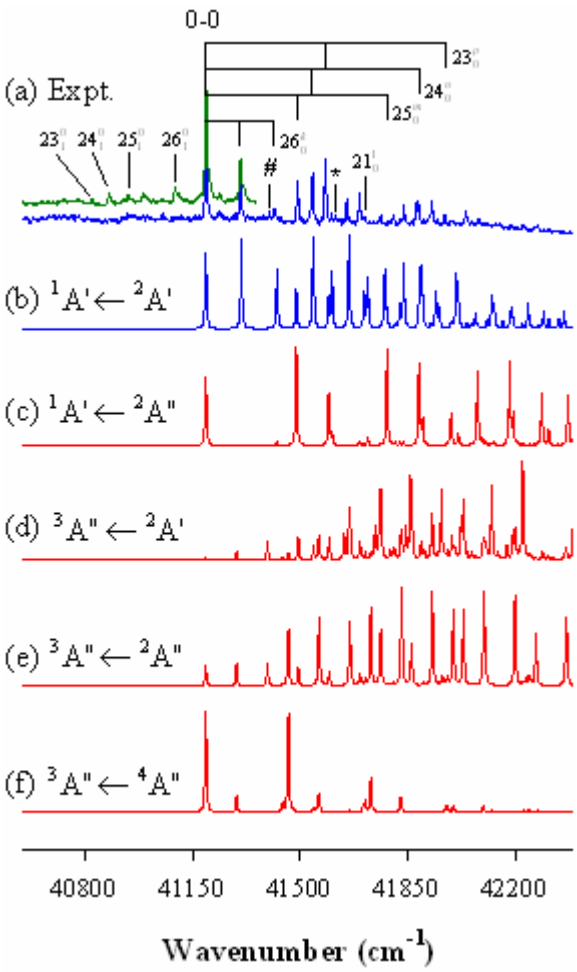

Figure 6.3. Sc-np ZEKE spectrum recorded with helium (top) and a 1-1 mixture of helium-argon (bottom) carrier gases (a) and spectral simulations (B3LYP/B1) of various spin-allowed transitions (b) – (f). B1 = 6-311+G(d,p) for all atoms.

atomic transition of tantalum, an impurity of the scandium rod.

To assign the observed vibrational intervals to specific modes, the measured frequencies are compared to those of the bare np^+ ligand and Sc-bz. In the two color (1 + 1′) threshold photoelectron spectroscopy (TPES) of the free np ligand in a supersonic free jet, several vibrational modes were active.[281, 282] However, only two of these modes had comparable frequencies to those measured in the Sc-np ZEKE spectrum (Table 6.3). Thus, the measured frequencies of 389 and 516 cm^{-1} in the Sc-np ZEKE spectrum are assigned to ligand-based vibrations of the ionic complex, while the 370 cm^{-1} vibrational interval is assigned to a ligand-based mode of the neutral complex. These ligand-based vibrations mainly contain C-C out-of-plane bends. Further attempts to determine the nature of other vibrational modes are made by comparing the Sc-np ZEKE spectrum to that of Sc-bz. In the ZEKE spectrum of Sc-bz, the Sc^+/Sc-bz stretch modes were measured to have frequencies of 324 and 375 cm^{-1} for the neutral and ionic complex, respectively. Therefore, the 389 and 370 cm^{-1} vibrational intervals that have been assigned to ligand-based vibrations by comparison to np^+ frequencies may contain a Sc-np stretching component as well. In addition, the 347 and 315 cm^{-1} vibrational intervals are likely to have Sc-np stretch components as well by comparison to the measured Sc-bz frequencies. For Sc-np frequencies that were measured to be less than 300 cm^{-1}, spectral simulations were necessary to determine their nature.

Because scandium has three outer valence electrons, the electron-spin multiplicity of the ground state of Sc-np should be either two or four, and that of Sc^+-np should be one or three. Thus, our calculations were restricted to these four spin states. The simulations of various spin-allowed transitions are plotted below the experimental ZEKE spectrum in Figure 6.3(a) – (f). The simulated $^3A'' \leftarrow {}^2A'$ [Figure 6.3(d)] and $^3A'' \leftarrow {}^2A''$ [Figure 6.3(e)] transitions display extremely long progressions and do not match the experimental spectrum [Figure 6.3(a)] at all. The very long vibrational progressions observed in these simulations are not surprising due to the rather large structural differences between the two states. The $^3A'' \leftarrow {}^4A''$ transition [Figure 6.3(f)] has a shorter progression, but the calculated peak positions and FC structure do not match the experiment very well. Furthermore, the much higher energy $^4A''$ state is not expected to be populated in the cold molecular beam where vibrational temperatures have been

estimated to be 40 – 300 K depending on the carrier gas conditions.[236] Agreement between the simulation of the $^1A' \leftarrow {}^2A''$ transition [Figure 6.3(c)] and the experimental spectrum is also poor. Like the $^4A''$ state, the excited $^2A''$ state was not expected to be populated since this state is calculated to lie 3734 cm^{-1} above the ground electronic state. Out of all the spin-allowed transitions, only the simulation of the $^1A' \leftarrow {}^2A'$ transition [Figure 6.3(b)] matches the measured frequencies well, although the vibrational intensities are overestimated. Moreover, the $^2A'$ and $^1A'$ states were predicted to be the ground electronic states of neutral and ionic Sc-np, respectively, by our B3LYP calculations.

By comparing the experimental spectrum to the simulation of the $^1A' \leftarrow {}^2A'$ transition, the observed vibrational modes were determined. All active modes belong to the totally symmetric a′ representation in the C_s point group. All of these modes contain either in-plane or out-of-plane C-C-C bending motions. These out-of-plane bending motions deform the π-ring about particular C-C bonds that act as an axis for ring puckering. In addition to these C-C-C bending motions, some modes also include metal motions. For example, Sc^+/Sc rock components are identified in ν_{25}^+/ν_{25} along with an ring puckering about the C_7-C_{10} axis. Two Sc^+/Sc-np stretch motions are found in ν_{24}^+/ν_{24} and ν_{23}^+/ν_{23}. The other vibrational frequencies are mainly ligand-based, and further details about the nature of these modes are described in the Table 6.5 footnotes.

In hopes of improving the agreement between experiment and theory, the $^1A'$ and $^2A'$ states were calculated using different methods and basis sets. The simulations of the $^1A' \leftarrow {}^2A'$ transition with different levels of theory were compared to the experimental spectrum. Compared to the simulation from our B3LYP calculations, the B3P86 method simulated a shorter ν_{26}^+ vibrational progression and matched experiment slightly better, but not to our satisfaction. Although simulations from different DFT calculations do not usually show any substantial differences from one functional to the other, our investigation of the Ti-np complex illustrated that the BPW91 method was better than the B3LYP and B3P86 functionals in simulating the ZEKE spectrum of Ti-np (see Chapter 7). However, no improvement in the spectral simulation of the Sc-np ZEKE spectrum was found via the BPW91 method. Finding a suitable functional method that adequately

Table 6.5. Relative electronic energies (ΔE_{rel}, cm^{-1}), transition energies (T_{00}, cm^{-1}), vibrational frequencies of ion/neutral (ν^+/ν, cm^{-1}), bond lengths (R, Å), and dihedral angles (δ, degrees)[a] of Sc-np predicted by MP2 and DFT calculations with the B1, B2, and B3 basis sets.[b]

	ZEKE	B3LYP/B1	B3P86/B3	BPW91/B2	MP2/B1
ΔE_{rel}					
$^2A'$		0	0	0	0
$^4A''$		3330			
$^2A''$		3734			
$^1A'$		40780	44222	39569	39192
$^3A''$		42803			
T_{00}[c]					
$^1A' \leftarrow {}^2A'$	41193	41027	44446	39814	39071
$^1A' \leftarrow {}^2A''$		37697			
$^3A'' \leftarrow {}^2A'$		42939			
$^3A'' \leftarrow {}^2A''$		39609			
$^3A'' \leftarrow {}^4A''$		39585			
Frequencies[d]					
ν_{26}^+/ν_{26}	112/100	116/98	118/102	114/97	113/108
ν_{25}^+/ν_{25}	298/256	295/240	305/252	289/238	295/268
ν_{24}^+/ν_{24}	347/315	350/311	358/324	339/312	342/326
ν_{23}^+/ν_{23}	389/370	401/385	417/393	398/378	412/438
ν_{21}^+	516	528	535	513	524
Geometry[e]					
$R(C_1\text{-}C_2)$		1.475/1.473	1.473/1.471	1.479/1.475	1.481/1.491
$R(C_2\text{-}C_3)$		1.443/1.448	1.442/1.447	1.450/1.453	1.451/1.469
$R(C_3\text{-}C_4)$		1.387/1.377	1.387/1.378	1.394/1.385	1.394/1.385
$R(C_1\text{-}C_6)$		1.432/1.428	1.431/1.428	1.442/1.438	1.437/1.433
$R(C_1\text{-}C_{10})$		1.413/1.408	1.412/1.408	1.417/1.413	1.415/1.414
$R(C_9\text{-}C_{10})$		1.383/1.387	1.384/1.387	1.391/1.395	1.392/1.393
$R(C_8\text{-}C_9)$		1.405/1.400	1.405/1.400	1.409/1.405	1.409/1.407
$R(Sc\text{-}C_1)$		2.410/2.572	2.377/2.521	2.400/2.551	2.397/2.469
$R(Sc\text{-}C_2)$		2.195/2.254	2.165/2.223	2.183/2.244	2.179/2.163
$R(Sc\text{-}C_3)$		2.379/2.446	2.350/2.414	2.372/2.438	2.386/2.400
$R(Sc\text{-}C_{1,6})$[f]		2.301/2.471	2.267/2.418	2.289/2.448	2.287/2.363
$R(Sc\text{-}C_{2,5})$[g]		1.674/1.760	1.632/1.718	1.652/1.741	1.642/1.616
$R(Sc\text{-}C_{3,4})$[h]		2.275/2.347	2.245/2.314	2.267/2.338	2.282/2.297
δ(B-ring)		157.9/152.4	157.4/152.9	157.2/152.7	155.1/147.5
δ(N-ring)		178.7/179.9	178.6/179.8	178.8/179.9	178.6/179.3

[a] Ring puckering is determined by the $\delta(C_3\text{-}C_2\text{-}C_5\text{-}C_6) \equiv \delta$(B-ring) and $\delta(C_1\text{-}C_{10}\text{-}C_7\text{-}C_8) \equiv \delta$(N-ring) dihedral angles. [b] B1 = 6-311+G(d,p) for all atoms; B2 = 6-311+G(d,p) for C and H atoms and LanL2DZ for Sc atom; B3 = 6-31+G(d,p) for C and H atoms and 6-311+G(d) for Sc atom; B4 = 6-31G(d) for C and H atoms and 6-311+G(d) for Sc atom. [c] Includes zero-point vibrational energy corrections. [d] All active modes are totally symmetric (a′), and correspond to the $^1A'/{}^2A'$ states: ν_{26}^+/ν_{26} are ring bends about $C_1\text{-}C_6$ axis, ν_{25}^+/ν_{25} are ring puckering about $C_7\text{-}C_{10}$ axis with Sc^+/Sc rocks, ν_{24}^+/ν_{24} are Sc^+-np stretches with ring puckering about $C_7\text{-}C_{10}$ and $C_2\text{-}C_5$ axes, ν_{23}^+/ν_{23} are the Sc^+-np stretches with ring puckering about the $C_7\text{-}C_{10}$ and $C_2\text{-}C_5$ axes, and ν_{21}^+ is ring puckering about $C_7\text{-}C_{10}$ and $C_2\text{-}C_5$ axes. [e] Optimized geometrical parameters for the $^1A'/{}^2A'$ states. See Figure 6.1 for numeric labeling scheme. [f] Perpendicular distance from Sc to $C_1\text{-}C_6$ bond. [g] Perpendicular distance from Sc to $C_2\text{-}C_5$ bond. [h] Perpendicular distance from Sc to $C_3\text{-}C_4$ bond.

describes many different molecular systems is, indeed, an extremely challenging obstacle that theoreticians are working hard to overcome. As an alternative route, the more computationally expensive MP2 method was also tested against Sc-np. Although the size of the basis set is known to be less sensitive in DFT calculations, significantly different structures and relative electronic energies have been predicted by MP2 theory at different levels of basis for metal-ligand complexes.[23] Hence, our MP2 calculations were carried out at three levels of basis (B1, B2, and B4). The calculated frequencies by MP2 were not very sensitive to the size of the basis set. However, the MP2 simulations showed much better agreement to the experimental profile by calculating a much shorter ν_{26}^{+} vibrational progression that is more consistent with experiment. Unfortunately, at each basis set level, the intensities of the ν_{25}^{+}, ν_{24}^{+}, and ν_{23}^{+} vibrational progressions were underestimated, especially for ν_{23}^{+}. At the MP2/B2 level of theory, the length of the ν_{26}^{+} vibrational progression matched better, while the length of the ν_{23}^{+} and ν_{25}^{+} progressions matched worse. The B1 basis set seemed to be a good balance in predicting the intensities of the observed vibrational progressions, and this simulation is presented in Figure 6.4(b). Nevertheless, each set of MP2 and DFT calculations arrive at the same spectral assignment.

6.3.2.3 ZEKE spectroscopy of Y-np

The Y-np ZEKE spectrum recorded in a 15 % mixture of helium-argon carrier gases is presented in Figure 6.5(a). Three major progressions and four vibrational intervals start from the first strong peak at 40798 cm^{-1}. This strong peak is assigned to the vibrationless transition (0-0) from the ground electronic state of the neutral Y-np complex to the ground electronic state of the ionic Y^{+}-np complex. The FWHM of this peak and other major peaks is approximately 6 cm^{-1} wide. Due to the nature of the carrier gas mixture, vibrational temperatures of the neutral complexes are expected to be relatively lower than that in the Sc-np complex. Hence, no peaks are observed to the lower energy side of the band origin where hot transitions typically resonate. Unfortunately, attempts to record the ZEKE spectrum in pure helium carrier were unsuccessful

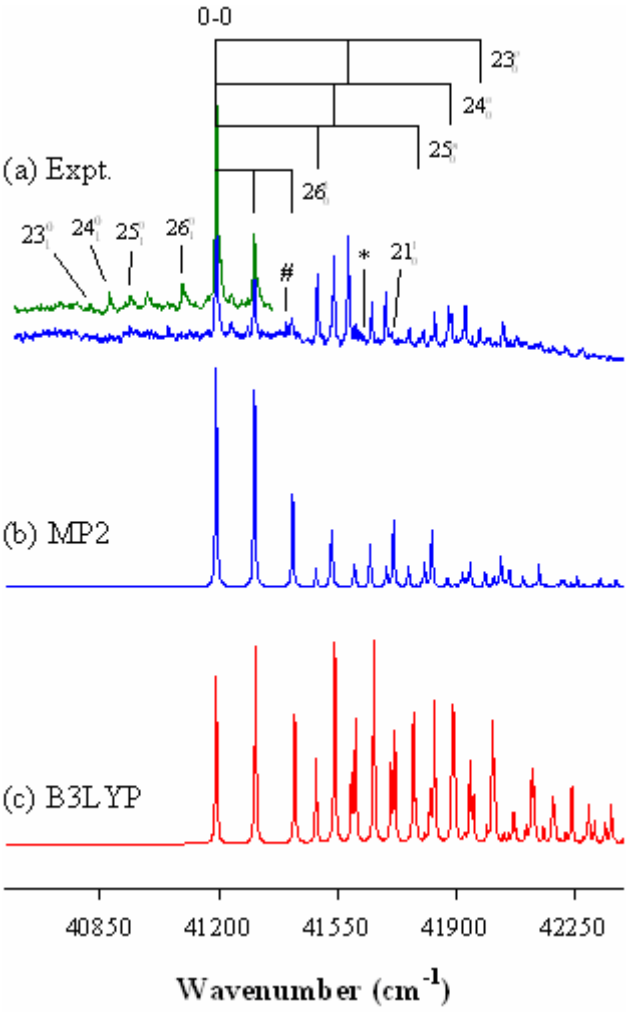

Figure 6.4. Sc-np ZEKE spectrum recorded with helium (top) and a 1-1 mixture of helium-argon (bottom) carrier gases (a) and spectral simulations of the $^1A' \leftarrow {}^2A'$ transition from MP2 (b) and B3LYP (c) calculations.

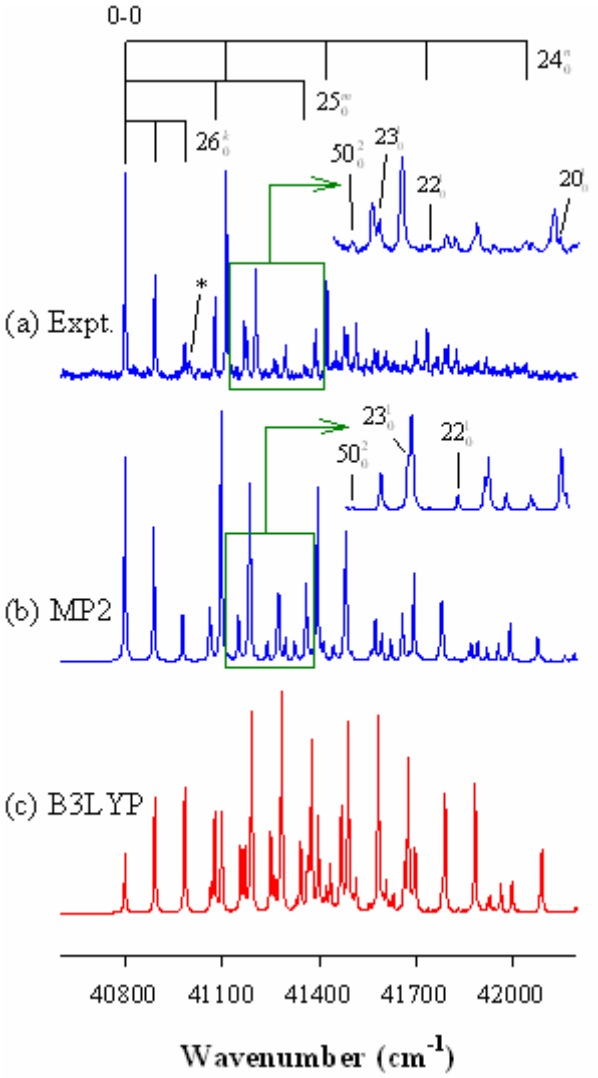

Figure 6.5. Y-np ZEKE spectrum recorded with a 15 % mixture of He-Ar carrier gas (a) and spectral simulations of the $^1A' \leftarrow {}^2A'$ transition from MP2 (b) and B3LYP (c) calculations. A portion of the spectra is expanded to more clearly label some vibrational intervals.

due to a much larger background signal. Also, a weak feature is observed at 197 cm^{-1} to the higher energy side of the origin band, which is marked by an asterisk.

Since scandium and yttrium have the same valence electron configuration, $(n\text{-}1)d^1 ns^2$, the electronic states of the metal complexes are expected to be the same. Because the bonding in metal-ligand complexes mainly involves the interaction of valence electrons, these two complexes are expected to have similar bonding as well. As a result, the ZEKE spectra of Sc-np and Y-np are quite similar. The band origin is only red shifted by 395 cm^{-1} from scandium to yttrium, and the vibrational intervals in the Y-np ZEKE spectrum are slightly red shifted. By comparison to the Sc-np ZEKE spectrum, most of the peaks in the Y-np ZEKE spectrum can be assigned. These assignments and the corresponding peak positions are listed in **Table 6.4**. The nature of most vibrational modes is analogous to those of the Sc-np complex. The details of these vibrations are given in the Table 6.5 footnotes. Each mode that was active in the scandium complex is also active in the yttrium complex. All of the vibrations are numbered the same in both complexes, except for one; the ν_{21}^+ mode of the Y^+-np complex is analogous to that of the ν_{22}^+ mode of the Sc^+-np complex.

In addition to these analogous vibrations, additional transitions (50_0^2, 20_0^1, and their combinations with other modes) were observed in the spectrum of Y-np. To identify these transitions, comparisons between theoretical calculations and experimental measurements are necessary. Figure 6.5(a) – (c) presents a comparison of the experimental and simulated spectra at two levels of theory. Only the $^1A' \leftarrow {}^2A'$ transition is simulated, because the Sc- and Y-np complexes should have the same ground electronic states as indicated by the similar spectral profiles. However, the vibrational progressions in the Y-np spectrum are predicted to be much too long by these DFT methods, just like for Sc-np. As in the case of the scandium complex, the simulation from the MP2 calculations [Figure 6.5(b)] displays a significantly better agreement with the experimental spectrum [Figure 6.5(a)] for the yttrium complex. Based on the good agreement between our experimental measurements and theoretical calculations, the other features in the spectrum could be assigned. Those peaks correspond to either overtone transitions of a nontotally symmetric a″ mode (ν_{50}^+) and/or the fundamental transition of a totally symmetric a′ mode (ν_{20}^+). From the overtone transition, the fundamental

frequency for ν_{50}^{+} is derived to be 173 cm^{-1}. The small feature labeled in the spectrum with an asterisk could not be assigned to a fundamental vibration, a combination transition, or an overtone. This feature could possibly be the result of a vibrational perturbation such as a Fermi resonance or Coriolis interaction. In these perturbations, two vibrational levels interact to form two new vibrational levels equally shifted to higher and lower energies. Unfortunately, these perturbations are not accounted for in our spectral simulation program. Thus, this assignment can only be considered tentative.

6.3.3 Comparison of Experiment and Theory

Table 6.3 summarizes the ionization energies and observed frequencies for the group 3 M-np complexes measured from experiment and predicted from *ab initio* theoretical calculations. The IEs of the bare metal atoms and the metal complexes decrease monotonically as the group is descended. Furthermore, the IEs of the metal complexes are red shifted with respect to that of the bare metal atom. This red shift establishes that the BE of the ionic complexes is larger than that of the neutral complexes according to the thermodynamic cycle: $\Delta BE = IE(M) - IE(M\text{-}np)$, where IE(M) is the ionization energy of the free atom and IE(M-np) is the ionization energy of the M-np complex. Stronger binding in the ion is not surprising due to the addition of an ion-quadrupole interaction that is not present in neutral molecules.

Furthermore, as the group is descended, ΔBE monotonically decreases. This trend is consistent with the anticipated monotonic increase of the binding energy in the neutral complexes as the group is descended due to an increasing polarizability of the metal atoms. This trend also suggests that the binding energy in the ionic complexes may decrease as the group is descended. The weaker binding in the heavier ionic complexes could be attributed to a smaller electrostatic force due to longer M^{+}-ligand distances. The calculated structures of the ionic complexes are consistent with this prediction, where Y^{+}-C distances are on average 0.172 Å longer than the Sc^{+}-C distances. However, the calculated binding energies show the heavier Y^{+}-np complex to be bound more tightly than that of the Sc^{+}-np complex. This relative energy comparison is not very meaningful,

because different basis sets were applied to Sc and Y in our calculations. This energy comparison is especially poor for the case of MP2 calculations, which are known to be more sensitive to basis sets.[23] On the other hand, the scandium and yttrium elements are both treated with the LANL2DZ effective core potential in the BPW91 calculations. In these calculations, the binding energy of the Sc^+-np complex was predicted to be 18 kcal/mol larger than that of the Y^+-np complex. Although the group 3 M-np structures predicted by BPW91 were not as good as those from MP2, the calculated relative electronic energies by BPW91 are found to be reliable according to our work on the group 4 M-np complexes (see Chapter 7).

The lesser expensive B3LYP method predicts very good IE values, within 0.4 and 1.1 % differences for Sc- and Y-np complexes, respectively. The more computationally expensive MP2 calculations also predicted fairly good IEs, but with slightly larger percent differences: 5.3 and 2.3 % for Sc- and Y-np, respectively. The measured and calculated frequencies also agree well by both DFT and MP2 methods. However, the simulated spectra from the MP2 calculations matched considerably better than those from DFT calculations. Thus, the structures from the MP2 calculations should be more reliable. On the other hand, DFT methods predicted reasonable relative energies and frequencies for the ground electronic states of these complexes. Therefore, these facilitative DFT calculations can initially be used to search for various states. Then, higher level calculations may be necessary to improve the quality of the theoretical results.

6.4 Conclusion

Group 3 metal-naphthalene compounds were formed in noble gas molecular beams and studied by ZEKE spectroscopy and *ab initio* calculations. The similar spectral profiles between Sc- and Y-np indicated that both complexes shared the same ground electronic states. The low-frequency modes measured in the spectra corresponded to mixtures of metal-ligand and ligand-based modes of the ion complex. In addition, several neutral vibrations were identified for Sc-np via hot transitions from vibrationally

excited neutral molecules. From the good agreement between the measured and simulated spectra, the ground electronic states of the Sc- and Y-np complexes were determined to be $^2A'$ and $^1A'$ for the neutral and ionic complexes, respectively. In these states, the metal complexes were formed by the interaction of the metal atom with a single six-membered π-ring. Upon coordination, the naphthalene ligand puckered away from the metal center to form a boat shaped M(2,5-η^2-np) complex under C_s symmetry. The ligand deformation is maintained upon ionization, while the metal migrates closer to the ligand as a result of a strong electrostatic ion-quadrupole force. The IE of La-np was measured via PIE spectroscopy only, because ZEKE experiments were unsuccessful due to the small-sized electron signal.

CHAPTER 7: ELECTRONIC STATES AND MOLECULAR STRUCTURES OF GROUP 4 M-Np COMPLEXES (M = Ti, Zr, Hf; Np = NAPHTHALENE) DETERMINED VIA ZEKE SPECTROSCOPY AND DFT CALCULATIONS

7.1 Introduction

The reliability and adequacy of DFT to describe complex molecular systems have been questioned over the years. For example, Zhao et al. suggested that DFT methods cannot adequately describe M-np systems (M = Al, Li, Ca; np = naphthalene).[273] However, their claim was not supported by any experimental evidence. Furthermore, our group has shown by comparison to experimental data that the structures and energies of group 3 M-np complexes (M = Sc, Y) predicted by the B3LYP functional are reliable. In fact, the ionization energies calculated from B3LYP matched slightly better to experiment than those from MP2 theory. On the other hand, the structures from MP2 theory were better according to a comparison of the measured and calculated spectra. Even though MP2 theory may, in some cases, provide better structures, this method is much more computationally expensive compared to the DFT approach. For these reasons, DFT is a suitable and more practical methodology for computing complex metal-PAH systems. Recently, Schultz et al. tested the reliability and adequacy of several DFT methods by comparing theoretical and measured bond dissociation energies of 21 different metal-containing species.[283] However, DFT method sensitivity was not tested against more complicated metal-arene systems, such as M-np complexes.

In this chapter, the vibronic spectra of the group 4 M-np complexes (M = Ti, Zr, Hf) is presented. The IEs and vibrational frequencies of these complexes are measured via ZEKE spectroscopy. The electronic states and corresponding molecular structures are determined by comparing measured and calculated spectra. Additionally, DFT method sensitivity is tested by comparing simulations from various DFT calculations to the measured Ti-np ZEKE spectrum.

7.2 Experimental and Computational Methods

The details of our ZEKE spectrometer were discussed in Chapter 2. M-np complexes were produced by reactions of gaseous metal atoms with naphthalene (99 % $C_{12}H_{10}$, Aldrich) in a supersonic jet. The metal atoms were produced by pulsed laser vaporization of a metal rod (99.7 % Ti or 99+ % Zr, Aldrich; 97 % Hf, Goodfellow) with the second harmonic output of a Nd:YAG laser (Lumonics, YM-800, 532 nm, ~ 1 mJ). The metal atoms were carrier by He and/or Ar (UHP, Scott-Gross) which were delivered by a piezoelectric pulsed valve at a stagnation pressure of ~ 50 psi. At room temperature, naphthalene vapor was introduced through a stainless steel tube to a small reaction chamber (~ 1.5 mL), a few centimeters downstream from the ablation region, where the ligand interacted with the metal atoms entrained in the carrier gas.

Molecular masses were measured by photoionization time-of-flight mass spectrometry. Ionization thresholds of the metal complexes were located using PIE spectroscopy. Prior to ZEKE experiments, the production of the target metal complex was maximized by adjusting the timing and power of the vaporization and ionization lasers, backing pressure of the carrier gas, and amount of ligand vapor allowed to enter the source chamber. ZEKE electrons were produced by photoexcitation of neutral molecules to high-lying Rydberg states, followed by delayed (~ 3.5 μs) pulsed electric field ionization (1.2 V/cm, 100 ns) of these Rydberg states. The photoionization and photoexcitation light was generated by the doubled-frequency output of a dye laser (Lumonics, HD-500) pumped by the third harmonic of a Nd:YAG laser (Continuum, Surelite-II, 355 nm). The pulsed electric field was provided by a delay pulse generator (Stanford Research Systems DG535). The ion and electron signals were detected by a dual microchannel plate detector (Burle), amplified by a preamplifier (Stanford Research Systems SR445), averaged by a gated integrator (Stanford Research Systems SR250), and stored in a laboratory computer. Laser wavelengths were calibrated against titanium or vanadium atomic transitions.[169] A field-dependent study was not performed, because the anticipated field-induced IE shift (1 ~ 2 cm^{-1}) is smaller than the measured linewidth of the peaks in our experiment.[284]

Geometry optimization and vibrational analysis were carried out with the

GAUSSIAN03 program package[74] on an SGI/Origin-300 server for the Ti-np complexes and on the University of Kentucky Hewlett-Packard Superdome cluster for the Zr- and Hf-np complexes. In these calculations the B3LYP, B3P86, and BPW91 functionals were employed for Ti-np. For Zr- and Hf-np, only the BPW91 method was used, except for Hf-np where MP2 theory was used to test the consistency of the BPW91 energetics. Geometry optimizations were performed with two levels of basis sets for the Ti-np complex: (B5) 6-311++G(d,p) for all atoms, and (B6) 6-311G(d) for C and H atoms and 6-311+G(d) for Ti atom. Geometry optimizations of the Zr- and Hf-np complexes were only performed with one level of basis set: (B7) 6-311++G(d,p) for C and H atoms and LANL2DZ for Zr and Hf elements. Like the group 3 M-np complexes, ligand distortions induced by metal coordination were considered in our survey for the lowest-energy structure of the neutral and ionic M-np complexes by doing symmetry-relaxed geometry optimizations. To determine the electronic symmetry, a second set of calculations was employed with the C_s symmetry constraint when appropriate. For each geometry, vibrational frequencies were calculated within the harmonic approximation to ensure a local minimum structure was located on the potential energy surface.

To simulate ZEKE spectra, multi-dimensional FC factors were calculated from the theoretical equilibrium geometries, harmonic vibrational frequencies, and normal coordinates of the neutral and ionic complexes.[68] The Duschinsky effect[45] was considered to account for normal mode differences between the neutral and ion in the FC calculations. Spectral broadening was simulated by giving each line a Lorentzian line shape with experimental linewidth. To account for non-Boltzmann temperatures in the molecular beam, the vibrational temperatures for low-frequency modes (< 400 cm^{-1}) were specified separately. To simulate hot transitions in the Hf-np ZEKE spectrum, the vibrational temperature of all modes were specified as 50 K, except for ν_{26} (60 K) and ν_{24} (100 K). Although the frequencies were not scaled, the calculated ionization energies were shifted to the experimental value to allow easier comparison of the measured and calculated FC profiles.

7.3 Results and Discussion

7.3.1 Ti-np Complex

7.3.1.1 Theoretical Structures

We have investigated neutral and monocation Ti-np complexes and found the Ti atom or ion binds to one π-ring of the naphthalene ligand under C_s symmetry. Like the group 3 M-np complexes, the titanium atom or ion binds to either an η^2- or η^6-np ligand (Figure 7.1). First, geometry optimizations (B3LYP/B6) were performed on the neutral Ti-np complexes in singlet, triplet, and quintet spin multiplicities, while the corresponding ion complex was optimized with doublet and quartet spin multiplicities. In previous theoretical investigations of Ti-bz,[140, 145, 159] the ground electronic states of the neutral and ion complexes were determined to have spin multiplicities of quintet and quartet, respectively. In contrast, our B3LYP/B6 calculations on Ti-np predict the lowest energy equilibrium structure for the neutral complex to be the $\widetilde{X}^3A''$ electronic state with an excited $\widetilde{A}^5A''$ state lying 1020 cm^{-1} higher in energy. The $\widetilde{B}^1A'$ state is calculated to be much higher in energy, 8070 cm^{-1} above the low-lying $\widetilde{A}^5A''$ excited state. For ionic Ti^+-np, the ground electronic state is predicted to be the $\widetilde{A}^4A''$ state with the $\widetilde{X}^2A''$ state 925 cm^{-1} higher in electronic energy. The energy separation between the ground electronic states of the neutral and ionic complexes is predicted to be 41867 cm^{-1}. Calculations at the BPW91/B5 and B3LYP/B5 levels of theory predict the same energy ordering of electronic states: $\widetilde{X}^3A'' < \widetilde{A}^5A'' < \widetilde{B}^1A' << \widetilde{A}^4A'' < \widetilde{X}^2A''$.

Because the Ti-np molecular structures calculated by the BPW91 method are found to be significantly better (discussed in the following sections), our structural and energy analysis will refer to the results from these BPW91 predictions unless otherwise noted. The predicted geometrical structures and relative electronic energies of each state are summarized in Table 7.1. The metal-ligand distances are reported as individual M-C_x distances, where *x* corresponds to the carbon numeric-labeling scheme shown in Figure 7.1. Metal-ligand distances are also reported as perpendicular distances to specific C-C bonds (Ti-$C_{1,6}$; Ti-$C_{2,5}$; and Ti-$C_{3,4}$). In these M-np complexes, the $\delta(C_3\text{-}C_2\text{-}C_5\text{-}C_6)$

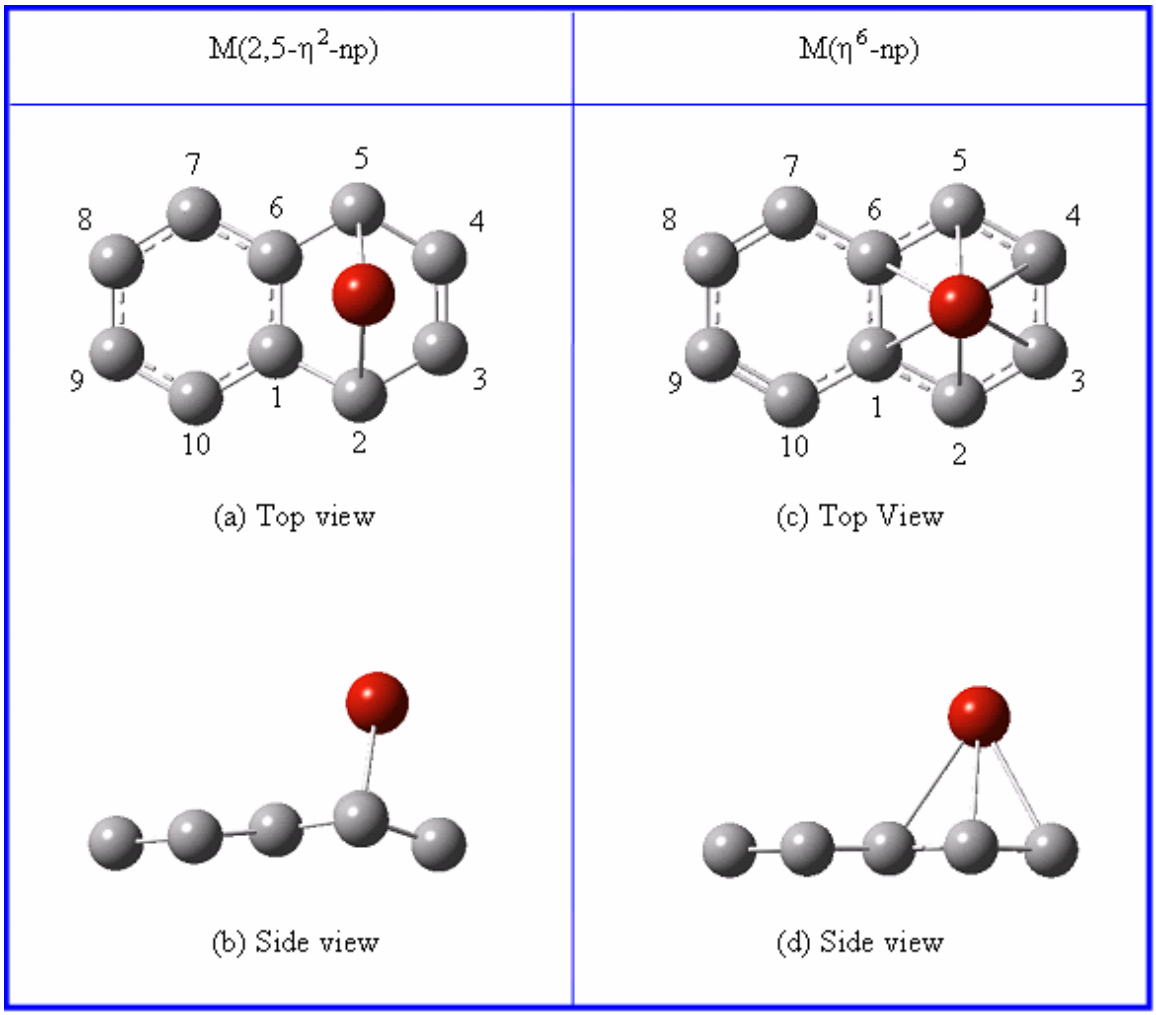

Figure 7.1. Molecular structures [C_s] of M(2,5-η^2-np) complexes from top (a) and side (b) views and M(η^6-np) complexes from top (c) and side (d) views. Metal atoms are red, carbon atoms are grey, and hydrogen atoms are omitted for clarity.

Table 7.1. Predicted electronic states, point groups, relative electronic energies (ΔE, cm^{-1}), adiabatic bond dissociation energies (D_o, kcal/mol), bond lengths (R, Å), and dihedral angles (δ, degrees)[a] for Ti^+/Ti-np complexes and free naphthalene ligand from BPW91/B5[b] calculations. See Figure 7.1 for numeric labels.

	BPW91/B5 (this work)						Expt.[c] (other)
	Ti-np (C_s)			Ti^+-np (C_s)		np (D_{2h})	np (D_{2h})
ΔE [d]	0	2335	5471	41867	42792		
State	$\tilde{X}^3A''$	$\tilde{A}^5A''$	$\tilde{B}^1A'$	$\tilde{A}^4A''$	$\tilde{X}^2A''$	^1A_g	
D_o [e]	42.1	34.3	27.3	88.2	85.9		
$R(C_1-C_2)$	1.466	1.438	1.453	1.441	1.476	1.424	1.422
$R(C_2-C_3)$	1.451	1.413	1.446	1.411	1.443	1.382	1.381
$R(C_3-C_4)$	1.411	1.426	1.446	1.429	1.397	1.419	1.417
$R(C_1-C_6)$	1.459	1.455	1.488	1.458	1.442	1.440	1.412
$R(C_1-C_{10})$	1.425	1.426	1.438	1.431	1.419	1.424	1.422
$R(C_9-C_{10})$	1.388	1.386	1.379	1.379	1.390	1.382	1.381
$R(C_8-C_9)$	1.415	1.419	1.431	1.424	1.410	1.419	1.417
$R(Ti-C_1)$	2.308	2.513	2.171	2.359	2.314		
$R(Ti-C_2)$	2.147	2.372	2.134	2.311	2.127		
$R(Ti-C_3)$	2.238	2.324	2.135	2.311	2.302		
$R(Ti-C_{1,6})$[f]	2.190	2.405	2.040	2.243	2.199		
$R(Ti-C_{2,5})$[g]	1.592	1.901	1.573	1.821	1.576		
$R(Ti-C_{3,4})$[h]	2.124	2.211	2.009	2.198	2.193		
δ(B-ring)	165.4	175.8	179.2	178.2	159.0	180.0	180.0
δ(N-ring)	179.6	179.7	179.6	179.0	178.2	180.0	180.0

[a] Ring puckering is determined by the $\delta(C_3-C_2-C_5-C_6) \equiv \delta$(B-ring) and $\delta(C_1-C_{10}-C_7-C_8) \equiv \delta$(N-ring) dihedral angles. [b] B5 = 6-311++G(d,p) for all atoms. [c] Experimental values from X-ray diffraction measurements.[280] [d] The ΔE values are relative to the $\tilde{X}^3A''$ state. [e] The adiabatic bond dissociation energies are calculated by subtracting the energy of the electronic state of the complex from the sum of the energies of the np ligand (^1A_g) and the metal atom (^5F) or ion (^4F) in their ground electronic states. [f] Perpendicular distance from Ti to C_1-C_6 bond. [g] Perpendicular distance from Ti to C_2-C_5 bond. [h] Perpendicular distance from Ti to C_3-C_4 bond.

dihedral angle [denoted hereafter as δ(B-ring)] is used as a point of reference to assess the degree of puckering on the bonding π ring, i.e. how puckered the np ligand becomes after metal coordination. The puckering on the nonbonding π ring is denoted by δ(N-ring) ≡ δ(C_1-C_{10}-C_7-C_8).

In general, metal-arene bonding is described by π electron donation from the ligand to unfilled metal orbitals and back-donation from the metal to empty antibonding π* orbitals of the ligand. Both electron donation and back-donation weaken the local carbon-carbon naphthalene framework, and, consequently, local C-C bond distances are elongated with respect to the free ligand (Table 7.1). The C-C bond distances on the other π-ring not involved in metal coordination remain essentially the same as that of the free ligand. Thus, only one of the two π-rings significantly participates in bonding for Ti-np just like in the group 3 M-np complexes.

Compared to the Ti-bz complex,[140, 145, 159] metal-ligand bonding in the ground state of Ti-np is quite different. Rather than maintaining a flat π-system, like in Ti-bz, the Ti atom slightly distorts the naphthalene C-C framework and the ligand puckers away from the metal atom or ion. This ligand puckering was also observed in the ground electronic states of the neutral and ionic group 3 M-np complexes as discussed in Chapter 6. Due to this ligand puckering, two M-C distances (Ti-C_2 and -C_5 = 2.147 Å) are much shorter than the others (Ti-C_3 and -C_4 = 2.238 and Ti-C_1 and -C_6 = 2.308 Å). Also, π electron localization causes the C_3-C_4 bond to shrink by 0.006 Å. This π electron localization indicates that the C_3 and C_4 atoms do not significantly participate in metal coordination as discussed in the previous chapter. Based on these structural characteristics, the Ti atom is coordinated to an (η^2-np) ligand in the ground electronic state of the neutral complex.

The degree of ligand puckering can be used to qualitatively assess the magnitude of the metal-π interaction. For example, the δ(B-ring) dihedral angle of Ti-np in the neutral $\widetilde{X}^3A''$ ground electronic state is puckered by ~ 15 ^{o} [i.e. 180.0 ^{o} – δ(B-ring)] with respect to the free ligand, while the other π-ring not significantly involved in metal-ligand bonding remains virtually flat, δ(N-ring) = 179.6 ^{o}. The excited $\widetilde{A}^5A''$ state of Ti-np, on the other hand, is suspected to have less metal-ligand interaction due to the much smaller

degree of puckering (~ 0 and 4 ^{o}). Furthermore, the carbon-carbon framework in the quintet state is not distorted as much as it is in the $\widetilde{X}^3A''$ state as shown by comparing the C-C distances in the quintet state to that of the free ligand. These structural characteristics suggest that the titanium atom in the quintet state should be bound more weakly than that in the triplet ground electronic state. Although the adiabatic bond dissociation energies of these M-np complexes have not been measured, they can be derived from the calculated energies of the metal atom, ligand, and metal complex. In these adiabatic dissociation processes, the parent molecule dissociates into fragments in their corresponding ground electronic states. Although experimental measurements have indicated that the ground electronic state spin multiplicity of Ti is a triplet, our calculations predicted the quintet state of Ti to be 4161 cm^{-1} lower in energy than that in the triplet state. Thus, our theoretical adiabatic dissociation energy of the $\widetilde{A}^5A''$ and $\widetilde{X}^3A''$ states correspond, respectively, to the processes: Ti-np ($\widetilde{A}^5A''$) $\rightarrow$ Ti (^{5}F) + np (^{1}A$_g$) and Ti-np ($\widetilde{X}^3A''$) $\rightarrow$ Ti (^{5}F) + np (^{1}A$_g$). Although the BPW91 calculations mistakenly predicts the relative energies of the bare metal atoms, the *difference* in the adiabatic bond dissociation energies of the metal complex is independent of the metal atom (or ion) and ligand electronic energies. Indeed, the theoretical adiabatic dissociation energy of the quintet state is predicted to be 7.8 kcal/mol smaller than that of the triplet state. Thus, the degree of ligand puckering seems to provide a reasonable means by which to qualitatively assess the amount of covalent bonding in M-np complexes.

The $\widetilde{B}^1A'$ state has shorter Ti-C distances but nearly flat π-rings. Each of the C-C bond lengths on the π-ring significantly involved in metal coordination is longer than those of the free ligand. In addition, each of the Ti-C distances is nearly the same, 2.134 to 2.171 Å. These structural characteristics indicate that, in the singlet state, the metal atom is bound to an η^6-np ligand like in the quintet state. According to the relative ligand puckering, the metal-ligand bonding in the $\widetilde{B}^1A'$ state is expected to be smaller than that in the $\widetilde{X}^3A''$ and $\widetilde{A}^5A''$ electronic states. Indeed, the BPW91 calculations predict the adiabatic dissociation energy of the singlet state [i.e. Ti-np ($\widetilde{B}^1A'$) $\rightarrow$ Ti (^{5}F) + np (^{1}A$_g$)] to be ~ 14.8 and 7.0 kcal/mol smaller than those of the triplet and quintet states,

respectively.

The ground electronic state of the ionic Ti^+-np complex is predicted to be the $\widetilde{A}^4A''$ state with the $\widetilde{X}^2A''$ state only 925 cm^{-1} higher in energy. In the quartet state, the Ti^+-C distances are predicted to be significantly longer than the corresponding neutral $\widetilde{X}^3A''$ ground electronic state [$\Delta R(Ti\text{-}C_{2,5}) = 0.229$ Å]. The longer Ti^+-C distances in the $\widetilde{A}^4A''$ ionic state compared to the neutral $\widetilde{X}^3A''$ ground electronic state indicates weaker covalent bonding in the ion. However, the ionic complexes have a much larger electrostatic bonding component from the ion-quadrupole interaction that is not found in the neutral complex. As a matter of fact, the calculated adiabatic dissociation energies of the ionic $\widetilde{A}^4A''$ and $\widetilde{X}^2A''$ states (88.2 and 85.9 kcal/mol, respectively) are greater than those of the $\widetilde{X}^3A''$, $\widetilde{A}^5A''$, and $\widetilde{B}^1A'$ states (42.1, 34.3, and 27.3 kcal/mol, respectively). A more sensible structural analysis involves the comparison among the complexes with the same hapticity. For the Ti-np system, the $\widetilde{B}^1A'$, $\widetilde{A}^4A''$, and $\widetilde{A}^5A''$ states were predicted to have (η^6-np) ligands, while the $\widetilde{X}^2A''$ and $\widetilde{X}^3A''$ states were predicted to have (η^2-np) ligands. Consistent with the addition of the electrostatic ion-quadrupole in the ionic complexes, the Ti^+-C distances in the $\widetilde{X}^2A''$ state of $Ti^+(2,5\text{-}\eta^2\text{-np})$ are predicted to be shorter than the Ti-C distances in the $\widetilde{X}^3A''$ state of $Ti(2,5\text{-}\eta^2\text{-np})$, and the Ti^+-C distances in the $\widetilde{A}^4A''$ state of $Ti^+(\eta^6\text{-np})$ are predicted to be shorter than the Ti-C distances in the $\widetilde{A}^5A''$ state of $Ti(\eta^6\text{-np})$. The shorter Ti^+-C distances in the ion compared to the neutral complex are due to the attraction between the negative end of the np quadrupole and the positively charged Ti^+ ion. The relatively short Ti-C distances in the $\widetilde{B}^1A'$ state compared to all the other calculated states is puzzling. This state should not have a significant electrostatic binding component, which is consistent with the much smaller predicted adiabatic dissociation energy of this state. Why the Ti-C distances are much shorter in this excited $\widetilde{B}^1A'$ state is still under consideration.

Due to significantly different geometric structures (i.e. twofold versus sixfold bonding), the $\widetilde{A}^4A'' \leftarrow \widetilde{X}^3A''$ and $\widetilde{X}^2A'' \leftarrow \widetilde{B}^1A'$ transitions are expected to have long vibrational progressions according to the FC principle. The $\widetilde{A}^4A'' \leftarrow \widetilde{A}^5A''$ and $\widetilde{X}^2A'' \leftarrow$

$\widetilde{X}^3A''$ transitions, on the other hand, should have short vibrational progressions since the initial and final states within each transition share the same hapticity. Thus, by measuring the vibronic spectrum of Ti-np, information about the electron spin multiplicities of the neutral and ionic species can be identified based on the spectral profile alone. The Ti-np ZEKE spectrum and corresponding simulations are discussed in the following two sections.

7.3.1.2 Ti-np ZEKE spectrum

Figure 7.2(a) presents the experimental ZEKE spectrum of Ti-np seeded in He carrier gas. A portion of the spectrum (green trace) is expanded ten-fold to more clearly show some small peaks. The first strong band in the ZEKE spectrum at 41764 cm^{-1} corresponds to the sharp onset of the PIE spectrum and is assigned to the vibrationless (0-0) transition between the ground electronic states of the neutral and ionized complexes. Each peak in the spectrum has similar line shapes with linewidths of approximately 11 cm^{-1} measured as the FWHM. This spectrum consists of two short vibrational progressions and five vibrational intervals starting from the origin band as labeled in Figure 7.2(a). Some smaller peaks appear to be broadened, because two transitions (42378 and 42384 cm^{-1}) nearly overlap. Almost all the features in this spectrum can be assigned to combinations of these vibrational intervals, except those labeled by asterisks. Those peaks labeled with asterisks, less than 3 % the intensity of the origin band, could not be assigned to a fundamental vibration, an overtone vibration, or a combination of the two. These peaks likely originate from a different spectral carrier. Unfortunately, line shape and width comparisons are difficult to assess due to the extremely small intensities of these two features.

The vibrational intervals in the Ti-np spectrum correspond to vibrational modes of the ion complex. The nature of these modes could be easily determined by comparison to the ZEKE spectra of Sc- and Y-np. These assignments and the corresponding peak positions are listed in Table 7.2. The description of each vibrational mode is listed in the Table 7.3 footnotes. Each active vibrational mode has the totally symmetric represent-

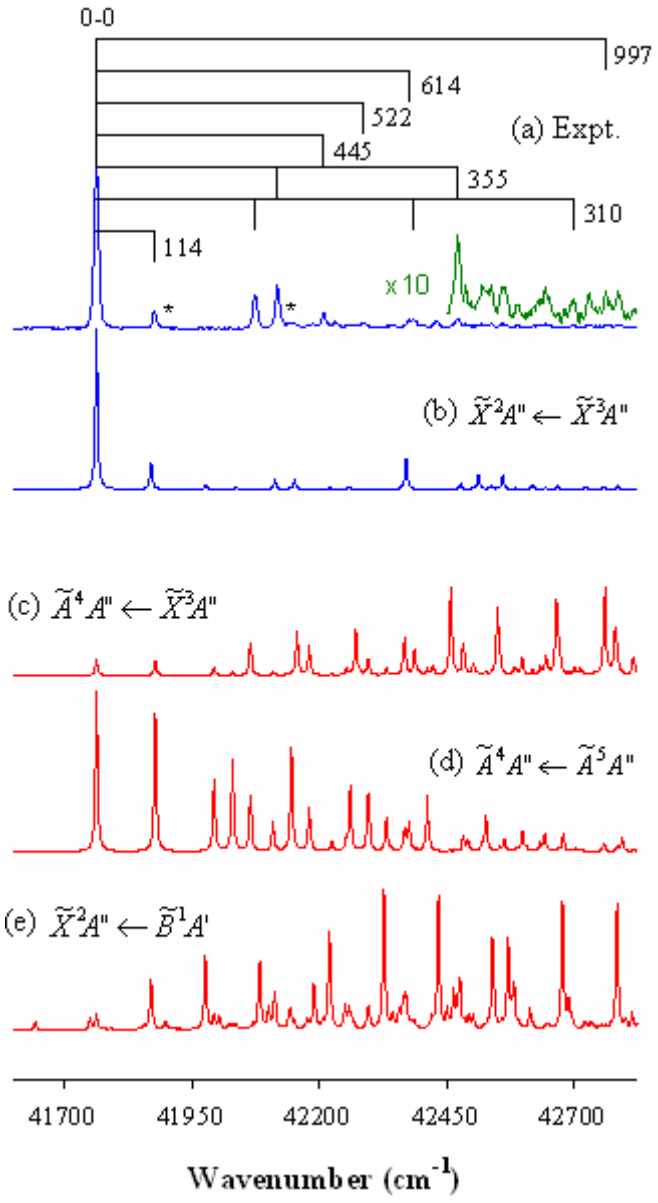

Figure 7.2. Experimental ZEKE spectrum of Ti-np recorded in helium carrier gas (a) and spectral simulations [B3LYP/B5] of various spin-allowed transitions (b) – (e).

Table 7.2. Peak positions (cm^{-1}) and assignments for the ZEKE spectra of the Ti-, Zr-, and Hf-np complexes.

Ti-np				Zr-np			
$\tilde{X}\ ^2A'' \leftarrow \tilde{X}\ ^3A''$				$\tilde{X}\ ^2A' \leftarrow \tilde{X}\ ^3A''$		$\tilde{B}\ ^2A'' \leftarrow \tilde{X}\ ^3A''$	
Peak	Assignment	Peak	Assignment	Peak	Assignment	Peak	Assignment
41764	0_0^0	42385	25_0^2	42094	0_0^0	42458	0_0^0
41878	26_0^1	42430	$24_0^1 25_0^1$	42226	26_0^1	42575	26_0^1
41905	*	42472	24_0^2	42390	25_0^1	42684	26_0^2
42075	25_0^1	42488	$20_0^1 26_0^1$	42416	24_0^1	42755	25_0^1
42119	24_0^1	42518	$23_0^1 25_0^1$	42520	$25_0^1 26_0^1$	42787	26_0^3
42146	*	42562	$23_0^1 24_0^1$	42684	25_0^2	42839	24_0^1
42188	$25_0^1 26_0^1$	42643	$21_0^1 24_0^1$	42715	$24_0^1 26_0^1$	42869	$25_0^1 26_0^1$
42209	23_0^1	42698	25_0^3	42739	24_0^2	42899	23_0^1
42231	$24_0^1 26_0^1$	42730	$21_0^1 23_0^1$	42974	25_0^3	42926	22_0^1
42287	21_0^1	42761	14_0^1			42958	$24_0^1 26_0^1$
42378	20_0^1	42787	$24_0^1 25_0^1$			43051	25_0^2
						43118	20_0^1
						43136	$24_0^1 25_0^1$
						43163	$25_0^2 26_0^1$
						43221	24_0^2
						43337	23_0^2

Hf-np: $\tilde{X}\ ^2A' \leftarrow \tilde{X}\ ^1A'$							
Peak	Assignment	Peak	Assignment	Peak	Assignment	Peak	Assignment
46399	25_1^0	46820	26_0^2	47071	$25_0^1 26_0^2$	47251	$23_0^1 24_0^1$
46480	$25_1^0 26_0^1$	46861	$24_0^1 26_1^0$	47093	$24_0^1 26_0^2$	47263	$24_0^1 25_0^1 26_0^1$
46508	26_2^0	46901	$23_0^1 26_1^0$	47111	$24_0^2 25_1^0 26_0^2$	47286	$24_0^2 26_0^1$
46559	$25_1^0 26_0^2$	46911	25_0^1	47113	$24_0^1 25_0^1 26_1^0$	47294	23_0^2
46585	26_1^0	46934	24_0^1	47135	$24_0^2 26_1^0$	47308	$24_0^3 25_1^0 26_0^1$
46660	0_0^0	46941	$24_0^1 26_1^1$	47152	$25_0^1 26_0^3$	47335	$23_0^1 24_0^1 26_0^1$
46667	26_1^1	46948	$24_0^2 25_1^0$	47174	$24_0^1 26_0^3$	47342	$24_0^1 25_0^1 26_0^2$
46674	$24_0^1 25_1^0$	46977	23_0^1	47185	$24_0^1 25_0^1$	47364	$24_0^2 26_0^2$
46679	*	46991	$25_0^1 26_0^1$	47190	$24_0^2 25_1^0 26_0^3$	47371	$23_0^2 26_0^1$
46740	26_0^1	47013	$24_0^1 26_0^1$	47208	24_0^2	47444	$24_0^2 26_0^3$
46748	26_1^2	47022	$24_0^1 26_1^2$	47218	$23_0^1 26_0^3$		
46761	$25_0^1 26_2^0$	47031	$24_0^2 25_0^1 26_0^1$	47223	$24_0^3 25_1^0$		
46782	$24_0^1 26_2^0$	47056	$23_0^1 26_0^1$	47235	20_0^1		

*** These peaks likely belong to a different spectral carrier.**

Table 7.3. Relative electronic energies (ΔE, cm^{-1}), spin-allowed vibrationless transition energies (T_{00}, cm^{-1}), vibrational frequencies (cm^{-1}), bond lengths (R, Å), and dihedral angles (δ, degrees)[a] of Ti-np predicted by DFT calculations. Where available, these predictions are compared to ZEKE measurements.

	B3P86/B6[b]	B3LYP/B6[b]	B3LYP/B5[c]	BPW91/B5[c]	ZEKE
ΔE[d]					
$\tilde{X}^3A''$	0	0	0	0	
$\tilde{A}^5A''$		1020	1251	2335	
$\tilde{B}^1A'$		8070	7917	5471	
$\tilde{A}^4A''$		39977	40479	41867	
$\tilde{X}^2A''$	50217	45553	46095	42792	
T_{00}[e]					
$\tilde{X}^2A'' \leftarrow \tilde{X}^3A''$	50642	46199	46541	43384	41764
$\tilde{X}^2A'' \leftarrow \tilde{B}^1A'$		38194	38754	38183	
$\tilde{A}^4A'' \leftarrow \tilde{X}^3A''$		40804	41208	42605	
$\tilde{A}^4A'' \leftarrow \tilde{A}^5A''$		39325	39596	39879	
Frequencies[f]					
ν_{26}^+	112	107	107	115	114
ν_{25}^+	293	274	274	308	310
ν_{24}^+	371	388	388	351	355
ν_{23}^+	408	350	350	395	445
ν_{21}^+	502	499	500	520	522
ν_{20}^+	609	608	607	606	614
ν_{14}^+	1029	1024	1021	994	997
Geometry[g]					
$R(C_1\text{-}C_2)$	1.459/1.460	1.466/1.467	1.466/1.467	1.476/1.466	
$R(C_2\text{-}C_3)$	1.425/1.442	1.425/1.447	1.426/1.448	1.443/1.451	
$R(C_3\text{-}C_4)$	1.401/1.392	1.405/1.393	1.406/1.393	1.397/1.411	
$R(C_1\text{-}C_6)$	1.432/1.439	1.435/1.440	1.435/1.441	1.442/1.459	
$R(Ti\text{-}C_{1,6})$[h]	2.195/2.222	2.261/2.301	2.261/2.295	2.199/2.190	
$R(Ti\text{-}C_{2,5})$[i]	1.588/1.596	1.641/1.638	1.641/1.637	1.576/1.592	
$R(Ti\text{-}C_{3,4})$[j]	2.110/2.136	2.145/2.172	2.143/2.170	2.193/2.124	
δ(B-ring)	164.9/162.3	164.5/160.1	164.6/160.4	159.0/165.4	

[a] Ring puckering is determined by the $\delta(C_3\text{-}C_2\text{-}C_5\text{-}C_6) \equiv \delta$(B-ring) dihedral angle. [b] B6 = 6-311+G(d) for Ti atom and 6-311G(d) for C and H atoms. [c] B5 = 6-311++G(d,p) for all atoms. [d] The ΔE values are relative to the $\tilde{X}^3A''$ state. [e] Includes zero-point vibrational energy corrections. [f] All active modes are totally symmetric (a′) and originate in the $\tilde{X}^2A''$ ionic state: ν_{26}^+ is ring bending about $C_1\text{-}C_6$ bond, ν_{25}^+ is ring puckering about $C_7\text{-}C_{10}$ bond with Ti^+ rock, ν_{24}^+ is ring puckering about $C_7\text{-}C_{10}$ and $C_2\text{-}C_5$ bonds, ν_{23}^+ is the Ti^+-np stretch with ring puckering about $C_2\text{-}C_5$ and $C_7\text{-}C_{10}$ bonds, ν_{21}^+ is ring puckering about $C_2\text{-}C_5$ and $C_7\text{-}C_{10}$ bonds, ν_{20}^+ is an in-plane ring distortion, and ν_{14}^+ is a C-H in-plane bending mode localized on the Ti-bound π-ring. [g] Optimized geometrical parameters for the $\tilde{X}^2A''$/ $\tilde{X}^3A''$ states. See Figure 7.1 for numeric labeling scheme. [h] Perpendicular distance from Ti to $C_1\text{-}C_6$ bond. [i] Perpendicular distance from Ti to $C_2\text{-}C_5$ bond. [j] Perpendicular distance from Ti to $C_3\text{-}C_4$ bond.

ation, a′ in the C_s point group. Most of these vibrations are C-C out-of-plane bending modes where the rings pucker at different ring locations (i.e. $\nu_{26}^+ = 114$, $\nu_{24}^+ = 355$ $\nu_{21}^+ = 522$, and $\nu_{20}^+ = 614$ cm^{-1}). In addition to these C-C-C bending modes, two metal-ligand vibrations were observed, ν_{25}^+ and ν_{23}^+. The ν_{25}^+ mode (312 cm^{-1}) is composed of C-C-C bending and Ti^+ rocking components, while the ν_{23}^+ mode (444 cm^{-1}) has C-C-C bending and Ti^+-np stretching components. Additionally, a C-H in-plane bending mode (ν_{14}^+) was measured with a frequency of 995 cm^{-1}. The longest vibrational progression in the spectrum consists of the Ti^+ rock ν_{25}^+ mode. This vibrational progression is consistent with our theoretical structures, where the Ti^+ ion is predicted to migrate from the outer edge of the ring towards the centroid.

To assign the electronic states, we consider the predicted relative electronic energies and the observed FC spectral profile. Because only short vibrational progressions are observed in the Ti-np ZEKE spectrum, the neutral and ion complexes are expected to have small structural differences based on the FC principle. From our theoretical analysis, the $\widetilde{B}^1A'$, $\widetilde{A}^4A''$, and $\widetilde{A}^5A''$ states of Ti(η^6-np) have flat π-rings, and the $\widetilde{X}^2A''$ and $\widetilde{X}^3A''$ states of Ti(2,5-η^2-np) have puckered π-rings. Therefore, the $\widetilde{A}^4A'' \leftarrow \widetilde{X}^3A''$ and $\widetilde{X}^2A'' \leftarrow \widetilde{B}^1A'$ transitions are not likely to match the experimental spectrum due to the long vibrational progressions that are expected in these electronic transitions. The $\widetilde{X}^2A'' \leftarrow \widetilde{X}^3A''$ and $\widetilde{A}^4A'' \leftarrow \widetilde{A}^5A''$ transitions, on the other hand, may match the observed spectrum. However, because the $\widetilde{A}^5A''$ state is calculated to be significantly higher in electronic energy at all levels of theory, this state is not expected to be populated in the cold molecular beam where the vibrational temperature has been estimated to be 40 – 300 K, depending on the carrier gas conditions.[236] Thus, transitions from this state will not be observed, since transition intensities are proportional to the population of the initial state. The $\widetilde{B}^1A'$ state, which is predicted to lie nearly 10,000 cm^{-1} above the ground electronic state, will not be populated either. Thus, the band origin can be rationally assigned to the $\widetilde{X}^2A'' \leftarrow \widetilde{X}^3A''$ transition. This assignment is confirmed by the DFT spectral simulations described in the following section.

7.3.1.3 Comparison of experimental and simulated spectra

Figure 7.2(a) – (e) presents a comparison of the experimental and simulated (B3LYP/B6) spectra of the various spin-allowed transitions. As anticipated, the $\widetilde{A}^4A'' \leftarrow \widetilde{X}^3A''$ and $\widetilde{X}^2A'' \leftarrow \widetilde{B}^1A'$ transitions are simulated to have very long vibrational progressions and do not match the experimental spectrum at all. The long vibrational progressions in these simulated transitions are consistent with the large structural differences between the initial and final electronic states, which have different hapticities. The transition from the higher energy $\widetilde{A}^5A''$ state does not match the experimental peak positions or intensities very well either. Out of these four spin-allowed transitions, only the $\widetilde{X}^2A'' \leftarrow \widetilde{X}^3A''$ transition matches experiment, because this simulation has a similar FC profile with comparable peak positions to the experimental spectrum. Hence, the doublet state is labeled as the ground electronic state of the ionic complex since both the $\widetilde{A}^4A''$ and $\widetilde{X}^2A''$ states are spin accessible via $\widetilde{X}^3A''$.

Simulation sensitivity with respect to different DFT methods and basis sets was tested by calculating the Ti-np ZEKE spectrum of the $\widetilde{X}^2A'' \leftarrow \widetilde{X}^3A''$ transition. Figure 7.3(a) – (e) compares the experimental spectrum to simulations from three different DFT methods (B3LYP, B3P86, and BPW91) and two different basis sets, B5 and B6. The two hybrid functionals (B3LYP and B3P86) simulate very similar spectra, because both methods have the same exchange functional, Becke's three parameter hybrid functional. The small differences between these two simulations arise from the different correlation functionals, LYP[285] and P86.[286] These two functionals have different expressions for treating electron correlation, which result in slightly different structures and relative electronic energies. The Ti^+/Ti-C distances are predicted to be longer by B3LYP than B3P86, as indicated in Table 7.3. The naphthalene C-C framework, on the other hand, is predicted to be nearly the same by both B3LYP and B3P86. The calculated frequencies by B3P86 are predicted to be closer to the experiment but not by much. The ionization energies are significantly overestimated with both DFT methods, but more so with B3P86. This large IE overestimation (~ 10 %) by the B3P86 method has also been observed for other metal-aromatic hydrocarbon complexes as well (see Chapter 8).

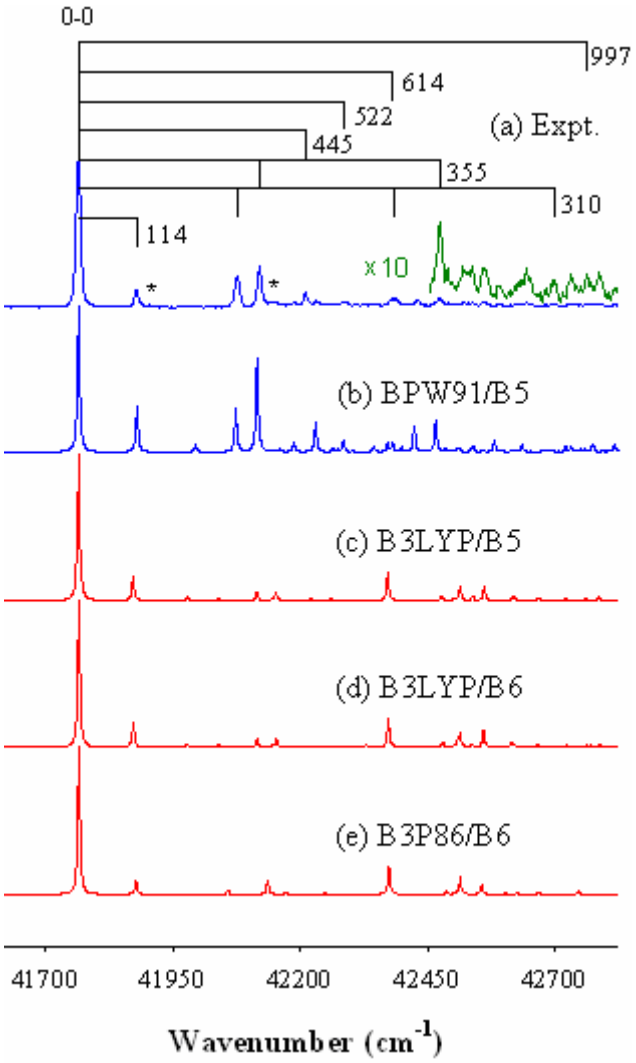

Figure 7.3. Experimental ZEKE spectrum of Ti-np recorded in helium carrier gas (a) and spectral simulations of the $\tilde{X}^2A'' \leftarrow \tilde{X}\ ^3A''$ transition at various levels of theory (b) – (e).

Because the B3LYP method predicts better IEs, basis set sensitivity is assessed by comparing simulations at the B3LYP/B5 and B3LYP/B6 levels of theory. For the B5 basis set, diffuse and polarization functions are used to treat every atom; for the B6 basis set, polarization functions are used on Ti and C atoms, while diffuse functions are limited to the Ti atom only. The main difference between these two basis sets is the treatment of H atoms, where the B5 basis set is larger. Using these two bases, the Ti^+/Ti-np structures are predicted to be virtually identical (Table 7.3). The similarity in structures can be explained by considering the bonding. Ti-np is formed by the interaction of a titanium atom with one of the π-rings of naphthalene. Because the np π-system originates from carbon 2p orbitals, choosing a proper basis for the carbon atoms is crucial to adequately describe this system. Increasing the basis set size for the H atoms has virtually no effect, as depicted by the simulations in Figure 7.3(c) and (d). Moreover, the low frequency modes measured in this spectrum are C-C and Ti-C based modes. Hence, the predicted frequencies are practically the same since Ti and C are treated nearly the same with the B5 and B6 basis sets. Likewise, the IEs are calculated to be nearly the same with both basis sets, because the first ionization energy of Ti-np does not originate from a hydrogen-based molecular orbital.

A significant improvement in the spectral simulation is found using the BPW91 method.[287] Not only do the FC profiles and frequencies match much better, but the calculated IE is also closer to the experimental value with respect to the other DFT methods tested in this work (Table 7.3). The better agreement between theory and experiment is attributed to both the different exchange functional (Becke's nonhybrid) and correlation functional (PW91). As a result, the BPW91 method predicts significantly different Ti^+/Ti-np structures compared to the other DFT methods employed in this work. Not only are the magnitudes in bond lengths and angles different, but the structural changes that occur upon ionization are predicted to follow rather different patterns. For example, the BPW91 method predicts that ionization via the $\tilde{X}^2A'' \leftarrow \tilde{X}^3A''$ transition causes the metal to migrate away from the C_3-C_4 bond while further puckering the carbon-carbon naphthalene framework. In contrast, the B3P86 and B3LYP methods predict that this ionization process causes the metal to approach the C_3-C_4 bond while the carbon-carbon naphthalene framework becomes less puckered. Additionally, the BPW91

method predicts a decrease in the C_3-C_4 bond from $\widetilde{X}^3A''$ to $\widetilde{X}^2A''$, whereas the other methods predict an elongation. Although the intensity of the 114 cm^{-1} vibrational interval matches better using results from the B3LYP and B3P86 calculations, the intensities related to the 310, 355, and 445 cm^{-1} vibrational progressions match better using results from the BPW91 calculations. Thus, the molecular structures from BPW91 are more reliable than those from B3LYP and B3P86, because the observed spectrum is directly related to the structural differences between the initial and final states.

The calculated IE and ν_{26}^+, ν_{25}^+, ν_{24}^+, ν_{21}^+, and ν_{14}^+ frequencies from BPW91 match closer to the experimental values than those from B3LYP and B3P86. Out of all the calculated frequencies from BPW91, the Ti^+-np stretch has the largest difference from experiment, a 12 % difference. The B3P86 method predicts this frequency closer to experiment, but still relatively far away, an 8 % difference. In addition, the intensity for this mode is also calculated to be much smaller than the observed intensity. Despite this minor discrepancy, all other vibrational frequencies calculated by the BPW91 method are within 1.4 % difference, and the intensities involving these frequencies match well with experiment. Thus, the metal-ligand bonding in the Ti-np system is adequately described by the BPW91 method. The following sections will address the reliability of this method with heavier group 4 M-np complexes (M = Zr and Hf).

7.3.2 Zr-np Complex

7.3.2.1 Calculated Electronic States

Table 7.4 summarizes the predicted electronic states, point groups, relative electronic energies, and molecular structures of the Zr^+/Zr-np complex from the BPW91/B7 calculations. As described in the previous section, the ground electronic state of Ti-np was predicted to be the $\widetilde{X}\ ^3A''$ state with the quintet and singlet states 2335 and 5471 cm^{-1} higher in energy, respectively. Because zirconium belongs to the same group as titanium, the electronic states of Zr-np are expected to have the same energy sequence. Indeed, the ground electronic state of Zr-np is predicted to be the $\widetilde{X}\ ^3A''$ state with excit-

Table 7.4. Predicted electronic states, point groups, relative electronic energies (ΔE, cm^{-1}), bond lengths (R, Å), and dihedral angles (δ, degrees)[a] for Zr^+/Zr-np complexes and free naphthalene ligand from BPW91/B7[b] calculations. See Figure 7.1 for numeric labeling scheme.

	Zr-np (C_s)[f]						Zr^+-np (C_s)[d]			np (D_{2h})
ΔE[e]	0	1969	2523	2752	3631	21881	42354	42410	43166	
State	$\tilde{X}\ ^3A''$	$\tilde{A}\ ^3A'$	$\tilde{B}\ ^3A''$	$\tilde{C}\ ^5A''$	$\tilde{D}\ ^1A'$	$\tilde{E}\ ^5A'$	$\tilde{X}\ ^2A'$	$\tilde{A}\ ^4A''$	$\tilde{B}\ ^2A''$	^1A_g
R(C_1-C_2)	1.463	1.482	1.455	1.440	1.455	1.445	1.478	1.441	1.469	1.424
R(C_2-C_3)	1.446	1.452	1.450	1.416	1.451	1.471	1.448	1.414	1.446	1.382
R(C_3-C_4)	1.405	1.390	1.448	1.429	1.449	1.393	1.395	1.430	1.415	1.419
R(C_1-C_6)	1.447	1.437	1.485	1.456	1.485	1.447	1.441	1.458	1.453	1.440
R(C_1-C_{10})	1.422	1.411	1.439	1.426	1.439	1.428	1.419	1.432	1.426	1.424
R(C_9-C_{10})	1.389	1.399	1.377	1.387	1.377	1.443	1.392	1.379	1.384	1.382
R(C_8-C_9)	1.413	1.401	1.434	1.418	1.434	1.373	1.408	1.425	1.418	1.419
R(Zr-C_1)	2.541	2.640	2.337	2.643	2.338	2.611	2.459	2.499	2.428	
R(Zr-C_2)	2.312	2.317	2.277	2.506	2.276	2.382	2.269	2.450	2.262	
R(Zr-C_3)	2.419	2.486	2.281	2.463	2.281	2.423	2.460	2.451	2.364	
R(Zr-$C_{1,6}$)[f]	2.436	2.541	2.216	2.540	2.217	2.509	2.351	2.390	2.317	
R(Zr-$C_{2,5}$)[g]	1.825	1.827	1.762	2.065	1.761	1.901	1.759	1.994	1.754	
R(Zr-$C_{3,4}$)[h]	2.315	2.387	2.163	2.357	2.163	2.320	2.359	2.344	2.256	
δ(B-ring)	162.6	152.8	177.9	175.9	177.8	165.0	158.3	178.1	166.2	180.0
δ(N-ring)	179.1	180.0	179.9	179.5	179.9	179.1	178.0	178.7	178.8	180.0

[a] Ring puckering is determined by the δ(C_3-C_2-C_5-C_6) ≡ δ(B-ring) and δ(C_1-C_{10}-C_7-C_8) ≡ δ(N-ring) dihedral angles. [b] B7 = 6-311++G(d,p) for C and H atoms; LANL2DZ for Zr atom. [c] A transition state ($^3A''$) in the neutral complex was calculated at 686 cm^{-1} above the $\tilde{X}\ ^3A''$ state. [d] A transition state ($^4A'$) in the ion was calculated at 6780 cm^{-1} above the $\tilde{X}\ ^2A'$ state. [e] The ΔE values are relative to the $\tilde{X}\ ^3A''$ state. [f] Perpendicular distance from Zr to C_1-C_6 bond. [g] Perpendicular distance from Zr to C_2-C_5 bond. [h] Perpendicular distance from Zr to C_3-C_4 bond.

ed quintet ($\widetilde{C}\ ^5A''$) and singlet ($\widetilde{D}\ ^1A'$) states at 2752 and 3631 cm^{-1} higher in energy, respectively. In addition, two other triplet states ($\widetilde{A}\ ^3A'$ and $\widetilde{B}\ ^3A''$) are calculated at 1969 and 2523 cm^{-1} above the ground electronic state, slightly lower in energy than the quintet and singlet excited states. At a much higher energy, 21 881 cm^{-1}, the $\widetilde{E}\ ^5A'$ state was also located. All of these states are local minimum energy structures according to our frequency analyses.

The geometry of Zr-np in the $\widetilde{X}\ ^3A''$ state is predicted to be very similar to that of the titanium analog. From Ti- to Zr-np, the carbon-carbon framework has a maximum deviation of only 0.003 Å and 0.9 ^{o} for C-C bonds and C-C-C-C dihedral angles, respectively. The M-C bond lengths of the zirconium complex are, on average, 7 % larger than the corresponding titanium complex. The longer M-C distances in Zr-np are not surprising since atomic radii increase from fourth to fifth row elements within the same group. The quintet and singlet states of Zr-np also have similar carbon-carbon frameworks to that of the corresponding states of the titanium complex. In these excited states, the Zr-C distances are also predicted to be longer than the Ti-C distances.

Upon zirconium coordination to form the $\widetilde{X}\ ^3A''$ state, the local naphthalene C-C framework weakens as indicated by the much longer C-C distances compared to the free ligand. This distortion is the result of metal-arene bonding, where ligand to metal electron donation and metal to ligand electron back-donation occurs. Because the metal atom interacts solely with one π-ring, the π-ring that does not significantly participate in bonding remains virtually the same as that of the free ligand. These structural changes were also observed in the Sc-, Y-, and Ti-np complexes. Like in the other M-np complexes, the bonding π-ring is puckered by about 17 ^{o} in the ground electronic state of Zr-np. In this puckered configuration, the zirconium atom is coordinated to an (η^2-np) ligand.

Compared to the $\widetilde{X}\ ^3A''$ electronic state, the excited states of Zr-np have either longer or shorter Zr-C bond lengths. At longer Zr-C distances, electron repulsions are reduced, but at the cost of less d-π overlap. Those states with much shorter Zr-C distances will have much better d-π overlap, but an increase in electron repulsion. Hence, the lowest energy structure ($\widetilde{X}\ ^3A''$) has intermediate Zr-C distances. In the $\widetilde{X}\ ^3A''$ state,

the naphthalene ligand is puckered by ~ 17 ^{o}, while the excited states are puckered from 2 to 27 ^{o}. Like the Zr-C distances, the degree of puckering is maintained by a balance between overlap and repulsions. In the puckered configuration, steric repulsions are reduced, and the metal atom is coordinated to an η^2-np ligand; in the other case, π conjugation is maximized, and the metal atom binds to an η^6-np ligand. Whether the np ligand is flat or puckered, the zirconium atom tends to interact towards the outer edge of the π-ring as denoted by the smaller Zr-$C_{3,4}$ distances compared to the Zr-$C_{1,6}$ distances.

In our theoretical survey of the ionic Zr^+-np complex, four different spin states were located. Like ionic Ti^+-np, the $\widetilde{A}\ ^4A''$ state is found to be lower in energy than the $\widetilde{B}\ ^2A''$ state. However, for Zr^+-np, the ground electronic state is predicted to be the $\widetilde{X}\ ^2A'$ state, albeit by only 56 cm^{-1}. A quartet state (^{4}A$'$) is predicted to be much higher in energy, 6779 cm^{-1} above the ionic $\widetilde{X}\ ^2A'$ state, and with a large imaginary frequency, 657i cm^{-1}. Therefore, this ^{4}A$'$ state is a local maximum on the potential energy surface and is not considered in our spectral analysis.

Compared to the ground electronic state of the neutral Zr-np complex, the ground electronic state of the corresponding ion is slightly more puckered by ~ 4 ^{o}. In the ionic complex, most Zr^+-C distances are slightly shorter than those of the neutral complex, as indicated in Table 7.4, except for the Zr^+-C_3 and -$C_{3,4}$ distances, which are slightly longer compared to the neutral complex due to stronger puckering in the ion. The overall smaller metal-ligand distance in the ionic complex is not surprising due to the addition of an ion-quadrupole interaction. This additional electrostatic interaction is known to generally increase the bond energy by 20 to 30 percent in metal-arene complexes.[278] Shorter metal-carbon distances in the ion were also predicted in the Ti-np system when comparing structures of the same hapticity, except for comparisons to those in the $\widetilde{B}^1A'$ state, which were surprisingly shorter than both electronic states of the ion.

7.3.2.2 Zr-np ZEKE Spectra

The ZEKE spectrum of Zr-np seeded in a 1:1 mixture of helium and argon is presented in Figure 7.4(a). In our spectral analysis, two electronic transitions were

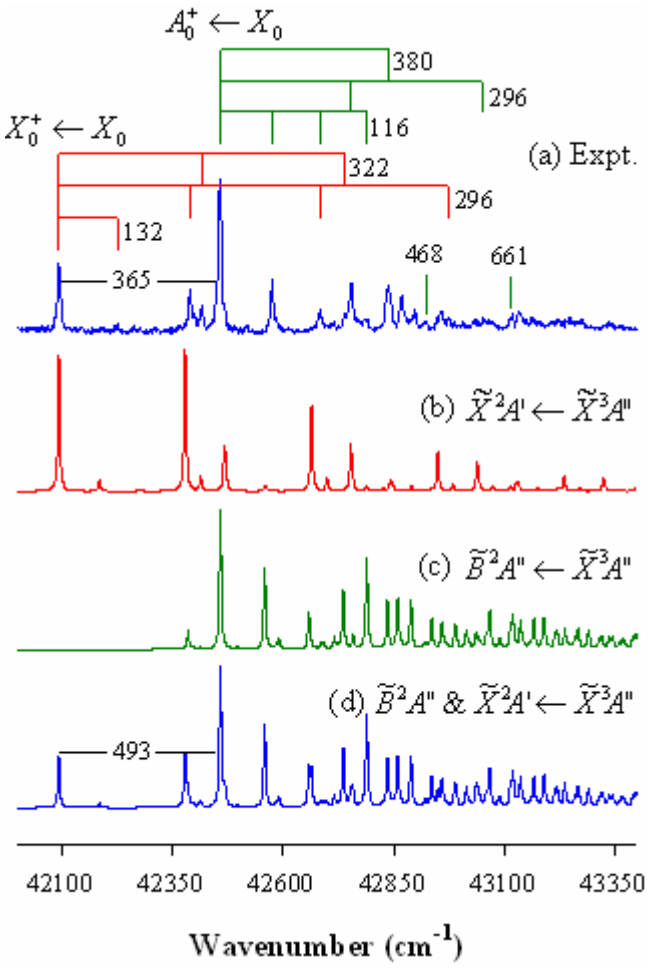

Figure 7.4. Experimental ZEKE spectrum of Zr-np recorded in a 1-1 helium-argon mixture carrier gas (a) and spectral simulations [BPW91/B7] of various spin-allowed transitions (b) – (d).

identified. The origin bands of each electronic transition, which are separated by 365 cm^{-1}, are labeled in the spectrum as $X_0^+ \leftarrow X_0$ and $A_0^+ \leftarrow X_0$. As indicated by the label, the first peak on the lower-energy side at 42094 cm^{-1} corresponds to the vibrationless transition between the ground electronic state of the neutral and ionized Zr-np complex. The other transition at 42458 cm^{-1} also originates from the same neutral ground electronic state, but ends at the first excited electronic state of the ionic complex, denoted generically as $A_0^+ \leftarrow X_0$. The linewidths of each peak in the spectrum, measured as the FWHM, are ~ 9 cm^{-1} wide. In the lower energy transition, three vibrational intervals of 132, 296, and 322 cm^{-1} are identified; in the higher energy transition, six vibrational intervals of 116, 296, 380, 440, 468, and 661 cm^{-1} are located. All other peaks in the spectrum are assigned to combinations of these vibrational intervals. The slightly different frequencies observed in both transitions are consistent with our assignment of two electronic transitions, which was also observed in the Sc-bz_2 ZEKE spectrum. Although the 365 cm^{-1} spacing between the two origin bands was initially thought to be a fundamental mode, no other 365 cm^{-1} intervals were identified in the spectrum. If this was another vibrational mode, several 365 cm^{-1} intervals should have appeared according to the FC principle due to the large intensity increase from 42094 to 42458 cm^{-1}. Hence, these two bands are instead assigned to two different origin bands of the Zr-np complex.

The vibrational intervals in both transitions are assigned to specific modes by comparison to the Ti-np ZEKE spectrum. In that spectrum, seven modes with frequencies of 114 (ν_{26}^+), 312 (ν_{25}^+), 355 (ν_{24}^+), 444 (ν_{23}^+), 522 (ν_{21}^+), 614 (ν_{20}^+), and 996 cm^{-1} (ν_{14}^+) were identified. Because Zr is in the same group as Ti, the same modes should be active in the ZEKE spectrum of these two metal complexes. Thus, in the Zr-np spectrum, the 116/132, 296/296, 380/322, 440/—, and 661/— cm^{-1} frequencies in the A_0^+ / X_0^+ states are analogously assigned to ν_{26}^+, ν_{25}^+, ν_{24}^+, ν_{23}^+, and ν_{20}^+ respectively. The 468 cm^{-1} vibrational interval is assigned to ν_{22}^+ based on comparison to that of the measured frequency in the Y^+-np complex (516 cm^{-1}).

All of the observed modes belong to the totally symmetric a′ representation in the C_s point group. ν_{26}^+ is the ring bending about the C_1-C_6 bond, ν_{25}^+ is ring puckering about the C_7-C_{10} bond with a Zr^+ rock, ν_{24}^+ is ring puckering about the C_7-C_{10} and C_2-C_5

bonds, and ν_{23}^{+} is the Zr^{+}-np stretch mode with ring puckering about the C_2-C_5 and C_7-C_{10} bonds. The detailed assignment of each peak and its associated peak position is listed in Table 7.2. These vibrational assignments are confirmed by comparison to our theoretical calculations. Furthermore, the electronic states of the neutral and ionic complex are identified via spectral simulations.

7.3.2.3 Comparison of Experimental and Simulated Spectra

In our theoretical survey, we located five neutral and three ionic electronic states. According to selection rules, only 13 transitions are spin-allowed, where the change in the electron spin multiplicities takes on values of ± 1. Details of the selection rules involved in photoelectron spectroscopy were discussed in Chapter 4. Simulations of the relevant spin transitions are compared to the measured spectrum in Figure 7.4(a) – (d). According to our theoretical calculations, the ground electronic state of the neutral complex is the $\widetilde{X}\ ^3A''$ electronic state. From this triplet state, all of our theoretical ionic states are electron-spin accessible. However, only simulations of transitions to the $\widetilde{X}\ ^2A'$ and $\widetilde{B}\ ^2A''$ states match experiment. The lower energy transition is simulated in Figure 7.4(b), where as the higher energy transition is simulated in Figure 7.4(c). From this assignment, the energy difference between the two doublet states is measured to be 365 cm^{-1}. This energy difference is comparable to the predicted separation of 493 cm^{-1} by the BPW91 calculations. The sum of these two simulations is plotted in Figure 7.4(d); the origin bands were shifted and normalized to the experimental value before adding the data points. A comparison of the summed simulations and the experimental plot makes our spectral assignment to these two transitions very convincing. Careful inspection of these two spectra shows a nice peak to peak correlation, although the intensities on the higher energy side are somewhat overestimated by theory.

From our spectral analysis, the BPW91 energetics and structures are reasonable. The assignment of these two electronic transitions designates the ground electronic state of the neutral complex to the $\widetilde{X}\ ^3A''$ state. This state also corresponds to the lowest energy structure predicted from our BPW91 calculations. Likewise, the ground

electronic state of the ion was determined to be the $\widetilde{X}\ ^2A'$ state, which is consistent with the BPW91 calculated electronic energies. However, the first excited ionic state in the ion is measured to be the $\widetilde{B}\ ^2A''$ state, whereas the $\widetilde{A}\ ^4A''$ state is predicted to be 342 cm^{-1} lower in energy than this state. In the $\widetilde{A}\ ^4A''$ state, the ion is coordinated to an η^6-np ligand as opposed to an η^2-np ligand like in the $\widetilde{X}\ ^3A''$, $\widetilde{X}\ ^2A'$, and $\widetilde{B}\ ^2A''$ states. Thus, either the BPW91 mistakenly predicts the relative energies of the ionic excited electronic states, or the FC overlap between states of Zr(η^6-np) and Zr(2,5-η^2-np) is so poor that these peaks could not be observed. The former explanation is not unreasonable, because these states are predicted to lie within only a few hundreds wavenumbers, within the numerical reliability of DFT. Nevertheless, the Zr-np ZEKE spectrum is assigned to two transitions: $\widetilde{X}\ ^2A' \leftarrow \widetilde{X}\ ^3A''$ and $\widetilde{B}\ ^2A'' \leftarrow \widetilde{X}\ ^3A''$. Interestingly, the ground electronic state of the ionic Zr^+-np complex is different from that of the Ti^+-np complex, although both metal elements belong to the same family. Studies on the hafnium analog were draw further insight into the interesting energetics of these apparently complicated group 4 M-np systems.

7.3.3 Hf-np Complex

7.3.3.1 Calculated Electronic States

The results from our electronic structure theoretical calculations of the Hf-np complex are summarized in Table 7.5. In contrast to Zr-np, two low-lying electronic states of the neutral molecule, $\widetilde{X}\ ^1A'$ and $\widetilde{A}\ ^3A''$, are predicted to lie within a very small energy window, only 705 cm^{-1}. Unlike the BPW91 calculations, MP2 theory predicts the $\widetilde{X}\ ^1A'$ state to be 3853 cm^{-1} lower in energy than the $\widetilde{A}\ ^3A''$ state. Thus, the $\widetilde{X}\ ^1A'$ state is labeled as the ground electronic state of the Hf-np complex. Compared to Zr-np, the $\widetilde{B}\ ^3A'$ state lies at a relatively lower electronic energy, only 761 cm^{-1} above the $\widetilde{X}\ ^1A'$ electronic state. The $\widetilde{C}\ ^5A''$ state, on the other hand, is predicted to lie relatively higher in energy (3246 cm^{-1} above the $\widetilde{X}\ ^1A'$ electronic state) compared to the Zr-np complex. A search for the Hf-np $^5A'$ state was not performed, since this state is expect-

Table 7.5. Predicted electronic states, point groups, relative electronic energies (ΔE, cm^{-1}), bond lengths (R, Å), and dihedral angles (δ, degrees)[a] for Hf^+/Hf-np complexes and free naphthalene ligand from BPW91/B7[b] calculations. See Figure 7.1 for numeric labeling scheme.

	Hf-np (C_s)				Hf^+-np (C_s)				np (D_{2h})
ΔE[c]	0	705	1466	3951	44032	45995	46983	50389	
State	$\widetilde{A}\ ^3A''$	$\widetilde{X}\ ^1A'$ [d]	$\widetilde{B}\ ^3A'$	$\widetilde{C}\ ^5A''$	$\widetilde{X}\ ^2A'$	$\widetilde{A}\ ^4A''$	$\widetilde{B}\ ^2A''$	$\widetilde{C}\ ^4A'$	^1A_g
R(1-2)	1.471	1.478	1.488	1.440	1.487	1.441	1.477	1.450	1.424
R(2-3)	1.455	1.457	1.462	1.419	1.458	1.415	1.456	1.414	1.382
R(3-4)	1.405	1.379	1.384	1.433	1.385	1.429	1.418	1.414	1.419
R(1-6)	1.440	1.427	1.435	1.461	1.432	1.458	1.456	1.449	1.440
R(1-10)	1.416	1.411	1.413	1.430	1.415	1.432	1.428	1.415	1.424
R(9-10)	1.392	1.395	1.396	1.385	1.392	1.377	1.383	1.396	1.382
R(8-9)	1.410	1.405	1.404	1.422	1.409	1.427	1.419	1.408	1.419
R(Hf-C_1)	2.645	2.670	2.581	2.530	2.515	2.487	2.372	2.643	
R(Hf-C_2)	2.278	2.286	2.266	2.464	2.219	2.421	2.200	2.470	
R(Hf-C_3)	2.392	2.552	2.498	2.440	2.479	2.421	2.312	2.538	
R(Hf-$C_{1,6}$)[e]	2.545	2.573	2.479	2.422	2.411	2.378	2.258	2.542	
R(Hf-$C_{2,5}$)[f]	1.795	1.824	1.761	2.010	1.713	1.960	1.666	2.028	
R(Hf-$C_{3,4}$)[g]	2.287	2.457	2.400	2.332	2.381	2.313	2.201	2.438	
δ(B-ring)	155.9	148.1	149.3	178.6	150.2	177.4	165.0	168.3	180.0
δ(N-ring)	179.6	179.4	179.5	178.8	178.4	178.9	178.9	178.7	180.0

[a] Ring puckering is determined by the δ(C_3-C_2-C_5-C_6) ≡ δ(B-ring) and δ(C_1-C_{10}-C_7-C_8) ≡ δ(N-ring) dihedral angles. [b] B7 = 6-311++G(d,p) for C and H atoms; LANL2DZ for Hf atom. [c] The ΔE values are relative to the $\widetilde{A}\ ^3A''$ state. [d] The $\widetilde{X}\ ^1A'$ state is predicted to be 3853 cm^{-1} lower in energy than $\widetilde{A}\ ^3A''$ by MP2 calculations. [e] Perpendicular distance from Hf to C_1-C_6 bond. [f] Perpendicular distance from Hf to C_2-C_5 bond. [g] Perpendicular distance from Hf to C_3-C_4 bond.

ed to lie more than 10,000 cm^{-1} above the ground electronic state, like in Zr-np.

The carbon-carbon naphthalene framework in the $\widetilde{X}\ ^1A'$ state of Hf-np is rather different from that of the ground electronic state of Zr-np. The metal-bound π-ring is more puckered in the hafnium complex by about 15 °, and the standard deviation in C-C bond length differences between the hafnium and zirconium complexes is 0.016 Å. The stronger puckering in Hf-np may be indicative of stronger metal-ligand bonding, which has also been observed in other heavy metal complexes due to the larger polarizability and the relativistic effect.[278] The relativistic effect is known to shrink the radius of sixth row elements. Thus, the Hf-np distance should be smaller (more d-π overlap) than that of Zr-np. However, comparing the metal-ligand distances between the Zr- and Hf-np complexes is not very straightforward. For example, although the Hf-C_2 and -C_3 distances are shorter than the Zr-C_2 and -C_3 bonds, the Hf-C_1 distance is longer than the Zr-C_1 bond. The longer Hf-C_1 distance may be due to slightly more ligand puckering, metal migration towards the outer edge of the bonding π-ring, or a combination of both. Because the size of the metal atom and degree of ligand puckering are different, trends in metal-ligand distances are difficult to assess among the M-np complexes.

In the $\widetilde{X}\ ^1A'$, $\widetilde{A}\ ^3A''$ and $\widetilde{B}\ ^3A'$ states, the C_3-C_4 is significantly shorter than those in the free ligand, and the bonding π-ring is severely puckered. These structural trends are consistent with a Hf(2,5-η^2-np) complex. During this type of metal coordination, the originally sp^2 C_2 and C_5 atoms change its hybridization by adding more *p* character. The resultant hybrid orbital on the two bonding carbon atoms (C_2 and C_5) of the η^2-np ligand is thought to be between sp^2 and sp^3 hybridization, where the C_1-C_2-C_3 and C_6-C_5-C_4 angles are smaller than 120 ° (e.g. 117, 119, and 114 ° in the $\widetilde{X}\ ^1A'$, $\widetilde{A}\ ^3A''$, and $\widetilde{B}\ ^3A'$ states, respectively). In the $\widetilde{C}\ ^5A''$ state, on the other hand, both the bonding and nonbonding π-rings are nearly flat. Each of the six bonding carbon atoms in this η^6-np ligand remains completely sp^2 hybridized with CCC angles of 120 °.

Like Zr^+-np, the lowest energy electronic state of Hf^+-np is predicted to be the $\widetilde{X}\ ^2A'$ state. However, the first excited state in the ion, the $\widetilde{A}\ ^4A''$ state, is predicted to lie at a relatively higher energy, 1963 cm^{-1} above the $\widetilde{X}\ ^2A'$ state. About 1000 cm^{-1} higher in energy, the $\widetilde{B}\ ^2A''$ state is located. The highest energy electronic state located in our

theoretical survey of Hf^+-np is the $\widetilde{C}\ ^4A'$ state at 6357 cm^{-1} relative to the ground electronic state of the ion.

Ionization of Hf-np in the $\widetilde{X}\ ^1A'$ state leads to the $\widetilde{X}\ ^2A'$ state of the Hf^+-np complex. In this ionization process, the ligand remains puckered, and the C-C distances do not change significantly. On the other hand, the Hf-C distances are reduced by an enormous amount; on average, the Hf^+-C distances in the $\widetilde{X}\ ^2A'$ state are 0.107 Å smaller than those in the $\widetilde{X}\ ^1A'$ state. The overall smaller Hf^+-np distance is the result of the smaller Hf^+ radius after removal of a Hf-based electron from a bonding type molecular orbital and the addition of an ion-quadrupole interaction. The large structural difference between these two states should, in principle, produce a long FC profile.

Like in the neutral molecule, excited states of the ionic complex have η^2- and η^6-np ligands. The first excited state in the ion, $\widetilde{A}\ ^4A''$, is only puckered by 3 °, and is therefore considered to be a Hf(η^6-np) complex. The $\widetilde{B}\ ^2A''$ and $\widetilde{C}\ ^4A'$ states, on the other hand, have moderately puckered bonding π-rings, 15 and 12 °, respectively. In these $\widetilde{B}\ ^2A''$ and $\widetilde{C}\ ^4A'$ states, the hafnium ion is coordinated to an η^2-np ligand.

The electronic states in the neutral and ionic Hf-np complex are predicted to lie within a relatively narrow energy range. To no surprise, different theoretical methods (BPW91 versus MP2) predicted different ground electronic states for the neutral Hf-np complex. Thus, identifying the ground electronic states of neutral and ionic complexes based solely on the predicted energies is not always practical. The energy sequence of electronic states should be established through experimental measurements as discussed in the next section.

7.3.3.2 Hf-np ZEKE Spectra

The ZEKE spectrum of the Hf-np complex seeded in helium carrier is presented in Figure 7.5(a). This spectrum consists of four vibrational progressions and three additional vibrational intervals that originate from the peak at 46660 cm^{-1}. On the higher energy side of this peak are 80, 274, and 317 cm^{-1} vibrational progressions and 251 and 575 cm^{-1} vibrational intervals. On the lower energy side of this peak is a 75 cm^{-1} vibrat-

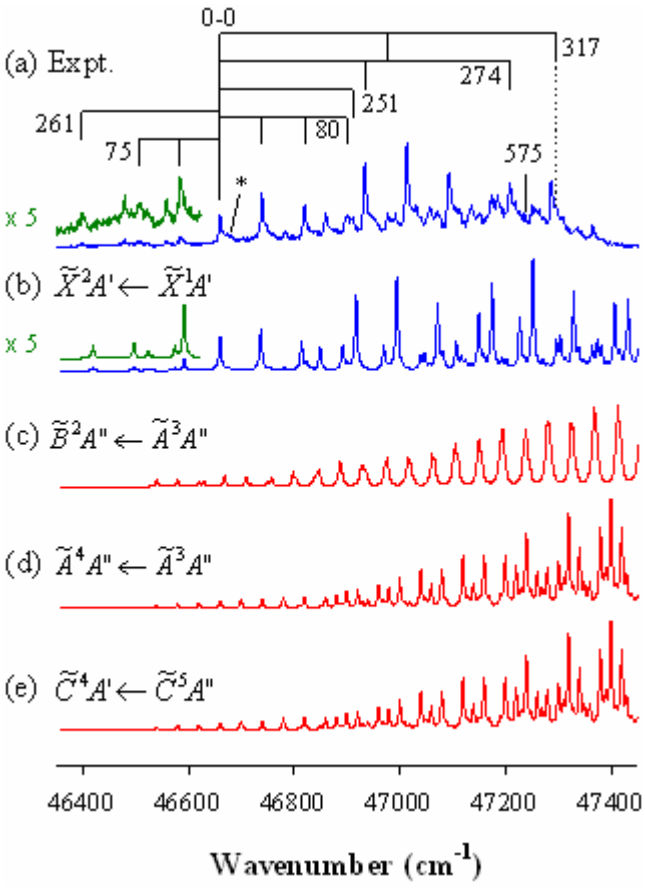

Figure 7.5. Experimental ZEKE spectrum of Hf-np recorded in helium carrier gas (a) and spectral simulations [BPW91/B7] of various spin-allowed transitions (b) – (e).

ional progression and a 261 cm^{-1} vibrational interval; a fivefold expansion (green trace) shows the peaks in this lower-energy region more clearly. From this spectral pattern, the peak at 46660 cm^{-1} can confidently be assigned to the origin band, the transition from the ground electronic state of the neutral molecule to the lowest-energy spin accessible state in the ion. The intervals on the red side of the origin band correspond to vibrations of the neutral molecule, while the intervals on the blue side of the origin band correspond to vibrations of the ionic molecule. All other peaks in this spectrum can be assigned to combinations of these seven vibrational intervals, except that marked by an asterisk at 46679 cm^{-1}. This peak likely originates from a different spectral carrier as it cannot be associated with any fundamental frequency, overtone frequency, or combination. Since this feature was not completely resolved, line shape and width comparisons to the other bands in the spectrum are not very practical. The observed spectral signature is consistent with the assignment to a single electronic transition, because all the line shapes and widths (FWHM ~ 6 cm^{-1}) of the major peaks are virtually the same. To confirm the identity of hot and cold transitions, spectral measurements using different carrier gases were performed. Unfortunately, these experiments were unsuccessful due to the much smaller signal to noise ratio.

The observed vibrational intervals can be assigned to specific modes by comparison to the ZEKE spectra of other M-np complexes presented thus far. The 80, 251, 274, 317, and 575 cm^{-1} intervals are assigned to ν_{26}^+, ν_{25}^+, ν_{24}^+, ν_{23}^+, and ν_{20}^+, respectively. These vibrational modes have already been described earlier in this chapter. However, the assignment of the two neutral vibrations cannot be made by analogy to other M-np complexes, because hot transitions were not observed in those spectra. On the other hand, vibrational levels that are populated in the neutral molecule are usually optically active in the ion. Thus, the 75 and 261 cm^{-1} vibrational intervals are preliminarily assigned to the ν_{26} and ν_{25} modes, respectively, of the neutral hafnium complex. The peak position of each peak and its corresponding assignment is listed in Table 7.2. FC simulations are used to confirm these assignments and for further spectral analysis.

7.3.3.3 Comparison of Experimental and Simulated Spectra

A comparison of the experimental Hf-np ZEKE spectrum to our spectral simulations of various transitions can be found in Figure 7.5(a) – (e). Although all 12 different spin-allowed transitions have been simulated, only a select few are presented in this figure. Three basic criteria were considered when selecting which transitions to present: (1) those simulations that have a similar spectral profile to experiment are included; (2) transitions to each ionic state are included, since most of the spectrum is attributed to vibrational modes of the ion; and (3) transitions from neutral states with relatively low electronic energy are included, because only these states have a chance to be populated in the molecular beam.

From the comparison of the experimental and simulated spectra, the $\widetilde{X}\ ^2A' \leftarrow \widetilde{X}\ ^1A'$ transition is clearly the best match. Simulations of the other transitions have much longer vibrational progressions than the measured spectrum, and the peak-to-peak correlations between those simulations and experiment are not very good. Furthermore, only the $\widetilde{X}\ ^2A' \leftarrow \widetilde{X}\ ^1A'$ transition matches the observed hot transitions on the lower energy side as illustrated in the fivefold expansion. Thus, the relative energies of the neutral Hf-np electronic states cannot be reproduced by the BPW91 method, because the $\widetilde{X}\ ^1A'$ state is calculated to be higher in energy than the $\widetilde{A}^3A''$ state. The inability of the BPW91 method to reproduce the energetics of the Hf-np complex is not very surprising, because heavier metal complexes are more difficult to model due to the larger number of electrons and complications from the relativistic effect. Our assignment of the observed spectrum to the $\widetilde{X}\ ^2A' \leftarrow \widetilde{X}\ ^1A'$ transition, however, is consistent with MP2 energetics. Unfortunately, MP2 simulations did not match the experimental spectrum very well.

Because the observed transition originates from a singlet state, the relative energy sequence of the electronic states in the ionic complex could not be determined due to selection rules. In other words, the relative energy difference between the doublet and quartet states could not be measured by our experimental method, because singlet to quartet transitions are spin forbidden. Thus, our assignment of $\widetilde{X}\ ^2A'$ to the ground electronic state of the ionic complex can only be considered tentative.

7.4 Trends in M-np Complexes

Table 7.6 summarizes the measured IEs, frequencies, and observed transitions of all the M-np complexes presented in this dissertation. The IEs of the bare metal atoms are larger than the IEs of the metal complexes. This IE shift indicates that the ionic complexes are bound more tightly than their neutral counterparts. The stronger binding in the ion is attributed to the addition of an ion-quadrupole interaction not present in neutral molecules.

Unlike the group 6 M-bz_2 complexes, the ΔIE values of the M-np complexes decrease as the group is descended. This monotonic decrease in ΔIE indicates that either the bond dissociation energy of the ionic complexes decreases or the bond dissociation energy of the neutral complexes increases as the group is descended. The heavier hafnium element should have larger atomic and ionic radii than those of the zirconium element due to the higher principal quantum numbers in the Hf valence shell. However, the relativistic effect shrinks the atomic and ionic radii of sixth row elements such that the atomic and ionic radii of hafnium (1.55 and 0.73 Å, respectively) are nearly the same as those of zirconium (1.55 and 0.72 Å, respectively).[288] On the other hand, hafnium is more polarizable than zirconium, because hafnium has 32 more electrons. Therefore, the more polarizable hafnium atom should, in principle, bind more strongly to the np ligand. Thus, the trend in ΔIE suggests that the bonding energy of the neutral complexes should significantly increase as the group is descended. In contrast, the calculated adiabatic bond dissociation energies of the neutral M-np complexes do not significantly increase from Ti- to Hf-np. In fact, the bond dissociation energy of Zr-np is predicted to be 3 kcal/mol larger than that of Hf-np. It seems that the BPW91 energetics for heavier metal complexes may not be as reliable as those in the lighter complexes. This unreliability is not surprising, because the quality of theoretical results decreases with increasing number of electrons. A measurement of the bond dissociation energies of these M-np complexes could provide additional insight into the reliability of the BPW91 energetics, but this work has not been done to our knowledge.

The measured IEs of each M-np complex agree with the predicted transition energies by more than 93 %. Thus, our assignment of each electronic state is energetic-

Table 7.6. Ground electronic state valence electron configurations (VEC) of corresponding neutral metal atom, IEs (cm^{-1}), assigned transitions (T_{00}), calculated adiabatic bond dissociation energies (D_o^+/D_o, kcal/mol), and measured frequencies (cm^{-1}) of M-np complexes (M = Sc, Y, Ti, Zr, Hf). Values in [brackets] are from BPW91 calculations.

	Group 3[a]		Group 4			
	Sc-np	Y-np	Ti-np[b]	Zr-np[c]		Hf-np[c]
VEC	d^1s^2	d^1s^2	d^2s^2	d^2s^2		$f^{14}d^2s^2$
IE	41193	40798	41764	42094	42549	46660
	[39814]	[40397]	[43384]	[42731]	[43224]	[43552]
T_{00}	$^1A' \leftarrow {}^2A'$	$^1A' \leftarrow {}^2A'$	$\tilde{X}\,^3A'' \leftarrow \tilde{X}\,^3A''$	$\tilde{X}\,^3A' \leftarrow \tilde{X}\,^3A''$	$\tilde{B}\,^3A'' \leftarrow \tilde{X}\,^3A''$	$\tilde{X}\,^3A' \leftarrow \tilde{X}\,^1A'$
ΔIE[d]	11729	9348	13308	11412	10957	8388
D_o^+/D_o[e]	[94 / 43]	[76 / 43]	[86 / 42]	[79 / 48]	[77 / 48]	[89 / 45]
$\nu_{26}^+/\ \nu_{26}$	112/100	93/--	114/--	132/--	116/--	80/75
	[114/97]	[91/--]	[115/--]	[92/--]	[100/--]	[77/68]
$\nu_{25}^+/\ \nu_{25}$	298/256	279/--	312/--	296/--	296/--	251/261
	[289/238]	[264/--]	[308/--]	[285/--]	[278/--]	[232/218]
$\nu_{24}^+/\ \nu_{24}$	347/315	314/--	355/--	322/--	380/--	274/--
	[339/312]	[299/--]	[351/--]	[320/--]	[331/--]	[257/236]
$\nu_{23}^+/\ \nu_{23}$	389/370	378/--	444/--		440/--	317/--
	[398/378]	[376/--]	[395/--]		[400/--]	[379/--]
$\nu_{22}^+/\ \nu_{22}$		516/--			468/--	
		[507/--]			[478/--]	
$\nu_{21}^+/\ \nu_{21}$	516/--		522/--			
	[513/--]		[520/--]			
$\nu_{20}^+/\ \nu_{20}$		597/--	614/--		661/--	575/--
		[585/--]	[606/--]		[583/--]	[583/--]

[a] C and H atoms are treated with 6-311+G(d,p) basis, while Sc is treated with the LANL2DZ basis. [b] B6 basis set was employed. [c] B7 basis set was employed. [d] $\Delta IE = IE_M - IE_{M\text{-}np}$, where IE_M is the ionization energy of the bare metal atom and $IE_{M\text{-}np}$ is the ionization energy of the M-np complex from ZEKE measurements. [e] Calculated adiabatic bond dissociation energies for each of the states in the observed transitions [final / initial].

ally reasonable. Unlike the metal-monobenzene systems, the low-spin states are favored over the high-spin states in naphthalene coordination. All identified states have singlet and doublet electron spin multiplicities, except for the neutral Ti- and Zr-np complexes where the triplet state was lower in energy. A preference for low spin multiplicities was also observed in M-bz$_2$ sandwich complexes.[14, 36, 278]

Interestingly, the electronic states identified in our investigation of the group 4 M-np complexes varied quite extensively as the group was descended. For neutral Ti- and Zr-np, the ground electronic states are the $\tilde{X}\ ^3A''$ state, while for neutral Hf-np the $\tilde{X}\ ^1A'$ state is determined to be the ground electronic state. For Ti^+-np, the ground electronic state corresponds to the $\tilde{A}^2A$" state. For Zr^+-np, on the other hand, the $\tilde{X}\ ^2A'$ state was measured to be 365 cm^{-1} lower in energy than the $\tilde{B}\ ^2A''$ state. Likewise, the Hf^+-np $\tilde{X}\ ^2A'$ state is found to be lower in energy than that of the $\tilde{B}\ ^2A''$ state. However, because the quartet state is inaccessible via the singlet state, we could not determine from experiment if the $\tilde{X}\ ^2A'$ state is the ground electronic state of Hf^+-np. But, our theoretical calculations support that this low-spin state is the most energetically favorable. The variety of states that are probed as this group is descended is very intriguing, since the ground electronic states in other similar metal-arene families were all the same.[278]

The relative metal-naphthalene binding strengths may be assessed by comparing the metal-ligand frequencies, $\nu_{25}^+/\ \nu_{25}$ and $\nu_{23}^+/\ \nu_{23}$. If the binding strengths of both group 3 and 4 M-np complexes are the same, the metal-ligand frequencies of group 4 are expected to be slightly lower due to the mass effect. Compared to group 3, the group 4 M-np complexes actually have slightly higher metal-based frequencies. Since the group 4 frequencies are higher, the binding energy of these complexes are likely larger than those in group 3. The stronger binding in group 4 versus group 3 metals towards π-surfaces is not surprising as Bauschlicher and coworkers predicted the bonding of titanium (group 4) to be about 37 % stronger than that of scandium (group 3) towards benzene.[145] Furthermore, the measured binding energy of Ti(TTB)$_2$ was determined to be higher than that of Sc(TTB)$_2$ according to iodinolytic batch titration calorimetric measurements in toluene [TTB = η^6-(1,3,5-^{t}Bu)$_3$C$_6$H$_3$].[146]

Within group 4 M-np complexes, the metal-ligand stretch frequencies follows the

order Ti-np > Zr-np > Hf-np. This trend is consistent with the increase in mass as the group is descended. However, the binding energies should monotonically increase from Ti to Hf due to the well-known relativistic effect. In fact, the binding energies of the group 4 M-TTB_2 complexes increased as the group was descended.[146] The frequency trend in the group 4 M-np complexes does not agree with the expected relativisticity, because these modes are more than just metal-based; these modes also contain C-C-C bending components. In addition, this simple diatomic model treats the entire naphthalene ligand as one large atom. Oftentimes, this drastic simplification can ultimately mislead the interpretation of experimental results.

CHAPTER 8: CLAMSHELL STRUCTURES OF GROUP 3 METAL-POLYPHENYL COMPLEXES: A ZEKE SPECTROSCOPIC AND THEORETICAL INVESTIGATION

8.1 Introduction

Biphenyl (bp = $C_{12}H_{10}$) has a planar structure in the crystalline state[289, 290] and is twisted in the gas phase.[291] The dihedral angle of the two phenyl rings is determined by competition between π-conjugation and steric repulsions; the former favors a coplanar configuration, while the latter prefers a non-planar form.[292-294] Transition metal-biphenyl complexes have been studied for many years in condensed-phase organo-metallic chemistry, because they are good models for conducting organometallic polymers.[295-301] Like metal-benzene complexes, each π-ring of biphenyl was suspected to have sixfold binding, and metal interaction with two π-rings formed dinuclear complexes.[295-298] In these dinuclear complexes, two metal atoms generally resided on opposite sides of the biphenyl plane to minimize steric repulsions, although structures with two metal atoms on the same side have been identified as well.[295, 298] On the other hand, metal-biphenyl complexes may form different structures in the gas phase due to the twisted configuration of the ligand and lack of stabilizing solvent and counterion molecules. Structural determination, however, has not been reported for metal complexes with biphenyl or other polyphenyls in the gas phase.[302]

We report here the clamshell structure of three metal-polyphenyl complexes: Sc- and La-bp and Sc-phnp (phnp = 1-phenylnaphthalene). These clamshell structures were identified by pulsed field ionization-zero electron kinetic energy (ZEKE) photoelectron spectroscopy, in combination with density functional theory (DFT) calculations. This work presents the first vibrational-electronic spectroscopy of any metal-polyphenyl species and shows a new binding mode of biphenyl and 1-phenylnaphthalene.

8.2 Experimental and Computational Methods

Details of our ZEKE spectrometer were discussed in Chapter 2. M-bp and -phnp complexes were produced by reactions of gaseous metal atoms with biphenyl (99 % $C_{12}H_{10}$, Aldrich) or 1-phenylnaphthalene (96 % $C_{16}H_{12}$, Aldrich) in molecular beams. The metal atoms were produced by pulsed laser vaporization of a metal rod (99.9 % Sc or 99.9 % La, Alfa Aesar) with the second harmonic output of a Nd:YAG laser (Lumonics, YM-800, 532 nm, ~1 mJ). The metal atoms were carried by He and/or Ar (UHP, Scott-Gross) which were delivered by a home-made piezoelectric pulsed valve[221] with stagnation pressures of 40 – 60 psi. A motor-driven device continuously rotated and translated the metal rod to ensure each laser pulse ablated a fresh surface. At room temperature, bp or phnp vapors were introduced through a stainless steel tube to a small reaction chamber (~1.5 mL) a few centimeters downstream from the ablation region, where the ligand interacted with the metal atoms entrained in the carrier gas.

Molecular masses were measured by photoionization time-of-flight mass spectrometry. Ionization thresholds of the metal complexes were located using PIE spectroscopy by recording the mass-selected ion signal as a function of ionization laser frequency. Prior to ZEKE experiments, the production of the target metal complex was maximized by adjusting the timing and power of the vaporization and ionization lasers, backing pressure of the carrier gas, and amount of ligand vapor in the reaction chamber. ZEKE electrons were generated by photoexcitation of neutral molecules to high-lying Rydberg states, followed by delayed (~ 3.5 μs) pulsed electric field ionization (1.2 V/cm, 100 ns) of these Rydberg states. A small DC field (~ 0.08 V/cm) was applied to help discriminate ZEKE electrons from kinetic energy electrons produced directly by photoionization. The photoionization and photoexcitation light was provided by the doubled-frequency output of a dye laser (Lumonics, HD-500) pumped by the third harmonic of a Nd:YAG laser (Continuum, Surelite-II, 355 nm). The pulsed electric field was generated by a delay pulse generator (Stanford Research Systems DG535). The ion and electron signals were detected by a dual microchannel plate detector (Burle), amplified by a preamplifier (Stanford Research Systems SR445), averaged by a gated

integrator (Stanford Research Systems SR250), and stored in a laboratory computer. Laser wavelengths were calibrated against vanadium or titanium atomic transitions.[169] A field-dependent study was not performed, because the anticipated IE shift ($1 \sim 2$ cm^{-1}) was smaller than the measured linewidth of the peaks in the experimental spectra.[182]

Geometry optimization and vibrational analysis were carried out with the GAUSSIAN98 and/or 03 program package.[183, 303] In these calculations, the hybrid density functional B3P86 method was employed and all atoms were treated with the 6-311+G(d,p) basis. Complete geometry optimizations were performed on various isomers of the free ligand and metal complexes. Subsequent frequency calculations were implemented to distinguish local minimum structures from transition states or second order saddle points on the potential energy surface.

To simulate spectra, multi-dimensional FC factors were calculated from the theoretical equilibrium geometries, harmonic vibrational frequencies, and normal coordinates of the neutral and ionic complexes.[68] The Duschinsky effect[45] was considered to account for normal mode differences between the neutral and ion in the FC calculations. Spectral broadening was simulated by giving each line a Lorentzian line shape with the experimental linewidth. To account for non-Boltzmann temperatures in the molecular beam, the vibrational temperatures for low frequency modes ($\lesssim 600$ cm^{-1}) were specified separately. Although the calculated frequencies were not scaled, the calculated ionization energies are shifted to the experimental value to allow easier comparison of the measured and calculated FC profiles.

8.3 Results and Discussion

8.3.1 Sc-bp

8.3.1.1 Theoretical Isomers

Because our experiments are done in the gas phase, geometry optimizations of the free ligand were only limited to the twisted D_2 configuration. On the other hand, six different isomeric structures were considered for the scandium complex with initial phenyl

torsion angles of 0, 45, or 90 ^{o} and metal interaction with a π ring or the bridging C-C bond. However, the resultant geometry optimizations only converged to two different structures: a half-sandwich structure with Sc binding to one ring [Figure 8.1(a)] and a clamshell structure with Sc binding to two rings [Figure 8.1(b)]. Table 8.1 summarizes the predicted bond lengths and angles for the Sc-bp complexes and free bp ligand. This table also compares the calculated relative electronic energies between different states of the metal complex.

The energy difference between the ground electronic states of the clamshell and half-sandwich structures is 3703 cm^{-1}, with the clamshell structure being lower in energy. For the clamshell structure, the ground electronic state spin multiplicity is a doublet ($^{2}B_{1}$), with a $3d^{3}$ valence electron configuration. To form the clamshell structure, the phenyl rings may be first rotated to become coplanar, then bent by ~ 52 ^{o} (i.e. 180.0 ^{o} – ∠[C_4-C_1-$C_{1'}$]) toward the Sc atom. This structure has a twelve-fold bonding mode with the shortest distance (2.143 Å) between Sc and the two carbon atoms of the junction bond. Distances between Sc and other carbon atoms are in the 2.412-2.531 Å range. Like in the Sc-np complex, the coordinated π-rings are puckered by about 18 ^{o} (i.e. 180.0 ^{o} – δ[C_6-C_1-C_4-C_3]). However, no π electron localization occurs in the phenyl rings of these clamshell complexes as indicated by the change in C-C bond lengths from the free ligand to the metal coordinated complex. Therefore, in these clamshell complexes, the scandium atom is coordinated to an η^{6}:η^{6}-bp molecule. On the other hand, a significant amount of π electron localization does occur on the bridging C_1-$C_{1'}$ bond which shrinks by ~ 0.044 Å during scandium coordination. An excited state ($^{4}B_{1}$) of the clamshell structure was located 11564 cm^{-1} higher in energy. Compared to the $^{2}B_{1}$ state, the phenyl rings in the excited quartet state bend towards the metal atom by a slightly smaller amount, ~ 41 ^{o}, and the phenyl rings are less puckered, ~ 11 ^{o}. Unlike the ground electronic state of the clamshell configuration, the bridging C_1-$C_{1'}$ bond in the $^{4}B_{1}$ state is virtually the same as that in the free ligand. In addition, C-C bond lengths are not elongated as much as those in the $^{2}B_{1}$ state, which indicates less d-π interaction in this excited quartet state.

For the half-sandwich structure, the ground electronic state spin multiplicity is also a doublet (^{2}A), but with a valence electron configuration of $3d^{2}4s^{1}$. The two rings in this structure remain twisted, although the dihedral angle is slightly reduced by ~ 3 ^{o} from

Table 8.1. Predicted point groups; electronic states; relative electronic energies (ΔE, cm^{-1}), bond lengths (R, Å), simple, dihedral, and torsion angles (∠, δ, and τ, degrees) for clamshell and half-sandwich structures of Sc^+/ Sc-biphenyl and the free biphenyl ligand from B3P86/6-311+G(d,p) calculations. See Figure 8.1 for numeric labels.

	Sc-biphenyl				Sc^+-biphenyl				biphenyl
	clamshell		half-sandwich		clamshell		half-sandwich		twisted
Point Group	C_{2v}		C_1		C_{2v}		C_1		D_2
Electronic State	$^2B_1$	$^4B_1$	^2A	^4A	$^1A_1$	$^3B_1$	^1A	^3A	^1A
ΔE [a]	0	11564	3703	3772	43498	51661	47649	48476	
R[Sc^+/ Sc-C_1]	2.143	2.258	2.453	2.415	2.150	2.208	2.388	2.347	
R[Sc^+/ Sc-C_2]	2.412	2.532	2.382	2.393	2.465	2.449	2.329	2.330	
R[Sc^+/ Sc-C_3]	2.531	2.819	2.235	2.407	2.558	2.653	2.176	2.350	
R[Sc^+/ Sc-C_4]	2.481	2.900	2.445	2.410	2.444	2.676	2.374	2.356	
R[Sc^+/ Sc-C_5]	2.531	2.819	2.385	2.402	2.558	2.653	2.351	2.348	
R[Sc^+/ Sc-C_6]	2.412	2.532	2.206	2.392	2.465	2.449	2.166	2.336	
R[C_1-C_2]	1.461	1.431	1.384	1.425	1.461	1.434	1.387	1.427	1.399
R[C_2-C_3]	1.396	1.400	1.459	1.411	1.380	1.400	1.457	1.414	1.389
R[C_3-C_4]	1.417	1.401	1.438	1.412	1.422	1.405	1.443	1.414	1.390
R[C_4-C_5]	1.417	1.401	1.374	1.412	1.422	1.405	1.377	1.414	1.390
R[C_5-C_6]	1.396	1.400	1.465	1.411	1.380	1.400	1.457	1.414	1.389
R[C_6-C_1]	1.461	1.431	1.456	1.425	1.461	1.434	1.462	1.426	1.399
R[C_1-$C_{1'}$]	1.434	1.472	1.474	1.472	1.427	1.481	1.473	1.475	1.478
R[$C_{1'}$-$C_{2'}$]	1.461	1.431	1.401	1.402	1.461	1.434	1.400	1.401	1.399
R[$C_{2'}$-$C_{3'}$]	1.396	1.400	1.387	1.388	1.380	1.400	1.386	1.387	1.389
R[$C_{3'}$-$C_{4'}$]	1.417	1.401	1.392	1.390	1.422	1.405	1.391	1.391	1.390
R[$C_{4'}$-$C_{5'}$]	1.417	1.401	1.389	1.392	1.422	1.405	1.390	1.390	1.390
R[$C_{5'}$-$C_{6'}$]	1.396	1.400	1.389	1.387	1.380	1.400	1.388	1.388	1.389
R[$C_{6'}$-$C_{1'}$]	1.461	1.431	1.400	1.403	1.461	1.434	1.401	1.402	1.399
∠[C_4-C_1-$C_{1'}$]	128.2	139.0	174.3	179.9	128.0	132.9	173.1	176.9	180.0
δ [b]	162.0	169.5	153.1	179.9	156.6	167.6	156.0	179.7	180.0
τ [c]	0.0	0.0	36.8	30.2	0.0	0.0	34.3	31.7	40.2

[a] ΔE is the relative electronic energy difference from the clamshell $^2B_1$ electronic state. [b] The δ[C_6-C_1-C_4-C_3] dihedral angle is reported for the clamshell configurations, and the δ[C_1-C_6-C_3-C_4] dihedral angle is reported for the half-sandwich configurations. [c] The [C_2-C_1-$C_{1'}$-$C_{2'}$] torsion angle.

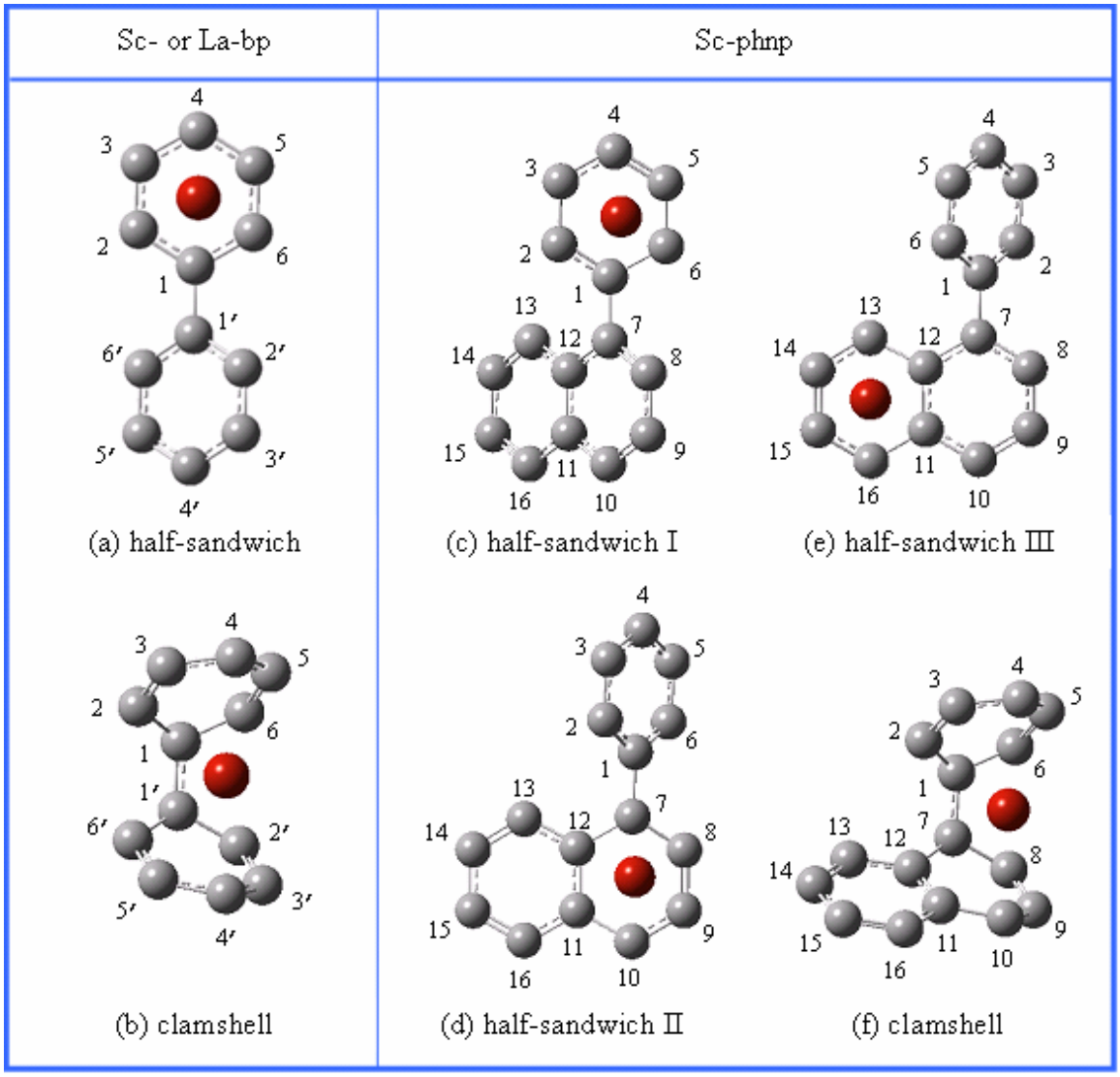

Figure 8.1. Clamshell and half-sandwich structures of M-bp (a) and (b) and -phnp (c) – (f). Metal atoms are red (Sc or La), carbon atoms are grey, and H atoms are omitted for clarity.

the free ligand to the complex. In this state, the metal coordinated π ring puckers away from the Sc atom by about ~ 27 °. Consequently, two Sc-C distances, 2.235 and 2.206 Å, are much shorter than the others, 2.382 to 2.453 Å. Like in the Sc(2,5-η^2-np) complex, a significant amount of π localization occurs on the Sc bound π ring at the C_1-C_2 and C_4-C_5 bonds. The Sc-C and C-C distances in this half-sandwich structure are consistent with a Sc(3,6-η^2-bp) complex. Unlike the clamshell structure, a low-lying excited quartet state is calculated to lie only 69 cm^{-1} above the doublet state. In this quartet state, both phenyl rings remain virtually flat, the Sc-C distances are nearly the same (2.392 to 2.415 Å), and no significant π electron localization occurs. These structural trends indicate that this excited quartet state has sixfold bonding between the scandium atom and phenyl ring.

Ionization of the clamshell structure removes a Sc $3d_\pi$ electron from the highest occupied molecular orbital (HOMO) of the $^2B_1$ state and yields the ground electronic $^1A_1$ ion state. This $^1A_1$ state is predicted to lie about 43498 cm^{-1} above the ground electronic state of the clamshell structure. Upon ionization of the $^2B_1$ state, Sc-C distances slightly elongate, and the phenyl rings pucker an additional 5 °. Interestingly, the phenyl rings are predicted to remain bent at the same angle (~ 52 °) in the ion while the bridging C_1-C_1' bond shortens by about 0.007 Å. Like in the neutral complex, an excited $^3B_1$ state in the ion is predicted at much higher energy, 8163 cm^{-1}. Compared to the $^1A_1$ state, the phenyl rings are less puckered, a majority of the Sc^+-C distances are longer, and the magnitude in the C-C bond lengths are more evenly distributed in the $^3B_1$ state.

Unlike the clamshell structure, ionization of the half-sandwich structure removes a Sc 4s electron from the ^2A state to produce the ^1A ion state. The singlet state of the ionic half-sandwich structure is predicted to lie about 43946 cm^{-1} above the doublet state of the neutral half-sandwich structure. Upon ionization of the half-sandwich structure, Sc-C distances shrink, the phenyl torsion angle is reduced by a few degrees, and the coordinated phenyl ring becomes slightly less puckered. Only 827 cm^{-1} above this singlet state of the half-sandwich structure is the excited triplet state of the ion. Compared to the singlet state, the triplet state has flat phenyl rings, more evenly distributed C-C bond lengths, and similar Sc^+-C distances, 2.330 to 2.356 Å versus 2.166 to 2.374 Å. Thus, the low-spin states form η^2-bp half-sandwich complexes while the high-spin states form η^6-bp half-sandwich complexes just like the naphthalene and benzene complexes.

8.3.1.2 Spectroscopy

A representative ZEKE spectrum of Sc-biphenyl is shown in Figure 8.2(a). Peaks from single vibrational-mode excitations are labeled in the figure, while others can be easily assigned to transitions involving two or more vibrational modes. The strongest transition occurs at 39114 (5) cm^{-1} [4.8495 (6) eV] and is the origin (0-0) of the electronic transition between the ground vibrational levels of the neutral and ionized molecules. The energy of the 0-0 peak corresponds to the first onset of the PIE spectrum as indicated in the inset (green trace) of Figure 8.2(a). On the higher energy side of the band origin, the ZEKE spectrum exhibits peaks spaced in 189, 284, 336, 378, and 568 cm^{-1} intervals. These peaks correspond to excitations of five vibrational modes in the ion complex. An additional peak (*h*) is observed at 13 cm^{-1} below the band origin, while a small peak is observed at 36 cm^{-1} above the band origin. The intensities of these peaks depend on the condition of the molecular beam and are attributed to hot transitions from excited vibrational levels of the neutral molecule. The transition intensity of a sharp line (*Ta*) at 39060 cm^{-1} has a strong power-dependence and corresponds to resonant two-photon ionization of Ta, an impurity of the Sc rod. All the other peak positions and corresponding assignments are presented in Table 8.2.

To determine the nature of the observed vibrational modes, the experimental ZEKE spectrum is compared to the vibrational spectra of the free biphenyl ligand and the Sc-$bz_{1,2}$ complexes. From a number of vibrational spectra, the fundamental modes of bp have been assigned by Zerbi and Sandroni[304, 305] and Barrett and Steele.[306] The fundamental frequencies for seven bp modes have frequencies < 600 cm^{-1} (112, 269, 315, 367, 403, 486, 543 cm^{-1}), which fall in the frequency range of the observed fundamental vibrations in the Sc-bp ZEKE spectrum. Assuming the Sc-bp complex has a clamshell configuration under C_{2v} symmetry, the fundamental frequencies of a_1 modes will be optically active in the ZEKE spectrum according to selection rules in vibronic spectroscopy. The frequencies of the free bp ligand were assigned based on the D_{2h} point group. Thus, only the modes with a_g and b_{3u} symmetry may be considered in our spectral assignment of the fundamental vibrational modes, because these representations correlate to the a_1 representation under the C_{2v} point group. Of course, other modes with different symm-

Table 8.2. Peak positions (cm^{-1}) and assignments[a] for the experimental ZEKE spectra of Sc-bp, Sc-phnp, and La-bp.

Sc-bp				La-bp		Sc-phnp			
Peak	Assignment	Peak	Assignment	Peak	Assignment	Peak	Assignment	Peak	Assignment
39060	Ta	40163	$17_0^2 16_0^1$	36516	0_0^0	37594	0_0^0	38220	$72_0^1 75_0^1$
39101	32_1^1	40193	$32_1^1 17_0^1 16_0^2$	36549	46_1^1	37675	81_0^1	38242	$71_0^1 75_0^1$
39113	0_0^0	40207	$17_0^1 16_0^2$	36720	La	37756[c]	81_0^2 & 79_0^1	38275	72_0^2
39149	46_1^1	40250	16_0^3	36773	17_0^1	37809	77_0^1	38302	$71_0^1 72_0^1$
39303	18_0^1	40353	$17_0^2 15_0^1$	36886	16_0^1	37820	76_0^1	38317	71_0^2
39397	32_0^2	40395	$17_0^1 16_0^1 15_0^1$	36937	$18_0^1 17_0^1$	37881	75_0^1	38332	$70_0^1 72_0^1$
39438	$32_1^1 17_0^1$	40417	$16_0^2 15_0^1$	37027	17_0^2	37897	$77_0^1 81_0^1$		
39450	17_0^1			37048	15_0^1	37928	73_0^1		
39492	16_0^1			37109	[b]	37934	72_0^1		
39681	15_0^1			37142	$17_0^1 16_0^1$	37956	71_0^1		
39787	17_0^2			37256	16_0^2	37963	$75_0^1 81_0^1$		
39816	$32_1^1 17_0^1 16_0^1$			37280	17_0^3	37992	70_0^1		
39827	$17_0^1 16_0^1$			37306	$17_0^1 15_0^1$	38036	$71_0^1 81_0^1$		
39852	$32_1^1 16_0^2$			37378	11_0^1	38049	$75_0^1 81_0^2$		
39868	16_0^2			37395	$17_0^2 16_0^1$	38094	67_0^1		
40016	$17_0^1 15_0^1$			37499	10_0^1	38151	65_0^1		
40060	$16_0^1 15_0^1$			37508	$17_0^1 16_0^2$	38165	75_0^2		

[a] Some peaks have a much narrower linewidth and are assigned to atomic transitions (Ta or La).
[b] This peak is marked by a brown asterisk [*] and has a narrower bandwidth than other peaks in the spectrum. This transition does not originate from the La-bp clamshell complex; its origin is unknown. **[c] This peak is tentatively assigned to the overlap of two transitions: the overtone of ν_{81} and the fundamental of ν_{79}.**

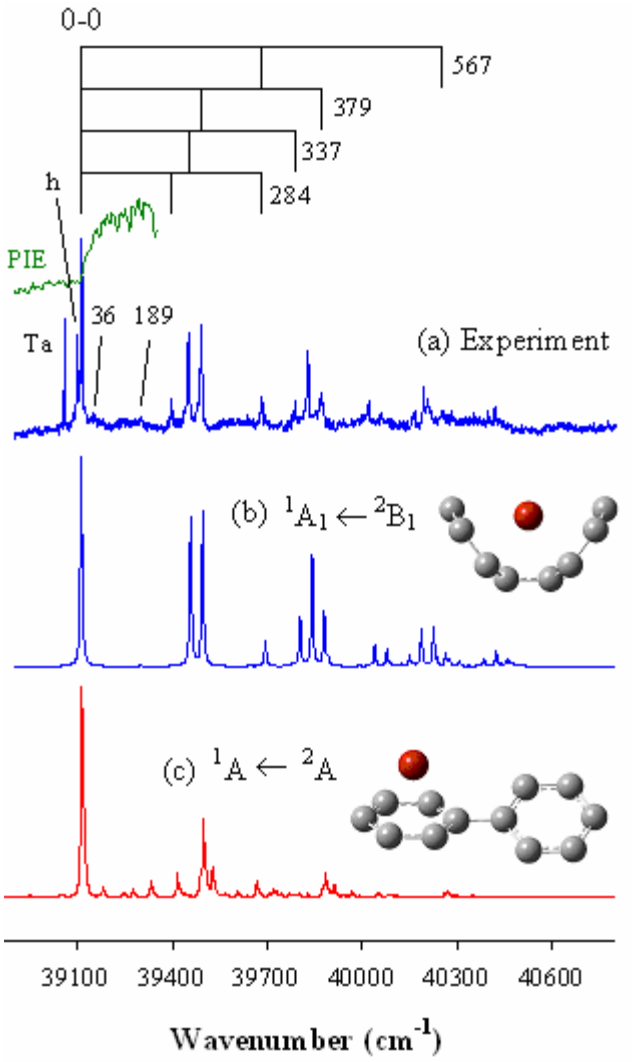

Figure 8.2. The experimental ZEKE spectrum (a) and simulations [10 K] of the clamshell (b) and half-sandwich (c) isomers of Sc-bp. A portion of the PIE spectrum (green trace) is plotted in the inset.

etry representations may also appear in the spectrum but as overtones or combination bands such that the resultant vibrational level contains the totally symmetric a_1 representation. After such symmetry considerations, only the 315 (a_g) and 486 (b_{3u}) cm^{-1} C-C-C bending modes of the free bp ligand can be observed in the Sc-bp ZEKE spectrum. Upon Sc coordination, the bp framework should become less rigid due to π electron donation to empty *d* orbitals of Sc and back-donation of *d* electrons into the empty π^* orbitals of bp; both electron donation and back-donation weakens C-C bonds of the bp ligand. Thus, C-C-C bending frequencies in the Sc complex should be red shifted with respect to the free ligand. Thus, the 379 cm^{-1} mode in the Sc-bp ZEKE spectrum is assigned to the phenyl ring distortion (ν_{16}^+), which is red shifted by 107 cm^{-1} with respect to the free bp ligand (i.e. 379 – 486 = -107 cm^{-1}). The large frequency shift from the free ligand to the Sc complex is attributed to the large conformational change of the ligand from D_{2h} to C_{2v} symmetry. Due to the large change in the ligand geometry, this assignment can only be considered preliminary. The other modes may be assigned by comparison to the spectroscopy of similar metal complexes.

In Chapter 3, the ZEKE spectra of Sc-bz and -bz_2 were presented. The Sc^+/Sc-bz stretch frequencies were measured to be 375 and 324 cm^{-1} in the $^3A_1$ and $^4A_1$ states, respectively. For the Sc-bz_2 sandwich complex, the symmetric bz-Sc^+-bz stretch frequencies were measured to be 206 and 201 in the $^1A_{1g}$ and $^3A_{1g}$ states, respectively. Thus, the 337 cm^{-1} vibrational frequency observed in the Sc-bp ZEKE spectrum may be attributed to the Sc^+-bp stretch mode. The magnitude of this Sc^+-bp stretch frequency is reasonable, because it falls within the stretch frequency range of the Sc-bz and -bz_2 complexes. The relatively different stretch frequency is consistent with the very different structural framework of the bp ligand that adopts a clamshell configuration. Due to the large structural change of the ligand framework upon Sc coordination, the assignment for the other observed vibrational modes is not very straightforward. Further spectral analysis considers a comparison of experimental data to calculated frequencies and spectral simulations.

8.3.1.3 Experimental and Theoretical Comparison

Under supersonic expansion, the molecular species are internally cooled to the ground electronic state and vibrationally depopulated to a large extent. In our previous spectroscopic measurements of other metal complexes,[15, 17-22, 24-28, 171, 182, 304, 305] the observed ZEKE spectra were entirely attributed to the lowest energy isomer of the metal-ligand adduct. Thus, if any higher energy isomers are prepared in our laser ablation source, they must be interconverted to the lowest energy isomer upon supersonic expansion. Therefore, the clamshell configuration is responsible for the observed Sc-bp ZEKE spectrum according to the calculated electronic energies. In addition, the rather large frequency shift of the ligand-based vibrations upon Sc coordination is consistent with the large geometrical change of the ligand from D_2 to C_{2v} symmetry.

The spectral simulations of the doublet to singlet transition of the clamshell and half-sandwich structures are presented in Figure 8.2(b) and (c), respectively. The simulated transition from the half-sandwich structure does not match the experimental spectrum that well, because some peaks are not simulated or are severely underestimated. In addition, it seems a number of small peaks appear in the simulation that are not observed in experiment. Simulation from the clamshell configuration, on the other hand, matches the experimental spectrum quite well, although it misses the weak peak at 284 cm^{-1}. This comparison shows clearly that the observed spectrum originates from the $^1A_1 \leftarrow {}^2B_1$ transition of the clamshell structure.

Based on the good agreement between experiment and theory, all the observed vibrational modes were determined. Those modes already assigned based on frequency comparisons to free bp and Sc-$bz_{1,2}$ are consistent with our spectral simulation. These modes are described in Table 8.3, which also compares the measured and calculated frequencies. The 336 cm^{-1} progression is assigned to excitations of the symmetric Sc^+-bp stretch, characterized largely by Sc^+ displacement (ν_{17}^+). The 378 and 568 cm^{-1} intervals are excitations of two symmetric ring out-of-plane deformations (ν_{16}^+ and ν_{15}^+). Peak *h* at 13 cm^{-1} below the band origin is due to a sequence transition between the first vibrational levels of a nontotally symmetric phenyl torsion mode in the neutral (ν_{32}) and ion (ν_{32}^+)

ground electronic states. This peak is partially overlapped with the band origin in the simulation. The 284 cm^{-1} interval does not correspond to any of the symmetric vibrations in the ion, but is about twice the predicted frequency of ν_{32}^{+}. Thus, it may be assigned to the first overtone of this torsion mode. The assignment of the 284 cm^{-1} and sequence peaks yields ν_{32}^{+} and ν_{32} frequencies of 142 and 155 cm^{-1}, which are close to the calculated values of 157 and 169 cm^{-1}, respectively.

Table 8.3 also compares the measured and calculated IEs, which are corrected by a 10 % IE overestimation of the B3P86 method. This IE overestimation by B3P86 has been observed for many other transition metal-aromatic hydrocarbon complexes. Figure 8.3 presents a bar graph that clearly illustrates this overestimation. This IE overestimation is derived by

$$\frac{\sum_{i}^{N}\left(\frac{IE_{B3P86,i}}{IE_{ZEKE,i}}-1\right)}{N}\times 100\% \qquad \textit{(8-1)},$$

where $IE_{B3P86,\,i}$ is the calculated ionization energy of complex *i*, $IE_{ZEKE,\,i}$ is the measured ionization energy of complex *i*, and the summation runs over *N* different complexes (i.e. 10). In addition to the great match between the measured and simulated Sc-bp ZEKE spectra, the calculated frequencies and corrected IEs of the clamshell structure match with experimental values quite well.

8.3.1.4 Formation of the Clamshell Configuration

To form the lowest energy C_{2v} clamshell configuration, metal coordination must have induced intramolecular rotation about the bridging C-C bond. Also, the phenyl groups partly enclose the metal atom, and the bridging C-C bond is shortened, a unique characteristic of the clamshell binding mode. This ligand transformation brings about some very interesting questions: (1) why does the clamshell structure form? And, (2) why does the bridging C-C bond shrink upon metal coordination? These structural

Table 8.3. Measured and calculated IEs (eV) and vibrational frequencies (cm^{-1}) for scandium and lanthanum complexes.

	Description	ZEKE	B3P86
Sc-bp	Clam, C_{2v}		
IE [a]	$^1A_1 \leftarrow {}^2B_1$	4.8494(6)	4.9203
ν_{18}^+	Phenyl ring bend	190	186
ν_{17}^+	Sc^+-$C_{12}H_{10}$ stretch [b]	337	345
ν_{16}^+	Phenyl ring distortion	379	384
ν_{15}^+	Sc^+-$C_{12}H_{10}$ stretch [b]	567	581
ν_{32}^+ / ν_{32}	Phenyl torsion	142 / 155	157 / 169
$\Delta\nu_{46}$ [c]	Sc rock	36	10
La-bp	Clam, C_{2v}		
IE [a]	$^1A_1 \leftarrow {}^2B_1$	4.5274(6)	4.6143
ν_{18}^+	Phenyl ring bend	164 [d]	162
ν_{17}^+	La^+-$C_{12}H_{10}$ stretch [b]	257	255
ν_{16}^+	Phenyl ring distortion	370	372
ν_{15}^+	La^+-$C_{12}H_{10}$ stretch [b]	532	535
ν_{11}^+	C-C out-of-plane bend	862	861
ν_{10}^+	Phenyl ring distortions	983	970
$\Delta\nu_{46}$ [c]	La rock	33	19
Sc-phnp	Clam, C_1		
IE [a]	$^1A \leftarrow {}^2A$	4.6611(6)	4.7684
ν_{81}^+	Phenyl-naphthyl torsion	81	81
ν_{79}^+	C-C out-of-plane bend	161	151
ν_{77}^+	Phenyl / naphthyl ring bends	215	216
ν_{76}^+	C-C out-of-plane bend	226	271
ν_{75}^+	C-C out-of-plane bend	287	289
ν_{73}^+	Sc^+ rock	334	335
ν_{72}^+	Sc^+-$C_{16}H_{12}$ stretch [b]	340	348
ν_{71}^+	C-C out-of-plane bend	362	366
ν_{70}^+	C-C in-plane bend	398	402
ν_{67}^+	Naphthyl ring distortion	500	499
ν_{65}^+	C-C out-of-plane bend [e]	557	554

[a] The calculated B3P86 IEs include zero-point vibrational energy corrections and an average 10 % IE overestimation correction. [b] These vibrations are mixed modes with Sc^+- or La^+-ligand stretch motions dominate over different C-C-C bending motions. [c] $\Delta\nu_{46} = \nu_{46}^+ - \nu_{46}$. [d] Frequency calculated based on the assignment of the $18_0^1 17_0^1$ band position. [e] Also contains a Sc^+-phnp stretch.

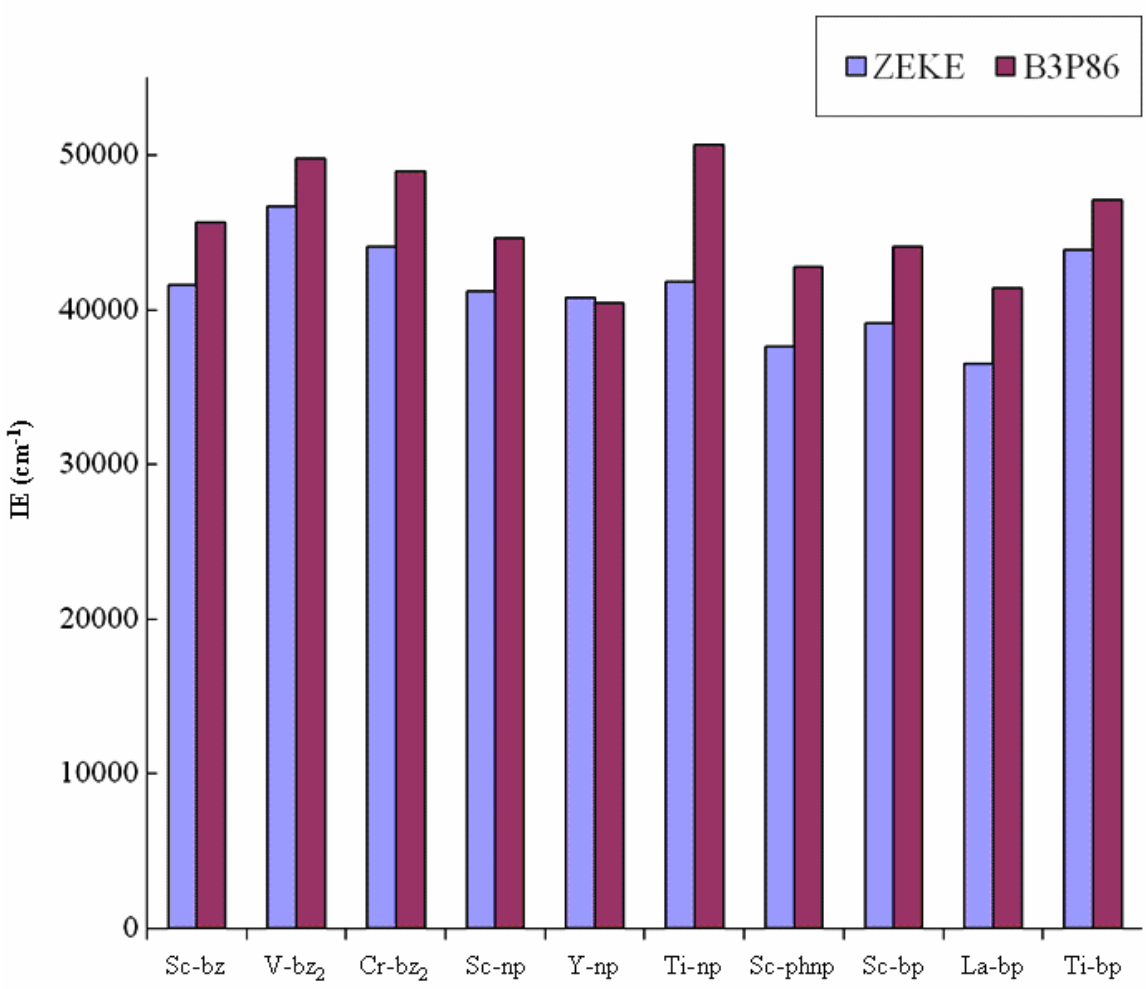

Figure 8.3. A comparison of measured and calculated IE values illustrates an average 10 % IE overestimation of transition metal-aromatic hydrocarbon complexes by the B3P86 method.

aspects can be explained from two different viewpoints: by electrostatic interactions and molecular orbital theory.

In considering electrostatic interactions, the charges on each atom must be taken into account. For the free ligand, the phenyl groups are generally regarded as electron-withdrawing groups. The two bridging carbon atoms should bear a partial positive charge due to equal pulling of the two phenyl electron-withdrawing groups. This assumption is confirmed by a Mulliken population analysis of the free biphenyl ligand, where small positive charges were predicted to reside on these two bridging carbon atoms. All the other carbon atoms on the free ligand are calculated to have partial negative charges. Thus, this ligand can be thought to have two local electric dipole moments that point in opposite directions. If this electrostatic system interacts with a scandium atom, the ligand will polarize the metal atom. In this case, the metal atom is considered to have a temporary dipole moment with a negative and positive end. The negative end of the metal atomic induced dipole will be attracted to the bridging C_1-C_1' bond that has two partially positively charged carbon atoms, while the positive end of the metal atomic dipole will be attracted to one of the negatively charged π rings. In the latter case, a stable half-sandwich structure forms; these states are local minima on the potential energy surface according to our frequency analyses. In the former case, where the metal atom interacts with the bridging C_1-C_1' bond, the negative end of the metal atomic induced dipole will interact with the partially positive carbon atoms of the junction C-C bond. In this process, the bridging C_1-C_1' bond is decreased by a reduction in the $C_1^{\delta+}$-$C_1'^{\delta+}$ repulsion. As the junction C-C bond length decreases, the negatively charged π rings are attracted to the positive end of the metal atomic dipole, which causes each π ring to rotate and bend towards the polarized scandium atom; the resultant structural configuration has a clamshell shape. In this configuration, the ortho H-H repulsions are kept to a minimum, because the rings are bent out of the plane. Compared to the half-sandwich structure, the clamshell structure seems to have many more electrostatic interactions. Thus, it is not unreasonable that this clamshell configuration is more stable than the half-sandwich structure from an electrostatic point of view. Further considerations take into account molecular orbital theory.

The relative energy of the clamshell and half-sandwich structures will depend

primarily on the relative energy of the HOMOs. The electron density map for the HOMOs of the clamshell and half-sandwich structures are presented in Figure 8.4(a) and (c). This figure displays how the corresponding MO of the product is formed. For example, the HOMO (b_1) of the Sc-bp clamshell structure is formed by the interaction of the $3d_{xz}$ orbital (b_1) with the second lowest unoccupied molecular orbital (LUMO + 1, b_1) of a clamshell-shaped bp molecule as illustrated in Figure 8.4(a). The MO electron density map of the clamshell-shaped bp molecule was obtained by doing a single point calculation on the ligand framework in the $^2B_1$ state after removal of the scandium atom. Similarly, the HOMO - 1 of the clamshell configuration (a_1) was formed by interaction of the $3d_{x^2-y^2}$ and $3d_{z^2}$ orbitals of Sc with the LUMO (a_1) of a clamshell-shaped bp molecule [Figure 8.4(b)]. The HOMO of the half-sandwich structure (no symmetry) is formed primarily by back-donation of a 4s electron of Sc (no symmetry under the C_1 point group) to the unfilled π^* orbital (no symmetry under the C_1 point group) of the twisted bp molecule.

The major difference between the electron density maps of the valence MOs is that the metal interacts with both phenyl π systems in the clamshell configuration and neither π system in the ring configuration. In the clamshell configuration, the metal apparently acts as a link to bring the two π systems on separate rings together as one. This π–d–π interaction stabilizes the clamshell structure substantially. Additionally, both the HOMO and HOMO - 1 of the complex have a large orbital overlap between the bridging C_1 and $C_{1'}$ atoms. Hence, it is not surprising that this bond is shortened upon metal coordination when forming the clamshell structure. Without this type of coordination, the ligand remains twisted with no π overlap between the two conjugated π systems as indicated in Figure 8.4(c).

8.3.2 La-bp

The discovery of this new clamshell binding mode of biphenyl is astounding. The clamshell configuration requires rotation about the junction bond and bending of the phenyl rings to clamp the metal atom. To further improve our understanding of this new

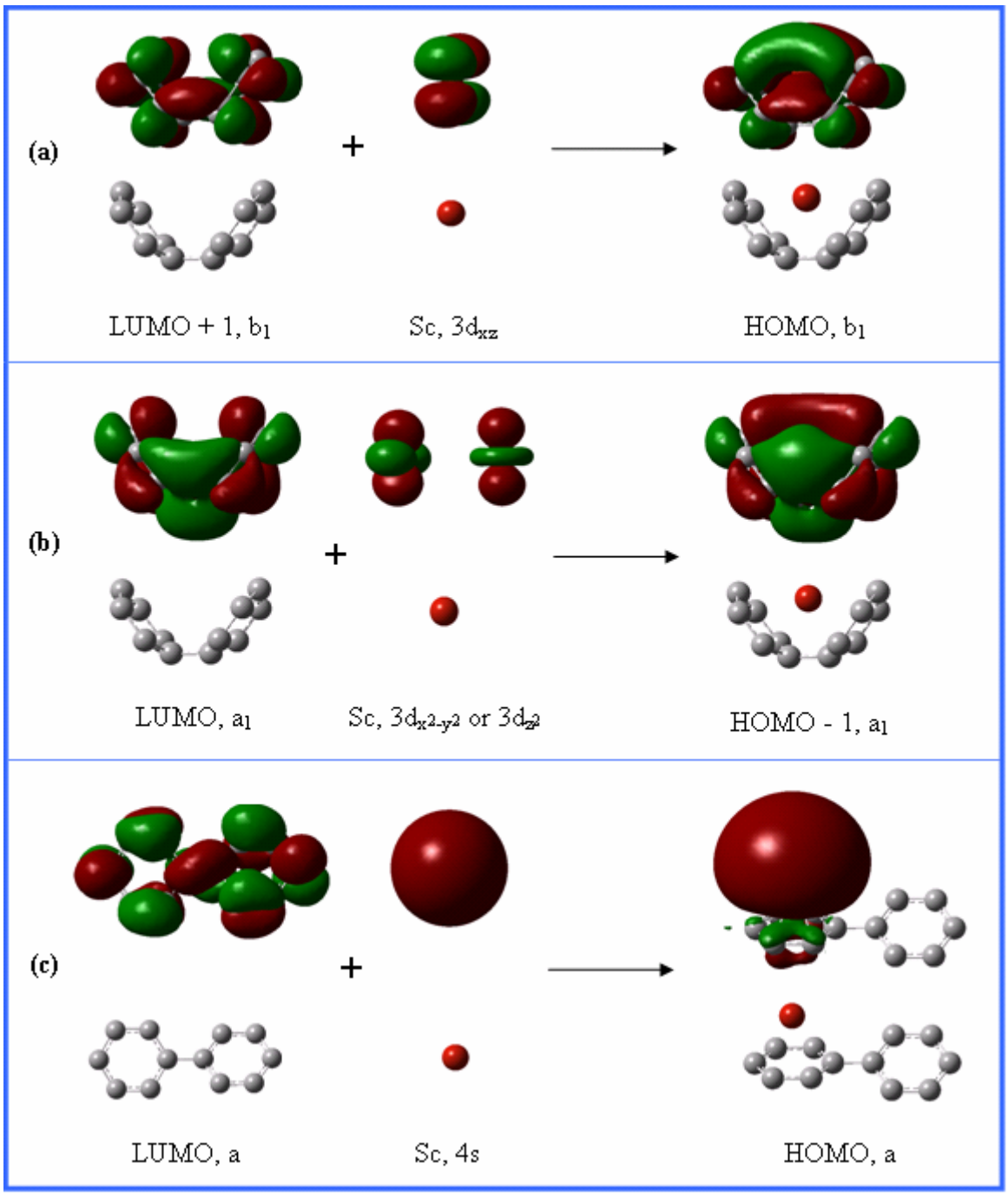

Figure 8.4. Scandium atom interaction with molecular orbitals of free bp ligands that form the HOMO of the neutral Sc-bp clamshell complex (a), the second HOMO of the neutral Sc-bp clamshell complex (b), and the HOMO of the neutral Sc-bp half-sandwich complex (c). The orientation of the molecule is presented below each MO electron density map for clarity.

clamshell binding mode of biphenyl, we have also studied the interaction of heavier metal atoms (i.e. La) with biphenyl. The results from this metal substitution experiment are presented in this section. Experiments and calculations on the Y-bp complex are still underway.

8.3.2.1 Theoretical Isomers

Table 8.4 summarizes the results from our theoretical calculations of the La-bp complex. Like Sc-bp, the lowest energy electronic state corresponds to the $^2B_1$ state of the clamshell configuration, while the ^2A state of the half-sandwich structure is predicted to lie only 837 cm^{-1} higher in electronic energy. The ^4A state of the half-sandwich structure is calculated to be 1411 cm^{-1} above this ^2A state. The $^4B_1$ state of the clamshell structure, on the other hand, is predicted to lie relatively much higher in electronic energy, 8709 cm^{-1} above the ground electronic $^2B_1$ state. Ionization of the $^2B_1$ state leads to the $^1A_1$ ground electronic state of the La^+-bp complex, which has a clamshell configuration as well. In the half-sandwich configuration, the singlet and triplet states were located at 3576 and 3660 cm^{-1} higher in energy than the $^1A_1$ state of the clamshell structure, respectively. Similar to the neutral La-bp complex, the higher spin $^3B_1$ state of the clamshell structure sits at relatively higher energy, 6611 cm^{-1} above the $^1A_1$ ground electronic state of the ion.

Compared to the $^2B_1$ state of the Sc-bp clamshell complex, the phenyl rings in La-bp are slightly less bent. The phenyl rings are predicted to bend by about 40 ^{o} upon La coordination versus ~ 52 ^{o} in Sc coordination. The slightly smaller bending angle of the phenyl rings in La-bp is the result of a relatively larger metal atom since the atomic radii of sixth row elements are generally larger than those of fourth row elements. In fact, the La-C bond lengths in the $^2B_1$ state of the La-bp clamshell structure are 2.472 to 2.962 Å compared to 2.143 to 2.531 Å in the scandium complex. As anticipated, many of the structural differences between the free ligand and the La-bp clamshell complex are similar to that in Sc coordination. For example, no π electron localization on the phenyl rings is predicted, and the La atom has twelve-fold bonding, sixfold on each phenyl ring. In

Table 8.4. Point groups; electronic states; and predicted relative electronic energies (ΔE, cm^{-1}), bond lengths (R, Å), simple, dihedral, and torsion angles (∠, δ, and τ, degrees) for clamshell and half-sandwich structures of La^+/ La-biphenyl and the free biphenyl ligand from B3P86/6-311+G(d,p) calculations. See Figure 8.1 for numeric labels.

	La-biphenyl				La^+-biphenyl				biphenyl
Point Group	clamshell C_{2v}		half-sandwich C_1		clamshell C_{2v}		half-sandwich C_1		twisted D_2
Electronic State	$^2B_1$	$^4B_1$	^2A	^4A	$^1A_1$	$^3B_1$	^1A	^3A	^1A
ΔE [a]	0	8709	837	2248	40673	47284	44249	44333	
R[La^+/La-C_1]	2.472	2.595	2.444	2.765	2.490	2.547	2.756	2.689	
R[La^+/La-C_2]	2.749	2.894	2.659	2.750	2.804	2.797	2.703	2.703	
R[La^+/La-C_3]	2.962	3.291	2.792	2.766	2.961	3.141	2.548	2.730	
R[La^+/La-C_4]	2.958	3.430	2.762	2.772	2.893	3.245	2.751	2.734	
R[La^+/La-C_5]	2.962	3.291	2.793	2.770	2.961	3.141	2.731	2.734	
R[La^+/La-C_6]	2.749	2.894	2.667	2.748	2.804	2.797	2.546	2.694	
R[C_1-C_2]	1.460	1.431	1.468	1.426	1.458	1.430	1.388	1.426	1.399
R[C_2-C_3]	1.397	1.399	1.397	1.411	1.383	1.404	1.457	1.412	1.389
R[C_3-C_4]	1.414	1.401	1.421	1.413	1.417	1.401	1.438	1.414	1.390
R[C_4-C_5]	1.414	1.401	1.423	1.412	1.417	1.401	1.378	1.413	1.390
R[C_5-C_6]	1.397	1.399	1.397	1.411	1.383	1.404	1.453	1.412	1.389
R[C_6-C_1]	1.460	1.431	1.467	1.427	1.458	1.430	1.451	1.427	1.399
R[C_1-$C_{1'}$]	1.434	1.464	1.442	1.469	1.431	1.478	1.475	1.473	1.478
R[$C_{1'}$-$C_{2'}$]	1.460	1.431	1.435	1.405	1.458	1.430	1.401	1.404	1.399
R[$C_{2'}$-$C_{3'}$]	1.397	1.399	1.396	1.386	1.383	1.404	1.386	1.388	1.389
R[$C_{3'}$-$C_{4'}$]	1.414	1.401	1.395	1.393	1.417	1.401	1.391	1.390	1.390
R[$C_{4'}$-$C_{5'}$]	1.414	1.401	1.396	1.390	1.417	1.401	1.390	1.391	1.390
R[$C_{5'}$-$C_{6'}$]	1.397	1.399	1.394	1.388	1.383	1.404	1.388	1.387	1.389
R[$C_{6'}$-$C_{1'}$]	1.460	1.431	1.434	1.403	1.458	1.430	1.400	1.402	1.399
∠[C_4-C_1-$C_{1'}$]	140.2	151.4	142.3	178.4	139.0	146.8	172.6	176.2	180.0
δ [b]	165.3	172.8	166.4	179.9	160.0	173.0	158.5	179.1	180.0
τ [c]	0.0	0.0	6.3	26.2	0.0	0.0	30.2	26.1	40.2

[a] ΔE is the relative electronic energy difference from the clamshell $^2B_1$ electronic state. [b] The δ[C_6-C_1-C_4-C_3] dihedral angle is reported for the clamshell configurations, and the δ[C_1-C_6-C_3-C_4] dihedral angle is reported for the half-sandwich configurations. [c] Defined as the [C_2-C_1-$C_{1'}$-$C_{2'}$] torsion angle.

addition, the bridging C_1-$C_{1'}$ bond shrinks by 0.044 Å, the La-C_1 and -$C_{1'}$ distances are shorter (2.472 Å) than other La-C bonds, and the phenyl rings pucker by ~ 15 ^{o} in La atom coordination. Although the bending angle of the two phenyl rings is rather different from Sc- to La-bp, the absolute average differences in C-C bond lengths are only 0.002 Å between these two $^2B_1$ states.

Ionization of the $^2B_1$ state of the La-bp clamshell structure generates the $^1A_1$ ion state, just like in the case of Sc-bp. Upon ionization of the $^2B_1$ state of La-bp, the phenyl rings become less puckered by approximately 5 ^{o} and less bent by 2 ^{o}. Consequently, most of the La^+-C distances are actually longer than those of the neutral complex. Also, the C_2-C_3 bond and its C_{2v} symmetry counterparts shrink by 0.014 Å. However, the La^+ ion still seems to be coordinated to an (η^6:η^6-bp) ligand, because the La^+-C distances are evenly distributed like those in the $^2B_1$ ground electronic state of the neutral complex.

The ^2A state of the half-sandwich structure is predicted to lie only 837 cm^{-1} above the $^2B_1$ ground electronic state of the clamshell structure. Upon La coordination to form this half-sandwich structure, the phenyl rings become almost coplanar with a torsion angle of only 6 ^{o}. In addition, this structure has very similar characteristics to a clamshell configuration. One of the phenyl rings bends by a large amount (38 ^{o}), while the other is only slightly bent (13 ^{o}). In this configuration, the La atom seems to have seven-fold bonding: six carbon atoms of one phenyl ring and the junction carbon atom on the other phenyl ring. Hence, this doublet state of the La-bp half-sandwich structure lies at much lower energy compared to that in the Sc-bp system.

Ionization of this ^2A electronic state yields the ^1A electronic state of the La^+-bp half-sandwich structure. This singlet state has large structural differences from the doublet state. The phenyl torsion angle increases by 24 ^{o} and the metal coordinated phenyl ring bends back by 30 ^{o}. In addition, the La-C_1 bond elongates by 0.312 Å while the others shrink. Such a large structural change should produce extremely long vibrational progressions according to the FC principle. Thus, the observed spectral profile from our ZEKE measurements should indicate which type of structure the La-bp complex adopts.

8.3.2.2 Spectroscopy

The experimental ZEKE spectrum of La-bp recorded in a 1:1 mixture of helium and argon carrier gases is presented in Figure 8.5(a). The first strong band at 36516 cm^{-1} corresponds to the (0-0) transition between the ground electronic states of the neutral and ionized complexes. The energy of the 0-0 peak corresponds to the first onset of the PIE spectrum as indicated in the inset (green trace) of Figure 8.5(a). On the higher energy side of the 0-0 band are two vibrational intervals of 257 and 370 cm^{-1} and three vibrational intervals of 532, 862, and 983 cm^{-1}. A fivefold vertical expansion (green trace) shows some small peaks more clearly in another inset of Figure 8.5(a). All the peaks in this spectrum can be assigned to combinations of these bands except the large brown peak marked by a brown asterisk and the small peak labeled with *La*. The linewidth of the small peak (*La*) is much narrower than others, and its intensity strongly depends on the power of the excitation laser. This peak is assigned to an atomic transition of La, and its ion resonates in the mass spectrum at 36720 cm^{-1}. The brown asterisked peak has an approximately 35 % narrower linewidth (3.5 cm^{-1}) than the other peaks in the spectrum, and its line shape is slightly different from the other peaks. These line shape and size comparisons are made by shifting the brown "*" peak to the blue "#" peak and scaling to the same intensity as shown in the "*/#" inset of Figure 8.5(a). Thus, this brown asterisked peak does not belong to the same spectral carrier as all the other peaks in the spectrum. Besides the atomic transition and this asterisked featured, the entire spectrum is attributed to one isomer of the La-bp complex.

To determine the molecular structure, electronic states, and the nature of the vibrational modes, the La-bp ZEKE spectrum was compared to that of the scandium complex. Since both the Sc- and La-bp ZEKE spectra have similar vibrational intervals and spectral profiles, the La-bp ZEKE spectrum is assigned to the $^1A_1 \leftarrow {}^2B_1$ transition of the clamshell structure as well. The assignment of the same electronic transition for both group 3 M-bp complexes is not surprising as this trend was also observed in the group 6 M-bz_2 sandwich complexes (Chapter 5). In the Sc- and La-bp ZEKE spectra, the ligand-based frequencies should be of comparable magnitude. Thus, the 164 and 370 cm^{-1} vibrational modes are assigned to ν_{18}^+ and ν_{16}^+, which were measured to be 190 and 379

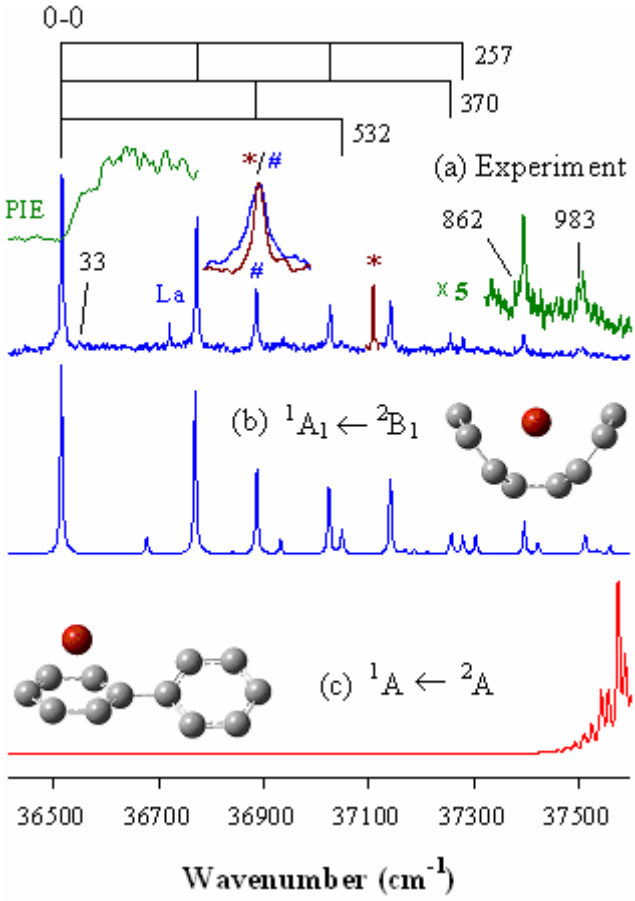

Figure 8.5. The experimental ZEKE spectrum (a) and simulations [40 K] of the clamshell (b) and half-sandwich (c) isomers of La-bp.

cm^{-1} in the scandium complex. The metal-ligand vibrational frequencies are also expected to be of similar magnitude in both group 3 metal complexes, because these modes also contain C-C out-of-plane bends. Thus, the 257 and 532 cm^{-1} vibrational frequencies were assigned to La^{+}-bp stretches, which are of comparable magnitude to those in Sc-bp: 337 and 567 cm^{-1}. The relatively lower metal-based frequencies in the La-bp complex are attributed to the heavier mass of the lanthanum element. The small peak at 33 cm^{-1} above the origin band is assigned to a sequence band of the La rock mode that was also observed in the Sc-bp ZEKE spectrum at 36 cm^{-1} above the origin band. To assign the 862 and 983 cm^{-1} vibrational intervals, frequencies of the free bp ligand were considered. However, several vibrational modes of the free ligand in the a_1 representation (i.e. 735, 740, 902, 964, and 1003 cm^{-1}) could be assigned to these two observed intervals of the La-bp ZEKE spectrum. Since the assignment of these two modes is not straightforward, further spectral analysis considers the calculated Sc-bp frequencies and spectral simulations.

8.3.2.3 Experimental and Theoretical Comparison

The spectral simulations of the doublet to singlet transition of the clamshell and half-sandwich structures are presented in Figure 8.5(b) and (c), respectively. As expected, the simulated $^1A \leftarrow {}^2A$ transition from the half-sandwich structure has extremely long vibrational progressions and does not match the experimental spectrum at all. The long vibrational progression in this simulation arises from the large structural differences between the neutral and ionized half-sandwich structures of La-bp. Simulation from the clamshell configuration, on the other hand, matches the experimental spectrum exceptionally well. The measured and calculated FC profiles are a close match, and each of the observed peaks are simulated except for the brown asterisked peak and the La atomic line. This comparison shows clearly that the observed spectrum originates from the $^1A_1 \leftarrow {}^2B_1$ transition of the clamshell structure of La-bp.

Based on the good agreement between experiment and theory, the nature of the observed vibrational modes is determined. These modes are described in Table 8.3,

which also compares their measured and calculated frequencies. Those assignments made by comparing the Sc- and La-bp ZEKE spectra are the same when comparing the measured and calculated La-bp ZEKE spectra. The 257 cm^{-1} progression is assigned to excitations of the La^+-bp stretch, characterized largely by the La^+ displacement (ν_{17}^+). The 370 and 532 cm^{-1} intervals are excitations of two symmetric ring out-of-plane deformations (ν_{16}^+ and ν_{15}^+). The ν_{15}^+ mode also has an associated La^+ displacement with this ring deformation. Although the fundamental of the ν_{18}^+ mode is not clearly observed in the La-bp spectrum, its combination with ν_{17}^+ is seen at 36937 cm^{-1}. This feature is very weak, which may indicate that the corresponding fundamental ν_{18}^+ frequency is buried under the noise. Nevertheless, the ν_{18}^+ mode is derived to be 164 cm^{-1} based on the peak position of the $18_0^1 17_0^1$ band, which agrees with the calculated frequency of 162 cm^{-1}. Some small peaks at 37378 and 37499 cm^{-1} that were not simulated are assigned to the fundamental of two totally symmetric vibrations, ν_{10}^+ and ν_{11}^+. The ν_{10}^+ mode (983 cm^{-1}) is a phenyl ring distortion, and the ν_{11}^+ mode (862 cm^{-1}) is a C-C out-of-plane bend. In addition, a small band about 33 cm^{-1} on the higher energy side of the band origin is a sequence transition of ν_{46}. This nontotally symmetric vibration is associated with a La rock motion.

Table 8.3 also compares the measured and calculated IEs, which are corrected by the 10 % IE overestimation of the B3P86 method. Again the corrected IEs match the measured values much better. The overall good agreement between experiment and theory further supports our identification of this fascinating clamshell binding mode of biphenyl. Apparently, this clamshell binding scheme is not very sensitive to the size of the metal atom since both Sc (radius ~ 1.60 Å)[306] and La (radius ~ 1.95 Å)[306] formed bp clamshell structures. Further insight into this clamshell conformation is obtained by studying different polyphenyls, i.e. phnp.

8.3.3 Sc-phnp

The phnp ligand is a special molecule in that it contains the components of all the ligands studied in this dissertation: benzene, naphthalene, and biphenyl. The phenyl group closely resembles a benzene ring, which is connected by a bridging C-C bond to a naphthyl group. The interaction between this ligand and a scandium atom should provide answers as to which binding mode is the most favorable. Will Sc bind to the phenyl ring like in Sc-bz? Or, will Sc bind to one of the naphthyl rings like in Sc-np? Perhaps Sc will bind to two π-rings simultaneously like in the clamshell structure of Sc-bp.

8.3.3.1 Theoretical Isomers

For 1-phenylnaphthalene, the torsion angle between the two aryl systems ($-C_6H_5$ and $-C_{10}H_7$) has been recorded in the condensed phase as 50 ^{o} by measuring the Kerr constant (a proportionality constant used to describe the change in the index of refraction of a material in response to an electric field)[307] or 66 ^{o} from the magnetic anisotropy.[308] Although the torsion angle has not been measured experimentally in the gas phase, a number of theoreticians predict this angle to fall in the range of 59 to 67 ^{o}.[309-316] Our B3P86 calculations predict a torsion angle at the lower limit of this range, 59 ^{o}. For metal complexation, three different rotational isomers of the phnp ligand were considered with torsion angles of 0, 45, and 90 degrees just like in Sc-bp. However, these geometry optimizations only resulted in four different structures: the half-sandwich I, II, and III structures and the clamshell structure. The molecular structures of these four Sc-phnp isomers are shown in Figure 8.1(c) – (f). The calculated bond lengths, angles, and torsion angles of the free phnp ligand and the scandium complexes are summarized in Table 8.5. A comparison of the electronic energies among the four isomerically different metal complexes is also listed in this table.

The neutral and cation clamshell structures are calculated to be lower in energy than the corresponding half-sandwich structures by more than 2700 cm^{-1}. In the neutral Sc-phnp complex, the ground electronic state is the ^{2}A state of the clamshell structure. A

Table 8.5. Predicted relative electronic energies (ΔE, cm^{-1}), bond lengths (R, Å),[a] simple, dihedral, and torsion angles (∠, δ, and τ, degrees) for clamshell and half-sandwich structures of Sc^+/ Sc-phnp and the free phnp ligand from B3P86/6-311+G(d,p) calculations. See Figure 8.1 for numeric labels.

	Sc-phnp							Sc^+-phnp		phnp
	Clam-shell[b]	Half-sandwich I		Half-sandwich II		Half-sandwich III		Clam-shell	Half-sandwich III	Twisted
State	^2A	^2A	^4A	^2A	^4A	^2A	^4A	^1A	^1A	^1A
ΔE [c]	0	4578	4810	3082	5756	2793	5613	42042	46528	
R[Sc-C_n]	2.150 2.196	2.444	2.423	2.236	2.419	2.523	2.470	2.154 2.166	2.364	
R[Sc-C_{n+1}]	2.378 2.428	2.360	2.391	2.412	2.390	2.543	2.488	2.475 2.418	2.382	
R[Sc-C_{n+2}]	2.510 2.507	2.229	2.399	2.414	2.400	2.224	2.402	2.557 2.508	2.161	
R[Sc-C_{n+3}]	2.492 2.429	2.440	2.404	2.225	2.405	2.413	2.392	2.454 2.385	2.346	
R[Sc-C_{n+4}]	2.529 2.668	2.373	2.397	2.516	2.477	2.423	2.401	2.566 2.586	2.358	
R[Sc-C_{n+5}]	2.412 2.646	2.207	2.396	2.531	2.500	2.227	2.406	2.458 2.582	2.169	
R[C_1-C_2]	1.457	1.386	1.424	1.402	1.401	1.399	1.399	1.458	1.398	1.399
R[C_2-C_3]	1.404	1.464	1.413	1.387	1.388	1.389	1.389	1.381	1.389	1.389
R[C_3-C_4]	1.411	1.436	1.413	1.392	1.391	1.391	1.391	1.422	1.390	1.391
R[C_4-C_5]	1.416	1.376	1.413	1.389	1.390	1.390	1.390	1.418	1.391	1.390
R[C_5-C_6]	1.400	1.467	1.413	1.391	1.389	1.390	1.390	1.380	1.389	1.390
R[C_6-C_1]	1.457	1.452	1.423	1.400	1.400	1.397	1.398	1.464	1.399	1.398
R[C_1-C_7]	1.432	1.477	1.479	1.482	1.479	1.482	1.482	1.429	1.480	1.483
R[C_7-C_8]	1.467	1.382	1.382	1.452	1.417	1.392	1.380	1.460	1.390	1.379
R[C_8-C_9]	1.390	1.406	1.405	1.374	1.411	1.393	1.409	1.389	1.396	1.408
R[C_9-C_{10}]	1.415	1.369	1.370	1.439	1.403	1.382	1.371	1.408	1.379	1.369
R[C_{10}-C_{11}]	1.446	1.415	1.414	1.467	1.430	1.403	1.417	1.449	1.407	1.414
R[C_{11}-C_{12}]	1.432	1.429	1.430	1.427	1.447	1.427	1.447	1.426	1.431	1.429
R[C_{12}-C_7]	1.471	1.432	1.433	1.484	1.447	1.417	1.434	1.472	1.423	1.430
R[C_{12}-C_{13}]	1.406	1.417	1.417	1.405	1.421	1.469	1.433	1.405	1.472	1.417
R[C_{13}-C_{14}]	1.381	1.372	1.372	1.384	1.372	1.445	1.407	1.379	1.440	1.372
R[C_{14}-C_{15}]	1.402	1.409	1.409	1.395	1.411	1.374	1.413	1.403	1.384	1.409
R[C_{15}-C_{16}]	1.380	1.370	1.370	1.382	1.371	1.441	1.405	1.377	1.436	1.370
R[C_{16}-C_{11}]	1.411	1.415	1.416	1.404	1.420	1.469	1.432	1.412	1.472	1.416
∠ [d]	130.2 125.5	176.2	179.1	179.3	178.1	178.1	178.2	128.5 126.0	178.2	178.0
δ [e]	164.8 151.8	153.4	179.3	152.6	177.0	152.2	177.0	155.9 151.3	158.7	179.4 ± 0.5
τ [f]	9.3	53.6	52.1	61.7	52.7	126.1	125.0	5.0	127.9	40.2

[a] For clamshell, n = 1 (top) and n = 7 (bottom); for half-sandwich I, n = 1; for half-sandwich II, n = 7; and for half-sandwich III, n = 11. [b] Calculations of the quartet state starting from the clamshell configuration converged to the half-sandwich I structure. [c] ΔE is the relative electronic energy difference from the clamshell ^2A electronic state. [d] The [C_4-C_1-C_7] angle; for the clamshell configuration, the [C_1-C_7-C_{10}] angle is also listed (bottom). [e] For clamshell, δ = [C_2-C_1-C_4-C_5] (top) and [C_8-C_7-C_{10}-C_{11}] (bottom); for half-sandwich I, δ = [C_4-C_3-C_6-C_1]; for half-sandwich II, δ = [C_8-C_7-C_{10}-C_{11}]; and for half-sandwich III, δ = [C_{12}-C_{13}-C_{16}-C_{15}]. For the free phnp ligand, the average and standard deviation of these four dihedral angles are presented. [f] The [C_2-C_1-C_7-C_{12}] torsion angle.

quartet state of the clamshell configuration could not be located in our theoretical survey; these calculations converged back to either the half-sandwich I or II structure. For each half-sandwich structure, the doublet was predicted to be lower in energy than that of the quartet state. The lowest-lying excited state corresponds to the ^{2}A state of the half-sandwich III structure at 2793 cm^{-1} above the doublet state of the clamshell structure. The corresponding quartet state is predicted to lie 5613 cm^{-1} above the clamshell doublet state. The doublet states of the half-sandwich I and II structures are 4578 and 3082 cm^{-1} higher in energy than the clamshell doublet state. The quartet states of half-sandwich I and II are predicted to be 232 and 2674 cm^{-1} above their doublet states, respectively. Ionization of the lowest energy clamshell and half-sandwich structures of Sc-phnp produce singlet states of the ionic complex. The IEs of the clamshell and half-sandwich III structures are predicted to be 42042 and 43735 cm^{-1}, respectively, with neither zero point energy corrections nor the 10 % B3P86 IE overestimation. The energy difference between these two singlet states of the ion complex is predicted to be 4486 cm^{-1}.

The clamshell and half-sandwich Sc-phnp complexes are predicted to have similar hapticities to those of Sc-bz, -np, and -bp. The clamshell complexes have twelve-fold (η^6:η^6) bonding, and the half-sandwich complexes have either two- or sixfold bonding. The high-spin states of the half-sandwich structures have sixfold bonding, whereas the low-spin states have twofold bonding just like in Sc-bz and -np. The Sc-C distances in the clamshell structure of Sc-phnp are predicted to be about the same as those in Sc-bp. The Sc-C_1 and -C_7 bond lengths (2.150 and 2.196 Å) are significantly shorter than others (2.378 to 2.668 Å). In the half-sandwich structures, the Sc^+/Sc-C are more evenly distributed in the high-spin states compared to those in the low-spin states. For all the calculated Sc-phnp structures, significant changes in the C-C bond lengths from the free ligand are observed only in the ring(s) coordinated to the scandium atom. In general, these C-C distances increase upon metal coordination, because both ligand to metal and metal to ligand charge transfer disturbs and weakens the local conjugated π-system. For all the half-sandwich structures, the bridging C_1-C_7 bond is not significantly altered upon metal coordination, whereas this bond shrinks by 0.051 Å in the clamshell structure. For the doublet states of the half-sandwich structures some C-C bonds in the π-ring are also shorter than those in the free phnp ligand. In addition, the π-rings coordinated to the

metal atom become puckered in these doublet states. This π electron localization and ring puckering is consistent with an η^2-phnp ligand.

Since we synthesize these metal complexes in a supersonic molecular beam, any higher energy isomers that may form during the laser ablation process will likely either dissociate or interconvert to a lower energy structure upon expansion into vacuum. Thus, we may only consider ionization of the clamshell and half-sandwich III structures which are relatively low in electronic energy. Upon ionization of the clamshell structure, half of the Sc-C distances shrink while the other half is elongated. The shorter Sc^+-C distances in the ion is consistent with the smaller atomic radius of the ion and an electrostatic pull from the quadrupole moment of the phnp ligand. The other half of longer Sc^+-C distances seem to arise from perturbations of the carbon-carbon framework as found in the case of Sc- and La-bp. The Sc-bound π-rings are slightly more bent and more puckered in the ion. Moreover, the phenyl-naphthyl torsion angle decreases an additional 4 ^{o} upon ionization. With such large differences in the carbon-carbon framework, trends in the Sc-C distances are difficult to assess just like in the naphthalene complexes as discussed in Chapters 6 and 7.

Ionization of the doublet state of the half-sandwich III structure produces a singlet state. The Sc-C bonds shrink on average by 0.096 Å in this process. The much shorter Sc^+-C distances in the ion is consistent with the reduced ionic radius and the electrostatic pull from the quadrupole moment of the ligand. Unlike the clamshell structure, the carbon-carbon framework of the ligand remains nearly unchanged upon ionization. The largest C-C bond length difference is only 0.006 Å (C_{12}-C_7). The torsion angle rotates by only 2 ^{o}, and the bonding π ring puckers ~ 6 ^{o}. Although the carbon-carbon framework does not significantly change, a long metal-ligand stretch vibration is expected since the Sc-C distances of the half-sandwich structure are severely reduced upon ionization.

8.3.3.2 Spectroscopy

The experimental Sc-phnp ZEKE spectrum [Figure 8.6(a)] has a strong 0-0 transition located at 37594 cm^{-1} with a FWHM of ~ 5 cm^{-1}. The energy of the 0-0 peak

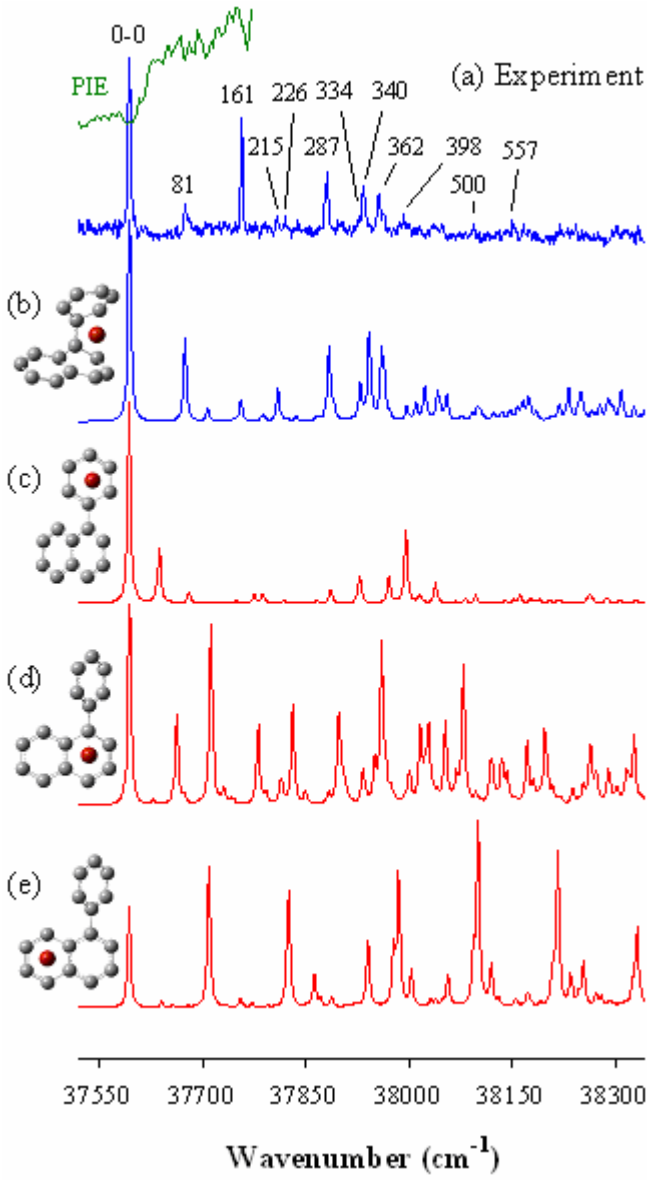

Figure 8.6. The experimental ZEKE spectrum (a) and simulations [20 K] of the $^{1}A \leftarrow {}^{2}A$ transition for four isomeric structures of Sc-phnp (b) – (e).

corresponds to the first onset of the PIE spectrum as indicated in the inset (green trace) of Figure 8.6(a). To the blue of the origin band are a number of vibrational intervals (81, 162, 214, 226, 287, 334, 340, 362, 398, 500, and 557 cm^{-1}) that correspond to various normal modes of the ionic complex. The third peak, which is located at 37756 cm^{-1} in the spectrum, may be the second quantum of the 81 cm^{-1} vibrational interval, the first quantum of a 161 cm^{-1} vibrational interval, or both. However, this peak has an unusually large intensity, because the second quantum excitation of the 161 cm^{-1} mode is not observed. Thus, this assignment is only considered tentative. All the other peaks in this spectrum can be assigned to combinations of these 11 vibrational intervals. These peak positions and assignments are listed in Table 8.2.

To propose which Sc-phnp structure is produced in our molecular beam and to assign the vibrational modes, the experimental spectrum is compared to those of the previously studied Sc-bz, -np, and -bp molecules. Presumably, a half-sandwich I structure should generate a spectral profile similar to that of Sc-bz, half-sandwich II or III structures should generate a spectral profile similar to that of Sc-np, and a clamshell structure should generate a spectral profile similar to that of Sc-bp.

For Sc-bz, only one mode was optically active in the ion, the metal-ligand stretch (375 cm^{-1}). One interval in the Sc-phnp spectrum (362 cm^{-1}) is comparable to this frequency. However, the Sc-phnp ZEKE spectrum shows only one-quantum excitation of this mode as opposed to three-quantum excitation, as was the case for Sc-bz. Additionally, the observed spectral profiles of Sc-bz and -phnp are rather different, which indicates that the half-sandwich I structure may not be responsible for the observed ZEKE spectrum. The fact that the half-sandwich I structure may not be the spectral carrier is consistent with stronger bonding in M-np complexes compared to M-bz complexes due to the more polarizable np ligand.[269, 272] Indeed, the doublet state of the half-sandwich I structure sits at a relatively higher electronic energy than those of the half-sandwich II or III structures.

The Sc-np ZEKE spectrum is found to have a similar spectral profile to Sc-phnp. Four different modes in the Sc-np ZEKE spectrum were optically active (112, 298, 347, and 389 cm^{-1}) which had similar frequencies to Sc-phnp (81, 287, 340, and 362 cm^{-1}). However, the ionization energy of Sc-phnp is red shifted by more than 3500 cm^{-1} with

respect to Sc-bz and -np. This relatively large IE shift suggests that the binding scheme of Sc-phnp adopts the clamshell mode like Sc-bp; the IE of Sc-bp (39114 cm^{-1}) was also significantly red shifted with respect to those of Sc-bz (41600 cm^{-1}) and -np (41193 cm^{-1}). Moreover, some of the measured frequencies of Sc-bp (337, 379, and 567 cm^{-1}) are also very similar to those measured in the Sc-phnp ZEKE spectrum (340, 362, and 557 cm^{-1}). Spectral differences between these two scandium complexes may arise from the different symmetry of the phnp complex (C_1) compared to the bp complex (C_{2v}). Consequently, further spectral analysis considers the comparison of the experimental and simulated spectra.

8.3.3.3 Experimental and Theoretical Comparison

Simulations of the $^1A \leftarrow {}^2A$ transition from each of the four isomeric structures of Sc-phnp are compared to the experimental ZEKE spectrum in Figure 8.5(a) – (e). The calculated spectral profiles from the higher energy half-sandwich structures do not match the experimental spectrum nearly as well as the lowest energy clamshell structure. The major discrepancy between the measured and calculated (clamshell) profile is the band at 37756 cm^{-1}. However, the observed intensity of this feature is abnormal based on the FC principle as discussed earlier in the previous section.

Despite this discrepancy, the simulated and experimental spectra are in rather good agreement with one another. Like Sc- and La-bp, the Sc-phnp complex also adopts a clamshell structure, and the first ionization energy corresponds to the doublet to singlet transition. From the good agreement between experiment and theory, the vibrational modes are determined. The details of each vibrational mode are described in Table 8.3. The phenyl-naphthyl torsion mode (ν_{81}^{+}) is measured to be 81 cm^{-1}. Four modes (ν_{79}^{+} = 161 cm^{-1}, ν_{75}^{+} = 287 cm^{-1}, ν_{70}^{+} = 398 cm^{-1}, and ν_{67}^{+} = 500 cm^{-1}) are ligand-based C-C-C bending modes localized mainly on the naphthyl group. On the other hand, the 226, 362, and 557 cm^{-1} intervals are assigned to ν_{76}^{+}, ν_{71}^{+}, and ν_{65}^{+} respectively, ligand-based C-C-C bending modes involving both the naphthyl and phenyl rings. A metal-ligand stretching mode (ν_{72}^{+} = 340 cm^{-1}) and rocking mode (ν_{73}^{+} = 334 cm^{-1}) are identified in the

spectrum, which also has C-C-C bending components. Similar to the phenyl ring bending modes in Sc- and La-bp, the ν_{77}^{+} mode (215 cm^{-1}) of Sc-phnp is characterized by a phenyl and naphthyl ring bending motion.

Additional structural evidence for the Sc-phnp clamshell structure involves a comparison of the measured frequencies of Sc-phnp to that of Sc-np, -bz, and -bp. Compared to the Sc^{+}-bz and -np complexes, the Sc^{+}-phnp stretch frequency is red shifted by 33 and 49 cm^{-1}, respectively. On the other hand, the Sc^{+}-bp and -phnp stretch frequencies were measured to be nearly the same, 337 and 340 cm^{-1}, respectively. Thus, the clamshell structure of Sc-phnp is more sensible than a half-sandwich I, II, or III structures based on the measured metal-ligand stretch mode. Likewise, a comparison of ligand-based modes in Sc-np, -bp, and -phnp follows a similar trend. For example, the analogous ν_{77}^{+} mode of Sc-phnp is blue shifted by 103 cm^{-1} in Sc-np and only 25 cm^{-1} in Sc-bp. The much closer ligand-based Sc-phnp vibrational frequency to that of Sc-bp is consistent with the clamshell-shaped ligands in both of these complexes. Furthermore, the analogous ν_{71}^{+} and ν_{16}^{+} ligand-based modes of Sc-phnp and -bp, respectively, are within 17 cm^{-1} of each other, while this mode is not observed in the Sc-np complex. Other Sc-phnp ligand-based modes that were observed in Sc-np were shifted by a considerable amount (by 72 and 41 cm^{-1} for ν_{76}^{+} and ν_{65}^{+}, respectively), because these modes contain C-C out-of-plane bending components on the naphthyl *and phenyl* rings. Therefore, in addition to the good agreement between experiment and theory, the observed clamshell structure of Sc-phnp is consistent with the measured frequencies among the Sc-bz, -np, -bp, and -phnp complexes.

8.4 Conclusion

A new binding mode for polyphenyl ligands is discovered through ZEKE spectroscopy and DFT calculations on its metal complexes. The Sc- and La-bp and Sc-phnp systems adopt a clamshell structure, which is stabilized through a π–d–π interaction. The ionization energies of these polyphenyl complexes are red shifted a considerable amount (2000 ~ 3500 cm^{-1}) compared to half-sandwich scandium-aromatic compounds

measured by our group.[171, 305] These polyphenyl complexes are determined to have low-spin doublet and singlet ground electronic states. The discovery of this new binding mode opens the doorway for many other experiments. Will significantly different M-bp structures form for later transition metals like in the bz complexes? The following chapter provides a first step in answering this question as we begin our march across the row: the interaction between Ti ($3d^2 4s^2$) and bp.

CHAPTER 9: ZEKE SPECTROSCOPY AND DENSITY FUNCTIONAL THEORY CALCULATIONS OF THE TITANIUM-BIPHENYL CLAMSHELL COMPLEX

9.1 Introduction

In the previous chapter, a new binding mode was discovered for the simple organic ligand biphenyl ($C_{12}H_{10}$, bp) coordinated to the group 3 Sc and La metal elements. In this coordination process, the twisted angle between the two phenyl rings diminishes, and the π-rings act like a clamp to bind to the metal atom with both phenyl rings. In this clamshell configuration [Figure 9.1(a)], the M-bp complex has similar structural characteristics to that of the metal bis(benzene) sandwich complexes. Since the coordination of Sc and Ti to benzene was similar, it is expected that the Ti-bp complex will adopt the clamshell configuration as well. In this chapter, the first spectroscopic investigation of the Ti-bp complex is reported, and the ZEKE spectrum is compared to simulations from DFT calculations to determine the electronic states and corresponding molecular structures.

9.2 Experimental and Computational Methods

Details of our ZEKE spectrometer were discussed in Chapter 2. Ti-bp complexes were produced by reactions of gaseous titanium atoms with biphenyl (99 % $C_{12}H_{10}$, Aldrich) in a supersonic jet. The titanium atoms were produced by pulsed laser vaporization of a titanium rod (99.7 % Ti, Aldrich) with the second harmonic output of a Nd:YAG laser (Lumonics, YM-800, 532 nm, ~ 1 mJ). The titanium atoms were carried by helium gas (UHP, Scott-Gross) which were delivered by a home-made piezoelectric pulsed valve at a stagnation pressure of ~ 50 psi. At room temperature, naphthalene vapor was introduced through a stainless steel tube to a small reaction chamber (~ 1.5 mL), a few centimeters downstream from the ablation region, where the ligand interacted with the titanium atoms entrained in the carrier gas.

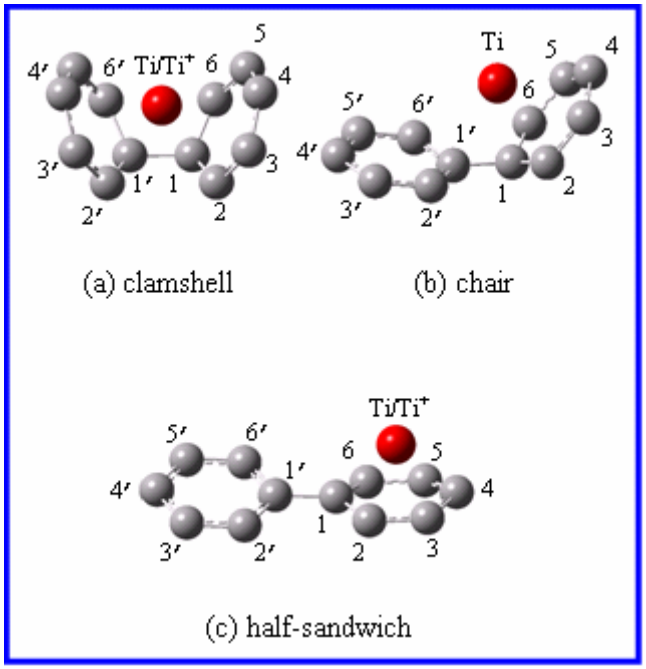

Figure 9.1. The clamshell (a), chair (b), and half-sandwich (c) structures of Ti-bp. Titanium atoms are red, carbon atoms are grey, and hydrogen atoms are omitted for clarity.

Molecular masses were measured by photoionization time-of-flight mass spectrometry. Ionization thresholds of the biphenyl complexes were located using PIE spectroscopy by recording the mass-selected ion signal as a function of ionization laser wavelength. Prior to ZEKE experiments, the production of the target complex was maximized by adjusting the timing and power of the vaporization and ionization lasers, backing pressure of the carrier gas, and amount of ligand vapor allowed to enter the reaction chamber. ZEKE electrons were produced by photoexcitation of neutral molecules to high-lying Rydberg states, followed by delayed (~ 3.5 μs) pulsed electric field ionization (1.2 V/cm, 100 ns) of these Rydberg states. The photoionization and photoexcitation light was generated by the doubled-frequency output of a dye laser (Lumonics, HD-500) pumped by the third harmonic of a Nd:YAG laser (Continuum, Surelite-II, 355 nm). The pulsed electric field was provided by a delay pulse generator (Stanford Research Systems DG535). The ion and electron signals were detected by a dual microchannel plate detector (Burle), amplified by a preamplifier (Stanford Research Systems SR445), averaged by a gated integrator (Stanford Research Systems SR250), and stored in a laboratory computer. Laser wavelengths were calibrated against titanium atomic transitions.[169] A field-dependent study was not performed, because the anticipated field induced IE shift (1 ~ 2 cm^{-1}) is smaller than the measured linewidth of the peaks in our experiment.[278]

Geometry optimization and vibrational analyses were carried out with the GAUSSIAN03 program package[74] on the University of Kentucky HP Superdome Cluster. In these calculations, the B3P86 density functional theory (DFT) method was employed, and all atoms were treated with the 6-311+G(d,p) basis set. Calculations were performed, where appropriate, with (C_{2v}) and without (C_1) symmetry constraints. Geometry optimizations of the metal complex yielded three different structures: clamshell, chair, and half-sandwich structures (Figure 9.1). For each geometry, vibrational frequencies were calculated within the harmonic approximation to ensure a local minimum energy structure was located on the potential energy surface of the metal complex.

To simulate the ZEKE spectra, multi-dimensional Franck-Condon (FC) factors were calculated from the theoretical equilibrium geometries, harmonic vibrational frequencies, and normal coordinates of the neutral and ionic complexes.[68] The Dusch-

insky effect[45] was considered to account for normal mode differences between the neutral and ion in the FC calculations. Spectral broadening was simulated by giving each line a Lorentzian line shape with experimental linewidth. Hot transitions in the Ti-bp ZEKE spectrum were simulated by assuming a Boltzmann distribution with a vibrational temperature of 250 K. The calculated ionization energies were shifted to the experimental value to allow easier comparison of the measured and calculated FC profiles.

9.3 Results and Discussion

9.3.1 Calculated Electronic States

We have investigated neutral and monocation Ti-bp complexes, in which the metal atom or ion interacts with one or two π-rings as indicated in Figure 9.1. In the previous chapter, the B3P86 method was found to adequately model group 3 metal polyphenyl systems. Hence, the B3P86 method was also used to predict the energetics of this titanium polyphenyl complex. Since Ti and Ti^+ have four and three valence electrons, respectively, only singlet, triplet, and quintet electron spin multiplicities were considered for the neutral species, while doublet and quartet electron spin multiplicities were considered for the ion.

Table 9.1 summarizes the predicted electronic states, point groups, relative electronic energies, and geometries of the Ti^+/Ti-bp complexes from the B3P86 calculations. In our previous investigation of group 3 M-bp complexes, the ground electronic states of the neutral and ion were determined to be the low-spin $^2B_1$ and $^1A_1$ states in the clamshell configuration (Chapter 8). Similarly, our B3P86 calculations predict the low-spin $\tilde{X}\ ^1A_1$ state of the Ti-bp clamshell structure to be the ground electronic state of the neutral complex. In the triplet spin state, the Ti-bp clamshell structure is predicted to be 2536 cm^{-1} higher in energy. Another triplet state was located at a lower energy, only 1570 cm^{-1} above the ground electronic state. In this state, the complex has a chair structure in which the Ti atom is bound to an (η^1:η^6-bp) ligand [Figure 9.1(b)]. In the half-sandwich configuration [Figure 9.1(c)], the triplet and quintet

Table 9.1. Predicted point groups, electronic states, relative electronic energies (ΔE, cm^{-1}), bond lengths (R, Å), and simple, dihedral, and torsion angles (∠, δ, and τ, degrees) for Ti^+/Ti-bp complexes and free bp ligand from the B3P86 calculations. See Figure 9.1 for numeric labeling scheme.

	Ti-bp					Ti^+-bp				bp
Point group	clamshell C_{2v}		chair C_1	half-sandwich C_1		half-sandwich C_1		clamshell C_{2v}		twisted D_2
State	$\tilde{X}\,^1A_1$	$\tilde{C}\,^3B_1$	$\tilde{A}\,^3A$	$\tilde{B}\,^3A$	$\tilde{D}\,^3A$	$\tilde{X}\,^4A$	$\tilde{B}\,^2A$	$\tilde{A}\,^2B_1$	$\tilde{C}\,^2A$[a]	^1A
ΔE[b]	0	2536	1570	1697	2684	45854	49604	46605	53348	
R(Ti^+/Ti-C_1)[c]	2.043	2.074	2.054 2.282	2.142	2.382	2.330	2.289	2.062	2.076	
R(Ti^+/Ti-C_2)	2.252	2.353	2.246	2.239	2.356	2.304	2.285	2.335	2.460	
R(Ti^+/Ti-C_3)	2.372	2.473	2.323	2.241	2.362	2.315	2.300	2.434	3.179	
R(Ti^+/Ti-C_4)	2.348	2.436	2.283	2.154	2.363	2.317	2.281	2.342	3.500	
R(Ti^+/Ti-C_5)	2.372	2.473	2.323	2.251	2.354	2.313	2.298	2.434	3.179	
R(Ti^+/Ti-C_6)	2.252	2.353	2.240	2.230	2.353	2.310	2.294	2.335	2.460	
R(C_1-C_2)	1.456	1.458	1.466	1.454	1.419	1.421	1.428	1.458	1.439	1.399
R(C_2-C_3)	1.412	1.393	1.394	1.395	1.408	1.409	1.404	1.388	1.398	1.389
R(C_3-C_4)	1.411	1.415	1.426	1.444	1.408	1.409	1.414	1.417	1.391	1.390
R(C_4-C_5)	1.411	1.415	1.425	1.440	1.409	1.410	1.416	1.417	1.391	1.390
R(C_5-C_6)	1.412	1.393	1.393	1.394	1.408	1.408	1.403	1.388	1.398	1.389
R(C_6-C_1)	1.456	1.458	1.464	1.459	1.419	1.421	1.427	1.458	1.439	1.399
R(C_1-$C_{1'}$)	1.465	1.447	1.452	1.466	1.475	1.475	1.474	1.445	1.455	1.478
R($C_{1'}$-$C_{2'}$)	1.456	1.458	1.430	1.406	1.399	1.399	1.400	1.458	1.439	1.399
R($C_{2'}$-$C_{3'}$)	1.412	1.393	1.387	1.388	1.389	1.388	1.387	1.388	1.398	1.389
R($C_{3'}$-$C_{4'}$)	1.411	1.415	1.396	1.390	1.390	1.390	1.391	1.417	1.391	1.390
R($C_{4'}$-$C_{5'}$)	1.411	1.415	1.388	1.392	1.391	1.391	1.391	1.417	1.391	1.390
R($C_{5'}$-$C_{6'}$)	1.412	1.393	1.395	1.387	1.388	1.387	1.387	1.388	1.398	1.389
R($C_{6'}$-$C_{1'}$)	1.456	1.458	1.432	1.408	1.400	1.401	1.402	1.458	1.439	1.399
∠(C_4-C_1-$C_{1'}$)	123.4	126.4	131.1	176.1	179.5	179.5	177.7	124.5	157.8	180.0
∠($C_{4'}$-$C_{1'}$-C_1)	123.4	126.4	171.3	178.9	179.6	179.4	179.6	124.5	157.8	180.0
δ[d]	166.7	161.2	164.8	166.6	179.5	179.7	176.9	160.0	176.7	180.0
τ[e]	0.0	0.0	19.2	12.4	36.8	34.5	30.9	0.0	0.0	40.2

[a] This $\tilde{C}\,^2A$ state has C_{2v} symmetry, but the electronic symmetry species could not be identified using the C_{2v} symmetry constraint. [b] The ΔE values are relative to the clamshell $\tilde{X}\,^1A_1$ state. [c] For the chair structure, the Ti-$C_{1'}$ distance is also listed (bottom). [d] The δ[C_6-C_1-C_4-C_3] dihedral angle. [e] The τ[C_2-C_1-$C_{1'}$-$C_{2'}$] torsion angle.

states were predicted to lay 1697 and 2684 cm^{-1} above the $\widetilde{X}\ ^1A_1$ ground electronic state, respectively. In addition to these low-lying electronic states, a singlet state of the chair structure, a singlet state of the half-sandwich structure, and two quintet states of the clamshell structure were predicted to lie at much higher energies: 5231, 5927, 8971, and 16902 cm^{-1}, respectively (not listed in Table 9.1).

Like Sc- and La-bp, the lowest energy structure of Ti-bp corresponds to the clamshell configuration. In this configuration, the titanium atom interacts with both π-rings simultaneously, acting as a link to join the two separate π-systems together. According to the Ti-C and C-C distances, this clamshell structure has 12-fold bonding, sixfold bonding to each phenyl ring. The $\widetilde{X}\ ^1A_1$ state of the neutral Ti-bp clamshell structure has very similar structural characteristics to that of the $^2B_1$ state of the neutral Sc-bp clamshell structure. The average absolute difference in C-C bond lengths is only 0.012 Å for these two different M-bp complexes. The average metal to ligand distance in these two clamshell structures, however, is significantly shorter (by 0.142 Å) in Ti-bp compared to Sc-bp. The much longer Sc-bp distance is consistent with the larger atomic radius of Sc compared to Ti.[317] The shorter Ti-C distances in the Ti-bp clamshell structure are also consistent with the larger bending angles of the phenyl rings, i.e. 180.0 ^{o} – ∠(4-1-1′) and 180.0 ^{o} – ∠(4′-1′-1). In the Ti-bp complex, the phenyl rings are more bent (57 ^{o}) than those in the Sc-bp complex (52 ^{o}), while the phenyl rings are less puckered (13 ^{o} in Ti-bp versus 18 ^{o} in Sc-bp).

In the excited $\widetilde{C}\ ^3B_1$ state of the clamshell structure, the ligand framework remains nearly the same as that in the $\widetilde{X}\ ^1A_1$ state but with a slightly longer Ti-bp distance. In addition, the phenyl rings are less bent by a few degrees. In the triplet state of the chair structure [Figure 9.1(b)], the bending angles of the phenyl rings are rather different from one another, 131 and 171 ^{o}. Compared to the clamshell structure, the triplet state of the chair structure is ~ 966 cm^{-1} lower in energy. The relative energy of these two states, however, is puzzling, because two d-π interactions should be energetically favored over one d-π interaction. The assumption that the chair structure has only one d-π interaction is consistent with the calculated Ti-C distances and C-C bond lengths. Furthermore, the steric repulsion between the ortho hydrogen atoms is

smaller in the clamshell structure; the ortho H-H distances in the triplet states of the clamshell and chair structures are 2.219 and 2.087 Å, respectively. In addition, the twisted angle between the two phenyl rings is still quite large in this chair structure (19 ^{o}), and a majority of the C-C distances on the phenyl ring not significantly involved in metal-ligand bonding are nearly the same as those in the free ligand.

Due to the small energy difference between the triplet states of the clamshell and chair structures, the potential energy surface along the phenyl bending angles may be shallow. A potential energy surface scan along the phenyl bending angles of biphenyl is presented in Figure 9.2. This curve was generated by fixing the C-C bond lengths in the $\widetilde{X}\ ^1A_1$ state of the Ti-bp clamshell structure while scanning both phenyl bending angles simultaneously in 4 ^{o} increments from 120 to 180 ^{o}. Each data point on the surface corresponds to a single point energy calculation at the B3P86/6-311+G(d,p) level of theory. Not only is this potential energy well somewhat shallow, but also the minimum energy structure has slightly bent phenyl rings, ~ 10 ^{o}. Although the optimal phenyl bending angle of the corresponding neutral Ti-bp $\widetilde{X}\ ^1A_1$ state (123 ^{o}) lays about 63 kcal/mol higher in energy, two sets of d–π interactions from the titanium atom will provide substantial electronic energy stabilization. According to this potential energy surface, the clamshell configuration requires that the bond dissociation energy of each Ti-C bond be at least 5.25 kcal/mol (5.25 × 12 = 63 kcal/mol). This clamshell binding mode seems to be thermodynamically feasible since the bond dissociation energy of Ti-CH_3 has been measured to be ~ 40 kcal/mol.[29]

In the half-sandwich structure, the triplet state is predicted to be lower in energy than the quintet state by 987 cm^{-1}. The structural differences between these two states are consistent with this predicted energy sequence. In the triplet state, the bonding phenyl ring is more puckered by ~ 13 ^{o}, an indication of more d-π overlap compared to the quintet state. Also, the Ti-C distances are on average 0.20 Å shorter in the triplet state, which generally indicates stronger bonding. The Ti-bp distance in the $\widetilde{X}\ ^1A_1$ state of the clamshell structure and the $\widetilde{B}\ ^3A$ state of the half-sandwich structure are of comparable magnitude according to the predicted Ti-C bond lengths. However, the clamshell $\widetilde{X}\ ^1A_1$ state is predicted to lay ~ 1697 cm^{-1} lower in energy due to an additional d-π interaction

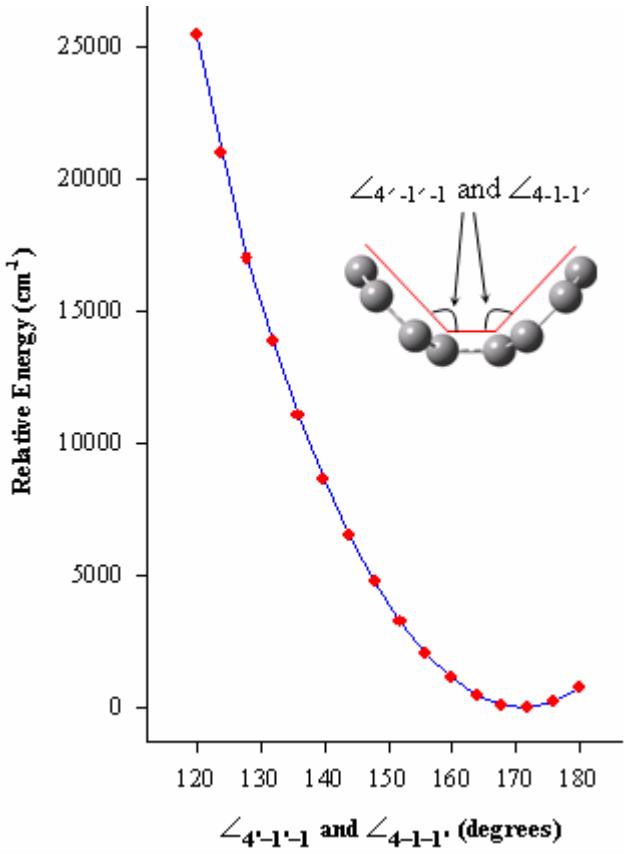

Figure 9.2. Potential energy surface of free biphenyl along the phenyl bending angle coordinate. Both angles were scanned simultaneously in 4 degree increments from 120 to 180 degrees, while freezing the C-C bond lengths.

not present in the half-sandwich structure. Also, the two separate π-systems can mix via π-d-π overlap.

The $\widetilde{X}\ ^4A$ electronic state of the half-sandwich structure is predicted to be the ground electronic state of the ionic Ti-bp complex. The $\widetilde{B}\ ^2A$ state of the half-sandwich structure lies much higher in energy, 3750 cm^{-1} above the $\widetilde{X}\ ^4A$ state. In the clamshell configuration, on the other hand, the $\widetilde{A}\ ^2B_1$ state is predicted to lie only 751 cm^{-1} above the $\widetilde{X}\ ^4A$ state. Another clamshell doublet state was also located ($\widetilde{C}\ ^2A$), but at much higher energy, ~ 7500 cm^{-1} above the $\widetilde{X}\ ^4A$ state of the half-sandwich structure. A search for the clamshell quartet state was unsuccessful; all calculations converged back to the $\widetilde{X}\ ^4A$ state of the half-sandwich structure.

In the ground electronic state of the ion ($\widetilde{X}\ ^4A$), both phenyl rings are completely flat, and the titanium ion binds to one phenyl ring to form a half-sandwich $Ti^+(\eta^6$-bp) structure. In the doublet state of the half-sandwich structure, the Ti^+-C distances are slightly shorter, and the twisted angle between the two phenyl rings is decreased by ~ 4 °. The bp ligand in both of these states is nearly the same as indicated by the C-C bond lengths and the simple (∠), dihedral (δ), and torsion (τ) angles. Although the structural difference between these two electronic states is small, the energy difference is rather large, 3750 cm^{-1}. This large energy difference indicates that the energy separation among the HOMO – 2, HOMO – 1 and the HOMO of the $\widetilde{X}\ ^4A$ state of the half-sandwich structure is small. In other words, the electron pairing energy must be much larger than the energy separation between the HOMO – 2 and HOMO. Therefore, when electrons are paired in the HOMO – 2, the electronic energy is significantly raised like in the $\widetilde{B}\ ^2A$ state. A lower-energy structure forms when the three valence electrons are unpaired: one in the HOMO – 2, one in the HOMO – 1, and one in the HOMO.

Like in the neutral $\widetilde{X}\ ^1A_1$ state, the titanium ion binds to both phenyl rings simultaneously in the $\widetilde{A}\ ^2B_1$ state of the clamshell structure. In the $\widetilde{A}\ ^2B_1$ state, the Ti^+-C_1 and -$C_{1'}$ distances (2.062 Å) are much shorter than others (2.335 to 2.434 Å). Both π rings are puckered by ~ 20 °, and a majority of the C-C bond lengths are elongated with respect to the free ligand. This geometry is consistent with a twelve-fold bonding scheme,

sixfold on each ring. Another doublet state ($\widetilde{C}\ ^2A$) of the clamshell structure was located almost 7500 cm^{-1} above the ground electronic state of the ion. In this state, the phenyl rings are less bent, 22 versus 56 ^{o} in the $\widetilde{A}\ ^2B_1$ state. With such small phenyl bending angles, many of the Ti^+-C distances are much longer. Consequently, the d-π overlap is reduced, and the overall energy of this state is significantly raised, 6743 cm^{-1} higher than the $\widetilde{A}\ ^2B_1$ state of the clamshell structure. Compared to the $\widetilde{A}\ ^2B_1$ state, the metal-ligand bonding in the $\widetilde{C}\ ^2A$ state is only sixfold, three-fold on each phenyl ring [i.e. a Ti(η^3:η^3-bp) complex].

In our experiments, ionic complexes are produced via photoionization of the neutral molecule, which is governed by Franck-Condon principles. Thus, our ZEKE measurements are expected to probe vibrational levels of the neutral and ionic metal complexes with the same isomeric structure. In other words, we do not expect to observe the $\widetilde{X}\ ^4A$ state of the half-sandwich ion via ionization of the $\widetilde{X}\ ^1A_1$ state of the clamshell structure of the neutral complex. Thus, structural changes induced by ionization are obtained by comparing the geometries in the $\widetilde{X}\ ^1A_1$ and $\widetilde{A}\ ^2B_1$ states of the clamshell structure. Upon ionization of the ground electronic $\widetilde{X}\ ^1A_1$ state of the clamshell structure, the Ti^+-C_2, -C_3, -C_5, and -C_6 distances elongate on average by ~ 3 %, while the Ti^+-C_1 and -C_4 distances remain nearly the same. The relatively larger elongation of the Ti^+-C_2, -C_3, -C_5, and -C_6 distances compared to the Ti^+-C_1 and -C_4 distances is a result of additional phenyl ring puckering (7 ^{o}) where the C_2, C_3, C_5, and C_6 atoms move further away from the metal center. In this more puckered configuration, the C_2-C_3 and C_5-C_6 bonds are shorter while the phenyl rings remain bent by about the same degree. The slightly longer Ti^+-C distances compared to the neutral complex results from the removal of an electron from a metal-ligand bonding b_1 orbital. The bonding is described in more detail in section 9.3.4.

9.3.2 Ti-bp ZEKE Spectrum

The ZEKE spectrum of Ti-bp recorded in helium carrier gas is presented in Figure 9.3(a). The bandwidths in this spectrum, measured as the FWHM, are approximately 14 cm^{-1} wide. Four vibrational progressions and three vibrational intervals originate from the most intense peak in the spectrum at 43842 cm^{-1}. Two of the vibrational progressions (194 and 350 cm^{-1}) proceed to the higher energy side, while the other two (208 and 326 cm^{-1}) proceed to the lower energy side of this peak. On the blue side of this intense peak is a single vibrational interval at 986 cm^{-1}, while two vibrational intervals of 445 and 595 cm^{-1} are located on the red side. Thus, this intense peak (43842 cm^{-1}) is assigned to the vibrationless (0-0) transition from the ground electronic state of the neutral molecule to the lowest spin-accessible electronic state of the ion. The two vibrational progressions (194 and 350 cm^{-1}) and single vibrational interval (986 cm^{-1}) on the higher energy side of the origin band correspond to vibrational frequencies of the ion complex, while the other vibrational progressions (208 and 326 cm^{-1}) and vibrational intervals (445 and 595 cm^{-1}) on the lower energy side of the origin band correspond to vibrational frequencies of the neutral complex. All the other peaks in the spectrum can be assigned to combinations of these vibrational intervals as indicated in the figure. To confirm our assignment of the hot transitions, spectral measurements were attempted with different carrier gases, but these experiments were unsuccessful; in pure argon or even argon-helium mixtures, the electron signal was unfortunately too small to record a spectrum.

A majority of the vibrational intervals in the Ti-bp ZEKE spectrum are assigned to specific modes by comparison to the ZEKE spectra of Sc- and La-bp. These vibrational frequencies are compared in Table 9.2. The 196 cm^{-1} vibrational frequency of Ti-bp is assigned to the phenyl bending mode (ν_{18}^{+}) based on the similar frequencies to that in the Sc-bp (190 cm^{-1}) and La-bp (164 cm^{-1}) complexes. The 353 cm^{-1} frequency of Ti-bp could be assigned to either ν_{17}^{+} or ν_{16}^{+} by comparison to those frequencies in the Sc- and La-bp complexes. The ν_{16}^{+} mode is a ligand based mode, whereas ν_{17}^{+} is a metal-ligand stretch mode. Hence, the ν_{16}^{+} ligand-based modes in Sc- and La-bp were measured to be nearly the same, 379 and 370 cm^{-1}, respectively. Thus, the 353 cm^{-1}

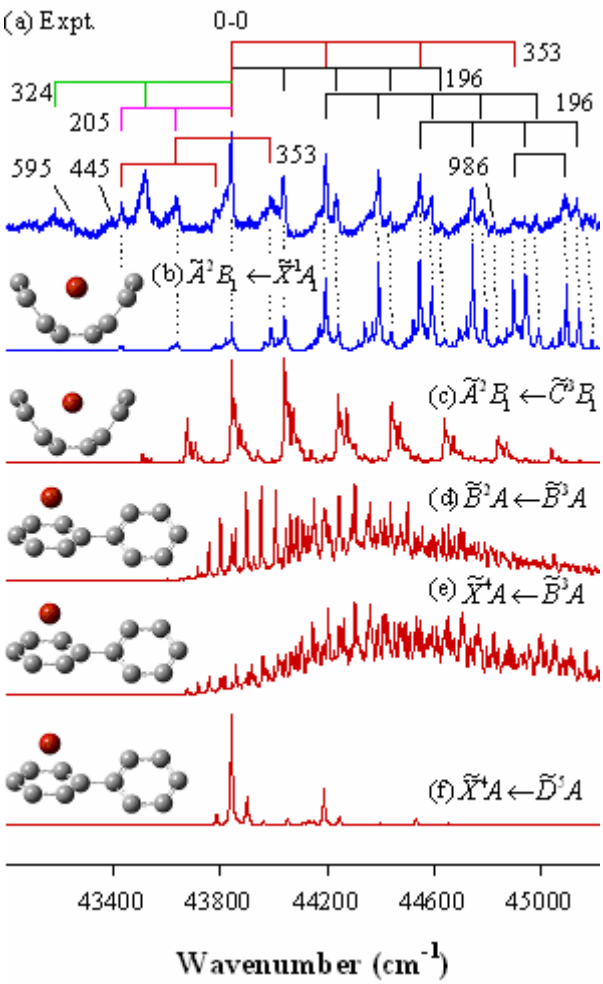

Figure 9.3. The experimental ZEKE spectrum of Ti-bp seeded in helium carrier gas (a) and spectral simulations (B3P86) of different transitions from clamshell and half-sandwich structures.

Table 9.2. Assigned electronic transitions (T_{00}), ionization energies (IE, cm^{-1}), frequencies[a] (cm^{-1}), and adiabatic bond dissociation energies (D_o^+ and D_o, kcal/mol) of M^+/M-bp complexes (M = Sc, La, Ti) measured by ZEKE spectroscopy and/or predicted by B3P86 calculations. Absolute uncertainties in IEs are ~ 5 cm^{-1}.

	Group 3 [b]				Group 4	
	Sc(η^6:η^6-bp)		La(η^6:η^6-bp)		Ti(η^6:η^6-bp)	
T_{00}	$^1A_1 \leftarrow {}^2B_1$		$^1A_1 \leftarrow {}^2B_1$		$\tilde{A}\,{}^2B_1 \leftarrow \tilde{X}\,{}^1A_1$	
Method	ZEKE	B3P86 [c]	ZEKE	B3P86 [d]	ZEKE	B3P86 [c]
IE [e]	39110	39685	36512	37217	43842	42394
ΔIE [f]	13812	12157	8468	6294	11230	8601
D_0^+ / D_0 [g]		77.7 / 42.9		66.1 / 48.1		67.6 / 43.0
ν_{18}^+ / ν_{18}	190 / --	186 / --	164 / --	162 / --	196 / 205	199 / 204
ν_{17}^+ / ν_{17}	337 / --	345 / --	257 / --	255 / --	353 / 324	351 / 409
ν_{16}^+ / ν_{16}	379 / --	383 / --	370 / --	372 / --	-- / 445	-- / 419
ν_{15}^+ / ν_{15}	567 / --	581 / --	532	535	-- / 595	-- / 594
ν_{10}^+			983	970	986	970

[a] All frequencies have a_1 symmetry: ν_{18}^+/ν_{18} has phenyl ring bends along the 4-1-1′ and 4′-1′-1 angles, and all of the other modes (ν_{17}^+/ν_{17}, ν_{16}^+/ν_{16}, ν_{15}^+/ν_{15} and ν_{10}) have C-C out-of-plane bending components. ν_{17}^+/ν_{17} and ν_{15}^+/ν_{15} also contain M^+-bp stretches. [b] From Chapter 8. [c] 6-311+G(d,p) basis set used for all atoms. [d] 6-311+G(d,p) basis set used for C and H atoms, LANL2DZ used for La atoms. [e] The predicted IEs are scaled by the average 10 % B3P86 IE overestimation. [f] ΔIE = IE of bare metal atom – IE of metal complex. The theoretical ΔIE does not include the 10 % B3P86 IE overestimation. [g] The dissociation pathways correspond to endothermic loss of the intact bp ligand: M^+/ M-bp → M^+/ M + bp, where the electron-spin multiplicity of the metal atom or ion corresponds to that of its ground electronic state (i.e. adiabatic dissociation).

vibrational frequency is assigned to a Ti^+-bp stretching mode (ν_{17}^+), since this frequency is relatively far from the ν_{16}^+ ligand-based modes of Sc- and La-bp. The 986 cm^{-1} vibrational frequency of the Ti^+-bp complex is extremely close to the ligand-based mode in the La^+-bp complex (983 cm^{-1}). Thus, this mode is assigned to a phenyl ring distortion (ν_{10}^+). The other vibrational frequencies measured in the Ti-bp ZEKE spectrum correspond to normal modes of the neutral complex. No vibrational frequencies of the neutral complex were measured in the ZEKE spectra of Sc- or La-bp. However, the vibrational frequencies of the ionic and neutral complex are expected to be of comparable magnitude. Therefore, the 205 and 324 cm^{-1} frequencies are assigned to ν_{18} and ν_{17}, which are comparable to those in the ion, 196 and 353 cm^{-1}, respectively. The 595 cm^{-1} vibrational interval is similar in magnitude to the ν_{15}^+ mode of Sc- and La-bp. Thus, this frequency is preliminarily assigned to the ν_{15} mode of the neutral Ti-bp molecule. The 445 cm^{-1} interval observed in the Ti-bp ZEKE spectrum cannot be unambiguously assigned based on spectral comparisons to the Sc- and La-bp ZEKE spectra.

Based on our assignment of nearly all observed vibrational frequencies, the Ti-bp complex can be assumed to adopt the clamshell configuration as well. Further spectral analysis considers theoretical calculations and spectral simulations to identify the electronic states and to complete the spectral assignment.

9.3.3 Comparison of Measured and Simulated Spectra

In our theoretical survey, we located eight neutral and four ionic electronic states. According to selection rules, only 23 out of the 32 transitions are spin-allowed, where the electron spin multiplicity changes by ± 1. Further details of the selection rules involved in photoelectron spectroscopy were discussed in Chapter 4. To rationalize which transitions are observed in experiment, the predicted structures and energies of these states are considered too. For example, transitions between clamshell and half-sandwich structures are neglected, because this geometry change is much too large. Such a substantial structural transformation would generate an extremely long vibrational progression in the spectrum, much longer than those that were observed. Under these structural consider-

ations, the total number of realistic electronic transitions is reduced to 10 out of the original 32 possibilities. From the calculated energies, the spectrum must originate from the $\widetilde{X}\ ^1A_1$ state of the clamshell structure, i.e. the ground electronic state of the neutral complex; all other spectral measurements of metal complexes by our group were found to originate from the ground electronic state of the neutral complex as well, if excited states had significantly higher energies.[12, 13, 32, 36-38, 318, 319] Thus, the spectrum is assigned to the $\widetilde{A}\ ^2B_1 \leftarrow \widetilde{X}\ ^1A_1$ transition under the clamshell configuration.

Simulations from half-sandwich and clamshell structures are compared to the experimental spectrum in Figure 9.3(a) – (f). Compared to the measured spectral profile, simulations from the half-sandwich structure do not match at all. Also, these higher energy structures are not likely to be populated in the molecular beam where the vibrational temperature has been estimated to be between 40 and 300 K depending on the carrier gas conditions. Only transitions from the clamshell structures match experiment. Simulation of the $\widetilde{A}\ ^2B_1 \leftarrow \widetilde{C}\ ^3B_1$ transition predicts only one long vibrational progression in ν_{18}^+ on the blue side of the origin band and a short progression in ν_{18} on the red side of the origin band. Simulation of the $\widetilde{A}\ ^2B_1 \leftarrow \widetilde{X}\ ^1A_1$ transition, on the other hand, predicts both vibrational progressions in the ion (ν_{17}^+ and ν_{18}^+), the ν_{18} vibrational progression, and the corresponding combination bands. The pattern from the $\widetilde{A}\ ^2B_1 \leftarrow \widetilde{X}\ ^1A_1$ simulation matches the experimental spectral pattern much better according to the excellent peak-to-peak correlation as indicated by the dotted lines drawn from Figure 9.3(a) to (b). In addition, the predicted transition energy of the $\widetilde{A}\ ^2B_1 \leftarrow \widetilde{X}\ ^1A_1$ transition (42384 cm^{-1}) matches closer to the experimental IE (43842 cm^{-1}) than that of the $\widetilde{A}\ ^2B_1 \leftarrow \widetilde{C}\ ^3B_1$ transition (40144 cm^{-1}). These predicted transition energies are corrected by the ~ 10 % IE overestimation by the B3P86 functional that was discussed in Chapter 8. Moreover, the peaks in the simulation that correspond to ν_{18} of the neutral $\widetilde{X}\ ^1A_1$ state (204 cm^{-1}) matches closer to the experimental value (205 cm^{-1}) than that in the $\widetilde{C}\ ^3B_1$ state (167 cm^{-1}). Although the peak at 43395 cm^{-1}, i.e. the 445 cm^{-1} vibrational interval, is not simulated in the $\widetilde{A}\ ^2B_1 \leftarrow \widetilde{X}\ ^1A_1$ transition, this frequency is assigned to ν_{16} based on the calculated frequency (419 cm^{-1}) of an a_1 mode of the neutral complex. This

ligand-based C-C out-of-plane bending mode was also measured for the ionic Sc^+- and La^+-bp complexes. The modes assigned based on comparison to the ZEKE spectra of Sc- and La-bp are also consistent with assignments made by comparison to the spectral simulation of the $\tilde{A}\ ^2B_1 \leftarrow \tilde{X}\ ^1A_1$ transition of the Ti-bp clamshell structure. All the peak positions and assignments of the Ti-bp ZEKE spectrum are listed in Table 9.3.

9.3.4 Trends in Early Transition Metal-Biphenyl Complexes

Table 9.2 summarizes the electronic states and transitions for the M-bp complexes presented in this dissertation. A number of significant conclusions can be drawn from this table.

All these M-bp complexes adopt the clamshell configuration. Like the M-bz_2 sandwich complexes, these clamshell structures prefer the low electron spin states. The determination of the low-spin electronic states in these clamshell complexes can be explained by comparison to the metal bis(benzene) complexes (e.g. Chapter 5). Ideally, the dibenzene complexes have a sixfold principal rotational axis and are in D_{6h} symmetry. Under this symmetry, metal atomic 3d orbitals span three irreducible representations, which are energetically ordered as $3de_{2g}$ (δ,$d_x2_{-y}2_{, xy}$) < $3da_{1g}$ (σ,d_z2) < $3de_{1g}$ (π,$d_{xz, yz}$).[251, 252] Electron occupation of the $3de_{2g}$ (δ) orbitals maximizes the electron back donation into the lowest unoccupied π^* orbitals on the benzene rings and increases the metal-ligand interaction. The $3de_{1g}$ (π) orbitals overlap with the benzene highest occupied π orbitals and are strongly antibonding because of favorable spatial overlap and small energy differences between the interacting orbitals. The overlap of the $3da_{1g}$ (σ) orbital with benzene should be small since it is compact and points into the center of the benzene ring, and it has a much higher energy than the benzene a_{1g} π orbitals. The ground electronic states of the metal bis(benzene) complexes depends on how many valence electrons the metal atom has and how the metal electrons are filled in these orbitals. To maximize the metal-to-ligand electron back donation and thus metal-ligand interaction, all three electrons of Sc or four electrons of Ti are filled into the e_{2g} orbital to form a $^2E_{2g}$ ($3de_{2g}^3$) state for Sc-bz_2 or a $^1A_{1g}$ ($3de_{2g}^4$) state for Ti-bz_2. However, the degenerate $^2E_{2g}$

Table 9.3. Peak positions (cm^{-1}) and assignments for the Ti-bp ZEKE spectrum of the $\tilde{A}\ ^2B_1 \leftarrow \tilde{X}\ ^1A_1$ transition.

Position	Assignment	Position	Assignment	Position	Asssignment
43185	17_2^0	44038	18_0^1	44783	$17_0^1 18_0^3$
43247	15_1^0	44195	17_0^1	44828	10_0^1
43395	16_1^0	44234	18_0^2	44899	17_0^3
43432	18_2^0	44392	$17_0^1 18_0^1$	44937	$17_0^2 18_0^2$
43519	17_1^0	44434	18_0^3	44981	$17_0^1 18_0^4$
43637	18_1^0	44546	17_0^2	45090	$17_0^3 18_0^1$
43782	$17_0^1 18_2^0$	44588	$17_0^1 18_0^2$	45133	$17_0^2 18_0^3$
43842	0_0^0	44631	18_0^4		
43991	$17_0^1 18_1^0$	44741	$17_0^2 18_0^1$		

state of Sc-bz_2 undergoes a Jahn-Teller distortion to form a structure of lower symmetry, which is determined to be D_{2h} with the ground state of $^2B_{1g}$. If we consider the clamshell structures as a distortion of these metal bis(benzene) complexes from D_{6h} or D_{2h} to C_{2v} symmetry, then the e_{2g} orbitals will split into a set of a_1 and b_1 orbitals. Thus, the ground electronic state of the Sc-bp clamshell complex is the $^2B_1$ state with a valence electron configuration of $a_1^2 b_1^1$. Adding an electron into the HOMO gives a $^1A_1$ electronic state, which was observed in the clamshell structure of Ti-bp. Ionization of this singlet state of Ti-bp will remove an electron from a b_1 ($3d_{xz}$) orbital to give a $^2B_1$ state. Ionization of the doublet state of Sc-bp also removes an electron from the b_1 ($3d_{xz}$) orbital and yields a $^1A_1$ state. The La^+/La-bp complexes have the same ground electronic states as those of Sc^+/Sc-bp since the valence electron configurations of both metal atoms or ions are the same.

The predicted ionization energies are scaled by an average 10 % overestimation of the B3P86 method. After this correction, the agreement between the measured and calculated IEs is much more satisfactory like the scaled IEs presented in Chapters 7 and 8. The IEs of the bare metal atoms are larger than the IEs of the metal complexes. This IE shift (denoted as ΔIE) indicates that the ionic complexes are bound more tightly than their neutral counterparts. The stronger binding in the ion is attributed to the addition of an ion-multipole interaction not present in neutral molecules. The smaller ΔIE in Ti-bp compared to Sc-bp indicates that either the bond dissociation energy of the neutral Ti-bp complex is larger than that of the scandium complex, the bond dissociation energy of the ionic Ti^+-bp complex is smaller than that of the scandium complex, or both. Unfortunately, the bond dissociation energy of these M^+/M-bp complexes has not been measured. Further discussion of the bond dissociation energies considers the predicted structures, measured frequencies, and calculated adiabatic bond dissociation energies.

Metal-carbon distances in the M-bp clamshell complexes decrease, and the M^+-bp stretch frequencies (ν_{17}^+) increase from La to Sc to Ti. The reduction of the M-C distances is consistent with the size decrease from La to Sc to Ti. The reduction from the Sc-C to Ti-C distances may also be associated with an increased metal-to-ligand electron back donation, which enhances the metal-ligand bonding. The Ti-bp complex has four back-donating electrons ($a_1^2 b_1^2$), while Sc-bp has only three such electrons ($a_1^2 b_1^1$). Ion-

ization increases the M-C distances, because ionization removes a bonding b_1 electron in Sc-, La-, and Ti-bp. A similar trend was also found in the case of early transition metal bis(benzene) sandwich complexes (see Chapter 5).

The trends in both the metal-carbon distances and M^+-bp stretch frequencies suggest that the bond energies in these complexes should increase from La to Sc to Ti. On the contrary, our calculated adiabatic bond dissociation energies are not consistent with the expected outcome. For example, the bond dissociation energy of the Ti^+-bp complex is predicted to be about 10 kcal/mol smaller than that of Sc^+-bp. This discrepancy may arise from the different spin states between the metal complex and metal atom or ion, or from computational errors. In addition, the predicted ground electronic state spin multiplicity of the titanium atom (quintet) is not the same as that measured by experiment (triplet).[169] Thus, a discussion about the calculated bond dissociation energies is not very reliable.

Instead, the ΔIE values are discussed as they were measured directly from experiment. The ΔIE decreases drastically from Sc- to La-bp. This ΔIE difference is a result of relatively weaker bonding in La^+-bp and/or stronger bonding in La-bp compared to Sc^+- and Sc-bp, respectively. The stronger bonding in the neutral La-bp complex can be explained by the more polarizability of the larger La atom. The weaker bonding in La^+-bp compared to Sc^+-bp is attributed to the weaker electrostatic force in La^+-bp where the La^+-C distances are predicted to be on average 0.379 Å longer than Sc^+-C distances; electrostatic forces decay rapidly as the distance between the two interacting moieties increases. The ΔIE also decreases from Sc- to Ti-bp, but to a much smaller extent (2582 cm^{-1} = 7.4 kcal/mol). Since an additional valence electron fills the bonding b_1 orbital in the Ti-bp complex, the dissociation energy of the neutral Ti-bp is expected to be larger than that of Sc-bp, consistent with the ΔIE difference. However, experiments (e.g. CID) are required to confirm our discussion of these bond dissociation energies, which, to my knowledge, have not been reported.

9.4 Conclusions

The helium gas seeded Ti-bp complex was studied by ZEKE spectroscopy and DFT calculations. From this investigation, we have determined that the Ti-bp complex adopts the clamshell binding scheme under the C_{2v} point group. The electronic states involved in the observed transition are the neutral $\tilde{X}\ ^1A_1$ (ground) and ionic $\tilde{A}\ ^2B_1$ states. In these two states, the titanium atom or ion binds to both phenyl rings simultaneously. Producing this clamshell structure requires a rotation of the phenyl rings by 40 ^{o} and bending of the phenyl rings by ~ 57 ^{o}. The energy cost of this transformation is compensated by the formation of 12 M-C bonds.

CHAPTER 10: SUMMARY OF DISSERTATION

In this dissertation, the IEs and low-frequency vibrational modes of 17 different transition metal aromatic hydrocarbon complexes were measured via ZEKE spectroscopy. By comparing the ZEKE spectra to FC simulations, the electronic states and corresponding molecular structures were determined. The observed transitions, molecular symmetries, IEs, ΔIEs, and metal-ligand stretch frequencies of these metal complexes are summarized in Table 10.1.

Each naphthalene complex has a puckered π-ring, and the metal atom or ion is coordinated to an (η^2-np) ligand. The benzene complexes, on the other hand, have planar π-rings, and the metal atom or ion is coordinated to one or two (η^6-bz) rings to form a half-sandwich or sandwich complex, respectively. Likewise, the metal-polyphenyl complexes were determined to have sixfold bonding per π-ring. However, the bp and phnp ligands adopt a clamshell shape such that the metal atom or ion binds to two π-rings simultaneously. In this clamshell structure, the metal atom or ion has twelve fold bonding, sixfold to each π-ring.

Although the neutral Sc-bz complex favors a high-spin quartet electron-spin multiplicity, the other complexes favor relatively low spin states with respect to the bare metal atom. The relatively low spin states in these metal complexes are a result of *d* orbital splitting, where the originally fivefold degenerate atomic orbitals are split into nondegenerate molecular orbitals. The magnitude of this *d* orbital splitting depends on the ligand field, the symmetries of the atomic and molecular orbitals, the relative energies of the atomic and molecular orbitals, and the spatial overlap between the atomic and molecular orbitals.

For all these transition metal complexes, the ΔIE values are positive, which indicates that metal-ligand bonding in the ionic complexes is stronger than that in the corresponding neutral complexes. Stronger bonding in the ionic complexes is attributed to the addition of an ion-quadrupole interaction that is not present in the neutral complexes.

Metal-ligand vibrations were observed in all of the ZEKE spectra of these metal

Table 10.1. Observed transitions; associated molecular symmetries; measured transition energies (T_{00}, cm^{-1}), IE differences (ΔIE, cm^{-1}); and metal-ligand stretch frequencies of the ionic complex (ν_s^+, cm^{-1}) for the transition metal-aromatic hydrocarbon complexes presented in this dissertation. The IEs (cm^{-1}) of the corresponding bare metal atom [IE(M)] and ligand [IE(L)] are also listed. The electron spin multiplicity (ESM = 2S + 1) is also indicated for the ground electronic state of the bare metal atom and ion.

Complex	Symmetry final ← initial	Transition final ← initial	T_{00}	IE(M)[a]	IE(L)[b]	ΔIE[c]	ESM[a] M^+ / M	ν_s^+
Sc-bz	$C_{6v} \leftarrow C_{6v}$	$^3A_1 \leftarrow {}^4A_1$	41600	52922	74557	11322	3 / 2	375
Sc-bz$_2$	$D_{2h} \leftarrow D_{2h}$	$^1A_{1g} \leftarrow {}^2B_{3g}$	40883	52922	74557	12039	3 / 2	206
	$D_{6h} \leftarrow D_{2h}$	$^3A_{1g} \leftarrow {}^2B_{3g}$	42112	52922	74557	10810	3 / 2	201
Ti-bz$_2$	$D_{2h} \leftarrow D_{6h}$	$^2B_{1g} \leftarrow {}^1A_{1g}$	46228	55072	74557	8844	4 / 3	228
V-bz$_2$	$D_{2h} \leftarrow D_{6h}$	$^3B_{1g} \leftarrow {}^2A_{1g}$	46655	54411	74557	7756	5 / 4	230
Cr-bz$_2$	$D_{6h} \leftarrow D_{6h}$	$^2A_{1g} \leftarrow {}^1A_{1g}$	44081	54575	74557	10494	6 / 7	264
Mo-bz$_2$	$D_{6h} \leftarrow D_{6h}$	$^2A_{1g} \leftarrow {}^1A_{1g}$	44581	57204	74557	12623	6 / 7	277
W-bz$_2$	$D_{6h} \leftarrow D_{6h}$	$^2A_{1g} \leftarrow {}^1A_{1g}$	43634	63427	74557	19793	6 / 5	370
Sc-np	$C_s \leftarrow C_s$	$^1A' \leftarrow {}^2A'$	41193	52922	65687	11729	3 / 2	347, 389
Y-np	$C_s \leftarrow C_s$	$^1A' \leftarrow {}^2A'$	40798	50146	65687	9348	1 / 2	314, 378
La-np[d]			36360	44980	65687	8620	3 / 2	
Ti-np	$C_s \leftarrow C_s$	$\tilde{X}\ {}^2A'' \leftarrow \tilde{X}\ {}^3A''$	41764	55072	65687	13308	4 / 3	355, 444
Zr-np	$C_s \leftarrow C_s$	$\tilde{X}\ {}^2A' \leftarrow \tilde{X}\ {}^3A''$	42094	53506	65687	11412	4 / 3	322
	$C_s \leftarrow C_s$	$\tilde{B}\ {}^2A'' \leftarrow \tilde{X}\ {}^3A''$	42459	53506	65687	10957	4 / 3	380, 440
Hf-np	$C_s \leftarrow C_s$	$\tilde{X}\ {}^2A' \leftarrow \tilde{X}\ {}^1A'$	46660	55048	65687	8388	2 / 3	274, 317
Sc-bp	$C_{2v} \leftarrow C_{2v}$	$^1A_1 \leftarrow {}^2B_1$	39113	52922	67300	13812	3 / 2	337, 567
La-bp	$C_{2v} \leftarrow C_{2v}$	$^1A_1 \leftarrow {}^2B_1$	36516	44980	67300	8468	3 / 2	257, 532
Sc-phnp	$C_1 \leftarrow C_1$	$^1A \leftarrow {}^2A$	37594	52922	--	15328	3 / 2	340
Ti-bp	$C_{2v} \leftarrow C_{2v}$	$\tilde{A}\ {}^3B_1 \leftarrow \tilde{X}\ {}^1A_1$	43842	55072	67300	11230	4 / 3	353

[a] From reference 320. [b] The IE of bz is from reference 321, the IE of np is from reference 281, the IE of bp is from reference 322, and the IE of phnp has not been measured. [c] $\Delta IE = IE(M) - T_{00}$. [d] ZEKE experiments with La-np were unsuccessful, although its IE (± 300 cm^{-1}) was measured via PIE spectroscopy.

complexes. These vibrational modes are the most important for understanding metal-ligand interactions. Due to the relatively weak interaction between the metal atom or ion and the aromatic ligand, metal-ligand stretch frequencies are rather low ($\lesssim$ 400 cm^{-1}). However, some metal-ligand stretch frequencies also contain ligand-based motions (i.e. C-C-C bends). These frequencies are consequently much higher in energy ($\gtrsim$ 400 cm^{-1}) and indicate that the ligand (i.e. np, bp, or phnp) is not rigid in the metal complex.

Other trends in IEs, bond dissociation energies, frequencies, and molecular structures among these metal complexes have already been discussed in further detail. That is, the trends in metal-benzene complexes were discussed in Chapters 3 and 5; trends in metal-naphthalene complexes were discussed in Chapter 7; and trends in metal-biphenyl complexes were discussed in Chapter 9. I leave the imagination of the reader to draw any additional insight into the rather fascinating chemistry of these exotic molecular species.

REFERENCES

1. Hornback, J. M., *Organic Chemistry*. Brooks/Cole Publishing Company: Pacific Grove, CA, 1998.
2. Rayner-Canham, G., *Descriptive Inorganic Chemistry*. 2nd ed.; Michelle Russel Julet: New York City, 2000.
3. Fishbane, P. M.; Gasiorowicz, S.; Thornton, S. T., *Physics for Scientists and Engineers*. 2nd ed.; Prentice Hall: Upper Saddle River, 1996.
4. Bernath, P. F., *Spectra of Atoms and Molecules*. Oxford University Press, Inc.: New York City, 1995.
5. Lux, F., *Chemie in Unserer Zeit* **1971,** 5, (2), 33-40.
6. Demortier, G., *Physik in Unserer Zeit* **1992,** 23, (1), 13-21.
7. Helmus, M. N.; Gammel, P.; Allen, F.; Migliorato, P., *American Laboratory (Shelton, CT, United States)* **2006,** 38, (6), 34-38.
8. Harmon, R. S.; De Lucia, F. C.; Munson, C. A.; Miziolek, A. W.; McNesby, K. L., *Proceedings of SPIE-The International Society for Optical Engineering* **2005,** 5994, (Chemical and Biological Sensors for Industrial and Environmental Security), 59940K/1-59940K/7.
9. *Chemical, Biological, and Industrial Applications of Infrared Spectroscopy*. John Wiley & Sons: New York City, 1985; p 399.
10. Mueller-Dethlefs, K.; Sander, M.; Schlag, E. W., *Chem. Phys. Lett.* **1984,** 112, 291-294.
11. Chupka, W. A., *J. Chem. Phys.* **1993,** 98, (6), 4520-4530.
12. Sohnlein, B. R.; Yang, D.-S., *Journal of Chemical Physics* **2006,** 124, (13), 134305/1-134305/8.
13. Sohnlein, B. R.; Fuller, J. F.; Yang, D.-S., *J. Am. Chem. Soc.* **2006,** 128, (33), 10692-10693.
14. Sohnlein, B. R.; Shenggang, L.; Yang, D. S., *J. Chem. Phys.* **2005,** 123, 214306(1)-214306(7).
15. Sohnlein, B. R.; Li, S.; Fuller, J. F.; Yang, D.-S., *J. Chem. Phys.* **2005,** 123, (1), 014318/1-014318/7.
16. Wang, X.; Yang, D.-S., *J. Phys. Chem. A* **2004,** 108, (31), 6449-6451.
17. Li, S.; Rothschopf, G. K.; Sohnlein, B. R.; Fuller, J. F.; Yang, D.-S., *Can. J. Chem.* **2004,** 82, (6), 1067-1076.
18. Li, S.; Sohnlein, B. R.; Rothschopf, G. K.; Fuller, J. F.; Yang, D.-S., *J. Chem. Phys.* **2003,** 119, (11), 5406-5413.
19. Li, S.; Rothschopf, G. K.; Fuller, J. F.; Yang, D.-S., *J. Chem. Phys.* **2003,** 118, (19), 8636-8644.
20. Li, S.; Fuller, J. F.; Sohnlein, B. R.; Yang, D.-S., *J. Chem. Phys.* **2003,** 119, (17), 8882-8889.
21. Rothschopf, G. K.; Li, S.; Yang, D.-S., *J. Chem. Phys.* **2002,** 117, (19), 8800-8804.
22. Li, S.; Rothschopf, G. K.; Yang, D.-S., *J. Chem. Phys.* **2002,** 116, (15), 6589-6594.

23. Li, S.; Rothschopf, G. K.; Sohnlein, B. R.; Yang, D.-S., *J. Phys. Chem. A* **2002,** 106, 6941-6944.
24. Yang, D. S., *Coord. Chem. Rev.* **2001,** 214, 187-213.
25. Rothschopf, G. K.; Li, S.; Shannon Perkins, J.; Yang, D.-S., *J. Chem. Phys.* **2001,** 115, (10), 4565-4572.
26. Li, S.; Rothschopf, G. K.; Pillai, D.; Sohnlein, B. R.; Wilson, B. M.; Yang, D.-S., *J. Phys. Chem.* **2001,** 115, (17), 7968-7974.
27. Yang, D. S.; Hackett, P. A., *J. Electron Spectrosc. Relat. Phenom.* **2000,** 106, (2-3), 153-169.
28. Rothschopf, G. K.; Perkins, J. S.; Li, S.; Yang, D.-S., *J. Phys. Chem. A* **2000,** 104, (35), 8178-8182.
29. Lide, D. R., *CRC Handbook of Chemistry and Physics, Internet Version 2007*. 87th ed.; http://www.hbcpnetbase.com Taylor and Francis, Boca Raton, FL: Vol. http://www.hbcpnetbase.com, p http://www.hbcpnetbase.com.
30. McQuarrie, D. A., *Quantum Chemistry*. University Science Books: Sausalito, 1983.
31. Born, M.; Oppenheimer, J. R., *Ann. Phys.* **1927,** 79, 361.
32. Sohnlein, B. R.; Yang, D. S., **Unpublished results, 2006**.
33. Wang, X.; Lee, J. S.; Yang, D.-S., *Journal of Chemical Physics* **2006,** 125, (1), 014309/1-014309/9.
34. Wang, X.; Yang, D.-S., *Journal of Physical Chemistry A* **2006,** 110, (24), 7568-7576.
35. Koch, W.; Holthausen, M. C., *A Chemist's Guide to Density Functional Theory*. Wiley-VCH: New York City, 2000; p 294.
36. Sohnlein, B. R.; Yang, D. S., **Unpublished results, 2006**.
37. Sohnlein, B. R.; Fuller, J. F.; Yang, D. S., **Unpublished results, 2006**.
38. Sohnlein, B. R.; Fuller, J. F.; Yang, D. S., **Unpublished results, 2006**.
39. Sohnlein Bradford, R.; Fuller Jason, F.; Yang, D.-S., *Journal of the American Chemical Society* **2006,** 128, (33), 10692-3.
40. Sohnlein Bradford, R.; Li, S.; Yang, D.-S., *The Journal of chemical physics* **2005,** 123, (21), 214306.
41. Sohnlein, B. R.; Fuller, J. F.; Yang, D. S., **Unpublished results, 2006**.
42. Franck, J., *Trans. Faraday Soc.* **1925,** 21, 536.
43. Condon, E., *Phys. Rev.* **1926,** 28, 1182.
44. Condon, E., *Phys. Rev.* **1928,** 32, 858.
45. Duschinsky, F., *Acta Physicochim. URSS* **1937,** 7, 551.
46. Sharp, T. E.; Rosenstock, H. M., *J. Chem. Phys.* **1964,** 41, 3453.
47. Doktorov, E. V.; Malkin, I. A.; Man'ko, V. I., *J. Mol. Spectrosc.* **1977,** 64, 302.
48. Hazra, A.; Nooijen, M., *Int. J. Quantum Chem.* **2003,** 95, 643.
49. Faulkner, T. R.; Richardson, F. S., *J. Chem. Phys.* **1979,** 70, 1201.
50. Kulander, K. C., *J. Chem. Phys.* **1979,** 71, 2736.
51. Faulkner, T. R., *J. Chem. Phys.* **1979,** 71, 2737.
52. Kupka, H.; Cribb, P. H., *J. Chem. Phys.* **1986,** 85, 1303.
53. Subbi, J., *Chem. Phys.* **1988,** 122, 157.
54. Roche, M., *Chem. Phys. Lett.* **1990,** 168, 556.
55. Lerme, J., *Chem. Phys.* **1990,** 145, 67.

56. Chen, P., *Unimolecular and Bimolecular Reaction Dynamics*. John Wiley & Sons: Chichester, 1994; p 371.
57. Ruhoff, P. T., *Chem. Phys.* **1994,** 186, 355.
58. Mebel, A. M.; Chen, Y.-T.; Lin, S.-H., *J. Chem. Phys.* **1996,** 105, 9007.
59. Malmqvist, P.-A.; Forsberg, N., *Chem. Phys.* **1998,** 228, 227.
60. Islampour, R.; Dehestani, M.; Lin, S. H., *J. Mol. Spectrosc.* **1999,** 194, 179.
61. Ruhoff, P. T.; Ratner, M. A., *Int. J. Quantum Chem.* **2000,** 77, 383.
62. Toniolo, A.; Persico, M., *J. Comput. Chem.* **2001,** 22, 968.
63. Kikuchi, H.; Kubo, M.; Watanabe, N.; Suzuki, H., *J. Chem. Phys.* **2003,** 119, 729.
64. Sando, G. M.; Spears, K. G., *J. Phys. Chem. A* **2001,** 105, 5326-5333.
65. Hougen, J. T.; Watson, J. K. G., *Can. J. Chem.* **1965,** 43, 298-320.
66. Eckart, C., *Phys. Rev.* **1935,** 47, 552-558.
67. Berces, A.; Zgierski, M. Z.; Yang, D. S., *Computational Molecular Spectroscopy*. Wiley: New York City, 2000; p 110.
68. Yang, D.-S.; Zgierski, M. Z.; Rayner, D. M.; Hackett, P. A.; Martinez, A.; Salahub, D. R.; Roy, P.-N.; Carrington, T., Jr., *J. Chem. Phys.* **1995,** 103, (13), 5335-42.
69. Shenggang, L. Threshold Photoionization and ZEKE Photoelectron Spectroscopy of Metal Complexes. University of Kentucky, Lexington, 2004.
70. Shenggang, L.; Clouthier, D., **Unpublished results, 2006**.
71. Proch, D.; Trickl, T., *Rev. Sci. Instrum.* **1989,** 60, 713.
72. Wiley, W. C.; McLaren, I. H., *Rev. Sci. Instrum.* **1955,** 26, 1150.
73. Fishbane, P. M.; Gasiorowicz, S.; Thornton, S. T., *Physics*. 2nd ed.; Prentice-Hall: Upper Saddle River, NJ, 1996.
74. *Gaussian03, Revision B.03* Gaussian, Inc.: Pisttsburgh, 2001.
75. Bhaduri, S.; Mukesh, D., *Homogeneous Catalysis: Mechanisms and Industrial Applications*. Wiley: New York, 2000.
76. Cornils, B.; Herrmann, W. A., *Applied Homogeneous Catalysis with Organometallic Compounds*. 2nd ed.; Wiley-VCH: Weinheim, 2002.
77. Collman, J. P.; Hegedus, L. S.; Norton, J. R.; Finke, R. G., *Principles and Applications of Organotranstition Metal Chemistry*. University Science Books: Mill Valley, 1987.
78. Wadepohl, H., *Angew. Chem. Int. Ed. Engl.* **1992,** 31, 247.
79. Bochkarev, M. N., *Chem. Rev.* **2002,** 102, 2089.
80. Mutterties, E. L.; Bleeke, J. R.; Wucherer, E. J.; Albright, T. A., *Chem. Rev.* **1982,** 82, 499.
81. Andrews, M. P.; Huber, H. X.; Mattar, S. M.; McIntosh, D. F.; Ozin, G. A., *J. Am. Chem. Soc.* **1983,** 105, 6170.
82. Albert, M. R.; Yates, J. T., *The Surface Scientist's Guide to Organometallic Chemistry*. ACS: Washington, DC, 1997.
83. Zaera, F., *Chem. Rev.* **1995,** 95, 2651.
84. Willey, K. F.; Yeh, C. S.; Robbins, D. L.; Duncan, M. A., *J. Phys. Chem.* **1992,** 96, 9106.
85. Jaeger, T. D.; Duncan, M. A., *J. Phys. Chem. A* **2005,** 109, 3311.
86. Heijnsbergen, D. v.; Jaeger, T. D.; Helden, G. v.; Meijer, G.; Duncan, M. A., *Chem. Phys. Lett.* **2002,** 364, 345.

87. Heijnsbergen, D. v.; Helden, G. v.; Meijer, G.; Maitre, P.; Duncan, M. A., *J. Am. Chem. Soc.* **2002,** 124, 1562.
88. Jaeger, T. D.; Pillai, E. D.; Duncan, M. A., *J. Phys. Chem. A* **2004,** 108, 6605.
89. Jaeger, T. D.; Heijnsbergen, D. v.; Klippenstein, S. J.; Helden, G. v.; Meijer, G.; Duncan, M. A., *J. Am. Chem. Soc.* **2004,** 126, 10981.
90. Jaeger, T. D.; Duncan, M. A., *J. Phys. Chem. A* **2005,** 108, 11296.
91. Jaeger, T. D.; Duncan, M. A., *J. Phys. Chem. A* **2004,** 108, 11296.
92. Jaeger, T. D.; Duncan, M. A., *Int. J. Mass Spectrom.* **2005,** 241, 165.
93. Afzaal, S.; Freiser, B. S., *Chem. Phys. Lett.* **1994,** 218, 254.
94. Cabarcos, O. M.; Weinheimer, C. J.; Lisy, J. M., *J. Chem. Phys.* **1999,** 110, 8429.
95. Cabarcos, O. M.; Weinheimer, C. J.; Lisy, J. M., *J. Chem. Phys.* **1998,** 108, 5151.
96. Knickelbein, M. B., *Ann. Rev. Phys. Chem.* **1999,** 50, 79.
97. Koretsky, G.; Knickelbein, M. B., *Chem. Phys. Lett.* **1997,** 267, 485.
98. Ketkov, S. Y.; Selzle, H. L.; Schlag, E. W.; Domrachev, G. A., *Chem. Phys. Lett.* **2003,** 373, (5,6), 486-491.
99. Ketkov, S. Y.; Selzle, H. L.; Schlag, E. W., *J. Chem. Phys.* **2004,** 121, (1), 149-156.
100. Choi, K.-W.; Kim, S. K.; Ahn, D.-S.; Lee, S., *J. Phys. Chem. A* **2004,** 108, (51), 11292-11295.
101. Nakajima, A.; Kaya, K., *Journal of Physical Chemistry A* **2000,** 104, (2), 176-191.
102. Kurikawa, T.; Takeda, H.; Hirano, M.; Judai, K.; Arita, T.; Nagao, S.; Nakajima, A.; Kaya, K., *Organometallics* **1999,** 18, (8), 1430-1438.
103. Yasuike, T.; Nakajima, A.; Yabushita, S.; Kaya, K., *Journal of Physical Chemistry A* **1997,** 101, (29), 5360-5367.
104. Hoshino, K.; Kurikawa, T.; Takeda, H.; Nakajima, A.; Kaya, K., *Journal of Physical Chemistry* **1995,** 99, (10), 3053-5.
105. Kurikawa, T.; Hirano, M.; Takeda, H.; Yagi, K.; Hoshino, K.; Nakajima, A.; Kaya, K., *J. Phys. Chem.* **1995,** 99, 16248.
106. Gerhards, M.; Thomas, O. C.; Nilles, J. M.; Zheng, W.-J.; Bowen, K. H., *J. Chem. Phys.* **2002,** 116, 10247.
107. Zheng, W.; Nilles, J. M.; Thomas, O. C.; Bowen, K. H., *Chemical Physics Letters* **2005,** 401, (1-3), 266-270.
108. Zheng, W.; Nilles, J. M.; Thomas, O. C.; Bowen, K. H., *Chem. Phys.* **2005,** 122, 44306.
109. Judai, K.; Nakamura, Y.; Tachibana, M.; Negishi, Y.; Nakajima, A.; Kaya, K., *Chem. Lett.* **2001,** 2, 114.
110. Judai, K.; Hirano, M.; Kawamata, H.; Yabushita, S.; Nakajima, A.; Kaya, K., *Chemical Physics Letters* **1997,** 270, (1,2), 23-30.
111. Green, J. C., *Structure and Bonding* **1981,** 43, 37.
112. Ketkov, S. Y.; Mehnert, C.; Green, J. C., *Chem. Phys.* **1996,** 203, (2), 245-55.
113. Li, Y.; McGrady, J. E.; Baer, T., *J. Am. Chem. Soc.* **2002,** 124, 4487.
114. Li, Y.; Baer, T., *J. Phys. Chem. A* **2002,** 106, (42), 9820-9826.
115. Chen, Y.-M.; Armentrout, P. B., *Chem. Phys. Lett.* **1995,** 210, 123.
116. Meyer, F.; Khan, F. A.; Armentrout, P. B., *Journal of the American Chemical Society* **1995,** 117, (38), 9740-8.
117. Amunugama, R.; Rodgers, M. T., *J. Phys. Chem. A* **2002,** 106, 5529.

118. Amunugama, R.; Rodgers, M. T., *J. Phys. Chem. A* **2002,** 106, 9092.
119. Weis, P.; Kemper, P. R.; Bowers, M. T., *Journal of Physical Chemistry A* **1997,** 101, (44), 8207-8213.
120. Miyajima, K.; Nakajima, A.; Yabushita, S.; Knickelbein, M. B.; Kaya, K., *Journal of the American Chemical Society* **2004,** 126, (41), 13202-13203.
121. Imura, K.; Kawashima, T.; Ohoyama, H.; Kasai, T.; Nakajima, A.; Kaya, K., *Phys. Chem. Chem. Phys.* **2001,** 3, 3593.
122. Imura, K.; Ohoyama, H.; Kasai, T., *Chemical Physics Letters* **2003,** 369, (1,2), 55-59.
123. Rabilloud, F.; Rayane, D.; Allouche, A. R.; Antoine, R.; Aubert-Frecon, M.; Broyer, M.; Compagnon, I.; Dugourd, P., *J. Phys. Chem. A* **2003,** 107, 11347.
124. Rayane, D.; Allouche, A. R.; Antoine, R.; Broyer, M.; Compagnon, I.; Dugourd, P., *Chem. Phys. Lett.* **2003,** 375, 506.
125. Berg, C.; Beyer, M.; Schindler, T.; Niedner-Schatteburg, G.; Bondybey, V. E., *J. Chem. Phys.* **1996,** 104, 7940.
126. Gapeev, A.; Dunbar, R. C., *Journal of the American Society for Mass Spectrometry* **2002,** 13, (5), 477-484.
127. Ho, Y.-P.; Dunbar, R., *Int. J. Mass Spectrom.* **1999,** 182/183, 175.
128. Ho, Y.-P.; Yang, Y.-C.; Klippenstein, S. J.; Dunbar, R., *J. Phys. Chem. A* **1997,** 101, 3338.
129. Dunbar, R.; Klippenstein, S. J.; Hrusak, J.; Stoeckigt, D.; Schwarz, H., *J. Am. Chem. Soc.* **1996,** 118, 5277.
130. Xu, Y. C.; Chen, Q.; Poehlein, S. K.; Freiser, B. S., *Rapid Communications in Mass Spectrometry* **1999,** 13, 645.
131. Lin, C.-Y.; Chen, Q.; Chen, H.; Freiser, B. S., *J. Phys. Chem. A* **1997,** 101, 6023.
132. Huang, Y.; Ranatunga, D. R. A.; Freiser, B. S., *J. Am. Chem. Soc.* **1994,** 116, 4796-4800.
133. Hirano, M.; Judai, K.; Nakajima, A.; Kaya, K., *Journal of Physical Chemistry A* **1997,** 101, (27), 4893-4899.
134. Schroder, D.; Brown, R.; Schwerdtfeger, P.; Schwarz, H., *Int. J. Mass Spectrom.* **2000** 203, 155.
135. Schroeter, K.; Wesendrup, R.; Schwarz, H., *Euro. J. Org. Chem.* **1998,** 4, 565.
136. Stoeckigt, D.; Hrusak, J.; Schwarz, H., *Int. J. Mass Spectrom. Ion Processes* **1995,** 149/150, 1.
137. Schroder, D.; Hrusak, J.; Hertwig, r. H.; Koch, W.; Schwerdtfeger, P.; Schwarz, H., *Organometallics* **1995,** 14, 312.
138. Caraiman, D.; Bohme, D. K., *Journal of Physical Chemistry A* **2002,** 106, (42), 9705-9717.
139. Wright, R. R.; Walker, N. R.; Firth, S.; Stace, A. J., *J. Phys. Chem. A* **2001,** 105, 54.
140. Pandey, R.; Rao, B. K.; Jena, P.; Blanco, M. A., *J. Am. Chem. Soc.* **2001,** 123, 3799.
141. Rao, B. K.; Jena, P., *J. Chem. Phys.* **2002,** 117, 5234.
142. Pandey, R.; Rao, B. K.; Jena, P.; Newsam, J. M., *Chem. Phys. Lett.* **2000,** 321, 142-150.
143. Kambalapalli, S.; Ortiz, J. V., *J. Phys. Chem. A* **2004,** 108, 2988.

144. Rabilloud, F., *J. Chem. Phys.* **2005,** 122, 134303.
145. Charles W. Bauschlicher, J.; Partridge, H.; Langhoff, S. R., *J. Phys. Chem.* **1992,** 96, 3273.
146. King, W. A.; Di Bella, S.; Lanza, G.; Khan, K.; Duncalf, D. J.; Cloke, F. G. N.; Fragala, I. L.; Marks, T. J., *Journal of the American Chemical Society* **1996,** 118, (3), 627-35.
147. Di Bella, S.; Lanza, G.; Fragala, I. L.; Marks, T. J., *Organometallics* **1996,** 15, 3985.
148. McKee, M. L., *J. Phys. Chem.* **1991,** 95, 7247.
149. Froudakis, G. E.; Andriotis, A. N.; Menon, M., *Chemical Physics Letters* **2001,** 350, (5,6), 393-398.
150. Feller, D.; Dixon, D. A.; Nicholas, J. B., *J. Phys. Chem. A* **2002,** 104, 11414.
151. Yang, C.-N.; Klippenstein, S. J., *J. Phys. Chem. A* **1999,** 103, 1094.
152. Diefenbach, M.; Trage, C.; Schwarz, H., *Helvetica Chimica Acta* **2003,** 86, 1008.
153. Diefenbach, M.; Schwarz, H., Electronic Encyclopedia of Computational Chemistry. In Schleyer, P. v. R.; Schreiner, P. R.; Schaefer, H. F.; Jorgensen, W. L.; Theil, W.; Glen, R. C., Eds. Wiley: Chichester, UK, 2004.
154. Hong, G.; Schautz, F.; Dolg, M., *Journal of the American Chemical Society* **1999,** 121, (7), 1502-1512.
155. Hong, G.; Dolg, M.; Li, L., *International Journal of Quantum Chemistry* **2000,** 80, (2), 201-209.
156. Dolg, M., *Journal of Chemical Information and Computer Sciences* **2001,** 41, (1), 18-21.
157. Stockigt, D., *Organometallics* **1998,** 18, 1050.
158. Stockigt, D., *J. Phys. Chem. A* **1997,** 101, 3800.
159. Chaquin, P.; Costa, D.; Lepetit, C.; Che, M., *J. Phys. Chem. A* **2001,** 105, 4541.
160. Sahnoun, R.; Mijoule, C., *J. Phys. Chem. A* **2001,** 105, 6176.
161. Yasuike, T.; Yabushita, S., *Journal of Physical Chemistry A* **1999,** 103, (23), 4533-4542.
162. Molina, J. M.; Dobado, J. A.; Melchor, S., *J. Molec. Struct. (Theochem)* **2002,** 589-590, 337-347.
163. Dargel, T. K.; Hertwig, R. H.; Koch, W., *Mol. Phys.* **1999,** 96, 583.
164. Ouhlal, A.; Selmani, A.; Yelon, A., *Chem. Phys. Lett.* **1995,** 243, 269.
165. Kim, D.; Hu, S.; Tarakeshwar, P.; Kim, K. S.; Lisy, J. M., *J. Phys. Chem. A* **2003,** 107, 1228.
166. Rayon, V. M.; Frenking, G., *Organometallics* **2003,** 22, 3304.
167. Berces, A.; Ziegler, T., *J. Phys. Chem.* **1994,** 98, (50), 13233-42.
168. Lyon, J. T.; Andrews, L., *Journal of Physical Chemistry A* **2005,** 109, (3), 431-440.
169. Moore, C. E., *Atomic Energy Levels*. National Bureau Standards: Washington, D.C., 1971.
170. Herzberg, G., *Molecular Spectra and Molecular Structure: III. Electronic Spectra and Electronic Structure of Polyatomic Molecules*. Krieger: Malabar, FL, 1991.
171. Sohnlein, B. R.; Fuller, J. F.; Li, S.; Yang, D. S., *unpublished results*.

172. van Heijnsbergen, D.; von Helden, G.; Meijer, G.; Maitre, P.; Duncan, M. A., *Journal of the American Chemical Society* **2002,** 124, (8), 1562-1563.
173. Jaeger, T. D.; Pillai, E. D.; Duncan, M. A., *Journal of Physical Chemistry A* **2004,** 108, (32), 6605-6610.
174. Jaeger, T. D.; Van Heijnsbergen, D.; Klippenstein, S. J.; Von Helden, G.; Meijer, G.; Duncan, M. A., *Journal of the American Chemical Society* **2004,** 126, (35), 10981-10991.
175. Cloke, F. G. N.; Dix, A. N.; Green, J. C.; Perutz, R. N.; Seddon, E. A., *Organometallics* **1983,** 2, (9), 1150-9.
176. Miyajima, K.; Muraoka, K.; Hashimoto, M.; Yasuike, T.; Yabushita, S.; Nakajima, A.; Kaya, K., *Journal of Physical Chemistry A* **2002,** 106, (45), 10777-10781.
177. Palmer, M. H.; Moyes, W.; Spiers, M.; Ridyard, J. N. A., *J. Mol. Struct.* **1978,** 49, 105.
178. Ketkov, S. Y.; Domrachev, G. A.; Razuvaev, G. A., *Journal of Molecular Structure* **1989,** 195, 175-88.
179. Ketkov, S. Y.; Domrachev, G. A., *Metalloorganicheskaya Khimiya* **1989,** 2, (4), 919-21.
180. Ketkov, S. Y.; Domrachev, G. A.; Razuvaev, G. A., *Zhurnal Obshchei Khimii* **1988,** 58, (3), 577-83.
181. Ketkov, S. Y.; Domrachev, G. A.; Razuvaev, G. A., *Metalloorganicheskaya Khimiya* **1988,** 1, (1), 40-6.
182. Sohnlein, B. R.; Yang, D.-S., *J. Chem. Phys.* **2006,** 124, 134305(1)-134305(8).
183. *Revision C.02*, Gaussian03,; Gaussian, Inc.: Pisttsburgh, 2001.
184. Sohnlein, B. R.; Li, S.; Yang, D.-S., *Journal of Chemical Physics* **2005,** 123, 214306.
185. Kandalam, A. K.; Rao, B. K.; Jena, P.; Pandey, R., *Journal of Chemical Physics* **2004,** 120, (22), 10414-10422.
186. Salomon, O.; Reiher, M.; Hess, B. A., *Journal of Chemical Physics* **2002,** 117, (10), 4729-4737.
187. Pandey, R.; Rao, B. K.; Jena, P.; Blanco, M. A., *Journal of the American Chemical Society* **2001,** 123, (16), 3799-3808.
188. Lyon, J. T.; Andrews, L., *J. Phys. Chem. A.* **2006,** 110, 7806.
189. Rayane, D.; Allouche, A.-R.; Antoine, R.; Broyer, M.; Compagnon, I.; Dugourd, P., *Chem. Phys. Lett.* **2003,** 375, 506.
190. Ketkov, S. Y.; Selzle, H. L.; Schlag, E. W., *Isr. J. Chem.* **2004,** 44, 65.
191. Ketkov, S. Y.; Selzle, H. L.; Schlag, E. W., *Organometallics* **2006,** 25, 1712.
192. Choi, D.-W.; Kim, S. K.; Ahn, D.-S.; Lee, S., *J. Phys. Chem. A* **2004,** 108, 11292.
193. Wang, J.; Acioli, P. H.; Jellinek, J., *Journal of the American Chemical Society* **2005,** 127, (9), 2812-2813.
194. McCamley, A.; Perutz, R. N., *Journal of Physical Chemistry* **1991,** 95, (7), 2738-44.
195. Andrews, M. P.; Mattar, S. M.; Ozin, G. A., *Journal of Physical Chemistry* **1986,** 90, (6), 1037-43.
196. Fantucci, P.; Balzarini, P.; Valenti, V., *Inorganica Chimica Acta* **1977,** 25, (2), 113-19.
197. Clack, D. W.; Smith, W., *Inorganica Chimica Acta* **1976,** 20, (1), 93-7.

198. Fischer, E. O.; Hafner, W., *Z. Naturforsch.* **1955,** 10B, 665-668.
199. Silverthorn, W. E., *Adv. Organomet. Chem.* **1975,** 13, 47.
200. E. L. Mutterties, J. R. B., E.J. Wucherer, and T. A. Albright, *Chem. Rev.* **1982,** 82, 499.
201. Wadepohl, H., *Angew. Chem. Int. Ed. Engl.* **1992,** 31, 247.
202. Hubig, S. M.; Lindeman, S. V.; Kochi, J. K., *Coord. Chem. Rev.* **2000,** 200/202, 831.
203. Bochkarev, M. N., *Chem. Rev.* **2002,** 102, 2089.
204. J. P. Collman; L. S. Hegedus; J. R. Norton; Finke, R. G., *Principles and Applications of Organometallic Metal Chemistry*. University Science Books: Mill Valley, CA, 1987.
205. Crabtree, R. H., *The Organometallic Chemistry of the Transition Metals*. 3rd ed.; Wiley: New York, NY, 2001.
206. Pignataro, S.; Lossing, F. P., *J. Organomet. Chem.* **1967,** 10, (3), 531-4.
207. Herberich, G. E.; Mueller, J., *J. Organomet. Chem.* **1969,** 16, (1), 111-17.
208. Mueller, J.; Goeser, P., *J. Organomet. Chem.* **1968,** 12, (1), 163-72.
209. Evans, S.; Green, J. C.; Jackson, S. E., *J. Chem. Soc., Faraday Trans. 2: Mol. Chem. Phys.* **1972,** 68, (2), 249-58.
210. Guest, M. F.; Hillier, I. H.; Higginson, B. R.; Lloyd, D. R., *Mol. Phys.* **1975,** 29, (1), 113-28.
211. Cabelli, D. E.; Cowley, A. H.; Lagowski, J. J., *Inorg. Chim. Acta* **1982,** 57, (2), 195-8.
212. Chizhov, Y. V.; Timoshenko, M. M.; Yureva, L. P.; Zaitseva, N. N.; Uralets, I. A.; Kravtsov, D. N.; Asfandiarov, N. L., *J. Organomet. Chem.* **1989,** 361, 79.
213. Ryan, M. F.; Richardson, D. E.; Lichtenberger, D. L.; Gruhn, N. E., *Organometallics* **1994,** 13, (4), 1190-9.
214. Evans, S.; Green, J. C.; Jackson, S. E.; Higginson, B., *J. Chem. Soc., Chem. Commun., Dalton Trans: Inorg. Chem.* **1974**, (3), 304-11.
215. Penner, A.; Amirav, A.; Tasaki, S.; Bersohn, R., *J. Chem. Phys.* **1993,** 99, (1), 176-83.
216. Even, U.; Levine, R. D.; Bersohn, R., *J. Phys. Chem.* **1994,** 98, (13), 3472-7.
217. Ketkov, S. Y.; Green, J. C.; Mehnert, C. P., *J. Chem. Soc., Faraday. Trans.* **1997,** 93, (15), 2461.
218. Ketkov, S. Y.; Selzle, H. L.; Schlag, E. W., *Isr. J. Chem.* **2004,** 44, (1-3), 65-69.
219. Meyer, F.; Khan, F. A.; Armentrout, P. B., *J. Am. Chem. Soc.* **1995,** 117, (38), 9740-8.
220. Lin, C.-Y.; Dunbar, R. C., *Organometallics* **1997,** 16, (12), 2691-2697.
221. Trickl, D. P. a. T., *Rev. Sci. Instrum.* **1989,** 60, 713.
222. *Revision A.11*, Gaussian98,; Gaussian, Inc.: Pisttsburgh, 2001.
223. Berces, A.; Zgierski, M. Z.; Yang, D.-S., *Computational Molecular Spectroscopy*. Wiley: New York, 2000; p 110.
224. F. A. Cotton; W. A. Dollase; Wood, J. S., *J. Am. Chem. Soc.* **1963,** 85, 1543.
225. Keulen, E.; Jellinek, F., *J. Organomet. Chem.* **1966,** 5, (5), 490-2.
226. Haaland, A., *Acta Chem. Scand* **1965,** 19, 41.
227. R. L. Williamson; Hall, M. B., *Int. J. Quantum Chem.* **1987,** 21, 503.
228. Luthi, H. P., *J. Mol. Struct. (THEOCHEM)* **1996,** 388, 299.

229. Yasuike, T.; Yabushita, S., *J. Phys. Chem. A* **1999,** 103, (23), 4533-4542.
230. Pandey, R.; Rao, B. K.; Jena, P.; Blanco, M. A., *J. Am. Chem. Soc.* **2001,** 123, (16), 3799-3808.
231. R. Sahnoun; Mijoule, C., *J. Phys. Chem. A* **2001,** 105, 6176.
232. Rayon, V. M.; Frenking, G., *Organometallics* **2003,** 22, 3304.
233. King, W. A.; Di Bella, S.; Lanza, G.; Khan, K.; Duncalf, D. J.; Cloke, F. G. N.; Fragala, I. L.; Marks, T. J., *J. Am. Chem. Soc.* **1996,** 118, (3), 627-35.
234. Dolg, M., *J. Chem. Inf. Comput. Sci.* **2001,** 41, 18.
235. Schaefer, L.; Southern, J. F.; Cyvin, S. J., *Spectrochimica Acta, Part A: Molecular and Biomolecular Spectroscopy* **1971,** 27, (7), 1083-90.
236. Fuller, J. F.; Li, S.; Sohnlein, B. R.; Rothschopf, G. K.; Yang, D.-S., *Chem. Phys. Lett.* **2002,** 366, (1,2), 141-146.
237. Ross, R. B.; Powers, J. M.; Atashroo, T.; Ermler, W. C.; LaJohn, L. A.; Christiansen, P. A., *J. Chem. Phys.* **1990,** 93, (9), 6654.
238. Hay, P. J.; Wadt, W. R., *J. Chem. Phys.* **1985,** 82, 299.
239. Hay, P. J.; Wadt, W. R., *J. Chem. Phys.* **1985,** 82, 270.
240. Hay, P. J.; Wadt, W. R., *J. Chem. Phys.* **1985,** 82, 284.
241. Cundari, T. R.; Stevens, W. J., *J. Chem. Chem. Phys.* **1993,** 98, 5555.
242. Stevens, W. J.; Basch, H.; Krauss, M., *J. Chem. Phys.* **1984,** 81, 6026.
243. Stevens, W. J.; Krauss, M.; Basch, H.; Jasien, P. G., *Can. J. Chem.* **1992,** 70, 612.
244. Bergner, A.; Dolg, M.; Kuechle, W.; Stoll, H.; Preuss, H., *Mol. Phys.* **1993,** 80, 1431.
245. Dolg, M.; Stoll, H.; Preuss, H.; Pitzer, R. M., *J. Phys. Chem.* **1993,** 97, 5852.
246. Dolg, M.; Wedig, U.; Stoll, H.; Preuss, H., *J. Chem. Phys.* **1987,** 86, 866.
247. Lide, D. R.; Frederikse, H. P. R., *CRC Handbook of Chemistry and Physics*. 78 ed.; CRC: New York, 1997.
248. Skinner, H. A.; Connor, J. A., *Pure & Appl. Chem.* **1985,** 57, (1), 79.
249. Wadt, W. R.; Hay, P. J., *J. Chem. Phys.* **1985,** 82, 284.
250. Cundari, T. R.; Stevens, W. J., *J. Chem. Phys.* **1993,** 98, 5555.
251. Cotton, F. A., *Chemical Applications of Group Theory*. 3rd ed.; Wiley: New York, 1990.
252. Elschenbroich, C.; Salzer, A., *Organometallics*. 2nd ed.; VCH: Weinheim, 1992.
253. Bauschlicher, C. W.; Partridge, H.; Langhoff, S. R., *J. Phys. Chem.* **1992,** 96, 3273.
254. Salama, F., *NATO ASI Series, Series C: Mathematical and Physical Sciences* **1996,** 487, (Cosmic Dust Connection), 103-115.
255. Boissel, P., *Astron. Astrophys.* **1994,** 285, L33-L36.
256. Ma, J. C.; Dougherty, D. A., *Chem. Rev.* **1997,** 97, 1303-1324.
257. Armentrout, P. B., *Topics in Organometallic Chemistry* **1999,** 4, (Organometallic Bonding and Reactivity), 1-45.
258. Pomije, M. K.; Kurth, C. J.; Ellis, J. E.; Barybin, M. V., *Organometallics* **1997,** 16, 3582-3587.
259. Arrais, A.; Diana, E.; Gervasio, G.; Gobetto, R.; Marabello, D.; Stanghellini, P. L., *Eur. J. Inorg. Chem.* **2004**, 1505-1513.
260. Connor, J. A.; Martinho-Simoes, J. A.; Skinner, H. A.; Zafarani-Moattar, M. T., *J. Organomet. Chem.* **1979,** 179, 331-356.

261. Ellis, J. E.; Blackburn, D. W.; Yuen, P.; Jang, M., *J. Am. Chem. Soc.* **1993,** 115, 11616-11617.
262. Thompson, R. L.; Lee, S.; Rheingold, A. L.; Cooper, N. J., *Organometallics* **1991,** 10, 1657-1659.
263. Graceffa, P.; Tuttle, T. R., *J. Phys. Chem.* **1972,** 77, (12), 1566-1567.
264. Hush, N. S.; Rowlands, J. R., *Molecular Physics* **1963,** 6, 201-8.
265. Goldberg, I. B.; Bolton, J. R., *J. Phys. Chem.* **1970,** 74, 1965.
266. Canters, G. W.; Corvaja, C.; Boer, E., *J. Chem. Phys.* **1971,** 54, 3026.
267. Konishi, S.; Morioka, Y.; Nakagawa, I., *Chem. Phys. Lett.* **1978,** 55, (3), 428-430.
268. Morand, P. D.; Francis, C. G., *Inorg. Chem.* **1985,** 24, 56-61.
269. Amunugama, R.; Rodgers, M. T., *Inter. J. Mass Spectrom.* **2003,** 227, 1-20.
270. Boissel, P.; Marty, P.; Klotz, A.; Parseval, P.; Chaudret, B.; Serra, G., *Chem. Phys. Lett.* **1995,** 242, 157-162.
271. Dunbar, R.; Uechi, G. T.; Asamoto, B., *J. Am. Chem. Soc.* **1994,** 116, 2466-2470.
272. Barbu, K. L.; Schiedt, J.; Weinkauf, R.; Schlag, E. W.; Niles, J. M.; Xu, S.-J.; Thomas, O. C.; Bowen, K. H., *J. Chem. Phys.* **2002,** 116, (22), 9663-9671.
273. Zhao, Y. L.; Lin, C. S.; Zhang, R. Q.; Wang, R. S., *J. Chem. Phys.* **2005,** 122, 194322/1-194322/6.
274. Mecozzi, S.; West, A. P.; Dougherty, D. A., *Proc. Natl. Acad. Sci. USA* **1996,** 93, 10566-10571.
275. Hashimoto, S.; Ikuta, S., *J. Molec. Struct. (Theochem)* **1999,** 468, 85-94.
276. Dunbar, R. C., *J. Phys. Chem. A* **1998,** 102, 8946-8952.
277. Ma, N. L., *Chem. Phys. Lett.* **1998,** 297, 230-238.
278. Sohnlein, B. R.; Yang, D. S., *J. Chem. Phys.* **2006,** 124, 134305/1-134305/8.
279. Sohnlein, B. R.; Li, S.; Yang, D.-S., *J. Chem. Phys.* **2005,** 123, 214306/1-214306/7.
280. Ketkar, N.; Fink, M., *J. Mol. Struct.* **1981,** 77, 139.
281. Cockett, M. C. R.; Ozeki, H.; Okuyama, K.; Kimura, K., *J. Chem. Phys.* **1993,** 98, (10), 7763-7772.
282. Scully, D. B.; Whiffen, D. H., *Spectrochim. Acta* **1960,** 16, 1409.
283. Schultz, N. E.; Zhao, Y.; Truhlar, D. G., *J. Phys. Chem. A* **2005,** 109, 11127-11143.
284. Sohnlein, B. R.; Yang, D. S., *J. Chem. Phys.* **2005,** submitted.
285. Lee, C.; Yang, W.; Parr, R. G., *Phys. Rev. B* **1988,** 37, (2), 785-789.
286. Perdew, J. P., *Phys. Rev. B* **1986,** 33, (12), 8822-8824.
287. Perdew, J. P.; Burke, K.; Wang, Y., *Phys. Rev. B* **1996,** 54, (23), 16533-16539.
288. Winter, M. WebElements™, The Periodic Table on the World Wide Web. http://www.webelements.com/
289. Charbonneau, G.-P.; Delugeard, Y., *Acta Crystallogr. B* **1976,** 32, 1420.
290. Hargreaves, A.; Rizvi, S. H., *Acta Cryst.* **1962,** 15, 365-73.
291. Almenningen, A.; Bastinasen, O.; Fernholt, L.; Cyvin, B. N.; Cyvin, S. J.; Samdal, S., *J. Mol. Struct. (Theochem)* **1985,** 128, 59.
292. Grein, F., *J. Phys. Chem. A* **2002,** 106, (15), 3823.
293. Goller, A.; Grummt, U.-W., *Chem. Phys. Lett.* **2000,** 321, 399.
294. Tsuzuki, S.; Uchimaru, T.; Matsumura, K.; Mikami, M.; Tenabe, K., *J. Chem. Phys.* **1999,** 110, (6), 2858.

295. Elschenbroich, C.; Heck, J., *J. Am. Chem. Soc.* **1979,** 101, (22), 6773.
296. Kupfer, V.; Thewalt, U., *Z. Anorg. Allg. Chem.* **2001,** 627, 1423.
297. Porter, L. C.; Bodige, S.; Selnau, H. E. J.; Murray, H. H. I.; McConnachie, J. M., *Organometallics* **1995,** 14, (9), 4222.
298. Geiger, W. E.; van Order, N. J.; Pierce, D. T.; Bitterwolf, T. E.; Rheingold, A. L.; Chasteen, N. D., *Organometallics* **1991,** 10, (7), 2403.
299. Perthuisot, C.; Edelbach, B. L.; Zubris, D. L.; Jones, W. D., *Organometallics* **1997,** 16, (10), 2016.
300. Ma, X.; Liu, L.; Jin, J.; Stair, P. C.; Ellis, D. E., *Abstracts of Papers, 230th ACS National Meeting, Washington, DC, United States, Aug. 28-Sept. 1, 2005* **2005**, GEOC-044.
301. Pettijohn, T. M.; Lagowski, J. J., *J. Organomet. Chem.* **1988,** 356, (1), 67.
302. Huang, Y.; Ranatunga, D. R. A.; Freiser, B. S., *J. Am. Chem. Soc.* **1994,** 116, 4796.
303. *GAUSSIAN98*, Revision A.11; Gaussian, Inc.: Pisttsburgh, 2001.
304. Wang, X.; Yang, D.-S., *J. Phys. Chem. A* **2004,** 108, (31), 6449-6451.
305. Sohnlein, B. R.; Li, S.; Yang, D. S., *J. Chem. Phys.* **2005,** 123, (21), 214306/1-214306/7.
306. Slater, J. C., *J. Chem. Phys.* **1964,** 39, 3199.
307. Bermann, E. D.; Robinavitz, M.; Aroney, M. J.; Fevre, R. J. W. L.; Radom, C.; Ritchie, G. L. D., *J. Chem. Soc. B* **1968**, 1551.
308. Cheng, C. L.; Murthy, D. S. N.; Ritchie, G. L. D., *Journal of the Chemical Society, Faraday Transactions 2: Molecular and Chemical Physics* **1972,** 68, (Pt. 10), 1679-90.
309. Nori-shargh, D.; Asadzadeh, S.; Ghanizadeh, F.-R.; Deyhimi, F.; Amini, M. M.; Jameh-Bozorghi, S., *Theochem* **2005,** 717, (1-3), 41-51.
310. Cioslowski, J.; Piskorz, P.; Moncrieff, D., *Journal of Organic Chemistry* **1998,** 63, (12), 4051-4054.
311. Cioslowski, J.; Piskorz, P.; Liu, G.; Moncrieff, D., *Journal of Physical Chemistry* **1996,** 100, (50), 19333-19335.
312. Todeschini, R.; Gramatica, P.; Provenzani, R.; Marengo, E., *Chemometrics and Intelligent Laboratory Systems* **1995,** 27, (2), 221-9.
313. Wang, X.; Ye, S., *Guangpuxue Yu Guangpu Fenxi* **1994,** 14, (2), 25-30.
314. Tsuzuki, S.; Tanabe, K.; Nagawa, Y.; Nakanishi, H., *Journal of Molecular Structure* **1990,** 216, 279-95.
315. Gustav, K.; Kempka, U.; Suehnel, J., *Chemical Physics Letters* **1980,** 71, (2), 280-3.
316. Gamba, A.; Rusconi, E.; Simonetta, M., *Tetrahedron* **1970,** 26, (3), 871-7.
317. Gutsev, G. L.; Bauschlicher, C. W., *Journal of Physical Chemistry A* **2003,** 107, (23), 4755-4767.
318. Sohnlein, B. R.; Shenggang, L.; Yang, D. S., *J. Chem. Phys.* **2005,** 123, 214306(1)-214306(7).
319. Sohnlein, B. R.; Fuller, J. F.; Yang, D. S., **Unpublished results, 2006**.
320. Sansonetti, J. E.; Martin, W. C., *Handbook of Basic Atomic Spectroscopic Data*. National Institute of Standards and Technology: Gaithersburg, 2003.

321. Neuhauser, R. G.; Siglow, K.; Neusser, H. J. r., *J. Chem. Phys.* **1997,** 106, (3), 896-907.
322. Ruscic, B.; Kovac, B.; Klasinc, L.; Gusten, H., *Z. Naturforsch. A* **1978,** 33A, 1006.

VITA

Personal

Born June 5, 1979 in Cincinnati, OH, USA

Education

B.Sc., Chemistry, University of Kentucky, Lexington, KY, 2001

Awards

Tuttle Fellowship Award, 2002 – 2007
UK Center for Computational Sciences Graduate Fellowship, 2004 – 2005
Department of Chemistry Fast Start Award, 2003
Chemistry Teaching Assistant of the Year Award, 2002
Cincinnatus Merit Scholarship, 1997 – 1999

Professional Experience

Graduate Research Assistant, University of Kentucky, 2002 – Present
Advisor: Professor Dong-Sheng Yang

Graduate Teaching Assistant, University of Kentucky, 2002 – 2004, 2007
Supervisors: Professor Dong-Sheng Yang and Dr. Manjiri Patwardhan

Course Lecturer, University of Kentucky, 2005
Coordinator: Paula Arnett

Laboratory Technician, Envirodata, 2001 – 2002
Supervisor: Robert King

Laboratory Technician, Proctor and Gamble, 2000
Supervisor: Emanuel Santos

Research Publications

1. Sohnlein, Bradford R.; Yang, Dong-Sheng. "Electronic States of Neutral and Cationic Bis(benzene) Titanium and Vanadium Sandwich Complexes: High-Resolution Photoelectron Spectroscopy and Theoretical Calculations," submitted to *J. Chem. Phys. A* (May 2007).
2. Sohnlein, Bradford R.; Fuller, Jason F.; Yang, Dong-Sheng. "Clamshell Structure of Sc(biphenyl) from High Resolution Photoelectron Spectroscopy," *J. Am. Chem. Soc.* **128**, 10692 (2006).
3. Sohnlein, Bradford R.; Yang, Dong-Sheng. "Pulsed-field ionization electron spectroscopy of group 6 metal (Cr, Mo, and W) bis(benzene) sandwich complexes," *J. Chem. Phys.* **124**(13), 134305 (2006).
4. Sohnlein, Bradford R.; Li, Shenggang; Yang, Dong-Sheng. "Electron-spin multiplicities and molecular structures of neutral and ionic scandium-benzene complexes," *J. Chem. Phys* **123**(21), 214306 (2005).
5. Sohnlein, Bradford R.; Li, Shenggang; Fuller, Jason F.; Yang, Dong-Sheng. "Pulsed-field ionization electron spectroscopy and binding energies of alkali metal-dimethyl ether and -dimethoxyethane complexes," *J. Chem. Phys*. **123**(1), 014318 (2005).
6. Li, Shenggang; Sohnlein, Bradford R.; Yang, Dong-Sheng; Miyawaki, Jun; Sugawara, Ko-Ichi. "Pulsed-field ionization electron spectroscopy and conformation of copper-diammonia," *J. Chem. Phys.* **122**(21), 214316 (2005).
7. Li, Shenggang; Fuller, Jason F.; Wang, Xu; Sohnlein, Bradford R.; Bhowmik, Paragranjita; Yang, Dong-Sheng. "Photoelectron spectroscopy and density functional theory of puckered ring structures of Group 13 metal-ethylenediamine," *J. Chem. Phys.* **121**(16), 7692 (2004).
8. S. Li, G. K. Rothschopf, B. R. Sohnlein, J. F. Fuller, and D.-S. Yang, "Zero Electron Kinetic Energy Photoelectron and Threshold Photoionization Spectroscopy of M-X$(CH_3)_3$ (M = Ga, In; X = P, As)," *J. Can. Chem.* (G. Herzberg Special Memorial Issue, June 2004).
9. S. Li, B. R. Sohnlein, G. K. Rothschopf, J. F. Fuller and D.-S. Yang, "Pulsed-Field Ionization Zero Electron Kinetic Energy Spectroscopy and Theoretical Calculations of Copper Complexes: Cu-X$(CH_3)_3$ (X = N, P, As),"*J. Chem. Phys.* **119**, 5406 (2003).
10. S. Li, J. F. Fuller, B. R. Sohnlein, and D.-S. Yang, "Zero Electron Kinetic Energy Photoelectron Spectroscopy and Density Functional Theory Calculations of Gallium-Methylamine Complexes," *J. Chem. Phys.* **119**, 8882 (2003).
11. S. Li, G. K. Rothschopf, B. R. Sohnlein, and D.-S. Yang, "Ionization and Dissociation Energies of Group 13 Metal Complexes with Group 15 Hydrides," *J. Phys. Chem. A* **106**, 6941 (2002).
12. J. F. Fuller, S. Li, B. R. Sohnlein, G. K. Rothschopf, and D.-S. Yang, "A Photoionization and Photoelectron Study of Vibrational and Electronic Cooling in Metal Molecular Beams," *Chem. Phys. Lett.* **366**, 141 (2002).
13. S. Li, G. K. Rothschopf, D. Pillai, B. R. Sohnlein, B. M. Wilson, and D.-S. Yang, "Spectroscopy and Calculations of Weakly Bound Gallium Complexes with Ammonia and Monomethylamine," *J. Chem. Phys.* **115**, 7968 (2001).